Materials Informatics Approaches Towards the Acceleration of Hard Metal Development



Joshua Berry

Department of Materials Science and Engineering

The University of Sheffield

A Thesis Submitted For The Degree of Doctor of Philosophy

2024

Preface

This thesis is submitted for the degree of Doctor of Philosophy at the University of Sheffield. The work described herein was carried out in the Department of Materials Science and Engineering at the University of Sheffield between October 2020 and September 2024 under the supervision of Prof. Katerina A. Christofidou. I, the author, confirm that the thesis is my own work. Except where reference is made to the work of others, the content of this thesis is entirely original. I am aware of the University's guidance on the use of unfair means (`www.sheffield.ac.uk/ssid/unfair-means`). This work has not been previously presented for an award at this, or any other, university. This thesis does not exceed the prescribed word limit of 80,000 words by the faculty of engineering.

Parts of this thesis have already been published:

Chapter 1

> [1] - Berry, J. and Christofidou, K.A. Supervised machine learning for multi-principal element alloy structural design. *Mater. Sci. Technol.* **41**(11), 773–790 (2025)

Chapters 3, 4, and 5

> [2] - Berry, J. *et al.* Design and Selection of High Entropy Alloys for Hardmetal Matrix Applications Using a Coupled Machine Learning and Calculation of Phase Diagrams Methodology. *Adv. Eng. Mater.* **26**(10), 2302064 (2024)

Acknowledgements

I am indebted to Oerlikon AM GmbH Europe and the EPSRC UK for their financial support for this project.

Firstly I would like to thank Kathy for all her support, encouragement, and invaluable insights over the countless hours I spent in her office. I am incredibly grateful to have had such an incredible supervisor who consistently goes above and beyond to help me be the best I can. I am so appreciative for the opportunities to travel to so many amazing places throughout my PhD journey.

Additionally I would like to thank my unofficial supervisor Lewis, for offering his valuable support and advice from a fresh perspective over the course of my PhD, and to my industrial supervisor Olivier for his industry guidance and prompt responses to all my questions and requests.

I would also like to express my appreciation towards the members of the technical staff, George, Neil, and Sylwester for their invaluable assistance. In particular to Yunus for his technical expertise, endless encouragement and dedicated support in manufacturing the most challenging alloy compositions.

Thank you to my colleagues and friends, to whom I owe so much. To Fran for putting up with me, for all the unforgettable memories, and for sharing all the incredible highs and lows of the PhD, I couldn't have made it this far without you. To Ben, thank you for all the good times that have kept me sane, from the endless office chats, to watching football at the pub and in person, I cannot thank you enough. To Lucy and Elaine, for being the best conference buddies and for always being up for a chat whenever I wandered into their office. Thank you to Mimi for her infectious positivity and to Henry for always being the funniest guy in the room, whether intentional or not.

Most importantly, thank you to my family, to whom I owe everything, none of this would have been possible without you and words cannot describe how grateful I am. To my mum who has supported and encouraged me at every step of the journey, always doing everything she can to help me succeed. To my dad who is always there for me and always reminds me how proud he is, especially when I need to hear it the most. To my brother, who I am so fortunate to have and share so much in common. Finally, to my grandparents, who have been my greatest source of encouragement, always believing in me and reminding me that I can achieve anything I set my mind to.

To Pops, who didn't get to see me finish university.

Abstract

High entropy alloys (HEAs) are a relatively new class of alloys comprising multiple principal elements in either equimolar ratios or with elemental concentrations between 5 and 35 at.%. These alloys exhibit exceptional properties, making them a promising alternative to conventional WC-Co cemented carbides, which have dominated metal tooling applications for nearly a century. HEAs offer the potential to meet the design criteria of metal tooling parts, including wear resistance, ductility, and compatibility with additive manufacturing (AM). However, the vast compositional space occupied by HEAs renders trial-and-error experimental approaches impractical due to time and cost constraints. Thus, machine learning (ML) has emerged as a powerful computational tool, capable of accelerating the alloy design process by predicting microstructural and mechanical properties across unexplored regions of compositional space based on existing experimental data. Herein, ML models were developed and trained to explore the HEA compositional space and identify candidate compositions with properties suitable for tooling applications. These ML-guided predictions were complemented by thermodynamic analysis using the calculation of phase diagrams (CALPHAD) method to refine alloy selection. Subsequently, nine novel alloy compositions were experimentally characterised, incorporating carbon reinforcement to enhance their microstructural and mechanical properties. While ML predictions did not perfectly align with experimental results, the combined ML and CALPHAD approach successfully accelerated alloy discovery, identifying several promising HEA compositions for tooling applications. Building on this success, a second iteration of the ML model was proposed, incorporating an expanded HEA database and an improved construction pipeline. However, the anticipated performance enhancements were not realised, highlighting key challenges and future opportunities for ML in the HEA field. This work underscores the critical need for significantly larger and more diverse experimental HEA datasets, along with standardised data reporting practices. Addressing these limitations will enable ML to realise its full potential in exploring uncharted compositional spaces and advancing HEA development for demanding industrial applications

Contents

Aims and Objectives **1**

Outline **3**

1 Literature Review **5**

1.1 Hardmetals and Cemented Carbides 5

1.1.1 WC-Co Production and Consumption 6

1.1.2 WC-Co Properties and Applications 6

1.1.3 WC-Co Drawbacks and Alternatives 9

1.2 High Entropy Alloys 11

1.2.1 Origins 11

1.2.2 Definition 12

1.2.3 What's in a name? 13

1.2.4 Biases in High Entropy Alloy Studies 13

1.2.5 Interest in High Entropy Alloys 14

1.2.6 Four "Core" Effects 15

1.3 FCC High Entropy Alloys 21

1.3.1 Precipitation Strengthening 23

1.3.2 Carbide Precipitation Strengthening 24

1.4 Hardmetal High Entropy Alloys 26

1.4.1 High Entropy Carbides 28

1.4.2 Hardmetals with High Entropy Alloy Binder 29

1.4.3 High Entropy Carbide Hardmetals with Binder 31

1.5 High Entropy Alloy Design Methodologies 33

1.5.1 Empirical Parameters 33

1.5.2 Empirical Parameter Application 42
1.5.3 CALPHAD: Thermodynamic Modelling 47
1.5.4 Density Functional Theory: Atomistic Modelling 50
1.5.5 Future Design Methodologies 52
1.6 Machine Learning 54
1.6.1 High Entropy Alloy Data 55
1.6.2 Addressing the Availability of High Entropy Alloy Data 56
1.6.3 Addressing the Imbalance of High Entropy Alloy Data 58
1.6.4 High Entropy Alloy Feature Engineering 60
1.6.5 Multicollinearity Analysis 62
1.6.6 High Entropy Alloy Feature Selection 63
1.6.7 Algorithms for High Entropy Alloy Design 65
1.6.8 Model Performance Assessment 67
1.6.9 Model Training 69
1.6.10 Model Hyperparameter Optimisation 69
1.6.11 From Algorithms to Application 70
1.6.12 Experimental Validation of Predictions 72
1.7 Applications of Machine Learning to High Entropy Alloy Design 74
1.8 Summary 77

2 Experimental and Computational Methodology 79
2.1 Material Production Methods 79
2.1.1 Vacuum Arc Melting 79
2.1.2 Homogenisation Heat Treatments 80
2.1.3 Material Preparation 80
2.2 Thermal Analysis Techniques 81
2.2.1 Differential Scanning Calorimetry 81
2.3 X-Ray Diffraction 82
2.4 Microscopy Analysis 83
2.4.1 Optical Microscopy 84
2.4.2 Scanning Electron Microscopy 84
2.5 Chemical Compositional Analysis 86
2.6 Hardness Testing 87

2.7 Additive Manufacturing . . . 88
2.7.1 Laser Passes . . . 88
2.8 Machine Learning Model Construction . . . 89
2.9 Thermodynamic Modelling . . . 89

3 Coupled Machine Learning and CALPHAD Method for Alloy Design 91
3.1 Dataset Selection . . . 93
3.2 Data Cleaning and Preprocessing . . . 93
3.3 Machine Learning Algorithm Selection . . . 94
3.4 Input Features . . . 95
3.5 Random Forest Model Training . . . 98
3.6 Random Forest Hyperparameters Optimisation . . . 100
3.7 Random Forest Performance Assessment . . . 100
3.8 Generation of Virtual Candidate Search Space . . . 106
3.9 High-throughput Machine Learning Predictions and CALPHAD Analysis . 107
3.10 Distribution of Downselected Alloys in Embedded Training Data Space . . 111
3.11 Summary . . . 115

4 Experimental Assessment of Downselected Alloys 117
4.1 Compositional Analysis . . . 117
4.2 Differential Scanning Calorimetry Analysis . . . 118
4.3 Microstructural Analysis of As-Cast and Homogenised Material . . . 119
4.4 Hardness Analysis of As-Cast and Homogenised Material . . . 132
4.5 Summary . . . 137

5 Integrated Machine Learning and Experimental Findings Discussion 139
5.1 Phase Formation and Microstructural Analysis . . . 140
5.1.1 Impact of Training Data Bias on Alloy Downselection . . . 140
5.1.2 Microstructural Characterisation and Observations . . . 142
5.1.3 Comparison of CALPHAD and Experimental Microstructures . . . 149
5.2 Mechanical Property Analysis . . . 149
5.2.1 Micro-Indentation Hardness Measurement Analysis . . . 150
5.2.2 As-Cast vs. Homogenised Material . . . 153
5.2.3 Optical Analysis of Micro-Indentations . . . 153

5.3 Summary . . . 155

6 Carbon Reinforcement and Laser Passes 159

6.1 Thermodynamic Analysis of Carbon Additions to High Entropy Alloys . . 161
6.2 Carbon Reinforcement . . . 164
6.3 Chemical Composition Analysis . . . 165
6.4 SEM and EDS Analysis . . . 166
6.5 X-Ray Diffraction Analysis . . . 173
6.6 Mechanical Property Analysis . . . 179
6.7 Additive Manufacturing Preliminary Trials . . . 184
6.7.1 Methodology . . . 185
6.7.2 Variable Scan Speed Investigation Results . . . 186
6.7.3 Repeated Scan Investigation Results . . . 191
6.8 Summary . . . 194

7 Machine Learning for Alloy Design II 197

7.1 Dataset Construction . . . 197
7.1.1 Data Collation . . . 201
7.1.2 Data Cleaning . . . 202
7.1.3 Target Data Distribution Analysis . . . 204
7.2 Feature Engineering . . . 206
7.2.1 Feature Correlation Analysis . . . 208
7.3 Machine Learning Model Selection . . . 211
7.3.1 Model Training . . . 211
7.3.2 Hardness Model . . . 211
7.3.3 Phase Model . . . 213
7.3.4 Analysis of Phase Prediction Model Performance . . . 216
7.3.5 Limitations and Opportunities for Model Enhancement . . . 221
7.4 Summary . . . 222

8 Concluding Remarks 225

9 Future Work 231

Bibliography 235

Aims and Objectives

The overarching aim of this thesis is to design novel metallic alloys for metal tooling applications, a field currently dominated by WC-Co cemented carbides. These alloys must balance wear resistance and damage tolerance, with hardness and ductility (phase composition) serving as proxies for these properties. The targeting of ductility enhances the alloy suitability for additive manufacturing, enabling the production of complex geometries, repairability, and improved sustainability.

To achieve these aims, this study set out the following objectives:

- Explore the capability of HEAs to meet the requirements of wear resistance, damage tolerance, and suitability for AM.
- Develop and leverage ML methods to screen the vast HEA compositional space, identifying unexplored regions with advantageous properties.
- Apply thermodynamic modelling techniques, such as CALPHAD, to gain deeper insights into phase stability and assist the ML in compositional downselection.
- Experimentally fabricate selected alloy compositions to evaluate their capability to meet the design criteria and validate the ML model predictions.
- Investigate the potential for carbon reinforcement to enhance the mechanical properties of promising alloy compositions to meet the design criteria.
- Assess the suitability of the designed alloy compositions for AM, focusing on their performance and adaptability to AM processes.
- Utilise insights from experimental results and lessons learned from the first ML iteration to guide the next iteration, enabling further screening of the HEA space within a circular design process.

Outline

This thesis begins with a comprehensive literature review in Chapter 1, exploring WC-Co hardmetals, HEAs, HEA design strategies, and the application of ML specifically to HEA development. Chapter 2 details the experimental and computational techniques used, including thermodynamic modelling and ML approaches. The subsequent three chapters are closely interconnected, with each building upon the findings of the previous one to form a continuous narrative. The insights gained in one chapter directly inform the focus and methods of the next. Chapter 3 focuses on the ML process, covering database selection, model training, virtual candidate search space generation, and high-throughput predictions using ML and CALPHAD. Chapter 4 presents the results of experimental fabrication and characterisation of HEA compositions selected through the coupled ML and CALPHAD approach, including analyses of microstructure, phase composition, and mechanical properties. This is followed by a combined discussion of the experimental findings and their implications for the ML process and outputs in Chapter 5. Chapter 6 describes the development and characterisation of fabricated carbon-reinforced HEAs and preliminary bead-on-plate trials to assess the amenability of these compositions towards additive manufacturing. Chapter 7 discusses the second iteration of ML, focusing on construction of an expanded database and improved feature space, trials of multiple ML models, and an analysis of the resulting predictions. Finally, the thesis concludes with a summary of the key findings and their implications, followed by recommendations for potential areas of future study that naturally lead on from the work already undertaken.

Chapter 1

Literature Review

1.1 Hardmetals and Cemented Carbides

Smaller atoms such as B, C, and N can fit into the interstices of aggregates of larger transition metal atoms to form boride, carbide, and nitride compounds. These compounds are extremely hard electronic conductors, thus are commonly known as "hardmetals" [3]. Hardmetals, of which cemented carbides are a class of, are composite materials with hard but brittle carbides embedded within a ductile metallic binder phase. The role of this metallic binder phase is to improve the toughness of the material without impacting the high hardness offered by the carbides, enabling plastic deformation to absorb energy without fracturing [4]. This hardmetal structure is fairly unique as the matrix binder phase is the minority phase within the microstructure [5].

In 1906, it was discovered that carbon can form extremely hard WC crystals [3]. Taking advantage of the high hardness of these carbides, in 1923, the first cemented carbides were created by Karl Schroeter at Osram Studiengeselleschaft, Germany [4, 5]. Subsequently, in 1927, workers at Krupp in Germany created the first cemented carbide composed of WC-Co [3–6]. WC-Co is still the most common hardmetal used today with $> 80\,\%$ of all cemented carbide grades containing WC, and many of them being pure WC-Co alloys [5].

1.1.1 WC-Co Production and Consumption

WC is currently manufactured via the direct carburisation of W powder, a costly process that first requires the synthesis of high-purity, fine W powder, followed by compaction and heat treatment in a carbon-rich inert atmosphere [7]. WC and Co powders are then sintered under vacuum to produce the WC-Co cemented carbides [8].

Global production of cemented carbides has been accelerating in recent years, largely driven by China's entry into the market. China holds over 54.3 % of the world's tungsten deposits and is the leading producer of tungsten [9], accounting for 83.6 % of global production [10]. In 1993, total global cemented carbide production was 20,000 tonnes, increasing to 30 000 tonnes by 2000 and 60 000 tonnes by 2008. By 2018, consumption had grown to 85 000 tonnes, with China alone consuming 55,000 tonnes, nearly 65 % of the total global consumption [5]. Approximately 54–72 % of globally produced W is used in its monocarbide form for manufacturing WC-Co cemented carbides [11].

1.1.2 WC-Co Properties and Applications

WC-Co cemented carbides primary application is as the major constituents in cutting tools [7, 8]. However, WC-Co is also widely used for drills, metal forming dies, mining tools and wear resistant parts. WC-Co is used in demanding applications due to its exceptional mechanical properties, such as high hardness, toughness, and wear resistance, which arise from the combination of a metallic binder and cubic carbides [10–14]. These properties also enable a significantly longer life span for these demanding applications in comparison to other materials [11]. The performance and service life of the cemented carbide is primarily determined by the metallic binder phase as it is responsible for the toughness and damage tolerance of the material [15]. In comparison to conventional ceramic materials, WC-Co has much higher toughness and ductility. However, when compared to traditional metal alloys, WC-Co possesses slightly lower ductility but a much higher hardness [16]. Additionally, WC is the hardest binary carbide at elevated temperatures [7] and most importantly WC-Co retains this hardness and its mechanical performance up to temperatures of around 600 °C [17–19]. In contrast, carbides such as TiC, are much harder at room temperature, but experience significant drops in hardness as the temperature increases, illustrated in Figure. 1.1 [3].

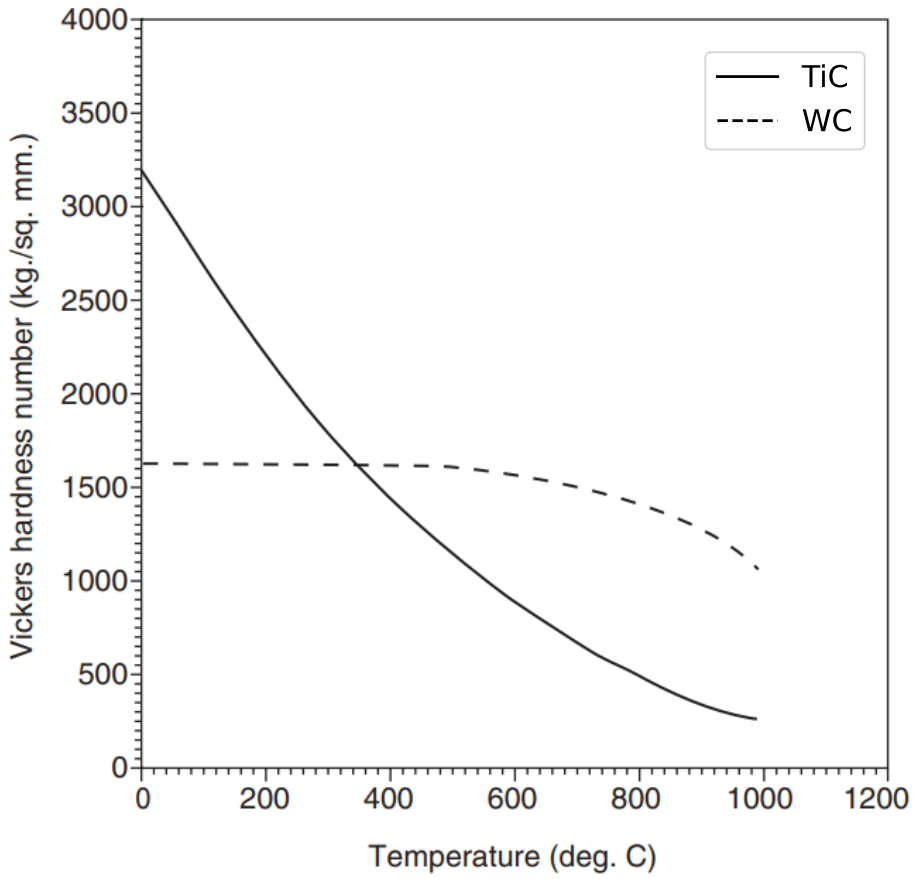


Figure 1.1: Comparison of the hardness of TiC (solid-line) and WC (dashed-line) with increasing temperature, showing the crossover at 350 °C. From Gilman [3].

The hardness and wear resistance of WC-Co originates from the grain size of the WC phase, while the amount of Co binder phase dictates the toughness and ductility of the composite [4, 12, 16]. Figure 1.2, illustrates how altering the grain size and amount of Co binder impacts the mechanical properties and hence application of the cemented carbide. Additionally, as expected the porosity of the cemented carbide impacts the hardness. The smaller the number of pores, the greater the density of the material and thus the greater the hardness [20]. Decreasing the WC grain size to submicrometer or nanometer scale increases the hardness, strength and wear resistance of the cemented carbide but decreases the ductility [5, 12, 21, 22]. WC also has the highest fracture toughness of any of the transition metal carbides because of the high fracture resistance of WC, which is further enhanced through the cementation of the carbides within the Co binder, impeding crack propagation [23]. The WC grains do not undergo fracture in an ideal brittle mode, but instead undergo some plastic deformation prior to fracture [4, 14]. Co is the most common binder phase used in cemented carbides due to its favourable wettability and interfacial bonding strength with WC grains [23, 24]. As previously stated, WC-Co is a unique

material with the matrix binder being the minority phase, typically constituting between 3–30 % of the cemented carbide [11]. A greater Co content leads to improved damage tolerance and ductility but lower overall hardness [5], with a Co content of around 10 % being the most common. Furthermore, strong wettability between the Co binder and WC grains supports the development of the alloy's already excellent mechanical properties [25]. Good wettability means strong interfacial bonds between phases, reduced voids and porosity, thus better densification. Hence, WC-Co hardmetals can be tailored for the desired application by varying the WC grain size and amount of Co binder to obtain the optimal mechanical properties [5, 21].

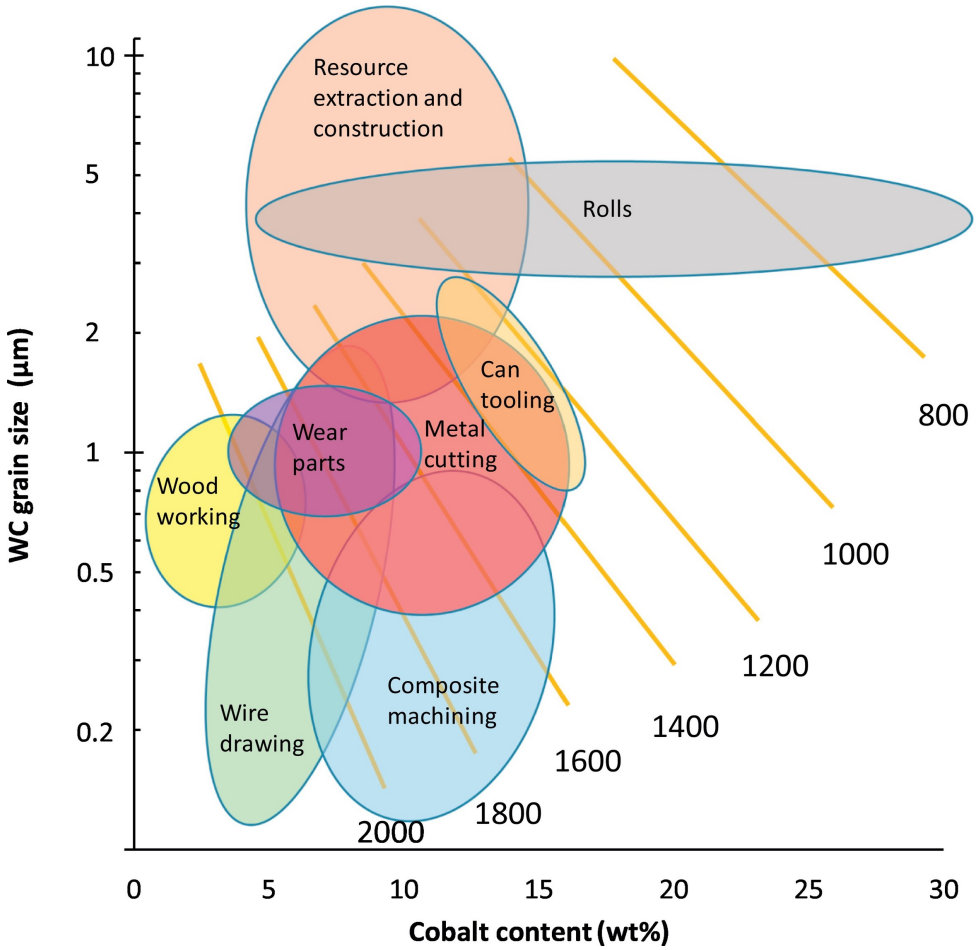


Figure 1.2: How the choice of WC grain size and Co binder content of WC-Co effects the mechanical properties and thus the chosen application of the cemented carbide. The lines indicate the values of hardness measured in HV. Data taken from AB Sandvik and figure from García *et al.* [5].

1.1.3 WC-Co Drawbacks and Alternatives

Over 100 years since the discovery of the first cemented carbides, the clear majority still consist of WC with a Co metal matrix binder and are still the hardmetal of choice for the most demanding cutting and machining applications [4, 26]. Konyashin [6] published a review of the past 100 years of research and innovation within the field of hardmetals. The main development during this period has been the broadening of WC grain size distributions, combined with varying Co binder concentrations, to achieve a diverse set of properties suited to a wide array of applications [26]. Despite these advancements, the primary concerns with regards to WC-Co is the use of Co as the binder material and its manufacturing process. In WC-Co cemented carbides, the Co content is inversely proportional to the hardness, oxidation/corrosion resistance and elevated temperature performance of the hardmetals [16, 23]. However, decreasing the Co content also leads to a decrease in toughness and ductility. In addition, the Co binder's significantly higher oxidation rate compared to the carbide leads to degradation in the hardness of cemented carbides and the formation of microstructural defects at elevated temperatures [15]. Therefore, it is necessary to maintain a low Co fraction to ensure rigidity of the system while also maintaining the exceptional mechanical properties of the cemented carbide [27]. Co also poses a non-negligible health risk, being classified as carcinogenic to humans even at the low concentrations present in WC-Co hardmetals [16]. However, the most critical concern for industry is the extreme price instability Co faces due to the competition for the limited cobalt resources needed in batteries and jet engines, as well as the political instability and ethical considerations associated with mining of Co within Central Africa [9, 28].

Thus, attempts have been made to replace the Co binder with a suitable alternative to reduce health risks, stabilise the material supply chain and lower costs [28]. During the early development of cemented carbides in the 1920s, metals such as Fe, Ni, and Cr were trialled as Co alternatives. In the 1990s and 2000s, intermetallic compounds such as Fe- and Ni-aluminides, as well as ceramics (metal oxides), were investigated [16]. Figure 1.3 shows a conventional WC-Co sample, while Figure 1.4 illustrates the various WC microstructures discussed here.

Calderon *et al.* [30] trialled the use of Cr as a novel binder matrix material, as it had been demonstrated previously that in a high Cr-containing system no classical two-phase region

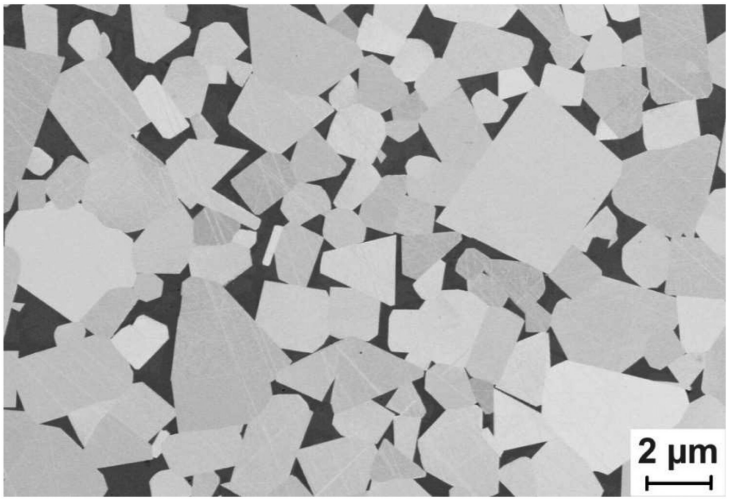


Figure 1.3: SEM micrograph illustrating the typical microstructure of a WC-16 vol.% Co (WC-10 wt.% Co) hardmetal. The bright regions correspond to WC grains, which display a bimodal grain size distribution. The darker regions represent the Co binder phase [29].

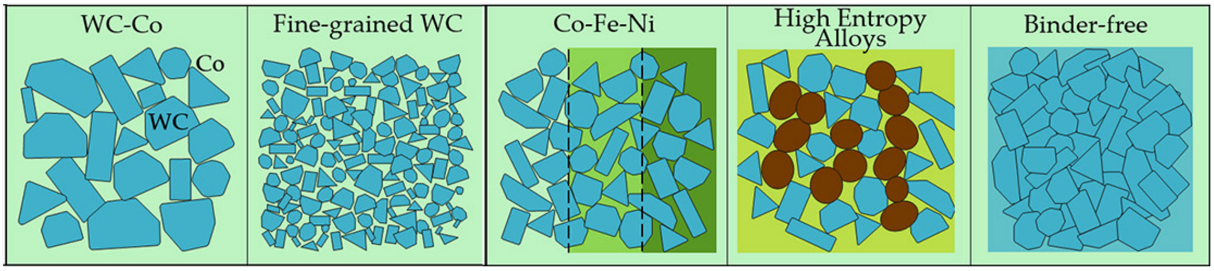


Figure 1.4: An illustration of the cemented carbide microstructures discussed within this work. Modified from García *et al.* [5].

exists [31]. Thus enabling formation of WC plus a single phase binder. However, it was found that if the maximum solubility of the Cr is exceeded then Cr-rich carbides form as Cr reacts with the carbides. The amount of the binder therefore decreases as these Cr-rich carbides form and the binder's properties decline due to the loss of Cr. Another study by Rosa *et al.* [20] attempted to use a ternary Fe-Ni-Nb system as the binder for a WC based cemented carbide. Promising results were found with comparable performance to WC-Co in hardness and fracture toughness assessments, but at higher sintering temperatures. Metal oxides, as previously mentioned, offer a potential Co binder replacement. Fazili *et al.* [32] studied partial substitution of Co with an Al_2O_3 ceramic metal oxide binder, which required a significant increase in sintering temperature and ultimately was found to be detrimental to mechanical properties. However, partial replacement with an equivalent amount of alumina achieved acceptable properties compared to Co-based samples. Similarly, Sandoval *et al.* [33] investigated gradual Co substitution with Ni, building up to full replacement with NiMo. Reporting that partial Ni substitution reduced yield

stress and strain hardening, while full replacement with NiMo improved both properties within the cemented carbide.

Thus far, none of these binder replacements have been successful enough to be commercialised and produced on an industrial scale to replace Co [16]. An alternative solution to the Co problem facing WC-Co cemented carbides is to remove the binder entirely, producing binderless WC. Ultimately, without the metallic binder matrix phase, the WC phase typically achieve full densification and exhibits abnormal grain growth. Silvestroni *et al.* [34] successfully sintered fully dense binderless WC, but this required hot pressing above 1800 °C and the addition of 5 vol.% SiC, technically making it not binderless. Consequently, binderless WC generally exhibits poor bending strength and fracture toughness, making it unsuitable as a WC-Co replacement [23].

Therefore, an alternative material to either replace the WC-Co hardmetals as a whole or specifically the binder material is needed to meet the ever increasing demands for industrial applications. A relatively new class of alloys known as high entropy alloys (HEAs) present a potential solution to this problem and have already shown promise as new matrix binder materials [35, 36].

1.2 High Entropy Alloys

Conventional alloy systems are historically based on the principal of a primary element, chosen for its suitability for the desired application, combined with multiple small additions of minor elements to both enhance the primary alloy properties and enable desirable secondary properties [37, 38]. This design philosophy has resulted in the development of many successful alloy systems, but restricts alloy design by constraining the compositional space [38]. In contrast, HEAs contain multiple principal elements and the numerous possible combinations, each with their own distinct set of properties, offer exciting opportunities for novel alloy design and development in previously unexplored areas of compositional space [39].

1.2.1 Origins

The first work on HEAs is typically attributed to Brian Cantor with his, at the time, undergraduate student Alain Vincent in 1981 [40]. The pair were working on equiatomic

alloys containing a broad range of elemental components. One such alloy system was $Fe_{20}Cr_{20}Ni_{20}Mn_{20}Co_{20}$, that was unexpectedly observed to form a single-phase FCC microstructure [38, 41]. However, it wasn't until 2004 that the concept of HEAs was first communicated to the scientific community with the publication of, "Nanostructured High-Entropy Alloys with Multiple Principal Elements: Novel Alloy Design Concepts and Outcomes" by Yeh *et al.* [42] and "Microstructural development in equiatomic multicomponent alloys" by Cantor *et al.* [43]. These two papers are a significant milestone in the rapid acceleration of research in the HEA field and acceptance of the term HEAs.

1.2.2 Definition

HEAs were originally defined by Yeh *et al.* [42] to be composed of five or more principal elements in either equimolar ratios or with elemental concentrations between 5–35 at.%. This definition implicitly includes alloys with minor elemental additions with atomic percentages even smaller than 5 % [44]. An alternative definition proposed by Miracle *et al.* [45] defines HEAs as any alloy with configurational entropy, $\Delta S_{\text{conf}} \geq 1.5R$ [46]. The configurational entropy is given by,

$$\Delta S_{\text{conf}} = -R \sum_{i=1}^{N} X_i \ln X_i \tag{1.1}$$

where X_i is the atomic fraction of element i, N is the number of elements and R (= 8.314 $\text{J mol}^{-1}\,\text{K}^{-1}$) is the molar gas constant.

The threshold of $1.5R$ was selected as it is approximately the median point for the configurational entropy of a five element, equiatomic system and far exceeds the maximum values observed in conventional alloys such as stainless steels ($1.15R$) and superalloys ($1.37R$) respectively [45, 46]. Although these two definitions seem similar and exhibit some compositional overlap, numerous compositions satisfy only one requirement or the other, and some alloys satisfy neither criterion yet are still labelled HEAs [47]. For example, the alloy $Fe_{5.9}Co_{29.4}Cr_{29.4}Ni_{29.4}Cu_{5.9}$ (at.%) satisfies the compositional definition, but its configurational entropy is only $1.414R$. Consequently, these definitions function as approximate guidelines for identifying HEAs. In most practical cases, HEAs are defined as alloys consisting of large proportions of five or more elements [44].

1.2.3 What's in a name?

HEAs are often referred to almost interchangeably as multi-principal element alloys, multicomponent alloys, complex concentrated alloys, compositionally complex alloys, and baseless alloys [44, 48]. Each term has an individual definition, with HEAs representing single phase, complex concentrated alloys containing intermetallics and multi-principal alloys encompassing everything else [48]. However, for the sake of consistency within this thesis, the term HEA will be used throughout to encompass all classes described above.

1.2.4 Biases in High Entropy Alloy Studies

Early HEA investigations focused on alloy families containing a limited range of transition metals, with Al, Co, Cr, Cu, Fe, Mn, Ni, and Ti being the most commonly used, as shown in Figure 1.5. Prior to 2017, Co, Cr, Fe, and Ni appeared in over 70 % of HEAs made to date [49]. However, the utility of HEAs extends well beyond this example. In recent years, exploration of broader compositional spaces has expanded the field to include refractory HEAs for extreme environments [50–52], noble and precious metal HEAs for electrocatalysis [53, 54], high entropy ceramics and oxides [55], high entropy carbides (HECs) [56, 57], and rare-earth-based HEAs [58–60].

One of the first HEAs, the equiatomic CrMnFeCoNi [43], was reported as a single-phase solid solution forming alloy. This shaped early HEA research toward single-phase solid solution microstructures with crystallographically simple phases [49]. A significant point of contention in the early HEA literature was whether alloys with more than one phase could still be classified as HEAs [45]. Consequently, initial HEA studies focused heavily on single-phase solid solutions [61]. However, this focus differs from that of alloys already in service, which often rely on intermetallic or ceramic strengthening phases to balance strength with damage tolerance [62]. Subsequently, research has shifted toward more technologically relevant microstructures such as multiphase HEAs [63, 64], including those with precipitation-hardened microstructures [65, 66] and eutectic compositions [67, 68].

Nevertheless, approximately 70 % of HEA microstructure studies focus solely on as-cast alloys, which do not represent the equilibrium state and may not reflect industrial applications. Furthermore, annealing these HEA systems often leads to multiple solid solution and intermetallic phases, even when the as-cast microstructure was single-phase [49, 69].

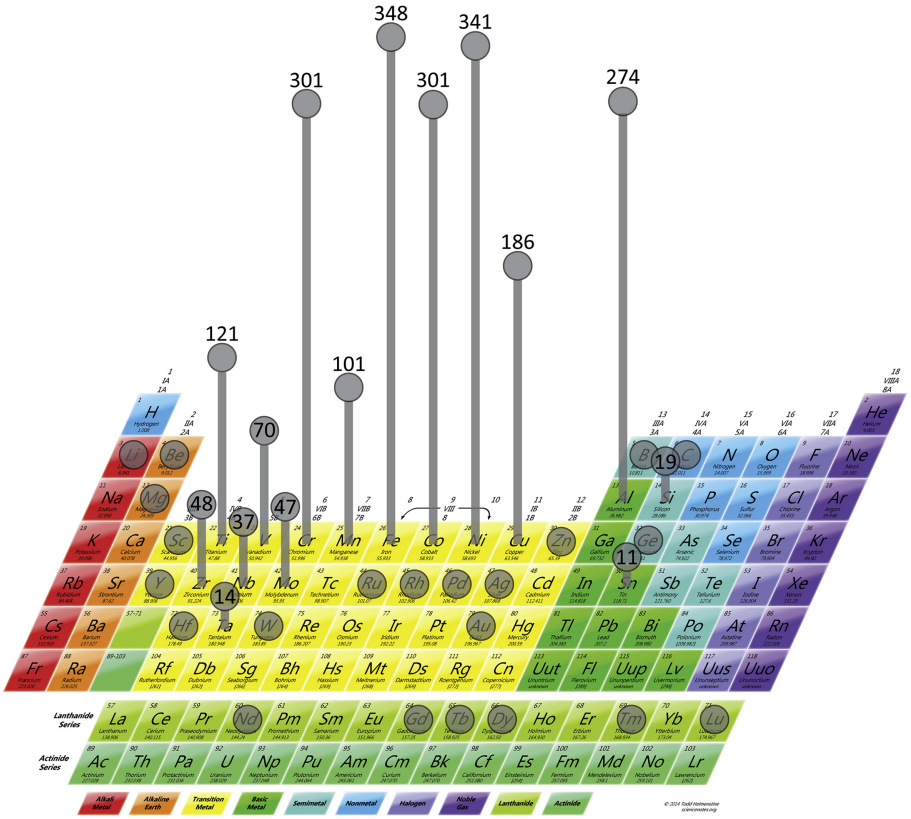


Figure 1.5: A periodic table illustrating the frequency with which elements are used in the 408 HEAs collected by Miracle *et al.* [49] No number is given when an element is used in fewer than ten alloys.

1.2.5 Interest in High Entropy Alloys

The popularity of HEAs in the material science community over the past decade has been rapidly increasing [70]. In 2022, there were 1 635 publications on HEAs in the material science field, with the number of publications increasing to 1 860 in 2023. So far in 2024 there have been 1 551 publications on HEAs within material science. Figure 1.6 illustrates the rapid increase in publications on HEAs from their inception in 2004 to August 2024.

Furthermore, a significant number of reviews on the state of the HEA field, such as those by Miracle *et al.* [49, 72], George *et al.* [73, 74] and Pickering *et al.* [62] have been published, providing both optimistic and critical assessments of the key ideas and outlook of the HEA field [75]. Scientific interest in HEAs originates from the potential to tailor their microstructural and mechanical properties by altering the elemental composition [76]. Consequently, HEAs can be designed with attractive properties for both structural and functional applications [48, 77]. However, these advantageous properties are primarily related to the combinations of elements used, rather than any "HEA effects".

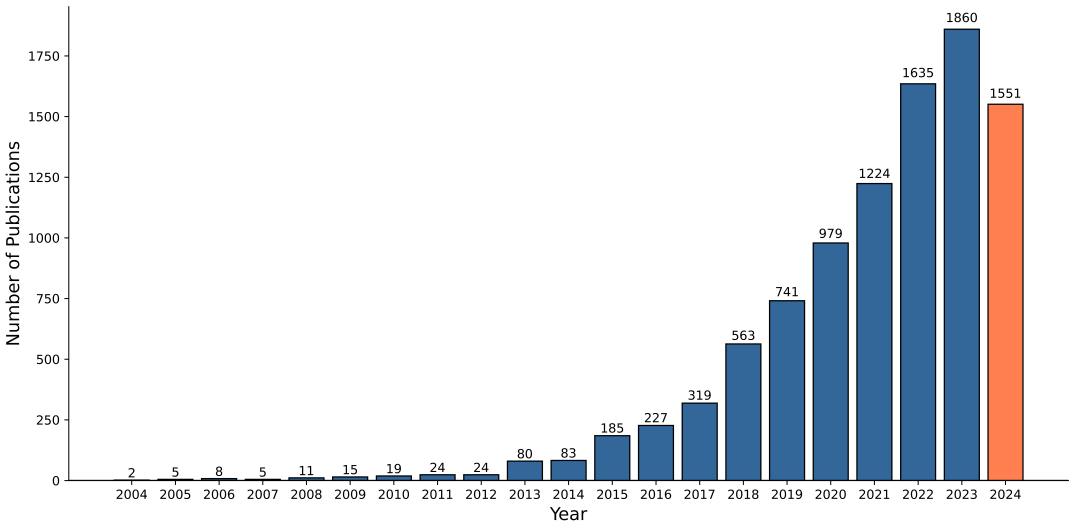


Figure 1.6: The publication rate for HEA literature since 2004 as of 03/08/24. Data gathered from Scopus [71] by searching for "High Entropy Alloy" in the journal article title.

Another key motivation for the exploration of the HEA space is the theoretically vast number of possible compositions, each potentially exhibiting combinations of desirable mechanical properties that remain largely unexplored [43, 61, 70]. This combinatorial complexity renders traditional trial-and-error alloy design methodologies impractical. However, recent work by Raymundo Arroyave and co-workers [78] highlights that when realistic, application-specific constraints are applied to the design space, only a small fraction of the nominal HEA space remains feasible. In their study of the WMoVTaNbAl system, just 0.54 % of the original compositional space met these criteria, reinforcing the view that while the HEA design space is large in principle, it is considerably narrower in practice when filtered for functional relevance.

1.2.6 Four "Core" Effects

Following Yeh *et al.*'s seminal paper in 2004 [42], Yeh and co-authors continued their research [79] and from this work in 2006 [80] proposed four "core" effects that influence the physical metallurgy of HEAs. The significance of these "core" effects has been consistently emphasised in numerous HEA studies, shaping the direction of much of the research in this field. However, the validity of these core effects is under question with evidence to the contrary. [62, 70].

High Entropy Effect

The definition of HEAs provided by Yeh *et al.* [42] was originally intended to encompass the range of compositions, for which the configurational entropy could overcome the enthalpy of formation of competing brittle intermetallic phases. Hence, favouring the formation of single-phase solid solution microstructures [62, 72]. However, there is limited evidence to support the idea of entropic stabilisation in HEAs. The equation for configurational entropy, Equation 1.1, shows that as the number of constituent elements in the alloy X_i, increases, the configurational entropy also increases. Configurational entropy also increases when the composition approaches the equimolar composition [81]. Hence, it would be expected that increasing the number of elements would increase the likelihood of single-phase solid solution formation. However, it is not just the number of different elements in a system, but which elements are present that determines the formation enthalpy of single-phase solid solutions or multiple phases, including brittle intermetallics.

At thermodynamic equilibrium, the phases present in the alloy depend on whether the Gibbs free energy of mixing,

$$\Delta G_{\text{mix}} = \Delta H_{\text{mix}} - T\Delta S_{\text{mix}}, \tag{1.2}$$

is more or less negative than the free energies of formation,

$$\Delta G_f = \Delta H_f - T\Delta S_f, \tag{1.3}$$

of all the possible intermetallic compounds of the HEA system [73].

It is not necessary for 100 % of the binary pairs of elements to transform entirely into binary intermetallic compounds; rather, intermetallics can precipitate within a solid solution that is rich in one of the elements. Another possibility is that the mixture decomposes into two solid solutions with different compositions, crystal structures, and/or lattice parameters, rather than forming a single solid solution.

Cantor *et al.* [43] also produced equiatomic alloys, containing 16 or 20 elements, which did not produce single-phase solid solutions, but instead formed multiple phases. Otto *et al.* [82] also investigated the effects of configurational entropy on the stabilisation of the single-phase solid solution in the equiatomic CrMnFeCoNi alloy. Different elements,

Cu, Mo, Ti and V, were substituted into the alloy one at a time, because if the total number of elements remains the same, then the configurational entropy of the alloy remains unchanged, according to Equation 1.1. Therefore, Otto *et al.* [82] expected that the alloy with the substituted elements would also to form a single-phase solid solution if the configurational entropy of HEAs was the controlling factor. However, configurational entropy is only one factor influencing phase stability. The substitution of different elements alters the enthalpy of mixing due to changes in atomic size, electronegativity, and bonding tendencies. Therefore, although the entropy term is preserved, changes in enthalpic interactions may still lead to differences in phase formation behaviour. Thus, only the base CrMnFeCoNi alloy was seen to produce a single-phase solid solution, with all modified alloys producing multiphase systems, including intermetallic, μ and σ phases. Otto *et al.* [82] concluded that if the alloy contains elements that are prone to form phases with each other in binary pairs, then this is typically replicated in the microstructure of the multiple primary component HEA. Further studies conducted by Otto *et al.* [69] on the CrMnFeCoNi alloy demonstrated the decomposition of the HEA to multiple phases after prolonged anneals of 500 days at temperatures below 800 °C. The heat treatments were performed over 500 days to approach thermodynamic equilibrium conditions, moving away from the traditional analysis of as-cast or short term annealed HEAs. At both 500 °C and 700 °C intermetallic structures were observed in the alloy, indicating that the single-phase structure is not thermodynamically stable at these lower temperatures. Instead, its persistence under standard processing conditions is due to sluggish diffusion and kinetic barriers. This suggests that entropic stabilisation can delay but not entirely prevent phase separation when given sufficient time to reach equilibrium [69].

Thus, the experimental evidence points to configurational entropy playing a limited role in HEA phase formation. Configurational entropy alone does not control the formation of solid solutions within HEAs [81]. There is limited evidence of entropic stabilisation of HEAs, with entropy, enthalpy and the competition between the two needing to be carefully considered, in the control of solid solution phase selection and stability [82, 83].

Lattice Distortion Effect

Another core principle associated with HEAs is lattice distortion, with every atom being theoretically surrounded by a different type of atom [38]. The elements in HEAs are

proposed to be randomly distributed across the lattice, resulting in an arrangement of far greater complexity than conventional dilute alloys [84], as demonstrated by the schematic in Figure 1.7. Elements of different atomic sizes will displace their neighbouring atoms from their ideal lattice positions, producing a highly strained structure due to the atomic size difference. The resulting local strain field will interact with and impede the motion of gliding dislocations in the material, potentially resulting in a significant amount of solid solution strengthening [62, 84].

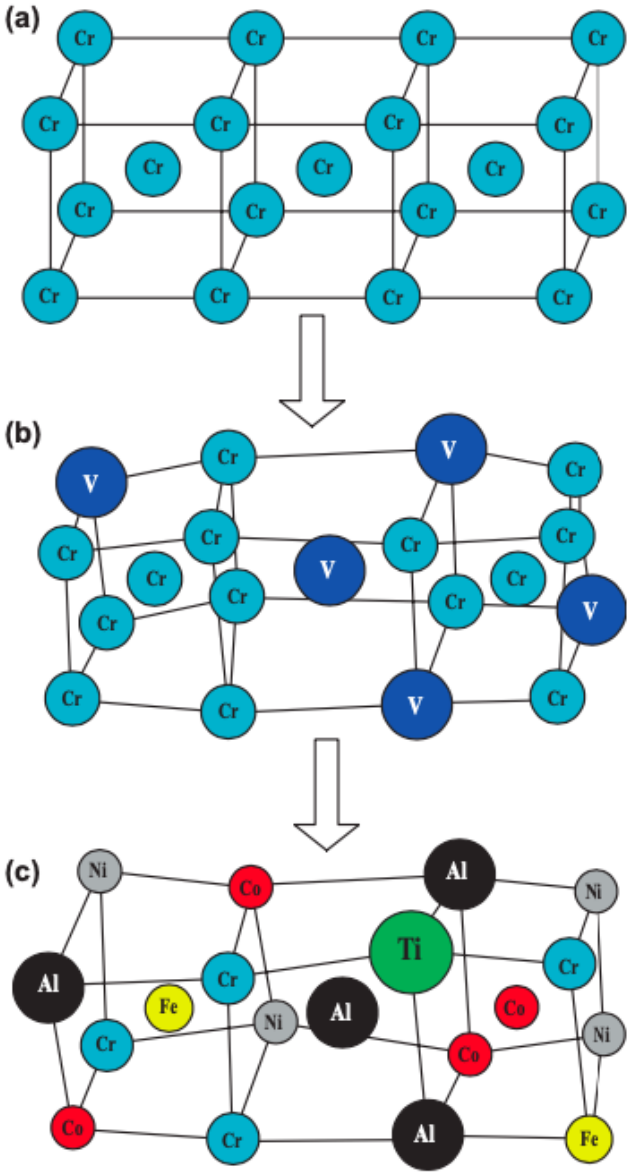


Figure 1.7: Schematic representation of the greater complexity of lattice arrangement and hence lattice distortion in HEAs (c), compared to pure elements (a) and conventional alloys (b). From Zhang *et al.* [85].

Nevertheless, it is theoretically unreasonable to assume that HEA lattices are distorted. Firstly, the Hume-Rothery rules state that a solid solution is unstable or less likely to form if the atomic size mismatch is $> 15\,\%$ [86]. Secondly, experimental measurements of the lattice strain in six single-phase FCC solid solutions, including equiatomic CrMnFeCoNi, conducted by Owen *et al.* [84] and shown in Figure 1.8, found no clear evidence that the strain in HEAs was disproportionally higher compared to conventional alloys.

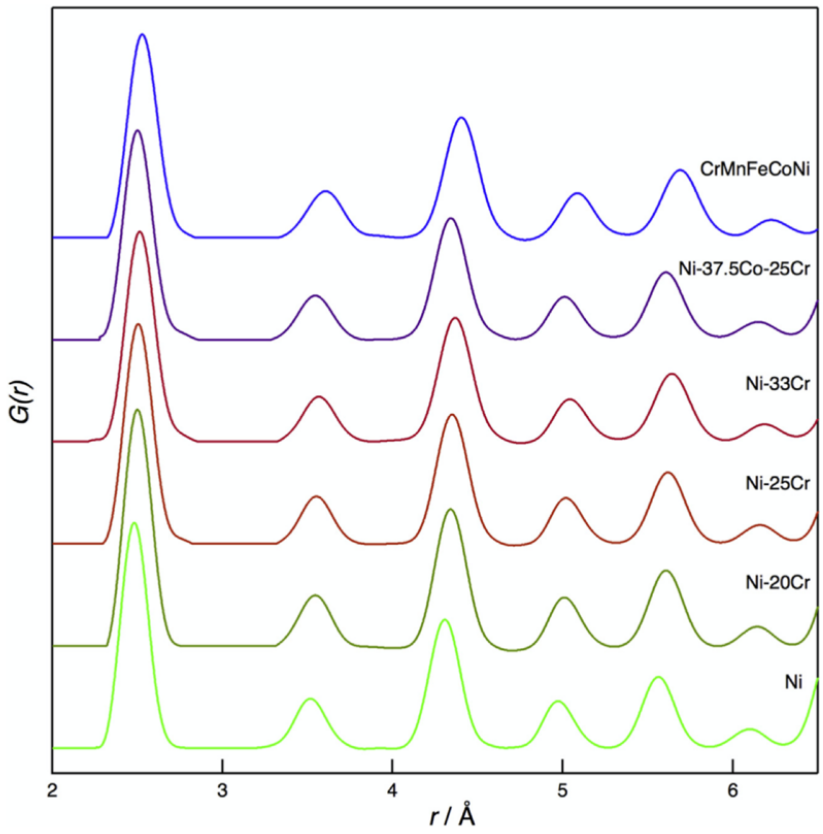


Figure 1.8: Normalised pair distribution functions for a series of alloys, limited to the first six coordination shells. Lattice distortion would be evidenced by peak broadening, however no broadening is observed. From Owen *et al.* [84].

Sluggish Diffusion Effect

The sluggish diffusion effect suggests that the diffusion of atoms in HEAs is unusually slow compared to conventional alloy systems. It has been proposed that this reduced diffusion arises from larger fluctuations in lattice potential energy between lattice sites, stemming from the significant atomic size and electronegativity differences among the constituent elements in HEAs. These variations in lattice potential could lead to a highly distorted energy landscape, serving as traps and making atomic migration via diffusion more en-

ergetically demanding. [38], demonstrated in Figure 1.9. However, there is sufficient evidence to suggest that diffusion in HEAs is not inherently sluggish, as demonstrated by the presence of precipitation in as-cast microstructures, even under conditions of rapid cooling and quenching [62].

Despite this effect being commonly referenced in the literature since its first inception in 2006 [80], it wasn't until 2013 when Tsai *et al.* [87] conducted the first experimental investigations into sluggish diffusion within HEAs. Tsai *et al.* [87] investigated the diffusion within the seminal HEA, CrMnFeCoNi, and reported that the alloy indeed had larger lattice potential energy fluctuations over traditional FCC systems and elements, leading to observation of the sluggish diffusion effect. However, the methodology and underlying approximations have been subject to scrutiny, with Paul [88] arguing that the diffusion coefficients obtained through this approach may be inaccurate and of limited significance. A response by Tsai *et al.* [89] further engaged with these concerns.

More recent studies by Zhang *et al.* [90] and Dąbrowa *et al.* [91] concluded that the diffusion behaviour of HEAs does not significantly deviate from that of well-characterised commercial alloys. Despite attempts to confirm the presence of sluggish diffusion within HEAs, current evidence remains inconclusive. The observed sluggish behaviour in specific HEA systems seems to be caused by the presence of particular elements rather than being a universal trait solely related to the number of components in the alloy [92].

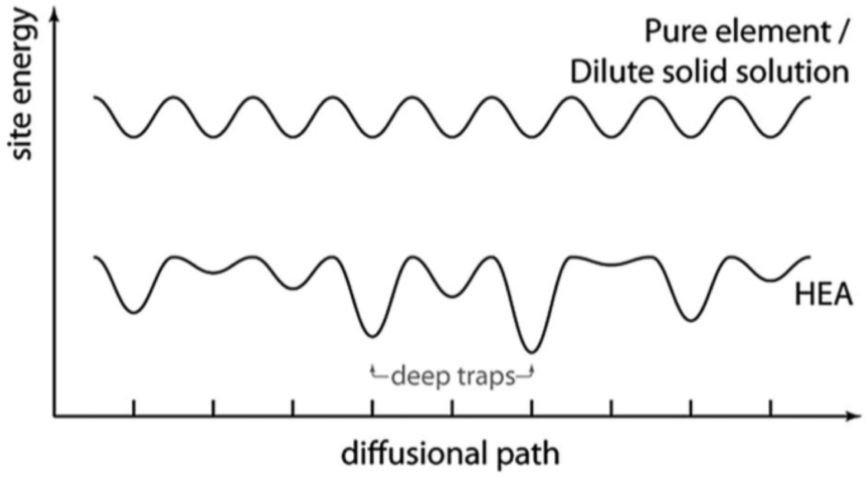


Figure 1.9: Schematic representation of the proposed difference in lattice potential energy profile along an atomic diffusion path in a pure element or dilute solid solution (top) and a HEA lattice (bottom). From Pickering and Jones [62].

Cocktail Effect

The term cocktail effect with respect to HEAs originated from a publication by Ranganathan[93] in 2003 and implies that a simple linear superposition of the properties of the individual components, will not be successful at predicting the final alloy properties [70]. However, this concept simply reflects the fundamental principle of alloying, wherein the resulting material exhibits superior properties compared to its individual elements, enabling it to meet the performance requirements of demanding applications, such as Ni-based superalloys.

1.3 FCC High Entropy Alloys

Of the single-phase HEA studies, a significant amount of research focuses on the FCC subclass because of their mechanical properties. Single-phase FCC HEAs typically display a lower hardness than their BCC counterparts [36], but exhibit a significantly higher ductility [62, 73, 76] via the easy motion of dislocations through the crystal structure [94]. This is demonstrated by Figure 1.10, where two strength-ductility maps are shown, one for yield strength and the other for ultimate tensile strength. The FCC HEAs included in this map predominantly appear in the low-strength, high-ductility domain [95], with yield strength values typically reported in the 150–350 MPa range at room temperature [96]. The ultimate tensile strength in FCC HEAs is also typically observed to be substantially higher than the yield strength, indicative of strain hardening [97]. This strain hardening effect invalidates any quantitative comparison of hardness and initial yield strength, unlike for BCC HEAs where it has been demonstrated to be successful [74]. The formation of intermetallic compounds within FCC HEAs negatively impacts the alloys tensile properties as the intermetallics are conventionally very brittle and act as initiation sites for failure [94, 98]. This ductility is observed to be high across a range of temperatures from cryogenic to ambient, however the poor yield strength of FCC HEAs is an issue that needs addressing in future FCC HEA design [99].

Comparing the tensile properties of HEAs with more conventional alloys reveals that the single-phase FCC HEAs closely resemble the Ni-based superalloys or austenitic stainless steels which contain similar 3d transition metal alloying elements [74]. This resemblance is a result of the first published HEA composition being observed to form a single-phase

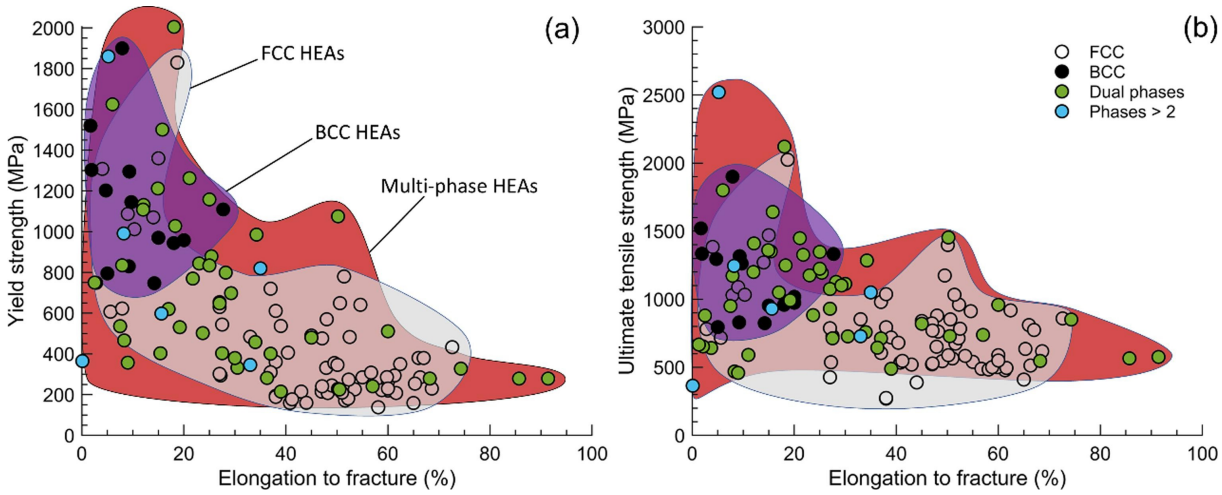


Figure 1.10: Maps of a) tensile yield strength and b) ultimate tensile strength versus elongation to fracture of HEAs, grouped by phase structure. From Li *et al.* [95].

FCC solid solution [43]. Therefore, for the FCC branch of the HEA field it has been difficult to escape the 3d transition metal avenue of CrCoNi-based alloys [94], primarily because without Ni it would be difficult to form these FCC crystal structures [100]. Hence the CoCrFeMnNi HEA, and its variants dominate the discussion of FCC HEAs. Extensive investigations have been conducted on the phase stability and mechanical properties of the CoCrFeMnNi alloy and its constituent binaries, tertiaries and quaternaries [74]. Wu *et al.* investigated the constituent systems to determine which would form FCC solid solutions in the as-cast and homogenised state [101], demonstrated in Figure 1.11, as well as their mechanical properties [102]. Wu *et al.* [102] found that the Cr containing alloys were generally the strongest in agreement with Bracq *et al.* [100] where it was shown that Cr acts to destabilise the FCC solid solution with increasing concentration.

However, as discussed previously in Section 1.2.6, the CoCrFeMnNi has been demonstrated to decompose from a single-phase FCC solid solution to multiple phases after prolonged annealing [69]. This is indicative of other studies on FCC HEA systems that attempt to diverge from the CoCrFeMnNi system, but are still based on CoCrNi. Bloomfield *et al.* [103] investigated the phase stability of the Al_xCrFeCoNi HEA system. This system has been demonstrated to form single phase FCC structure for $x \leq 0.2$ but decomposes to form multiple phases based on annealing temperature and concentration of Al. At $x = 0.25$, B2 precipitates begin to form, with their volume fraction increasing proportionally with Al concentration, eventually becoming the majority phase at $x \approx 0.7$. For $x = 0.5$ a dual phase FCC and B2 microstructure is observed at temperatures $\geq 1000\,°C$,

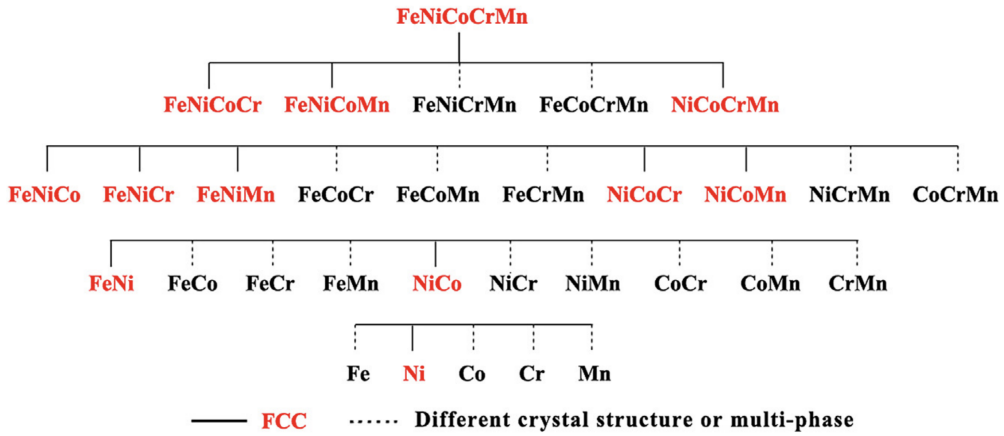


Figure 1.11: Family tree of the quinary CoCrFeMnNi HEA after homogenisation treatments. The single-phase FCC forming compositions are identified in red with a solid black line, while those with a different crystal structure or multiple phases are denoted in black with a dashed line. From Wu *et al.* [101].

with σ precipitates forming after heat treatments at lower temperatures. When the Al concentration is increased further to $x = 1.0$, FCC, BCC and B2 structures are formed above 940 °C, with lower temperatures resulting in the BCC phase being replaced by a σ phase. Two separate investigations by Jones *et al.* on the precipitation [104] and phase evolution [105] within the $Al_{0.5}$CrFeCoNiCu HEA system, demonstrated that at high temperatures, two distinct FCC phases are formed simultaneously. However, at lower annealing temperatures one of these FCC phases decomposes into a NiAl-based B2 phase and a Cr-rich σ phase. The B2 phase forms rapidly due to the ordering reaction, in contrast to the sluggish, kinetically inhibited formation of the σ phase. This is thought to be due to the σ phase formation being related to the destabilisation of the FCC matrix around the B2 precipitates, as this phase has little solubility for the Cr that eventually forms the σ phase.

1.3.1 Precipitation Strengthening

As discussed, the solid solution FCC structure provides good ductility, but relatively low strength and hardness and in the majority of systems has been shown to decompose to intermetallic phases based on a combination of composition and temperature. Critically, a single-phase FCC microstructure is typically insufficiently strong to be utilised for practical applications [106]. Thus, compositional control, engineered for careful precipitation to enhance mechanical properties without sacrificing the ductility of the primary FCC

phase has been investigated [107]. This controlled precipitation is universally used in more traditional alloy systems as an effective strengthening mechanism [108, 109]. There are multiple mechanisms in operation, but simplistically this strengthening phenomenon occurs because of the increased resistance to dislocation motion and crack propagation caused by lattice strains at the matrix-precipitate boundary [110]. Precipitation strengthening of FCC HEAs can be realised by the introduction of hard complex intermetallic phases into the microstructure [108]. For example, additions of Mo [111], Ti [112], and Ti and Al [106, 107] to the FeCoNiCr FCC HEA, resulted in precipitation of extremely hard σ and μ phases in the case of Mo, and $L1_2$-structured γ' nano-precipitate phases for Ti, Al and Mo additions, respectively. These precipitates greatly enhanced the yield strength and ultimate tensile strength without a significant reduction in ductility. Following the prior discussion on FCC HEA systems that attempt to diverge from the traditional CoCrFeMnNi system, the additional strengthening effects from the ordered precipitates forming organically through specified heat treatments within the Al_xCoCrFeNi system were explored. Gwalani *et al.* [96] investigated the case of $x = 0.3$ and found that the strengthening contributions of ordered $L1_2$ and B2 precipitates enhanced the yield strength from 159 MPa to 490 MPa and the ultimate tensile strength from 410 MPa to 840 MPa, while still maintaining adequate ductility with 45 % elongation. Additionally, Yang *et al.* [108] considered the case where $x = 0.5$, achieving increases in yield strength and ultimate tensile strengths from 475.3 MPa to 1000.1 MPa and 619.2 MPa to 1221.5 MPa, respectively. From this increase in strength, ductility subsequently decreased from 47.3 % to 21.3 %.

1.3.2 Carbide Precipitation Strengthening

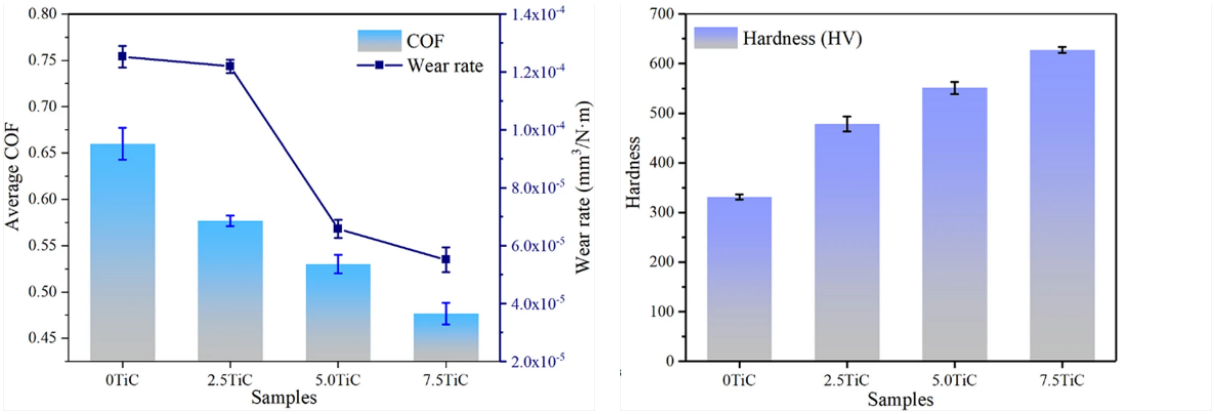
Another promising secondary phase that forms nanoscale precipitates and could be utilised to strengthen FCC HEAs are carbides. Numerous studies have been conducted on the addition of smaller amounts of carbon to HEAs containing transition metal elements, such as CoCrFeNiMn. Carbon contents of 1–2 at.% were found to result in the precipitation of $Cr_{23}C_6$ and Cr_7C_3 type carbide particles, enhancing both the wear resistance and mechanical properties such as hardness [56, 113]. Peng *et al.* [113] added 1.3 at.% carbon to the equiatomic FeCoCrNiMn alloy, which is just below the 1.38 at.% saturated solubility limit of carbon within the alloy. This study demonstrated that the resultant

microstructure formed nanoscale $M_{23}C_6$ precipitates which were stable inside the FCC matrix. Assessment of the mechanical properties revealed an enhanced yield strength of 1040 MPa with an elongation of 12 %.

Gao *et al.* [114] also investigated NbC carbide precipitation within the CrMnFeCoNi alloy instead of the sole addition of carbon. Nb and carbon were added at 0.8 at.% each, promoting the formation of nanoscale NbC carbides within the grains and significantly coarser microscale NbC and $M_{23}C_6$ at the grain boundaries. The yield strength and ultimate tensile strength were observed to increase from 353 MPa to 732 MPa and 635 MPa to 911 MPa respectively. Additionally, a high ductility of 32 % elongation, compared to the base 43 % was retained. Su *et al.* [115] investigated the addition of interstitial carbon in $Fe_{50}Mn_{30}Co_{10}Cr_{10}C_{0.5}$, finding a substantial increase in yield strength, but also a significant improvement in ductility from 14 % to 60 % following post processing with cold rolling and subsequent tempering and annealing techniques. Suggesting that small additions of carbon may not result in embrittlement of the alloy and could benefit ductility unlike that observed in stainless steels.

The precipitation of a reinforcing carbide phase has been demonstrated to enhance wear resistance within BCC alloys through mechanisms that can easily be transferred to FCC systems. Wu *et al.* [116] utilised vacuum induction melting to *in situ* carbon reinforce the BCC, $Ni_{0.6}CoFe_{1.4}$ alloy with TiC precipitates. The TiC precipitates were found to be semi-coherent with the matrix and increase in size with the addition of greater amounts of TiC. A decrease in wear rate and increase in hardness, demonstrated in Figure 1.12, correlates to an increase in the carbide phase content. This enhancement in hardness originates from the obstruction of dislocation movement by the fine TiC precipitates and the semi-coherent interface inhibiting dislocation slip and enabling transfer of loads from the softer matrix to the significantly harder precipitates. Furthermore, the reduced wear rate is a result of the carbide precipitates being exposed from the matrix as the surface is worn, mitigating the wear of the softer matrix.

These investigations into the reinforcement of FCC HEAs through the precipitation of secondary phases, in particular carbides, have demonstrated that it is an effective methodology to enhance mechanical properties while minimising the impact on ductility.



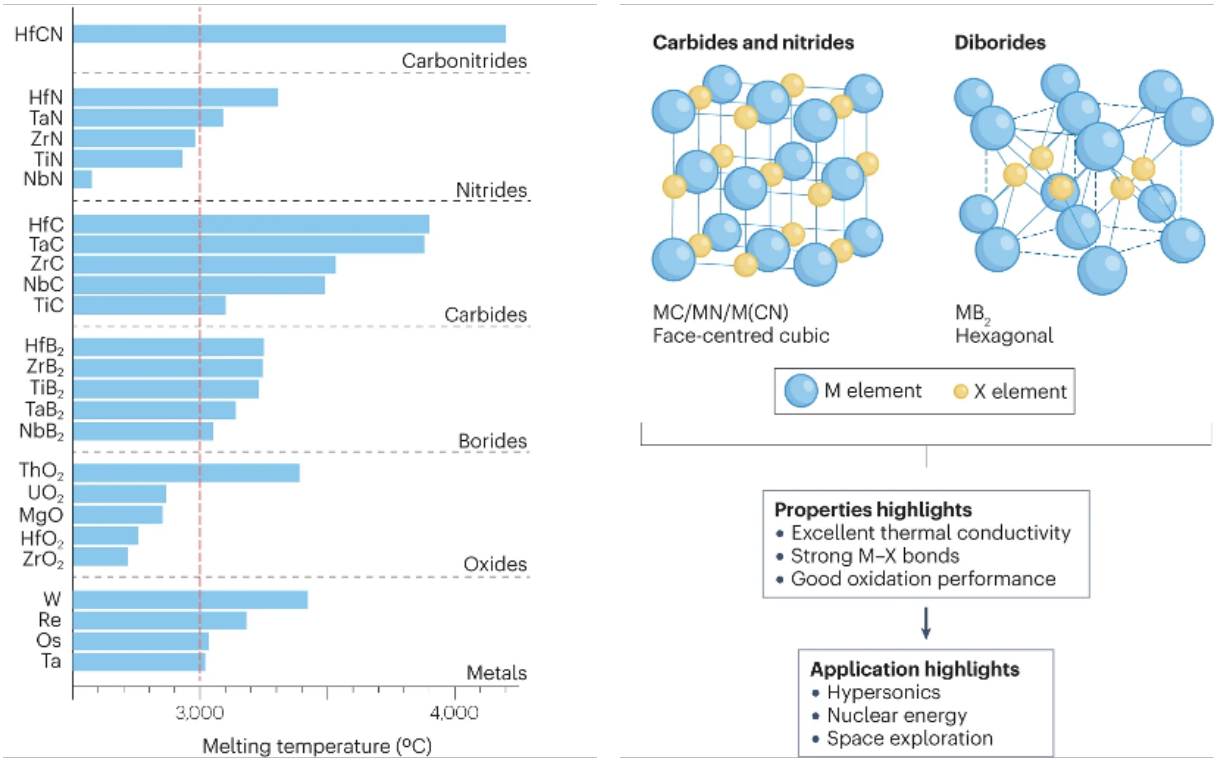
a) b)

Figure 1.12: a) Average coefficient of friction (COF) and wear rate of TiC_x–$Ni_{0.6}CoFe_{1.4}$ composites and b) hardness of TiC_x–$Ni_{0.6}CoFe_{1.4}$ composites [116].

1.4 Hardmetal High Entropy Alloys

Ultra-high temperature ceramics are a rapidly growing class of materials designed for use in extreme environments. They are typically defined by their melting points exceeding 3000 °C, as shown in Figure 1.13a, and are almost exclusively binary compounds of B, C, or N bonded to a transition metal, as illustrated in Figure 1.13b [57, 117].

Their exceptional thermal stability is primarily attributed to the strong bonding between constituent elements. In particular, transition metal borides and carbides exhibit high hardness, elastic modulus, and critically melting temperatures [57, 119, 120]. Rost *et al.* [55] were the first to extend the entropy stabilisation concept from HEAs to ceramics, demonstrating that entropically stabilised phases can enable high-temperature properties thought unachievable [121]. Thus, Rost *et al.* [55] fabricated the first bulk high entropy ceramic material, $(Co_{0.2}Cu_{0.2}Mg_{0.2}Ni_{0.2}Zn_{0.2})O$ and demonstrated its ability to form a single-phase microstructure following quenching from high temperature. Subsequently, Gild *et al.* [122] produced several high entropy diborides, forming single-phase solid solution microstructures and displaying higher hardness and improved oxidation resistance over the average performance of the individual diborides. Inspired by the synergy of high entropy and ceramic materials, a new class of materials, high entropy carbides (HECs), high entropy carbide ceramics or hardmetal HEAs, has emerged [119, 123], demonstrating potential for the holistic replacement of WC-Co-based hardmetals in tooling applications. The structure of these high entropy ceramics is depicted in Figure 1.14.



a) b)

Figure 1.13: a) Bar chart of the melting temperatures of some example metallic and ceramic materials, illustrating the definition of ultra-high temperature ceramic materials as having a melting point $> 3000\,°C$. b) Schematic representation of the crystal structure of ultra-high temperature ceramic carbides, nitrides and diborides as wells as their critical properties and applications [118].

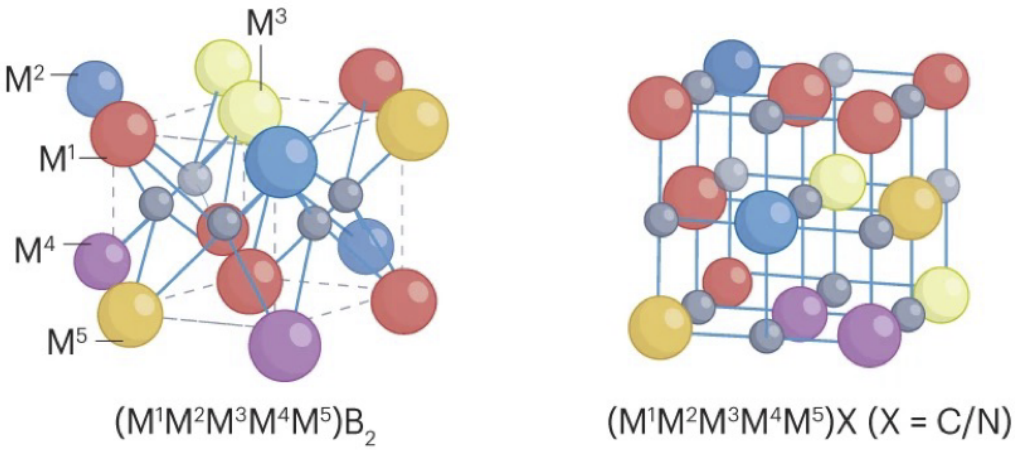


Figure 1.14: Schematic representation of high entropy transition metal diboride and carbide or nitride crystal structures [118].

1.4.1 High Entropy Carbides

Fabrication of HECs to achieve the high carbon contents of around 50 at.% using conventional methods such as vacuum arc melting are challenging, with carbon contents frequently measuring below the target [56]. Castle *et al.* [57] fabricated two bulk equiatomic four metallic component HECs, (HfTaZrNb)C and (HfTaZrTi)C, by ball milling and spark plasma sintering. This is the conventional fabrication route for HECs [124, 125]. Spark plasma sintering, also known as field-assisted sintering technique, is a method used for the fast densification of ceramic metal matrix composites, heating the powder sample by pulsing direct current through a graphite die [126]. Alternative methods, such as flake powder metallurgy using graphene oxide [127] and spark plasma sintering [128] have been shown to be effective methods for fabrication of HECs. In both cases Castle *et al.* [57] found the wear rate of the HECs decreased and the hardness increased in comparison to the base monocarbide materials. The (HfTaZrNb)C composition was observed to more readily form a single phase solid solution than the (HfTaZrTi)C and both exhibited a significantly enhanced hardness compared to the monocarbides. Similarly, Zhou *et al.* [123] investigated an equiatomic (TiZrHfNbTa)C HEC also manufactured using spark plasma sintering. The aim of this study was to investigate oxidation behaviour, with the HEC showcasing higher oxidation resistance in comparison to the constituent components. Another study inspired by the work of Rost *et al.* [55] on high entropy ceramics, by Harrington *et al.* [121], investigated twelve (eleven novel) bulk equiatomic five metallic component HECs with the aim of exploring this new compositional space for improved ultra-high temperature ceramics. All of the HECs fabricated in this study showcased enhanced hardness over the rule of mixtures predicted values, but the addition of Mo and W was determined to minimise the potential of single-phase formation. In the studies outlined, where the carbon content is typically around 50 at.%, there is no discussion of ductility. The ceramic materials fabricated in these studies are very likely highly brittle due to the substantial amount of carbon. Additionally, these high entropy ultra-high temperature ceramic studies focus on refractory elements such as Hf, Zr, Ta, Nb, etc., in order to obtain the required high melting temperatures.

1.4.2 Hardmetals with High Entropy Alloy Binder

As discussed in Section 1.1.3, replacing the Co binder with HEAs offers a promising path for advancing WC-based cemented carbides [35]. HEAs are particularly suitable due to their potential to simplify the number of phases in hardmetals while reducing reliance on costly and toxic elements [36]. To function as a binder material, a metallic alloy must exhibit satisfactory wetting behaviour and partial solubility with the hard carbide phase particles. Wetting refers to the ability of a liquid to interact and maintain contact with a solid surface. Thus, Prieto *et al.* [36] designed and fabricated two HEA compositions, FeCrAlTiMo and FeCrAlTiMoNi, aiming for a single-phase BCC structure and evaluated their properties relative to cemented carbides with conventional binders. Mechanical testing showed improved hardness and compressive strength, while wetting assessments confirmed both HEAs exhibited good wetting behaviour with a TiCN hardmetal substrate.

Zhou *et al.* [129] fabricated a WC-based cemented carbide with 10 and 20 wt.% BCC AlFeCoNiCrTi HEA binder. The HEA binder inhibited WC grain growth in comparison to the Co binder. As a result, the WC-10 wt.% HEA showed much finer grains than the WC-10 wt.% Co hardmetal, 200 nm to 600 nm respectively, both the hardness and compression strength of the WC-10 wt.% HEA are enhanced. The hardness of WC-10 wt.% HEA is 2231 HV, while the hardness of WC-10 wt.% Co is only 1 910 HV. When the HEA content is increased to 20 wt.%, the hardness increases further to 2 358 HV. Additionally, the compression strength of WC-10 wt.% HEA is 5 219 MPa, significantly higher than the 3 595 MPa measured for WC-10 wt.% Co. However, when the HEA content increases the compression strength only increases by 3.8 %. To further establish HEAs as a suitable candidate for hardmetal binder materials, Zhou *et al.* [130] investigated the application of AlCrFeCoNi as a binder material in WC cemented carbides. It was found in this study that during the sintering process Al would precipitate out from the HEA, react with O_2 to form alumina and deposit on the surface of pores in the hardmetal. This would hinder the shrinkage of the pores, negatively impacting the densification of the material and cause a BCC-to-FCC transformation in the binder. As in the previous work, the HEA was found to inhibit WC grain growth and result in an enhanced hardness of 2 160 HV and compressive strength of 4 395 MPa. However, the fracture toughness of the WC-10 wt.% HEA was found to be slightly lower than conventional WC-10 wt.% Co.

While the above studies considered BCC HEAs as binder materials, both Chen *et al.* [131] and Velo *et al.* [132] investigated FCC HEAs. Chen *et al.* used $Co_xFeNiCrCu$ ($x = 1, 1.5, 2, 2.5$) in WC–10 wt.% HEA composites, while Velo *et al.* incorporated CoCrFeNiMn into WC-based composites at 10, 20, and 30 vol.%. However, Chen *et al.* [131] found that the FCC phase gradually transforms into a BCC phase as the amount of Co is increased, with only the BCC phase being present when $x = 2.5$. Compared to the more close packed structure of the FCC phase, the BCC phase allows easier diffusion of the WC, enabling a larger WC grain size with increased amounts of Co in the binder. This is demonstrated in Figure 1.15.

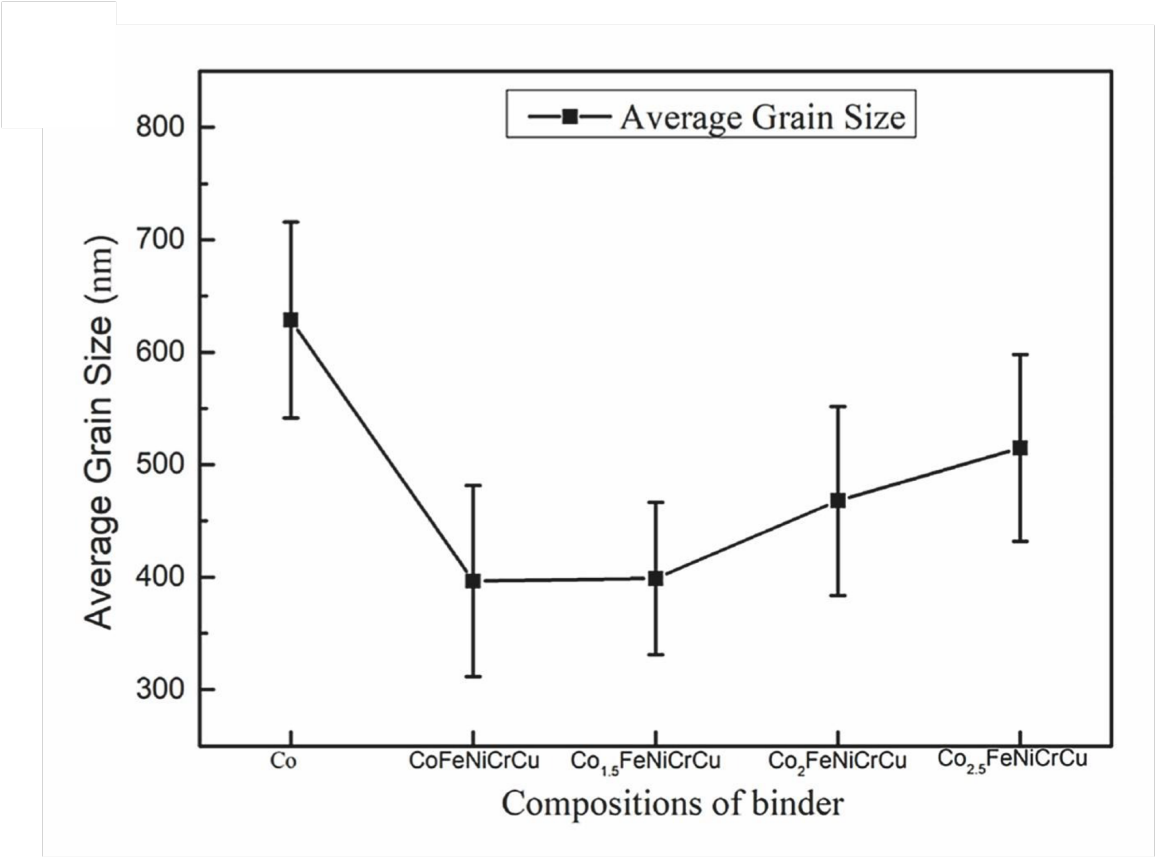


Figure 1.15: Average grain size against the binder composition. Illustrates the impedance of grain growth by the HEA binder compared to Co and the gradual increase in grain size as the amount of Co is increased in the HEA [131].

The overall performance of the cemented carbides with the HEA binder was enhanced compared to the conventional WC-Co cemented carbide, as illustrated by Figure 1.16. The optimal performance of hardness and fracture toughness was obtained for $x = 1.5$, with an average WC grain size of (398 ± 68) nm, Vickers hardness of (2080 ± 40) MPa, and fracture toughness of (11.6 ± 0.1) MPa $m^{1/2}$.

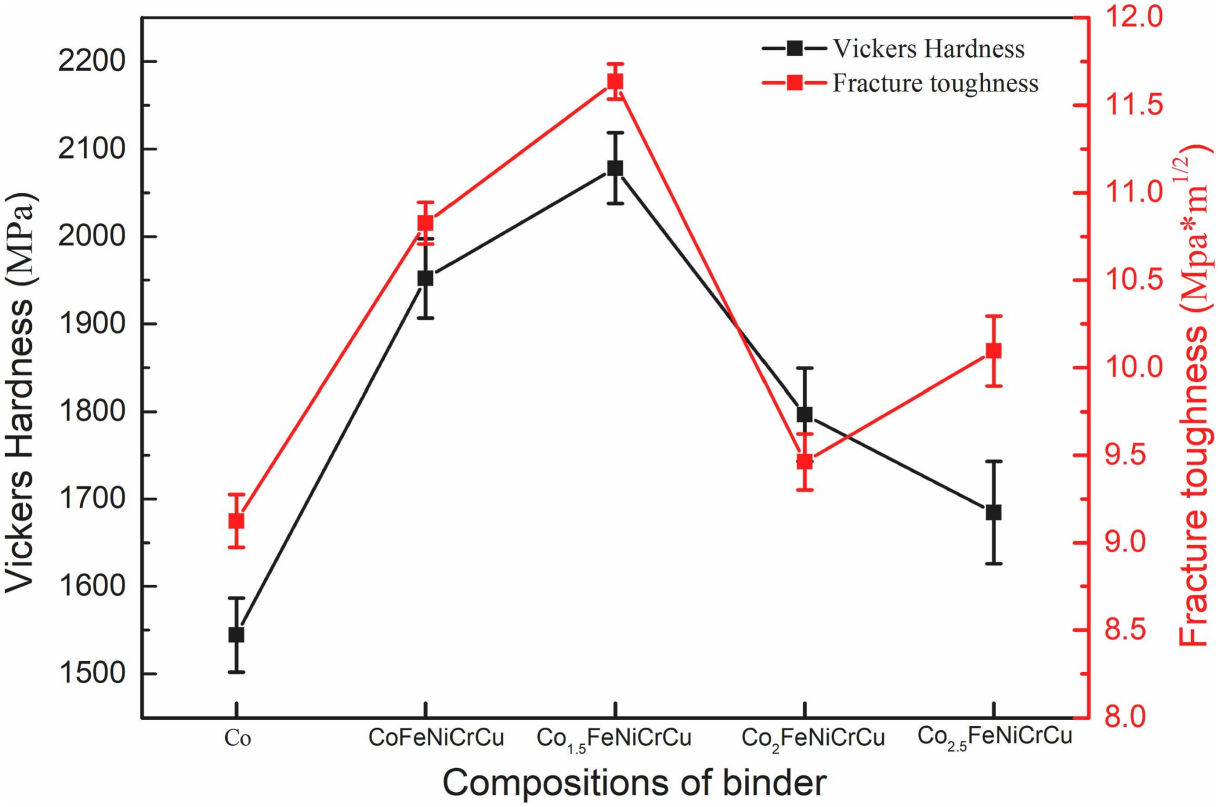


Figure 1.16: Vickers hardness and fracture toughness of the cemented carbides with different binders. Shows enhanced performance of the cemented carbides compared to the Co binder and the peak in performance of the cemented carbide when x = 1.5 [131].

1.4.3 High Entropy Carbide Hardmetals with Binder

Unlike the application of HEAs as the binder material within more conventional WC based hardmetals as discussed above, Pötschke *et al.* [125] investigated the possibility of utilising the HEC as the hardmetal. Two HECs with Co binders, namely (HfTaTiNbV)C-19.2 vol.% Co and (TaTiNbVW)C-19.2 vol.% Co were fabricated by ball milling, hot isostatic pressing and finally sintering. A skeletal HEC microstructure of cubic carbides that are mixed together and embedded in a Co binder was observed in both cases, demonstrated by Figure 1.17. The hardness and fracture toughness of the two alloys were measured and compared with a WC-12 wt.% Co (WC-19.2 vol.% Co) hardmetal. The hardness (HV10) of the two alloys, (1200 ± 20) HV and (1430 ± 10) HV respectively, are both lower than that of the medium-grain WC-12 wt.% Co hardmetal at (1460 ± 20) HV [133]. This reduced hardness is likely due to the larger grain size of the HEC-Co hardmetals. In addition, the fracture toughness of the two fabricated HEC-Co hardmetals was lower than the corresponding WC-Co hardmetal [125].

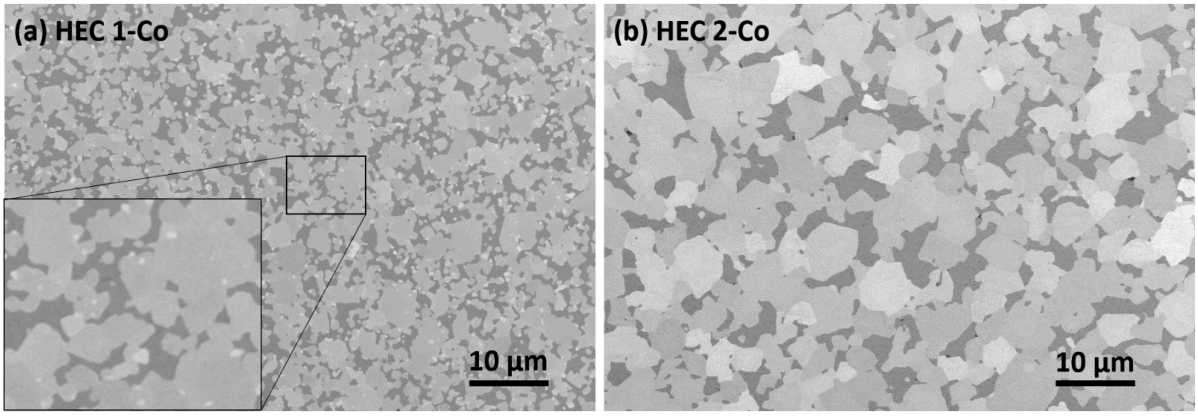


Figure 1.17: SEM micrographs of the HEC-Co samples: a) (HfTaTiNbV)C-19.2 vol.% Co, b) (TaTiNbVW)C-19.2 vol.% Co. In both cases the dark grey phase indicates the Co binder [125].

Following this study, Pötschke *et al.* [29] explored the influence of different metallic binder materials on HEC based hardmetals. The (TaNbTiVW)C HEC was chosen as the base hardmetal and the impact of three different binder materials, Co, Ni, and FeNi at volume fractions of 16 % and 24 % on the microstructure and mechanical properties were analysed. As in the previous study, comparisons to a WC-16 vol.% Co were drawn [133]. The samples containing the FeNi binder showed a tendency to form additional phases, such as small amounts of a W-rich phase. Furthermore, the grain size of the HEC with the Ni and FeNi binders was significantly larger than the Co-binder hardmetal. As highlighted in the preceding study, the WC-Co based hardmetal outperformed all the HEC metallic binder combinations in fracture toughness. The Co binder performed best in terms of hardness (HV30) (1490 ± 20) HV and (1330 ± 20) HV at 16 vol.% and 24 vol.% respectively compared to (1230 ± 20) HV for WC-16 vol.% Co. The Ni binder performed best in terms of fracture toughness of the HEC metallic binder samples. This is thought to be caused by the lower solubility of the metallic elements within the HEC phase in Ni compared to Co and FeNi [29].

Thus, while HECs combined with metallic binders show potential, their mechanical performance remains insufficient to replace established WC–Co hardmetals. Conversely, as demonstrated, HEAs and high-entropy materials more broadly offer promise for the development of next-generation hardmetals, though substantial further research is needed to optimise their properties and enable application-specific design.

1.5 High Entropy Alloy Design Methodologies

Early HEA design and development efforts were largely driven by trial-and-error experimentation [134, 135], in which elements and their proportions were selected iteratively [136, 137], and at times arbitrarily [138], to explore novel alloy compositions. These compositions are then fabricated via vacuum arc melting and characterised to assess their properties, a time intensive and expensive process. Therefore, these experimental trial and error methodologies to design new alloy systems within the HEA space are unfeasible due to the expanse of compositional space to explore and the associated cost of experiments. Hence, a way to predict the structural properties such as phase formation and mechanical performance of HEAs to guide experimental searches is urgently required within the HEA field.

1.5.1 Empirical Parameters

The first attempt to parametrise HEA design involved developing a series of empirical rules to predict solid solution stability and phase formation in alloys containing multiple principal elements [85]. These rules are based on the Hume-Rothery criteria for substitutional solid solutions, which describe the conditions under which one element can dissolve into another in a binary alloy system [110]:

1. The difference in atomic radii of the two elements must be less than 15 %.
2. The crystal structures of the elements must be similar.
3. The two elements must have comparable electronegativities, if the difference is too great then intermetallic compounds are likely to form.
4. The two elements must have comparable valences, a metal is more likely to dissolve a metal of higher valency than one of lower valency.

The bulk metallic glass community initially explored the application of these substitutional solid solution rules to systems with complexities beyond binary alloys [139]. This foundational work has since been expanded upon by the HEA community, which has further developed and applied these rules to systems containing multiple principal elements. Each of the rules will be discussed in turn in below.

Hume-Rothery Based Rules

Atomic Size Difference

Atomic size difference δ,

$$\delta = \sqrt{\sum_{i=1}^{n} c_i \left(1 - \frac{r_i}{\bar{r}}\right)^2}, \tag{1.4a}$$

where c_i is the atomic fraction of the i^{th} element, r_i is the atomic radius and $\bar{r}$ is the average atomic radius, given by

$$\bar{r} = \sum_{i=1}^{n} c_i r_i, \tag{1.4b}$$

takes the average effect of the atomic size difference of all the alloy's constituent elements [140], to provide a description of how well the atoms can fit together within the lattice structure. This parameter originates from the first Hume-Rothery rule described above [110]. However, the HEA equivalent of this rule does not have explicit solute and solvent elements as there is no distinctly identifiable solute and solvent atoms in HEAs [140]. BCC formation has been found to become increasingly favourable over FCC in HEAs with increasing atomic size difference, due to BCC crystal structures being less constrained than FCC. Hence, BCC structures can accommodate atoms of different sizes with less strain energy penalty [141]. Furthermore, HEA hardness has been observed to increase monotonically with increasing δ [142].

Values of δ as low as possible are preferred with Guo *et al.* stating maximum values of 8.5 % [143] and 6.5 % [144] for solid solution formation. At larger values of δ, intermetallic and amorphous phases can form. However, these limits also depend on other thermodynamic quantities, with only solid solutions forming when δ is below 4 %, while the mixing enthalpy and mixing entropy are sufficiently controlled [143].

Atomic Packing Parameter

The atomic packing parameter γ,

$$\gamma = \frac{\omega_S}{\omega_L}, \tag{1.5}$$

is a geometrically-derived metric used to quantify the distortion in local atomic environments within HEAs. It expands upon δ by incorporating the concept of local packing asymmetry. Here, ω_L and ω_S are dimensionless quantities related to the local packing efficiency around atoms with the largest and smallest radii in the alloy, respectively, and are defined as:

$$\omega_L = 1 - \sqrt{\frac{(r_S + \bar{r})^2 - \bar{r}^2}{(r_S + \bar{r})^2}}, \qquad \omega_S = 1 - \sqrt{\frac{(r_L + \bar{r})^2 - \bar{r}^2}{(r_L + \bar{r})^2}}, \tag{1.6}$$

where r_L and r_S denote the largest and smallest atomic radii respectively. The packing parameter γ thus provides a useful indication of how far the local atomic environment deviates from ideal packing, influencing the stability of solid solutions [140]. An illustration of the atomic packing around the largest and smallest atoms is shown in Figure 1.18. Wang *et al.* [140] note that $\gamma < 1.175$ is indicative of solid solution formation within HEAs. However, despite the authors suggesting that γ can capture phase selection better than δ, it is still highly dependent on mixing enthalpy, electronegativity and valence electron concentration. Furthermore, few studies utilise γ compared to δ which appears in almost all empirical studies of HEA phase formation.

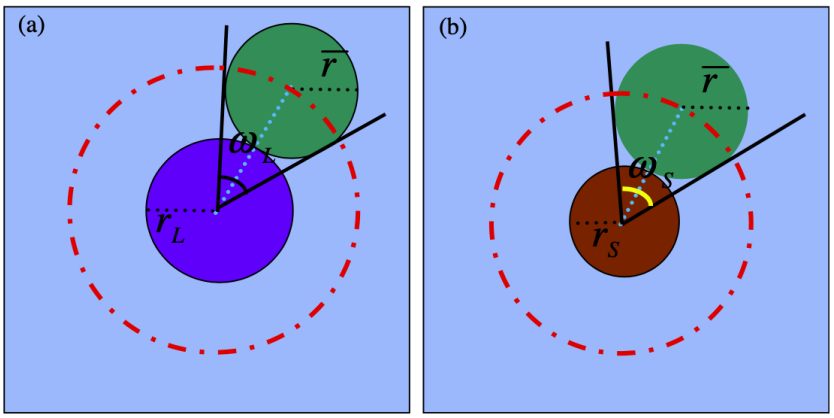


Figure 1.18: Illustration of the atomic packing, around (a) the largest atom and (b) the smallest atom in the HEA system. From Wang *et al.* [140].

Pauli Electronegativity Difference

Pauli electronegativity difference $\Delta\chi$,

$$\Delta\chi = \sqrt{\sum_{i=1}^{n} c_i \left(\chi_i - \bar{\chi}\right)^2}, \tag{1.7a}$$

where χ_i denotes the Pauling electronegativity of the i^{th} element and $\bar{\chi}$ denotes the average electronegativity of the constituent elements,

$$\bar{\chi} = \sum_{i=1}^{n} c_i \chi_i, \tag{1.7b}$$

originates from the third Hume-Rothery rule. However, as with the atomic size difference, as there is no dominant element in HEAs, an average of the constituent elements electronegativities is used [139]. $\Delta\chi$ is often included as a feature in HEA phase prediction studies. As stated in the Hume-Rothery rules, a low value of $\Delta\chi$ is found to be conducive to solid solution formation and the suppression of intermetallics [145]. However, there are other parameters that are significantly more important in determining phase selection, such as δ and mixing enthalpy [145, 146].

Valence Electron Concentration

Valence electron concentration (VEC),

$$\text{VEC} = \sum_{i=1}^{n} c_i (\text{VEC})_i, \tag{1.8}$$

is a very common and robust empirical parameter for predicting phase formation in HEAs, based upon the fourth Hume-Rothery rule. It is simply defined as the weighted average of the VEC of all constituent elements, where $(\text{VEC})_i$ indicates the VEC of the individual elements of the alloy [146]. VEC provides a measure of an element's electron density available for metallic bonding and provides insight into the electronic interactions that influence phase stability [147]. Studies have identified VEC as a key factor governing the formation of solid solution phases in HEAs [148]. Alloys with higher VEC values (typically > 8) tend to stabilise FCC structures, while lower VEC values (≤ 6.87) favour BCC phases [146, 149].

Number of Itinerant Electrons

Just as γ was proposed as an extension of the widely accepted δ, so too the number of itinerant electrons per atom e/a, has been introduced as an extension of VEC,

$$e/a = \sum_{i=1}^{n} c_i (e/a)_i, \tag{1.9}$$

where $(e/a)_i$ represents the itinerant electron concentration of the i^{th} element. The e/a value is calculated from the diameter of the Fermi sphere in reciprocal space, and for an HEA, is simply determined by the weighted average e/a of the constituent elements [146]. Values of e/a for the constituent elements are taken from Mizutani *et al.* [147, 150].

e/a has been suggested to be preferential to VEC for classification of phases within HEAs [151]. For HEAs in particular, e/a differentiates phase formation into three distinct domains corresponding to FCC, BCC and intermetallic phase formation respectively [152, 153].

- Domain I: FCC, $e/a < 1.53$
- Domain II: Mixed Phases, $1.53 < e/a < 1.88$
- Domain III: BCC, $e/a > 1.88$

Gibbs Free Energy Based Rules

Enthalpy of Mixing

The enthalpy of mixing ΔH_{mix},

$$\Delta H_{\text{mix}} = 4 \sum_{i=1, i<j}^{n} c_i c_j \Omega_{ij}, \tag{1.10}$$

is frequently used as a criterion for solid solution and phase formation in HEAs using alternative prediction techniques, such as parametric methods. Here, c_i and c_j are the atomic fractions of elements i and j respectively, while Ω_{ij} represents the binary interaction enthalpy between them. For HEAs to form solid solutions, parametric studies suggest that, the enthalpy of mixing needs to be small, to avoid compound formation at higher negative

values -22 < ΔH_{mix} < 7 kJmol^{-1} [85, 143]. The most common method for calculating the enthalpy of mixing is the Miedema model which combines first-principles-derived enthalpies with empirical fitting to experimental data [154, 155]. The overall enthalpy of the alloy is calculated by assigning a coefficient to each binary pair of elements based on their thermochemical compatibility and then taking a composition weighted average across the whole system. The enthalpy coefficients used are taken from the Miedema enthalpy table compiled by Takeuchi and Inoue [155]. ΔH_{mix} is one of the most commonly used parameters in HEA solid solution and phase prediction studies. It is commonly paired with the δ to make these predictions [143, 144], as discussed later in Section 1.5.2.

Entropy of Mixing

Entropy of mixing ΔS_{mix},

$$\Delta S_{\text{mix}} = -R \sum_{i=1}^{n} c_i \ln c_i, \tag{1.11}$$

is the configurational entropy derived by Boltzmann's law [143]. Entropy is a key parameter for HEA predictions as its large values in HEAs are not only the origin of the naming convention, but also the key tenet for the field. However, its significance on the formation of single phase solid solutions and enhanced mechanical properties is heavily debated [62]. From Equation 1.11, it is clear that increasing the number of elements will increase the entropy, with compositions containing five or more elements producing high values of ΔS_{mix}.

Melting Temperature

The majority of HEAs do not have a known melting temperature T_m, and hence it is approximated using the rule of mixtures.

$$T_m = \sum_{i=1}^{n} c_i (T_m)_i \tag{1.12}$$

A weighted average of the pure elements melting temperatures in Kelvin, $(Tm)_i$ is taken [156]. However, this is only a very simplistic approximation as it assumes a linear relationship between the melting temperature and the alloy composition.

Yang Thermodynamic Parameter

The Yang thermodynamic parameter Ω,

$$\Omega = \frac{T_m S_{\text{mix}}}{|H_{\text{mix}}|}, \tag{1.13}$$

was first published by Yang and Zhang in 2012 [156] and was designed specifically for use as a HEA solid solution formation predictor. It incorporates both the ΔH_{mix} and ΔS_{mix}, with the requirement for HEA formation being set at $\Omega > 1.1$. However, as with other parameters discussed above, this criterion is also coupled with δ, where a value of $\delta \leq 6.6\,\%$ is required for solid solution formation [156]. The Yang parameter has been used extensively in other HEA ML studies, but could cause issues of overlap, masking the impact of the true variables contained within the parameter.

Other Rules

In addition to the Hume-Rothery and thermodynamically derived rules, several alternative parameters commonly employed in the HEA literature for predicting phase formation and properties are outlined below.

Density

As with the weighted average melting temperature discussed above, the vast majority of HEA systems do not have an experimentally determined density. Hence, this can also be approximated using the rule of mixtures [157, 158],

$$\rho = \frac{\sum_{i=1}^{n} c_i A_i}{\sum_{i=1}^{n} c_i M_i} = \sum_{i=1}^{n} c_i \rho_i, \tag{1.14}$$

where, A_i and M_i are the molar mass and molar volume of element i at room temperature respectively. ρ_i, denotes the density of the i^{th} element.

Geometrical Parameter

Singh *et al.* [159] developed a new parameter in 2014 to predict the formation of disordered solid solutions within HEAs. This parameter Λ,

$$\Lambda = \frac{\Delta S_{\text{mix}}}{\delta^2}, \tag{1.15}$$

originates from the observations that an increased ΔS_{mix} promotes solid solution formation, while large values of δ instead promote intermetallic formation [156].

This parameter has been noted to discriminate the phase formation of solid solutions into three distinct domains [159].

- Domain I: Mixtures including intermetallics, $\Lambda < 0.24$
- Domain II: Two phase mixture, $0.24 < \Lambda < 0.96$
- Domain III: Single phase disordered solid-solutions, $\Lambda > 0.96$

However, Singh *et al.* [159] state that despite its success in predicting formation of solid solutions, it cannot effectively discriminate individual phases such as BCC or FCC. To extract detailed phase information, the Λ parameter has to be considered alongside VEC.

Young's Modulus Asymmetry

Young's modulus asymmetry $\Delta\mathcal{E}$,

$$\Delta\mathcal{E} = \sqrt{\sum_{i=1}^{n} c_i \left(1 - \frac{E_i}{\bar{E}}\right)^2}, \tag{1.16}$$

provides a description of the difference in the Young's modulus between the individual components of the HEA. It is calculated using the same method as δ, with E_i and $\bar{E}$, denoting the Young's modulus of the i^{th} element and the average Young's modulus respectively. This parameter is not very common, but has been utilised in recent HEA ML studies [160, 161] and could be useful to provide insights into the mechanical properties of HEA compositions in addition to phase formation.

Shear Modulus Asymmetry

The shear modulus asymmetry $\Delta\mathcal{G}$,

$$\Delta\mathcal{G} = \sqrt{\sum_{i=1}^{n} c_i \left(1 - \frac{G_i}{\bar{G}}\right)^2}, \tag{1.17}$$

is an extension to the Young's modulus asymmetry and is calculated using the same approach [161]. Again G_i and $\bar{G}$ denote the shear modulus of the i^{th} element and the average shear modulus respectively.

Bulk Modulus Asymmetry

As with the previous discussion of shear and Young's modulus asymmetry, the bulk modulus asymmetry $\Delta\mathcal{B}$,

$$\Delta\mathcal{B} = \sqrt{\sum_{i=1}^{n} c_i \left(1 - \frac{B_i}{\bar{B}}\right)^2}, \tag{1.18}$$

represents an extension to the Young's modulus asymmetry in three dimensions and is again calculated using the same approach. In this case B_i and $\bar{B}$ denote the bulk modulus of the i^{th} element and the average bulk modulus respectively.

1.5.2 Empirical Parameter Application

Many HEA studies have attempted to utilise these parameters and their combined relationships to map the solid solution or unique phase formation within the parameter space. Thus enabling the identification of solid solution and phase formation rules/zones and the design of new HEA systems within the identified domains.

Among the most common of the methods used to correlate these parameters are binary plots (biplots) [162, 163], also sometimes called parametric analysis plots [98]. One of the first to apply this method was Zhang *et al.* [85] in 2008, shown in Figure 1.19 using a combination of δ and ΔH_{mix}.

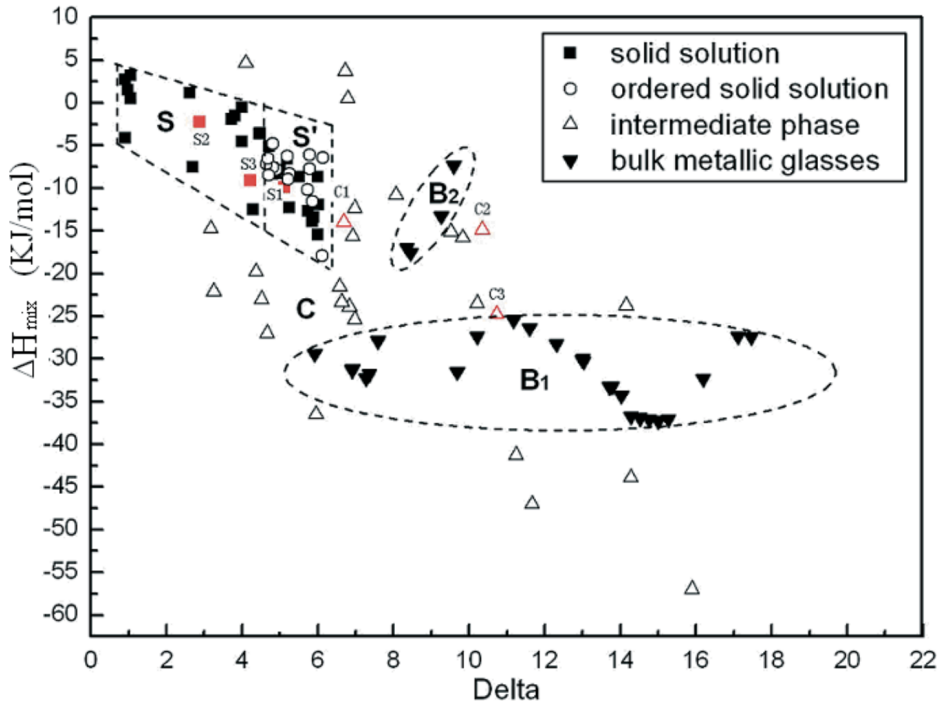


Figure 1.19: Experimental data showing the relationship between δ and ΔH_{mix}. The red symbols indicate the HEAs produced in the study to test the phase formation mapping shown in the plot. From Zhang *et al.* [85].

The region labelled S in the plot is of particular importance, as it corresponds to compositions where only solid solution phases are predicted to form. As anticipated, this zone occurs at low values of δ and small negative values of ΔH_{mix} so that the alloys cannot form compounds. As δ increases and ΔH_{mix} becomes more negative, the alloys move into the zone labelled S', where a solid solution is the primary phase, but a minority phase of ordered precipitates forms. Based on the zones indicated in Figure 1.19, Zhang *et al.* [85] fabricated six HEA system, designated in red. As expected, the three alloys located

in Zones S and S' formed solid solution like FCC or BCC structures, while the three alloys located in zone C contained complex structures with intermetallic formation. Guo *et al.* [143] also produced a binary plot of δ vs. ΔH_{mix} and utilised it to produce the simultaneous solid solution formation rules of $-22 \leq \Delta H_{\text{mix}} \leq 7\ \text{kJ mol}^{-1}$ and $\delta \leq 8.5\,\%$. With an additional requirement of $11 \leq \Delta S_{\text{mix}} \leq 19.5\ \text{J K}^{-1}\,\text{mol}^{-1}$.

In addition to the biplot, Zhang *et al.* [85] also produced a three-dimensional plot to incorporate the effect of ΔS_{mix} on HEA formation, shown in Figure 1.20. However, this is significantly less intuitive and more difficult to interpret than the two-dimensional plot. As a result, these empirical plots are typically restricted to two dimensions, since higher-dimensional data involving numerous parameters cannot be interpreted effectively without computational tools to reduce and visualise the complexity.

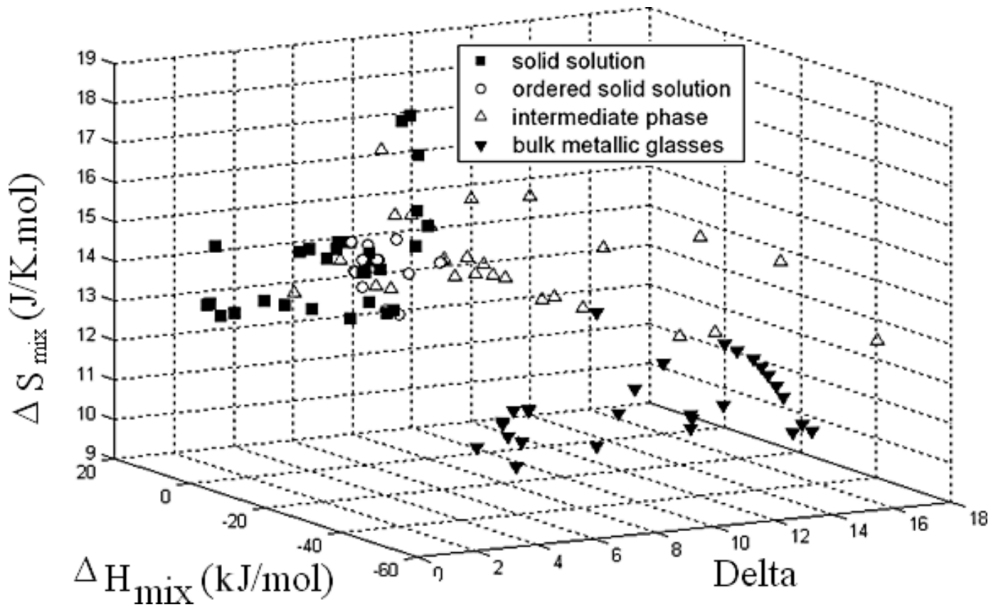
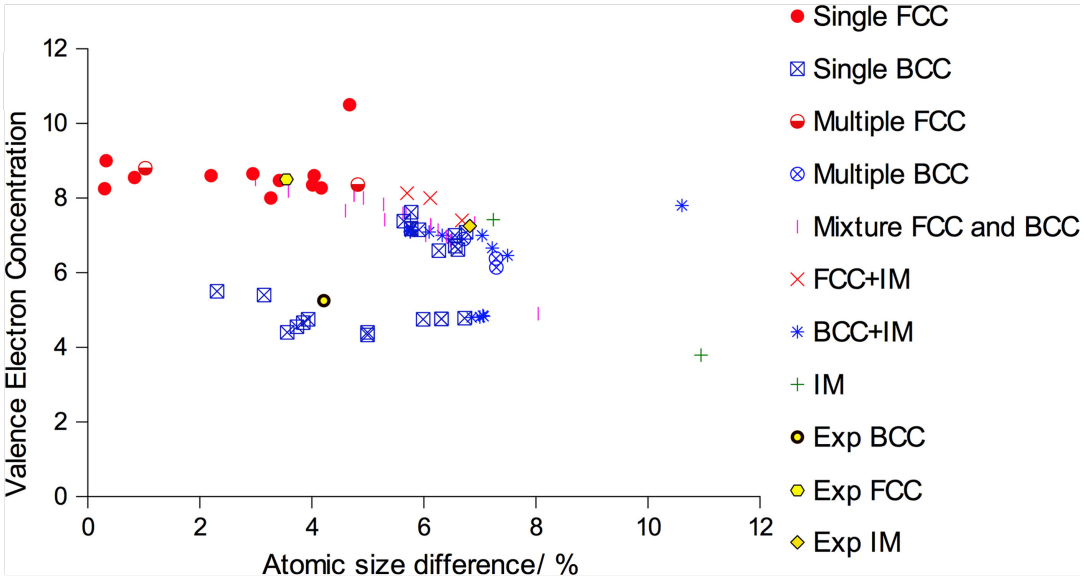


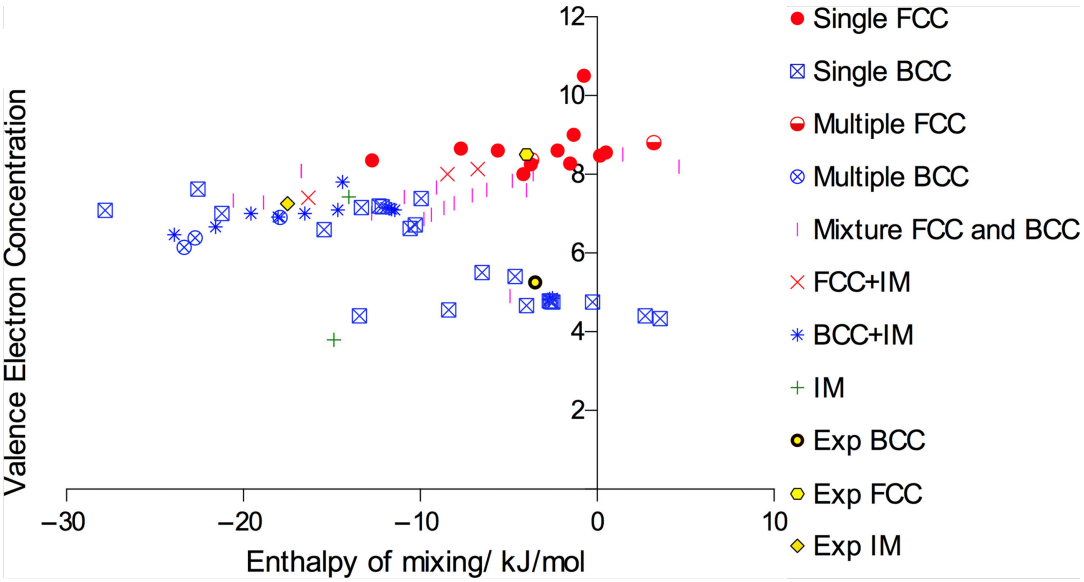
Figure 1.20: Experimental data showing the relationship between δ, ΔH_{mix} and ΔS_{mix}. From Zhang *et al.* [85].

Another of the most common relationships investigated in the literature is the combination of VEC with both δ and ΔH_{mix} [162–164]. To combat the issue of the lack of interpretability of high-dimensionality data, Domínguez *et al.* [164] utilised Principal Component Analysis (PCA) where a large number of variables can be compressed into one or two principal components that retain as much of the original information as possible. From this PCA, three novel alloy systems: TiMnFeNi, MnFeCoNi and TiVMnNb were produced to evaluate the relationships between the chosen parameters.

From Figure 1.21a it can be seen that while there are clear groupings of the phases into different regions, there is a more complex relationship between the parameters than presented by just δ and VEC. However, Figure 1.21b does demonstrate separation of the different phases into distinct regions of the ΔH_{mix} and VEC parameter space. The separation between single-phase and multiphase regions appears to be primarily influenced by ΔH_{mix}, while VEC governs the distinction between FCC and BCC phase formation, as proposed by Guo *et al.* [146]. Consequently, the combined use of ΔH_{mix} and VEC provides a valuable framework for guiding effective HEA design.



A



B

Figure 1.21: Plot demonstrating the correlation between a) δ and VEC, and b) ΔH_{mix} and VEC, with the phase formation of HEAs. From Domínguez *et al.* [164].

Yang and Zhang[156] introduced the parameter Ω (Equation 1.13) in 2012 and illustrated its relationship with δ in differentiating solid solution formation within HEAs. Figure 1.22 illustrates that HEAs forming solid solutions tend to cluster within a characteristic triangular region, defined by low values of δ and high values of Ω. In this region, the strain energy associated with lattice distortion is minimised, while ΔS_{mix} is sufficient to offset ΔH_{mix}, thereby favouring solid solution formation. This observation underpins the commonly cited criteria for solid solution stability: $\Omega \geq 1.1$ and $\delta \leq 6.6\,\%$.

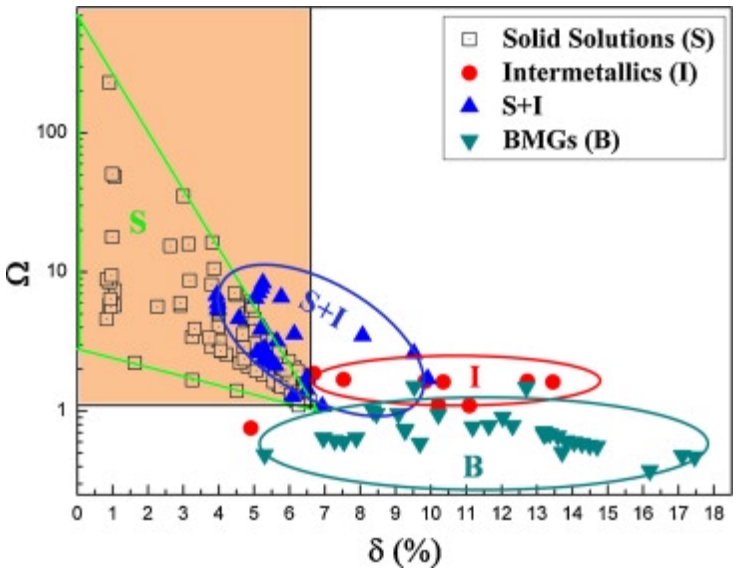
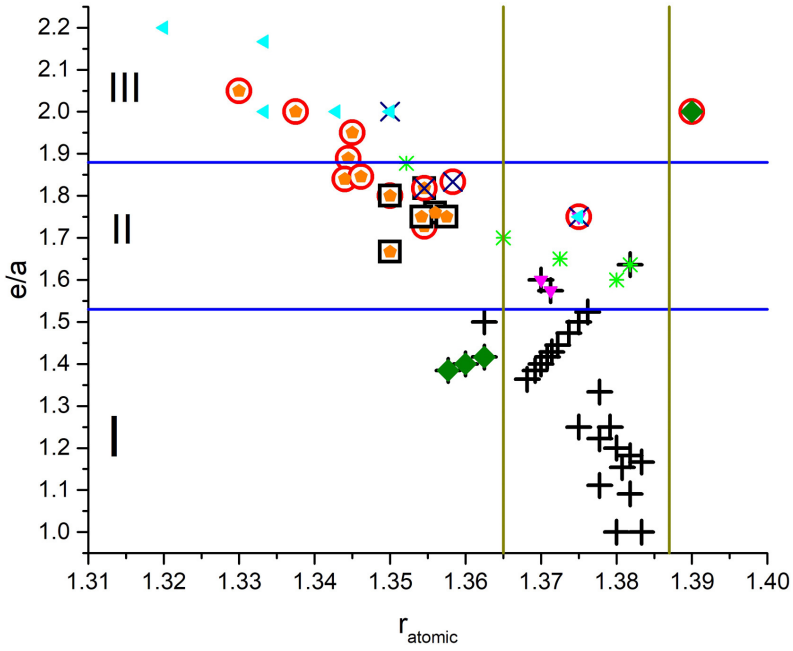
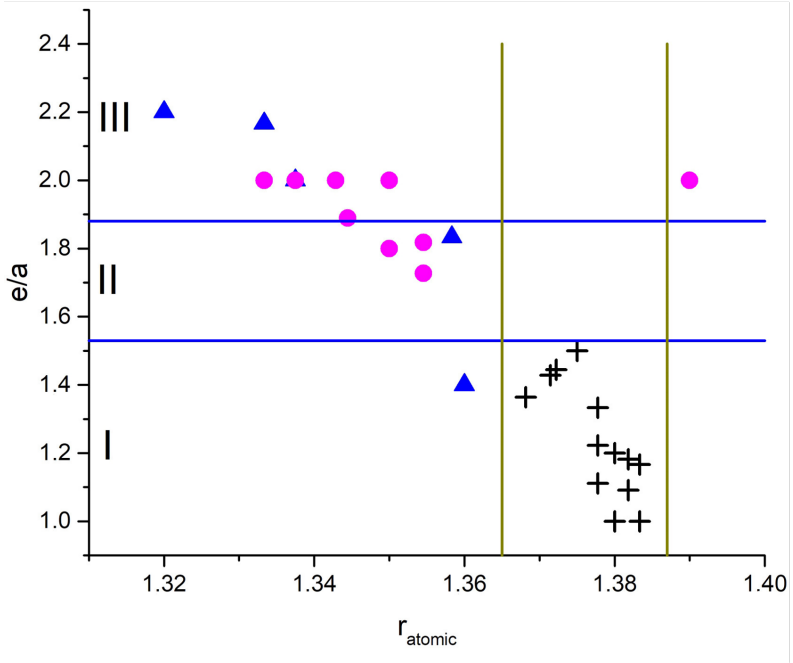


Figure 1.22: Illustration of the solid solution prediction zones forming from the combination of Ω with δ. From Yang and Zhang[156].

Calvo-Dahlborg *et al.* [151–153] also conducted extensive work to map not only the phase formation predictions, but also the bulk alloy hardness to the feature space of, e/a and average atomic radius r_{atomic}. Phase formation rules for e/a were established as discussed previously [151, 152] and these were utilised to design a series of alloys to further test these selection rules [153]. The results of the investigation of the designed HEA systems confirmed the combined influence of e/a and the atomic radius to distinguish between FCC, BCC, and HCP phase formation in addition to hardness. Therefore, these features could be applied to further design HEA compositions with desired phase formation and hardness.



A



B

Figure 1.23: e/a as a function of r_{atomic} for the investigated alloys in the study in the as cast form. The horizontal and vertical bars define the domains of e/a and r_{atomic} respectively. a) The different symbols indicate the phases identified by XRD. The key ones to consider are the plus signs indicating FCC, the circles denoting BCC and the square representing FCC + BCC. b) The symbols indicate the hardness of the HEAs measured by Vickers microhardness measurements. The black plus denotes HV $<$ 300, the purple circle represents 300 <HV< 450, the blue triangles indicate 450 <HV< 700, and the red stars are HV> 700. From Calvo-Dahlborg *et al.* [153].

1.5.3 CALPHAD: Thermodynamic Modelling

Calculation of phase diagrams (CALPHAD) is a thermodynamic modelling methodology developed in the 1970's [165] and used extensively in both academia and industry to determine the phase diagrams of materials, depicting the stable phases at equilibrium. The CALPHAD method models phase formation in higher order complex alloy systems, such as HEAs, by extrapolating thermodynamic data from simpler binary and ternary systems [166]. It evaluates the Gibbs free energy of all possible phases, including a potential solid solution phase ϕ, as described in Equation 1.19. The thermodynamic data for the constituent binary and ternary systems are sourced from experimental measurements, existing literature, and, in some cases, density functional theory (DFT) calculations [167]. The total Gibbs free energy of the system is then minimised by optimising the energy of each phase to determine the phases present in the equilibrium state of the system for a given composition, temperature and pressure [168].

$$G_m^{\phi} = \sum_i x_i G_i^{\phi} + RT \sum_i x_i \ln x_i + {}^{xs}G_m \tag{1.19}$$

Here, x_i denotes the composition of component i, G_i^{ϕ} is the Gibbs free energy of component i within the ϕ phase, T is the temperature and ${}^{xs}G_m$ is the excess Gibbs energy, which encompasses the non-ideal mixing enthalpy and entropy. The first term on the right hand side of the equation is the Gibbs free energy contributed from a mechanical mixture of the pure elements and the second term is the ideal configurational entropy. The excess Gibbs energy, Equation 1.20 contains the non-ideal mixing enthalpy and entropy.

$${}^{xs}G_m = \sum_i \sum_{j>i} x_i x_j \sum_{v=0}^{n} {}^{\nu}L_{ij}^{\phi}(x_i - x_j)^{\nu} + \sum_i \sum_{j>i} \sum_{k>j} x_i x_j x_k L_{ijk}^{\Phi} \tag{1.20}$$

Where ${}^{\nu}L_{ij}^{\phi}$ is the ν^{th}-order binary interaction parameter and L_{ijk}^{Φ} is the ternary interaction parameter. These can be described by the Redlich–Kister polynomial [169, 170] with temperature-dependent coefficients. The temperature dependence of these L parameters is what defines the excess entropy contribution [168, 171].

The CALPHAD method can be programmed independently or implemented via commercial software packages, such as Thermo-Calc, JMatPro or CompuTherm. In addition,

open-source implementations are available, such as PyCalphad. In this work the Thermo-Calc software package [172] was utilised and will hence be discussed in greater detail. Thermo-Calc can be used to determine the thermodynamics and phase diagram of a given elemental system. TC-Python, a Python language software development kit available with Thermo-Calc, enables integration with Python in order to perform high-throughput CALPHAD calculations [166]. The accuracy of the CALPHAD method largely depends on the quality of the database employed [167]. There are a large number of databases for a wide variety of material spaces, such as TCFE13 for steels, TCNI12 for Ni based superalloys, TCTI6 for Ti based alloys and SSOL8 for solid solutions of general alloys and substances [172]. However, these conventional thermodynamic databases designed for alloy systems with a single primary element are not suitable for HEA systems, as they typically focus on information for the binary and ternary systems of that primary element [167]. Thus, to facilitate the successful application of the CALPHAD method to HEAs, a database specifically designed for HEAs, TCHEA1 was developed in 2015 by Chen *et al.* [167]. This original database was heavily based upon TCNI8, as for a HEA database, the bigger the better, and TCNI8 contained a substantial number of binary and ternary systems. The HEA database has been constantly updated, with TCHEA7 released in 2024 containing new elements, binary and ternary systems and phases.

The predictive capabilities of CALPHAD present an opportunity for the design and development of novel HEA systems with enhanced properties for industrial applications. These CALPHAD calculations are used to identify compositional domains where single-phases are stable, refine the composition of an already known system [173], or design precipitation strengthened HEAs [174]. Choi *et al.* [175] applied the CALPHAD approach, utilising Thermo-Calc software and the TCFE2 steels database. The aim was to design a new FCC HEA by replacement of some or all of the Co with V. A new single-phase FCC HEA system was designed with all investigated alloys within this system displaying single-phase FCC structure above 800 °C. The authors highlight that the probability of identifying FCC single-phase HEAs increases when exploring non-equiatomic composition regions. They further note that CALPHAD thermodynamic calculations can serve as a powerful tool for guiding such discovery, so long as the limitations of the underlying thermodynamic database are appropriately accounted for. Li *et al.* [176] use CALPHAD to optimise a specified HEA system, TiZrHfNbTa, by investigating elemental substitutions

to improve phase stability at intermediate temperatures. CALPHAD analysis found Ta to be detrimental to phase stability at all concentrations and thus was removed. Hf was also found to be detrimental at high concentrations. Hence, in this study, the phase diagrams of $M_x(TiZrHfNb)_{100-x}$ were computed using CALPHAD, where M_x is a common refractory element. Therefore, based on the results of the CALPHAD assessment, a novel non-equimolar Hf-lean refractory HEA $Ti_{30}Zr_{30}Hf_{16}Nb_{24}$, was successfully located within the BCC single phase region at 600 °C. A variety of eutectic HEA studies utilise CALPHAD as the main design tool to probe for new compositions [177, 178]. Joseph *et al.* [135] investigated compositional optimisation through elemental substitution of a eutectic HEA, $AlCoCrFeNi_{2.1}$. Two separate avenues were explored, the substitution of Co with Ni and Cr with Fe, and the substitution of Co and Cr with Fe. A wide range of new eutectic HEA systems were proposed using the TCHEA5 database within Thermo-Calc, specifically designed to meet the established criteria of forming approximately 34 % B2 phase near the melting point of 1300 °C. The development of novel HEAs is particularly well-suited to CALPHAD-based approaches, which offer robust capabilities in modelling phase stability, transition temperatures, and complex phase diagram structures [41].

However, due to the compositional space that HEAs occupy, the most efficient application of CALPHAD to the design of new HEA systems is through large scale high-throughput investigations of phase formation across a wide compositional space. In 2015, Senkov *et al.* [179] utilised a new methodology to accelerate the search for HEAs with solid solution phases by screening a large number of possible compositions with CALPHAD. Phase diagrams for all equimolar combinations comprising 3, 4, 5, or 6 elements were calculated using a set of elements selected based on domain expertise and prior knowledge of HEA-forming systems. A total of 134 547 phase diagram calculations were performed, from which 51 equimolar alloys meeting the design criteria for high-temperature structural materials were selected for further investigation. The focus of this study is taken away from prioritising single phase microstructures, as most structural alloys achieve a difficult balance of competing properties by careful control of multi-phase microstructures. Following this work, Senkov *et al.* [180] performed a similar study in the search for HEAs for structural applications. Again, due to the shear number of possible compositions of HEAs, the search space was restricted to equiatomic combinations of 3, 4, 5, or 6 elements. Even with this constraint, the number of potential combinations remains extremely large, as

evidenced by the calculation of equilibrium phase diagrams and thermodynamic properties for 111 654 unique equiatomic HEAs. Highlighting the need for efficient screening strategies. From this investigation, 157 new equiatomic HEAs were identified as single phase at the solidus temperature, encouraging future studies.

Despite this volume of work, the credibility of CALPHAD, particularly for high-throughput HEA tasks, relies heavily on the size and quality of the available databases. Extrapolation to the high order equiatomic compositions can only be achieved if all the possible constituent binary and ternary systems of the equiatomic HEA have a complete thermodynamic description. However, a complete thermodynamic description of all the binaries and/or ternaries may not be available for the higher order systems in the thermodynamic databases [179, 180]. A further problem with the use of CALPHAD for high-throughput investigations is computational time. Although significantly quicker than experimental investigations, the thermodynamic modelling of hundreds of thousands of HEA compositions is not a quick process. Therefore, while CALPHAD can serve as a stand-alone method for predicting phase formation across the HEA space, it can also complement more accurate approaches like density functional theory or support faster, more computationally efficient methods such as ML.

1.5.4 Density Functional Theory: Atomistic Modelling

Density functional theory (DFT) is a quantum mechanics based computational methodology used to study the electronic structure, in particular the ground state, of atoms, molecules, and bulk solid phases. These calculations from first-principles can compute the behaviour of atoms and electrons in condensed matter such as metal alloys to define the atomic bonding [99]. Therefore, the characteristics of any material can be predicted by solving the time independent Schrödinger equation to obtain the ground state energy of the system, the lowest eigenvalue of the Hamiltonian [41]. However, unlike the case of a particle in a box, there are multiple nuclei interacting with multiple electrons, requiring the time independent many electron Schrödinger equation [181],

$$\hat{H}\psi = \left[\hat{T} + \hat{V} + \hat{U}\right]\psi = \left[-\frac{\hbar^2}{2m}\sum_{i=1}^{N}\nabla_i^2 + \sum_{i=1}^{N}V(\boldsymbol{r}_i) + \sum_{i=1}^{N}\sum_{j<i}U(\boldsymbol{r}_i,\boldsymbol{r}_j)\right]\psi = E\psi \quad (1.21)$$

where the term $\hat{T}$ defines the kinetic energy of each electron, $\hat{V}$ defines the interaction energy between each electron and the positively charged atomic nuclei and the final term $\hat{U}$ is the interaction energy between the electrons. $\hat{U}$ is the most critical term for solving the equation as it means this complex many body problem cannot be separated into simpler single particle equations, instead the full solution will be a function of $3N$ dimensions, where N is the number of electrons [181]. However, DFT addresses this problem by expressing the system in terms of the electron density $n(\boldsymbol{r})$, a function defined in three dimensions, thereby mapping the many-body problem onto an effective single-body problem without the interaction term $\hat{U}$. This reduces the complexity of solving the Schrödinger equation from $3N$ dimensions to just 3. Finding the electron density can be expressed in a way that requires solving a set of equations involving only a single electron.

$$\left[-\frac{\hbar^2}{2m}\nabla^2 + V(\boldsymbol{r}) + V_H(\boldsymbol{r}) + V_{XC}(\boldsymbol{r})\right]\psi_i(\boldsymbol{r}) = \varepsilon_i\psi_i(\boldsymbol{r}) \tag{1.22}$$

Here, the summation signs from the full Schrödinger equation have disappeared as the solutions are single-electron wave functions in only three dimensions [181]. V is the same as in the full Schrödinger equation and V_H describes the interaction between the electron under consideration and the total electron density defined by all the electrons. V_{XC} defines the exchange and correlation contributions to the single electron equations. For example, correcting for the self interaction of the electron under consideration in V_H [41, 181].

The solution to this problem is an iterative process to find the true electron density which corresponds to the solution to the Schrödinger equation, minimising the energy of the overall function. First, a trial electron density is defined. Then Equation 1.22 is solved using the trial electron density to determine the single particle wave functions $\psi_i(\boldsymbol{r})$. These single particle wave functions are then used to calculate the electron density [181].

$$n_{KS}(\boldsymbol{r}) = 2\sum_i \psi_i^*(\boldsymbol{r})\psi_i(\boldsymbol{r}) \tag{1.23}$$

If the trial electron density matches the calculated electron density, then this is the ground state electron density. However, if the densities are different then the trial density is updated and the process started again. This ground state electron density directly determines all the properties of the system such as the total energy [181]. Hence, from this the

bonding and bond lengths of the system can be defined as well as thermodynamic properties such as enthalpy [41]. Facilitating predictions on crystal structure, lattice constants, phase formation and stability, and mechanical properties such as elastic constants [99].

Therefore, DFT can be utilised by the HEA community for alloy design, searching the compositional space by predicting physical features, such as phase formation and mechanical properties without the need for experimental data [99]. King *et al.* [182] utilised DFT calculations to predict the formation and stability of 185 single-phase HEAs. These predictions were directly compared to predictions using an empirical Miedema methodology to assess its suitability for predicting single-phase formation. Despite the lack of accuracy of the empirical methodology, it captured the general trend of single-phase HEA formation predicted by the DFT calculations. Using this semi-empirical methodology would be orders of magnitude faster than DFT, allowing a large number of HEA systems to be investigated. In addition to phase formation, DFT can also be utilised to predict phase transformations within HEAs [183]. Rogal *et al.* [184] aimed to synthesise the HEA $Hf_{25}Sc_{25}Ti_{25}Zr_{25}$ and experimentally assess its mechanical properties. These experimental results were then compared to the DFT predictions of the mechanical properties. The results of the DFT predictions of the elastic constants compared favourably with experimental assessments, illustrating the suitability of DFT for the prediction of the mechanical properties of HEAs to aid in future design of HEA compositions.

However, DFT calculations are extremely computationally intensive, making them impractical for many HEA studies [98]. Additionally, DFT calculations are performed at absolute zero, hence the reliability of the calculations for practical scenarios is questionable and while methodologies to utilise temperature as a variable exist they significantly more computationally intensive than the standard calculations. Furthermore, DFT calculations also exhibit inaccuracies and uncertainties, especially when considering the d-orbitals of transition metal atoms [185] which are often the main constituents of HEAs [98].

1.5.5 Future Design Methodologies

ML presents a new tool to aid in the design of novel materials with exceptional properties and as such is rapidly growing in popularity within the materials science community. Unlike the parametric design methodologies outlined above [98], ML works well with high dimensionality data to learn trends and predict the desired properties from multi-

ple inputs. In addition, ML is extremely fast and computationally efficient compared to approaches such as CALPHAD and DFT, making it ideal for searching the HEA compositional space to design new systems for demanding applications. Figure 1.24, highlights the exponential growth and rapid adoption of ML within the HEA field. From this figure it is clear that the application of CALPHAD has stagnated and that ML has caught up to DFT in its popularity. The observed increase in HEA studies incorporating DFT over the last couple of years can also be partially attributed to the application of ML within DFT studies to accelerate this approach.

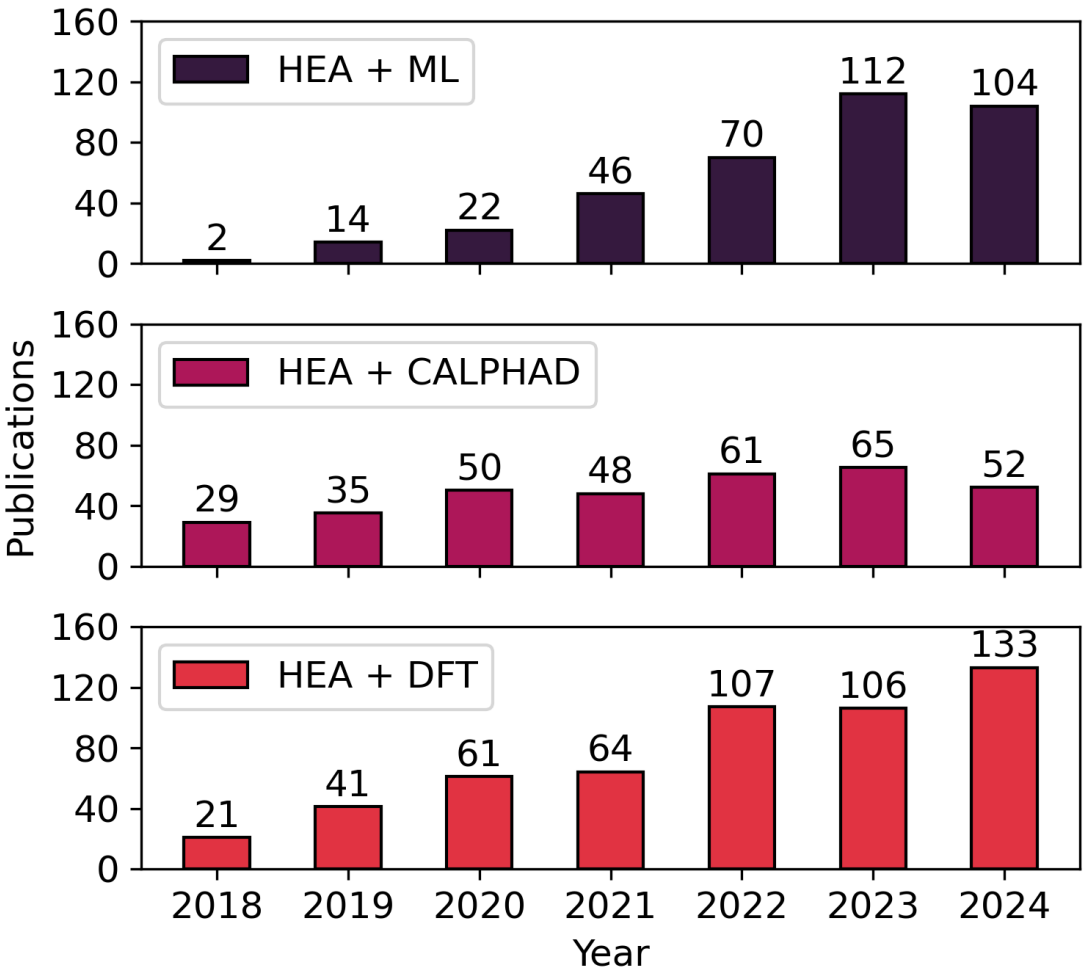


Figure 1.24: The publication rate for HEA literature combined with ML, CALPHAD and DFT methodologies since 2018 when ML was first introduced to HEAs. Data gathered from Scopus [71] by searching for "high entropy alloy" in combination with "machine learing", "calphad", and "density functional theory" respectively in the journal article title, abstract and keywords. Data accurate as of 03/08/2024.

1.6 Machine Learning

ML is a methodology whereby computer systems can learn to perform specific data-based tasks without any explicit programming. Broadly speaking, ML can be split into three different categories: supervised, unsupervised, and reinforcement learning [186]. Supervised learning involves training a model on a labelled dataset, where the input-output pairs are provided, to predict outcomes for unseen data based on the learned mapping [187, 188]. In contrast, unsupervised learning deals with unlabelled data, focusing on identifying patterns, structures, or groupings within the data, such as clustering. Reinforcement learning is a goal-driven approach where an agent learns to make decisions by interacting with an environment, receiving feedback in the form of rewards or penalties to optimise its behaviour over time. Supervised learning is by far the most popular type of ML used in materials discovery due to its suitability for handling tabular data. However, unsupervised ML is starting to see a steady increase in applications for materials discovery [189]. Thus, supervised learning was utilised in this work over the alternatives of unsupervised and reinforcement learning [188]. Supervised learning can be further subdivided into classification and regression tasks. Classification tasks assign discrete labels to data points, grouping predictions into distinct categories. In contrast, regression tasks predict continuous numerical values, modelling relationships between variables to estimate outcomes on a continuous scale [186]. This difference is highlighted in Figure 1.25.

As ML tools and materials data have become more accessible, their integration into materials science has expanded rapidly [190]. ML is increasingly recognised as a powerful approach for automating materials discovery workflows [98, 191]. Its use in computational materials design has enabled accelerated exploration of compositional spaces in an unconstrained manner [192], while also reducing reliance on costly trial-and-error experiments [134]. ML can guide these experimental investigations by uncovering patterns and trends in large quantities of high-dimensional data, whilst subsequently enabling property predictions [134, 191]. These predictions are fast, informative, reproducible, and scalable [186]. Newly available data can be directly incorporated into future iterations to improve the prediction capabilities [192]. Together, these capabilities lead to high throughput evaluation of numerous compositions, supporting the down selection of candidates for evaluation against application requirements.

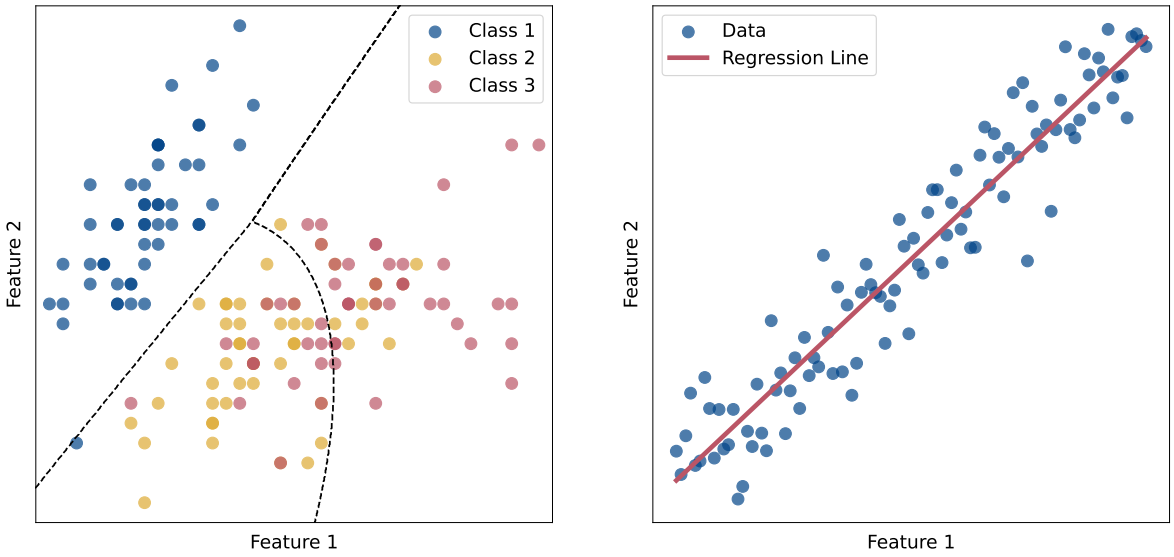


Figure 1.25: Scatter plots illustrating key differences between classification and regression tasks: A) Classification task, showing data points grouped into three distinct classes based on two features. Each class is represented by a unique colour, and decision boundaries delineate the regions associated with each class. B) Regression task, showing the relationship between two continuous features. A regression line is fitted to model the trend.

1.6.1 High Entropy Alloy Data

In any supervised ML task, the first step is collecting appropriate data to train and test the models [193]. ML excels when data relationships are too complex for humans to rationalise but often struggles to extract meaningful insights from small datasets [194]. Hence, to maximise the performance and predictive power of ML models, large volumes of high-quality and balanced data are essential [63, 191, 195, 196]. Furthermore, the dataset size is also critical in selecting the optimal ML algorithm for the required task. For small datasets, classical and statistical methods such as regression, clustering, and tree-based algorithms perform best due to their lower risk of overfitting and greater computational efficiency [194]. In contrast, more complex algorithms, such as neural networks, require large datasets, on the order of thousands of data points, for training, testing, and validation [194, 197].

Despite significant research and publications in the field of HEAs since 2004, the available HEA data for ML tasks is still sparse [63, 198, 199]. Many ML studies within the HEA field report that the paucity of data is the main limiting factor in the performance of ML models [98, 120, 158, 195, 198, 200–205]. In addition, HEA data is highly imbalanced

because of the initial emphasis towards the discovery of single-phase solid solution microstructures. Negative results from unsuccessful alloy design processes are also rarely published in peer-reviewed literature, further constraining the availability of data for meaningful integration into ML-driven materials discovery [48, 187, 190, 197, 206]. When working with real-world data, duplicated, poorly formatted, irrelevant, and incomplete entries are unavoidable. Therefore, data cleaning and pre-processing is a critical, time-consuming, yet often undocumented step within ML studies to prepare the raw data for analysis [63, 193, 194, 207].

There are a range of experimental HEA databases available in the published literature, covering a variety of properties. The most commonly reported property by far is phase formation [196, 208, 209], appearing in almost all experimental databases. However, other mechanical properties, such as hardness [210–212], yield strength [157, 210, 211], and fatigue life [213] are also detailed. Combinations of these databases are often used as the foundational training data for many published ML studies [214]. The available databases in the literature demonstrate that significantly more work is needed in making well populated HEA data open access in standardised formats, to prevent data siloing and facilitate data sharing [190, 191, 215]. In addition to these experimental databases there are many databases constructed from modelling simulations. One example of this is the Materials Project. Providing structural and property information on over 154 718 inorganic materials, including HEAs, from DFT calculations [216].

Because of the relative lack of availability of experimental HEA data, ML models are often constructed using sparse datasets. For example, to the authors' knowledge, the largest experimental training dataset was used by Pei *et al.* [217] and consisted of 1 252 datapoints. Whereas, a significant number of studies constructed models trained from databases containing 200 or fewer datapoints [198, 201, 203, 218, 219].

1.6.2 Addressing the Availability of High Entropy Alloy Data

To combat the insufficient data within the HEA field, many data supplementation techniques have been utilised. The CALPHAD method has been used to both generate databases and supplement existing experimental data. Vazquez *et al.* [197] performed single-point equilibrium calculations to generate a HEA database of 229 156 compositions. Similarly to CALPHAD, DFT calculations have also been applied to generate

HEA databases for ML training. Zhang *et al.* [199] generated a dataset of 3 579 quaternary HEAs while Kaufmann *et al.* [120] supplemented 134 experimental compositions with 1 664 DFT compositions. This use of CALPHAD and DFT to generate data for ML training begs the question, if it is possible to generate data in this way to train ML models, then why bother with the ML at all? There are multiple reasons for this. Firstly, CALPHAD is calculated based on the energy minimisation of experimental data which for most alloy systems often requires extrapolation from binary and ternary systems that comprise the thermodynamic databases. Secondly, ML is significantly faster and incurs lower computational costs [158] than both CALPHAD and DFT calculations [192, 197].

As discussed, HEA property data collected under a variety of experimental conditions are published in small datasets across a range of literature. Therefore, it would seem logical to enhance the quantity of HEA data for ML model training by aggregating these data sources. However, Ottomano *et al.* [220] argue that expanding datasets in this way may affect the organicity and overall quality of the available data. To demonstrate this, model performance of a range of algorithms was compared before and after aggregation using a variety of collation techniques. In all cases, classical ML algorithms such as random forest and logistic regression demonstrated a reduction in performance. In contrast, deep learning models showed greater robustness, but no significant change in performance. Therefore, when collating data to increase data quantity, it is critical to consider the type of ML algorithm being utilised and the difference in origin of the individual datasets.

Other methods to combat insufficient data can be as simple as employing an empirical relationship. For example, Huang *et al.* [98] utilised an empirical relationship,

$$\sigma_y(\text{MPa}) \approx \frac{1}{3}H(\text{MPa}) = \frac{9.81}{3}HV(\text{Hv}), \tag{1.24}$$

to convert reported yield strength data σ_y, to the target variable hardness HV.

However, such practices come at the risk of introducing low quality data into the training dataset. Equation 1.24 for example has been found to be accurate for BCC HEAs, but less so for FCC HEAs [98]. Thus, such practices are generally not recommended for HEA studies, unless sufficient evidence is present to ensure the fidelity of generated data. Alternatively to physics based or empirical modelling approaches towards data generation,

ML can also be used to generate data for other ML algorithms. Lee *et al.* [221] produced a Conditional Generative Adversarial Network (CGAN) to generate additional training data, and demonstrated that employing a CGAN in conjunction with a neural network can improve phase prediction performance for HEAs. However, the number and diversity of the generated samples depends on the original dataset. Hence, on smaller datasets, CGAN augmentation has limited improvement on model performance [195]. Finally, Pilania *et al.* [187] discuss the potential shift in focus towards utilising natural language processing techniques to strip materials knowledge and data from published literature. This approach offers a promising route to efficiently compile existing domain knowledge into substantial databases for HEA focused machine learning studies [222, 223]. This vision is increasingly becoming a reality, as demonstrated by recent efforts such as a recent semi-automated annotation framework tool, which employs large language models to extract structured materials data from text [224].

1.6.3 Addressing the Imbalance of High Entropy Alloy Data

As discussed previously, a major limitation of HEA databases arises from the inherent compositional imbalance, driven by a research focus on single-phase solid solutions that skews the data toward FCC and BCC microstructures, as shown in Figure 1.26. This data imbalance can significantly affect model performance, as the under-represented classes lack sufficient training data. Additionally, traditional classification tasks struggle with imbalanced data, often biasing predictions toward the majority class [193, 200], which is typically not the primary focus of most studies. For small imbalanced datasets the minority class is typically insufficient for learning, especially when there is a degree of overlap within the classes [193]. This is especially true for HEA databases where FCC and BCC phases dominate datasets and pronounced overlap exists between solid-solution and solid-solution plus intermetallic phase fields [49].

The most common methods to tackle the issue of imbalanced data are random oversampling and undersampling [193]. Oversampling supplements the available training data with clones of the minority classes in order to balance them with the majority class [225]. Risal *et al.* [225] applied random oversampling and found it to be effective for phase prediction based on the available dataset. Ren *et al.* [63] also utilised random oversampling to change the distribution of their datasets and although they did not directly comment

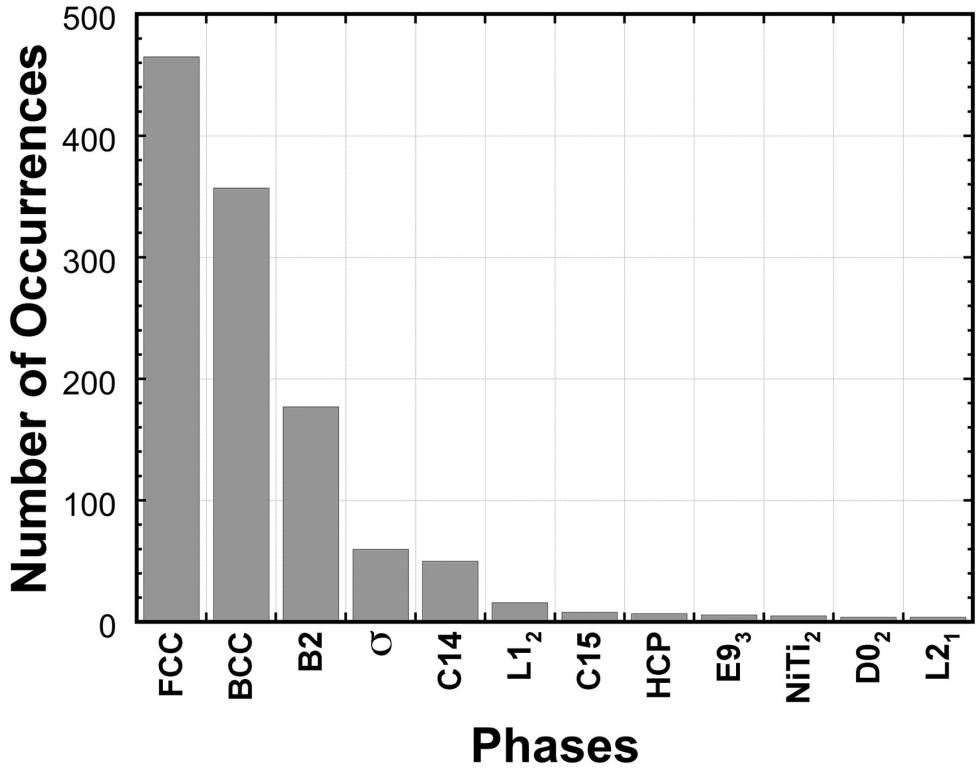


Figure 1.26: Data imbalance and domination of FCC and BCC phases across 648 published reports of microstructure within HEA studies. Phases appearing less than 4 times are not shown [49].

on the impact of the data augmentation, the method successfully produced two models to predict high hardness HEAs. In contrast, undersampling modifies the class distribution by reducing the data of every class to match the minority class [225]. This technique is significantly less popular in the HEA field as it means the removal of precious data from already small datasets. Hence, oversampling is generally preferred. Another technique to combat data imbalance is Synthetic Minority Oversampling Technique (SMOTE) [226]. SMOTE generates synthetic samples based upon the minority classes of the input dataset, using k-nearest neighbours to sample the feature space of the class, such that the distribution of data across all the classes is balanced. Crucially, this method does not alter the underlying distribution or characteristics of the data; it simply increases the number of data points by generating synthetic samples consistent with the original data distribution [200, 227]. Bansal *et al.* [227] reported an improvement in model prediction by increasing the quantity of datapoints using synthetic data. However, Singh *et al.* [228] argue that implementing augmented data to combat data imbalance is not reliable. The authors claim that accuracy alone is not the most robust measure for assessing performance from ML models constructed from imbalanced data. Furthermore, it cannot be guaranteed that the

generated samples are HEAs. To investigate this, multiple "vanilla" ML classifier models were compared with SMOTE-Tomek augmented models of the same algorithms. The best performing classifier was found to be a random forest model and despite the claims that augmenting data is not the optimal approach, the augmented models showed better performance scores in all cases than the "vanilla" models. Hareharen *et al.* [229] also find that SMOTE improves the ability of the ML model to differentiate between the various classes. However, improvements in classification metrics do not necessarily translate to enhanced alloy design workflows or better generalisability of the model across the wider materials space.

1.6.4 High Entropy Alloy Feature Engineering

Subsequent to data collection, feature engineering is the next step in construction of a supervised ML model and consists of feature generation and selection. Supervised ML tasks aim to predict a designated target variable, often phase formation [214, 230] as a proxy for microstructure which dictates the structural and mechanical properties, from a set of input features or descriptors [186]. These features, chosen for any ML model, must be both machine readable and relevant to the target variable [190]. Thus the input features, used frequently in ML based HEA studies, are often empirical relations originating from the Hume-Rothery Rules on solid-solution formation for binary systems [195, 231], as discussed in Section 1.5.1. These features exhibit clear trends with HEA microstructural and mechanical properties, which has led to their successful application in HEA-focused ML studies. For example, VEC and δ are commonly reported as two of the most important features by many authors investigating both microstructural and mechanical properties via application of ML methodologies [63, 98, 202, 203, 232], demonstrated in Figure 1.27.

An important decision when generating features for HEA ML studies is whether to include the chemical composition of the alloy as an input feature. Bakr *et al.* [205] demonstrated that an artificial neural network can be trained to predict both phase formation and hardness of HEAs using only chemical composition as input. Similar composition-only approaches have also been demonstrated in other studies [234–236]. However, He *et al.* [237] found that using only a small number of features performed significantly better than only utilising the composition. Similarly, Jain *et al.* [207] included the elemental compositions as features for phase predictions and used them as the only feature for hardness

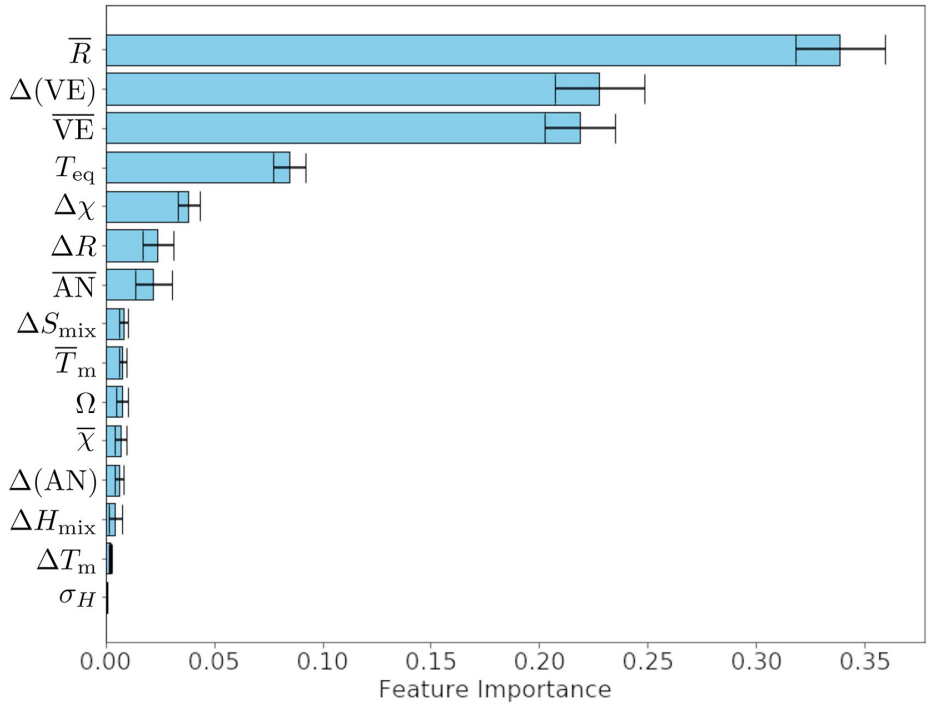


Figure 1.27: Feature importance scores of 15 features within an XGBoost model used for phase classification. In this case R denotes atomic radius and VE represents valence electron count [233].

predictions. However, Wen *et al.* [238] argue that utilising the elemental composition in conjunction with the elemental property features discussed above significantly outperforms just training ML models on the elemental composition. Furthermore, Morgan *et al.* [190] state that utilising composition as an input feature means that the model cannot be used to extrapolate to systems including elements outside of the training data. For example, Chen *et al.* [202] include the molar fraction of the six constituent elements of their HEA system as features for the model, but only hardness optimisation of a single alloy system was investigated. Hence, Morgan *et al.* [190] argue that it is better to represent each element with elemental properties to enable feature generation by taking compositionally averaged combinations of the constituent elements, as in Section 1.5.1. Hence, if utilising ML to optimise the composition of an already defined HEA system then including composition may be useful. However, if the goal of ML application is materials discovery, then evidence suggests otherwise.

Following the discussion of the need for high quantities of data to train ML models in Section 1.6.1, it could be assumed that the more features available to make predictions of the target, the better a model will perform. However, this is not the case and many HEA ML studies demonstrate that as the number of features increases, prediction accuracy plateaus [63, 238–240], illustrated in Figure 1.28, while introducing feature redundancy, overfitting and resulting in poor generalisability and computational efficiency [63, 190, 240]. Feature selection is an essential process that reduces the dimensionality of the ML task by identifying and removing irrelevant, noisy and redundant features, while retaining sufficient information and optimising the number and combination of features to maximise accuracy and improve ease of training [63, 158, 193, 195, 196, 214, 241].

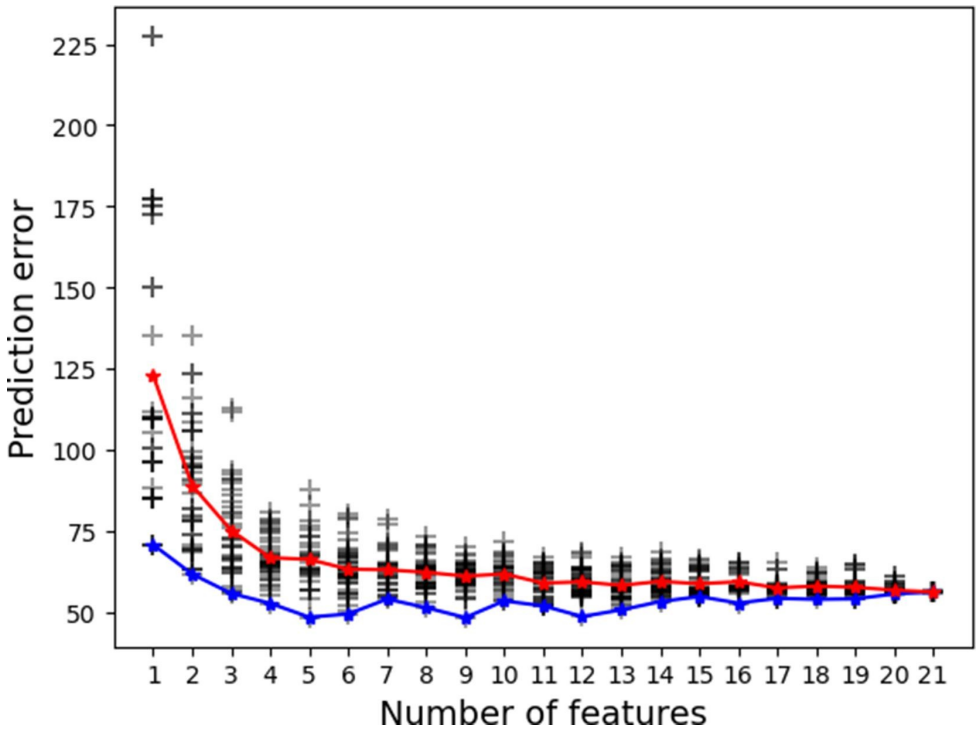


Figure 1.28: Model performance plateaus as the number of features is increased, in this case for a support vector machine model. The red and blue lines represent the average and lowest prediction error for that number of features respectively [240].

1.6.5 Multicollinearity Analysis

Collinearity of features is detrimental to model performance [63], computational efficiency and importantly, interpretability, making it difficult to ascertain the individual contribution of each feature to the model [242]. Hence, for features that are correlated, the least important feature is typically omitted [201, 204].

To detect collinearity, the most popular method is to measure the correlation of individual features using the Pearson Correlation Coefficient (PCC) [196, 243],

$$r = \frac{\sum_{i=1}^{n}(x_i - \bar{x})(y_i - \bar{y})}{\sqrt{\sum_{i=1}^{n}(x_i - \bar{x})^2 \sum_{i=1}^{n}(y_i - \bar{y})^2}}, \tag{1.25}$$

where x and y denote two of the features and $\bar{x}$ and $\bar{y}$ represent the mean of the two features, respectively. PCC values can range from $+1$ to -1, with positive values indicating a positive relationship between the variables and negative values indicating a negative relationship. Commonly in correlation analysis, features with PCC values > 0.80 are considered very strongly correlated [63, 202, 243]. However, there are no fixed cut-offs for the interpretation of feature correlation strength, rather, context is critical to understanding both the extent and impact of the correlation on the model [244, 245]. Despite this, in many HEA ML studies, the limit for where features are considered highly correlated is often set very close to 1, at PCC > 0.95 [201, 232, 240]. Typically, in HEA ML studies where the correlations are moderate, the issue of where to place the limit of correlation is avoided and authors often do not state at what point they would have considered features to be correlated and why [203, 204, 231]. It is also common for HEA ML studies to assess how important ML features are through their correlation with the outputs [207], but this is not an effective method for model interpretability.

1.6.6 High Entropy Alloy Feature Selection

Data, features, and models are extensively interlinked and so the optimal feature combinations for the available data must be found for each model tested. However, it can be computationally prohibitive to test every possible permutation [190]. Several techniques and approaches have been developed to enable feature engineering. The first and simplest method of feature selection is human context. Nonsensical features and those with no relation to the target variable should be removed [190]. Global ML interpretation methods describe the average behaviour of the model, showing the general mechanisms and trends. Permutation feature importance is one such technique, which measures the increase in prediction error as the model's features are permutated. A feature is considered important if randomly shuffling its values increases the model's error, as in this case the model relies upon this feature to make its predictions. In contrast, a feature is considered

unimportant if shuffling its values does not impact the model's error [186]. The greater the permutation importance, the greater impact the feature has on predictions. Local interpretation methods explain the individual predictions of the model. SHapley Additive exPlanations (SHAP) is a local interpretation method that can be used to explain an individual prediction by determining the contribution of each feature [246, 247]. The SHAP summary plot shown in Figure 1.29, combines feature importance and feature effects [186]. Each point represents a SHAP value for a feature and an individual prediction. Overlapping points are jittered in the y-axis to provide an illustration of the distribution of SHAP values per feature. Additionally, the features are ordered in the y-axis by their importance for predictions [186]. A positive SHAP value indicates a positive impact on model predictions, in the case of Figure 1.29 this indicates the model being more likely to predict a higher value of HEA hardness. While the colour of the points denotes the value of the feature as indicated by the legend.

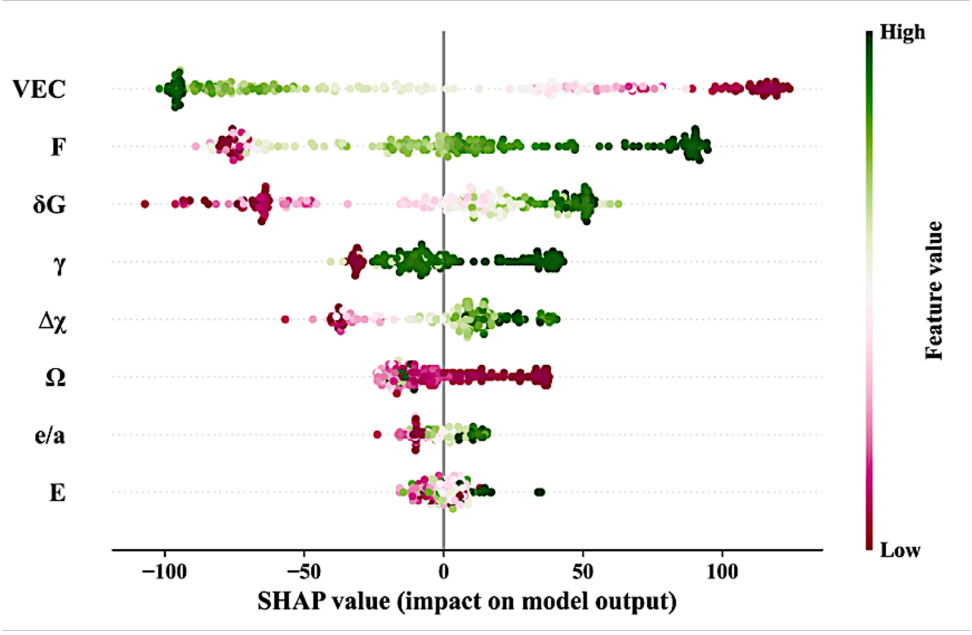


Figure 1.29: Example SHAP summary plot of a feature set. Feature importance increases from bottom to top and the colour reflects the magnitude of the feature value. A positive SHAP value indicates a positive impact on model output, i.e. a HEA with increased hardness and vice versa. From Ren *et al.* [63].

Several techniques have been developed to automate the feature optimisation process. Sequential feature selection iteratively adds or subtracts features from the dataset in order to maximise model performance [63, 190, 239]. Building upon this idea, Li *et al.* [240] utilised a genetic algorithm to find the optimal combination of features. The genetic algorithm mimics the mechanism of natural selection to arrive at the global optimum

performance without testing every possible combination. This saves on computational efficiency over the exhaustive sequential feature selection methods, especially for large feature spaces. HEA ML studies generally agree that a small number of features, typically four or five, are optimal for predicting phase formation [63, 238–240] and mechanical properties [134]. Although Huang *et al.* [201] concur that five features are sufficient for accurate phase prediction, they report that a considerably larger number, 13 features, is optimal for predicting hardness, in contrast to most HEA studies.

1.6.7 Algorithms for High Entropy Alloy Design

An exhaustive discussion on how each individual supervised ML algorithm functions is beyond the scope of this literature review. See Hastie *et al.* [230] and James *et al.* [242] for an overview. No supervised ML algorithm is by default superior to any other and the choice of optimal algorithm depends strongly on the available data and target output [194, 239]. Choosing a suitable algorithm is critical for improving model performance and efficiency [63]. Therefore, many ML studies trial a handful of potential ML algorithm candidates to determine which performs the best, for example [196, 201, 239], shown in Figure 1.30.

Alternatively, some ML HEA studies already have a specific algorithm in mind because of the benefits of that particular methodology. For example, Bhandari *et al.* [204] and Choudhury *et al.* [248] select a random forest algorithm for its simplicity and interpretability. Interpretability refers to the transparency of the model's decision making process and how easily the methodology of decisions is understood [193]. Figure 1.31 provides an illustration of this transparency to performance trade-off of different ML models.

Simple linear regression models are much easier to understand, but lack in predictive power and performance [194]. They are often too simple for the HEA prediction tasks. Clustering algorithms, such as k-nearest neighbours, suffer from low accuracy and when the data is imbalanced, the more frequent classes significantly dominate predictions, becoming more noticeable as the number of neighbours considered increases [98, 196]. Tree based algorithms have very high interpretability and training speed, but are susceptible to overfitting. However, ensemble tree based models, such as random forest, have anti-overfitting properties [156, 196]. Thus, there is very little incentive to utilise standard decision tree models at all. Instead, tree based models such as random forest, XGBoost

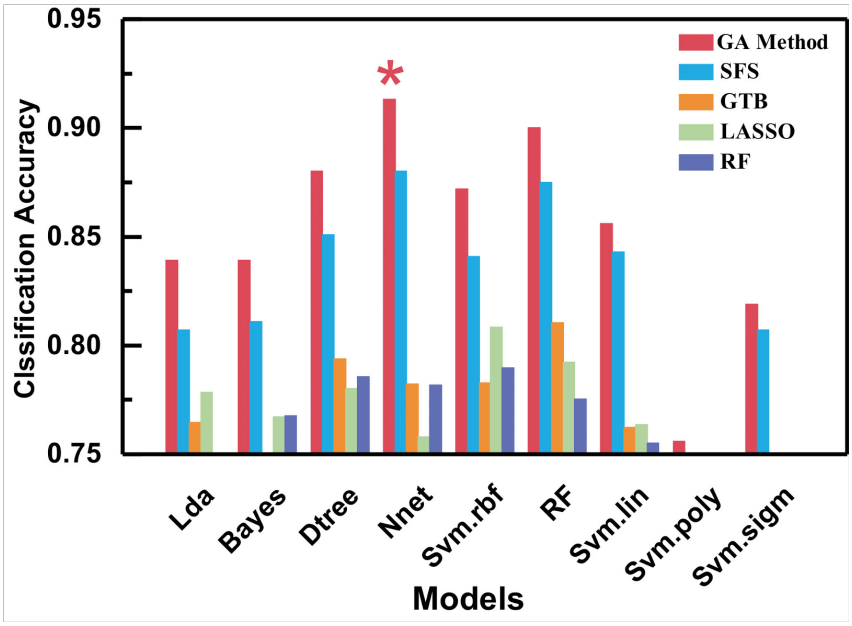


Figure 1.30: Comparison of model performance across the same experimental database, including linear discriminant analysis (Lda), decision tree (DTree), Naive Bayes (Bayes), neural network (NNet), random forest (RF) and support vector machine (SVM) with linear, polynomial, sigmoid or radial basis function kernel. Each column represents a different feature subset selected by application of the models, genetic algorithm (GA), sequential forward selection (SFS), gradient tree boosting (GTB), least absolute shrinkage and selection operator (LASSO), and random forest (RF) indicated in the legend [239].

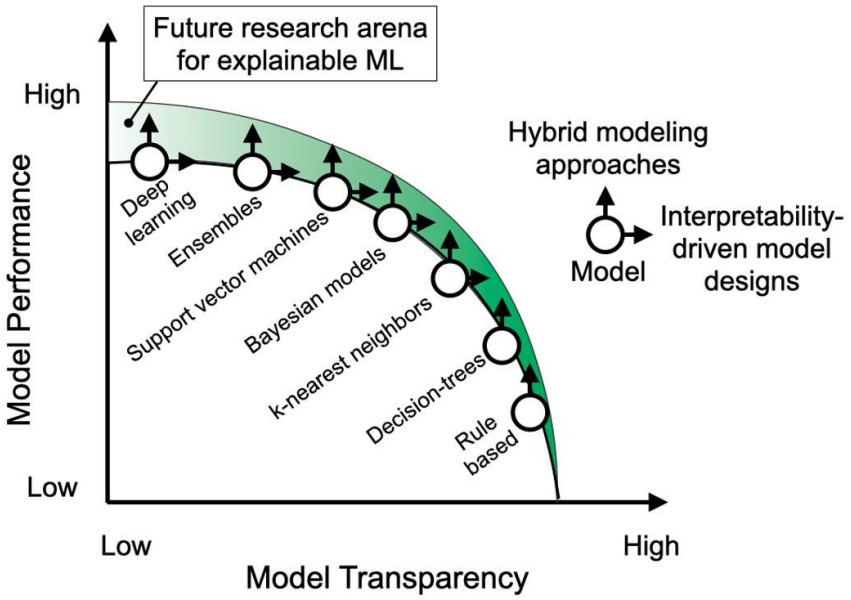


Figure 1.31: Schematic representation of the trade-off between model performance and model transparency in machine learning. Models such as deep learning and ensemble methods offer high performance but lower transparency, whereas rule-based and decision-tree models prioritise interpretability at the cost of performance. This figure serves as a conceptual framework rather than one based on empirical data [187].

and Extra-Trees should be trialled because of their prediction capabilities, but also because of their interpretability. In contrast, support vector machines and neural networks can provide a boost in predictive performance, at the cost of model interpretability and the need to scale input data. Support vector machines are especially powerful algorithms, but can struggle in cases where the target variables overlap within the feature space, which is often the case in HEA studies, as indicated in Section 1.5.2. Neural networks require significantly more computational power and training time for small gains in performance with very little interpretability [156, 193, 194]. Hence, neural networks are generally better suited for tasks with higher complexity and larger datasets than those typically found in the HEA field. They require tens of thousands of data points for adequate training and often overcomplicate the relatively straightforward, data-frame-based predictions used in ML-driven HEA studies [194].

1.6.8 Model Performance Assessment

To assess the predictive performance of supervised ML models a range of metrics are available, split between the classification and regression tasks, that assess the difference between the model's predicted outputs and the true outputs from the validation data set [190]. For classification tasks, accuracy, precision, recall, and F_1-score are the most common performance metrics in HEA ML studies, [200, 205, 214, 248].

$$Accuracy = \frac{TP + TN}{TP + TN + FP + FN} \tag{1.26a}$$

$$Precision = \frac{TP}{TP + FP} \tag{1.26b}$$

$$Recall = \frac{TP}{TP + FN} \tag{1.26c}$$

$$F_1 = 2 \times \frac{P \times R}{P + R} = 2 \times \frac{TP}{2TP + FN + FP} \tag{1.26d}$$

In the context of materials discovery, high accuracy is desirable as it reflects the overall reliability of the model's predictions across the full compositional space. High precision is important when experimental validation is costly, as it ensures that most predicted candidates are truly promising. High recall, however, is often prioritised in exploratory

searches, as it ensures potentially valuable candidates are not missed, even if some false positives are included. A more complete description of these performance metrics can be found in Dalianis [249].

True positives (TP) are the data points that are correctly predicted by the model for a class. False negatives (FN) are data points that are incorrectly predicted as a different class by the model. False positives (FP) are data points that are a different class, but are predicted to be the class under consideration. True negatives (TN) are data points that are a different class to the one under consideration and are predicted to be a different class, thus the class being considered is not involved. For regression models, root mean squared error (RMSE),

$$RMSE = \sqrt{\frac{\sum_{i=1}^{N}(y_i - \hat{y}_i)^2}{N}} \tag{1.27a}$$

and mean absolute error (MAE),

$$MAE = \frac{1}{N}\sum_{i=1}^{N}|y_i - \hat{y}_i| \tag{1.27b}$$

are the two most common metrics that HEA ML models will aim to minimise [63, 158, 190, 195, 250]. In addition, the coefficient of determination (R^2),

$$R^2 = 1 - \frac{\sum_{i=1}^{N}(y_i - \hat{y}_i)^2}{\sum_{i=1}^{N}(y_i - \bar{y}_i)^2} \tag{1.27c}$$

combined with parity plots of predicted vs actual data, provides an informative assessment of model quality, with values > 0.7 typically indicating a useful model [190]. Here, y denotes the true value, $\hat{y}$ represents the predicted value, $\bar{y}$ represents the mean of the true data, and N is the number of data points.

1.6.9 Model Training

To enable the model performance to be correctly validated using the metrics described above, the available data first needs to be split into training, validation and testing in a reproducible manner [194]. The training data is used by the model to relate the input features to the desired output. The validation data is then used to assess the performance of the model on the training data and optimise the chosen algorithm. The testing data is used to assess the error in the final optimised version of the model [190, 194].

There are two common ways to split the data to train an ML model and assess its performance. The first is train-test-split where the database is simply split into fixed fractions for training, validation and testing (e.g. 80 %–10 %–10 %). However, this can cause poor generalisability in the data across the fractions if the data distribution is imbalanced [63]. Bakr *et al.* [205] reported a significant difference between the RMSE of the training and testing data due to a different distribution of data across the two sets. The second approach is k-fold cross-validation, Figure 1.32. In this method the dataset is divided into k equal fractions, with each fraction used once as validation data while the other k-1 fractions are used for training. After k iterations, the model will have been trained and validated k times on the same database, eliminating the effect of sampling. This enables the average performance metrics to be calculated, providing a more appropriate assessment of model performance and is particularly useful for small datasets, such as those in the HEA field [63, 98, 205]. However, while the majority of HEA ML studies detail the methodology they have used to assess the performance of the model on the available data, very few discuss retraining the final model using the whole database. This is a key step in the application of ML to maximise the amount of training data. It is unclear if this step is not performed in HEA ML studies or is simply not discussed in the published literature, with the exception of Liu *et al.* [198].

1.6.10 Model Hyperparameter Optimisation

Hyperparameter optimisation is a key step in the development of ML models and features in the vast majority of HEA ML studies in one form or another. Hyperparameters are guidelines for the ML model construction that control the learning process [194]. For example, it could be controlling the maximum number of trees and branches in a random

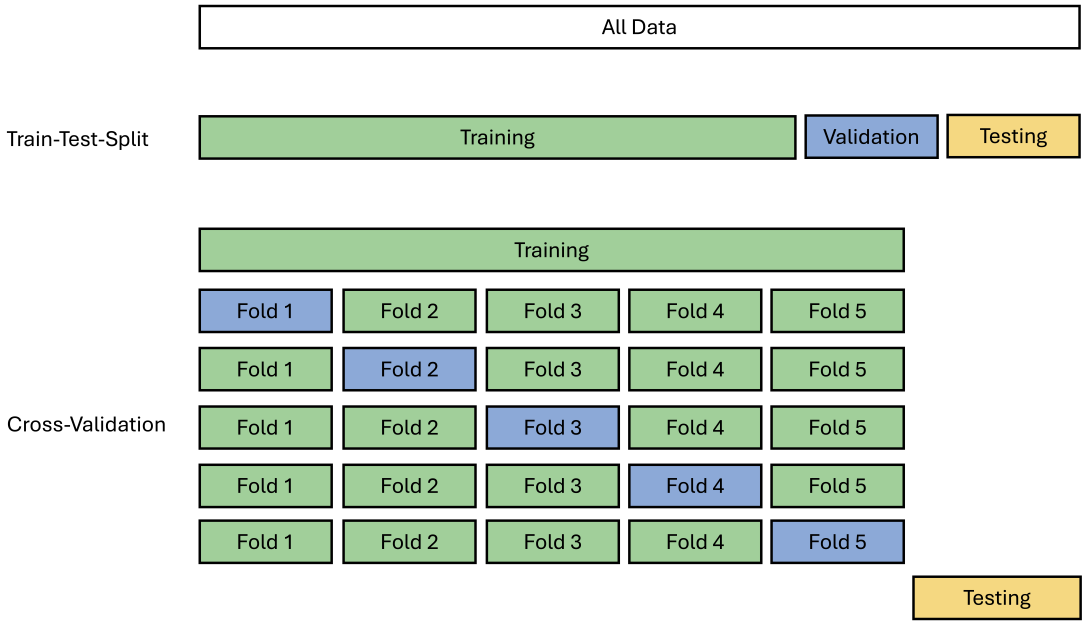


Figure 1.32: Comparison of the train-test-split and cross-validation model performance assessment methodologies. Highlights how cross-validation allows the model to be trained and validated multiple times before final testing.

forest or the number of nodes and layers in a neural network [231]. It is important to optimise the hyperparameters of an ML model to maximise the model performance and speed [63, 250]. The two most common methods of hyperparameter optimisation within HEA ML studies are grid search and Bayesian optimisation. For grid search, a range for each hyperparameter is specified and each possible combination of these parameters is tested against a baseline to find the optimal combination. This can also be performed randomly rather than exhaustively to save on computation time. In contrast, Bayesian optimisation minimises the loss on an error function to find the optimal hyperparameters for a model. Neither method is by definition better than the other, but both have been applied successfully in HEA ML studies [200, 232]. Hyperparameter optimisation is also often coupled with cross-validation to get a more accurate assessment of the impact on performance of the changes in hyperparameters [63, 120].

1.6.11 From Algorithms to Application

Once the models have been successfully constructed, optimised, trained, and their performance assessed, the next step is to use the model to predict on unseen data. To do this many HEA studies generate a virtual candidate search space by selecting a set of desired elements and considering all possible equimolar combinations within a specified system

size. While this enumeration based approach is widely used, alternative strategies such as inverse design aim to directly generate compositions with targeted properties, thereby reducing the need to exhaustively search the entire compositional space. An example of a virtual candidate search space is a study conducted by Zhang *et al.* [239] where the authors considered 30 different elements in HEAs, containing four to six elements in equimolar ratios. This produced a total of 763 686 unexplored alloy compositions for the ML to make predictions on the phase formation. This search space can be expanded to cover non-equimolar compositions, with each element typically being varied between 5–35 at.% with a compositional granularity of 1 at.% [232, 238]. In some HEA studies, restraints are placed on the search space to further narrow it down. For example, in the study by Akhil *et al.* [200], the search space was reduced by first applying the constraints, $\delta < 6.6\,\%$ and $(-15 < H_{\mathrm{mix}} < 5)$ kJ mol^{-1} to aid in the search for HCP forming HEAs. However, this is an unnecessary step as ML is a very fast process and if this constraint was suitable for mapping HCP formation, then it would be expected to be predicted accordingly by the ML model if trained correctly.

Alternatively, an inverse design methodology can be utilised [251]. In this case the final output property criteria is first specified as an input. The trained ML model then predicts feature configurations and hence, alloy compositions that could satisfy the chosen property criteria [252, 253]. Yang *et al.* [232] utilised an inverse design methodology by projecting samples in the optimal property zone of the performance space and then deducing the features yielding this performance by inverse projection. Finally, the HEA composition closest to the performance projection point by Euclidean distance was selected as the alloy composition to yield the high-performance property and was experimentally fabricated. From this inverse projection, three HEA compositions were downselected, synthesised and characterised. The best performing of these compositions exhibited a hardness 24.8 % higher than the highest composition in the original dataset. Guo *et al.*105 also apply inverse projection, but to optimise the composition of a pre-selected HEA system, AlCrFeNiTi, to maximise hardness. From this inverse projection, four of the optimised composition alloys were experimentally synthesised. The highest hardness of these demonstrated a higher hardness than any composition in the original dataset for the alloy system by 21.15 %.

Debnath *et al.* [254] performed a comparative study of forward and inverse design methodologies with a case study on the ultimate tensile strength of refractory HEAs. The authors observed that the inverse design methodology could identify a composition with the same constraints as the forward scheme, but produced a higher target property prediction. Additionally, the authors state that for the inverse design case, the addition of new conditions and generation of new candidates is incredibly fast compared to the forward case, which needs to be performed from scratch each time. However, inverse design is not without its disadvantages. Often numerous feasible solutions are presented by the inverse ML due to a greater number of variables than constraints. Additionally, minor variations in the desired property can produce significant changes in alloy composition prediction [255].

1.6.12 Experimental Validation of Predictions

The success of ML within the HEA field is intrinsically linked to the experimental exploration of the compositional space. However, a many HEA ML studies lack such experimental validation [192, 200, 204, 205]. The most common approach to experimental validation is to fabricate a small number of downselected samples, typically between five and ten, via vacuum arc or induction melting or through powder metallurgy routes [256].

Once the samples have been fabricated, the standard approach is to investigate the microstructure and mechanical properties to validate the results of the ML predictions and discover new compositions with exceptional properties. The vast majority of HEA ML studies perform this investigation via the application of scanning electron microscopy, in conjunction with energy dispersive X-ray spectroscopy, to determine the microstructure, compare the nominal to actual composition and observe any elemental segregation. X-ray diffraction is also used to further analyse the phase formation within the alloy. Mechanical property assessments, most commonly hardness, are performed using Vickers micro-hardness indentation [63, 158, 201, 238, 250]. Additional analysis techniques such as electron backscattered diffraction [196], transmission electron microscopy and selected area diffraction [257] can enable greater insight into the crystallographic phase formation of the fabricated HEAs. But this is typically above the resolution needed for simple ML model validation. However, there is a clear absence of extensive mechanical testing and post processing of the alloys, with Wang *et al.* [252] among the few to measure tensile properties of HEAs following different post processing regimes predicted through ML.

As discussed above, when HEA ML studies experimentally validate the ML model predictions they typically fabricate a small sample of compositions [198]. However, the combination of large HEA compositional space and capability of ML to rapidly make predictions across this unexplored space makes the connection of ML and HEAs to High-Throughput Experiments (HTEs) a logical advancement. These HTEs consist of a workflow involving AM in the form of laser powder bed fusion (LPBF) or direct energy deposition (DED) to rapidly and efficiently fabricate a large quantity of small trial samples. These samples are then also characterised in a high-throughput manner with conventional characterisation systems such as X-ray diffraction being configured to handle large quantities of samples consecutively or simultaneously. Enabling rapid synthesis and characterisations of HEAs to validate ML predictions with enhanced efficiency [258]. Thus, the application of HTE approaches to ML has the potential to further accelerate and reduce cost of HEA design [259]. Furthermore, the rapid generation of experimental data by implementation of HTEs can aid in constructing substantial HEA databases for the development of future ML models [198]. Moorehead *et al.* [260] utilised AM in the form of DED to construct arrays of different HEA compositions onto a single build plate. 50 individual HEA compositions are printed onto a single plate and X-ray diffraction, scanning electron microscopy and energy dispersive X-ray spectroscopy are all performed without removing the parts from the build plate. Moorehead *et al.* [260] also produced an arc-melted button, indicative of those typically produced by HEA ML studies for validation and found that AM enabled a time saving of an order of magnitude compared to conventional casting. Vecchio *et al.* [261] validated computational predictions of phase formation using CALPHAD, and hardness using an ML model with HTEs. HEA samples were printed using directed energy deposition with a special hopper system allowing 16 different alloy compositions to be printed per build cycle. The HEAs are built specifically to allow characterisation of microstructural and mechanical properties to also be performed in a high-throughput manner. In contrast, Liu *et al.* [198] applied HTE prior to ML to fabricate 138 HEA compositions of the chosen alloy system through powder metallurgy. These compositions were then used to train an ML model to reveal the complete composition-hardness relationships across the compositional range of the chosen system. In addition, future expansion of HTE methodologies to include the implementation of autonomous or self-driving laboratories could further accelerate the discovery and optimisation of materials [262–264], with HEAs representing a suitable materials candidate.

1.7 Applications of Machine Learning to High Entropy Alloy Design

The lack of development in HEA data availability is in stark contrast to the rapid acceleration of ML application to the HEA field. These studies mostly utilise standard ML algorithms and target phase formation classification [98, 192, 200, 231, 239, 248] because of the strong dependence of mechanical properties on microstructure [206]. Machaka[241] trialled eight different ML algorithms to predict phase formation from a database of 896 HEAs. The models were trained using a combination of train-test-split and ten-fold cross validation from a 13-dimension feature space. A random forest model was found to provide the best performance, with an accuracy of 97.5 % after utilising recursive feature optimisation to determine the optimal feature set. Following this model construction process, five alloy systems unknown to the model were used to assess its validity on unseen compositions. The model correctly predicted the stabilisation of the phases and predicted possible phase transitions. However, no new alloy systems were identified by this ML model and no experimental assessment was performed in this study. In a similar study by Pei *et al.* [217], a Gaussian process classifier was trained from a database of 1 252 unique HEA compositions using ten-fold cross-validation. Six unique input features were used to make predictions on phase formation and a very high accuracy of 93 % was achieved. However, again in this case no new alloy systems were designed and no experimental validation of the model was constructed. Instead, the model was evaluated against CALPHAD calculations using the TCNI8 database for compositions that were not included in the training set. A consistency as high as 94 % between the ML model and CALPHAD was reported.

However, phase formation prediction is a complex classification task with many possible phases that can form within HEAs. Hence, many HEA ML studies drastically simplify the phase space in order to simplify the ML task and improve performance. The phase classification tasks are simplified to binary and ternary cases, where the model predicts either the presence or absence of solid solution formation, or distinguishes between solid solution, intermetallic, and amorphous phases, respectively [98, 231, 248]. For example, the first application of ML to phase formation prediction within HEAs was in 2018 by Islam *et al.* [203]. In this study a neural network algorithm was constructed with two

hidden layers using the rectified linear unit activation function, shown in Figure 1.33. The model was trained using four-fold cross-validation on a dataset of 118 unique HEA compositions with five input features, to predict whether the HEA would form an amorphous, solid solution or intermetallic phase. A phase prediction accuracy of 83.0 % was achieved. However, no further application of the model to predict unseen HEA compositions phase formation or experimental validation was performed. Furthermore, the study has several methodological limitations. The dataset was small and imbalanced across phase classes, and no data augmentation was applied. The model was trained and evaluated using only cross-validation, with no separate test set, and cross-entropy loss was computed on the validation folds. In addition, the study did not report per-class performance metrics, making it difficult to assess model reliability across different phase types. Despite these issues, this work represents an early effort to apply machine learning to HEA phase prediction and highlights the need for more rigorous methodologies in subsequent studies.

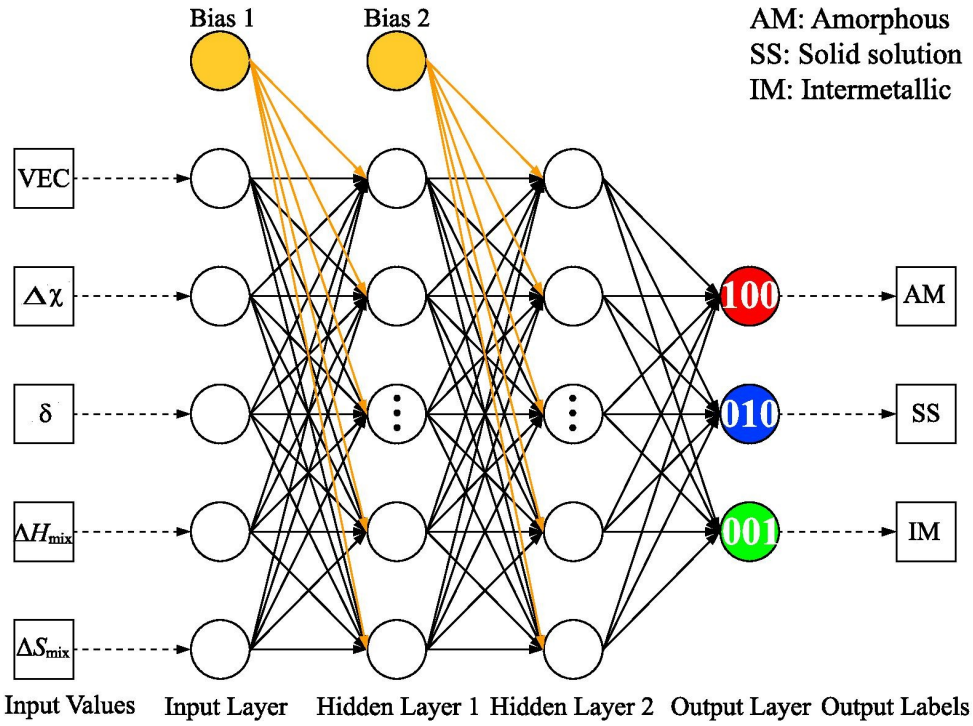


Figure 1.33: A neural network architecture containing, five input features, two hidden layers with ten neurons in each layer, and three outputs. From Islam *et al.* [203].

Another study by Han *et al.* [196] compared the performance of six different ML algorithms to predict solid solution formation. The resulting models were trained on a database of 867 compositions from 16 independent features, again using a combination of train-test-split and five-fold cross-validation. An XGBoost algorithm was found to pro-

duce the best performance on this dataset with prediction accuracies exceeding 85 %. In contrast to the cases described previously, two as cast HEA systems were experimentally fabricated and directly compared to the ML predictions in order validate the model performance. Electron backscatter diffraction was used to quickly and quantitatively analyse the phase formation within the HEAs and good agreement was found between the model predictions and experimental observations.

ML has also been directly applied to the prediction of mechanical properties, with hardness being the most commonly investigated in ML based HEA studies [195, 201, 202, 238, 240, 250], likely due to the ease of experimental measurement to validate model predictions and generate data [206]. Yang *et al.* [232] utilised a support vector machine algorithm with the radial basis function kernel to predict hardness. The model was trained using a combination of train-test-split and ten-fold cross-validation on a database of 370 experimentally measured hardness values. A PCC value of 0.94 and RMSE of 75 was obtained from the best performing model, which was subsequently utilised to locate the potential alloy compositions with high-performance properties through an inverse design process. Three optimised compositions were downselected and fabricated to test the hardness predictions. One sample reported a hardness value 24.3 % greater than the best hardness in the original dataset. Several studies have also attempted to predict a broader range of mechanical properties such as; Young's modulus [265], yield strength [204], ultimate tensile strength [252], elastic constants [257], fatigue life [266], and ductility [251]. These studies are often limited by the lack of experimental data for these target properties that are not as common or easy to measure.

A common trend within the application of ML to the HEA field, as highlighted in the discussions above, is the use of a small number of input features based on the intrinsic properties of the constituent elements. Furthermore, these studies typically utilise small databases, often with insufficient data to effectively train the more complex models, such as neural networks. In some cases these studies are lacking experimental validation of the model outputs, availability of data to enable future iterations on the model and sufficient consideration of the impact of manufacturing on HEA design.

1.8 Summary

This review of the literature highlights the significant potential of ML in the design of HEAs, particularly for the development of novel compositions tailored for demanding applications such as metal forming tooling. In this context, HEAs offer a promising alternative to conventional WC-Co hardmetals, either by minimising their use or providing a viable pathway toward their long-term replacement. By integrating ML with CALPHAD thermodynamic modelling, the predictive power of ML can be enhanced through access to reliable phase stability data, while mitigating the computational cost typically associated with CALPHAD simulations. This combined approach enables the identification of hard yet sufficiently ductile FCC HEA compositions that meet the design requirements for wear resistance and damage tolerance. Furthermore, the thermodynamic insights from CALPHAD can guide the optimisation of HEA composition and explore the incorporation of carbon-based reinforcements to tailor microstructure and improve mechanical performance.

Chapter 2

Experimental and Computational Methodology

This chapter provides an overview of the material fabrication methodology and characterisation techniques employed to analyse the HEA samples. Additionally, it includes a brief discussion of the general approach to constructing the ML models and implementation of CALPHAD in this work.

2.1 Material Production Methods

Material utilised in this study was fabricated via vacuum arc melting, followed by homogenisation heat treatments in a tube furnace.

2.1.1 Vacuum Arc Melting

Vacuum arc melting was performed on the Arcast Arc 200 at the Royce Discovery Centre at the University of Sheffield. This process involves the melting of the elemental constituents of the alloys in their bulk form under an inert Ar atmosphere. High purity, > 99.5 % by mass, bulk raw elements, weighed out to a precision of $\pm$ 0.01 g, are used to produce button ingots weighing 30–50 g. The bulk raw elements are loaded into a water cooled Cu crucible. The vacuum arc melting process is performed by delivering a large current, up to 400 A, to a W electrode and striking it on a W strike pin, forming an arc

between the W electrode and the Cu crucible in which the raw elements are situated. Once the arc has formed and is stable, it can then be directed to melt the raw elements in the Cu crucible by moving the W electrode. To achieve alloy melting and compositional homogeneity, the ingots are inverted and remelted for a minimum of five melting cycles with the same arc current intensity. In addition, an electromagnetic stirrer is used to mix the molten alloy to ensure compositional homogeneity and mitigate the possibility of unmelted material within the resultant ingot. This works using an alternating magnetic field to induce eddy currents within the molten metal, which in turn generate internal stirring. While multiple melting passes enhance mixing, repeated exposure to the arc can lead to slight compositional deviations from the target alloy due to the preferential loss of volatile elements with high vapour pressures. Thus, care must be taken to consider the relative melting and boiling points of the constituent elements of the intended alloys. For example, Mn has a low evaporation point compared to the melting points of other transition metal and refractory elements. Therefore, including additional Mn in the charge is required to account for the anticipated losses due to volatilisation during the manufacturing process.

2.1.2 Homogenisation Heat Treatments

Homogenisation heat treatments were performed at the University of Sheffield using tube furnaces. These heat treatments are used to homogenise the material, eliminating casting microsegregation and improving compositional homogeneity. The duration and temperature of homogenisation heat treatments were determined based upon differential scanning calorimetry (DSC) measurements of the phase transition temperatures and melting points of the alloys. To minimise the amount of oxidation damage during heat treatment, the homogenisation process was performed in an inert Ar atmosphere. In addition, only the centre of the ingots, far from the oxidation damage located at the surface, were characterised. All ingots were air cooled following the homogenisation process.

2.1.3 Material Preparation

Specimens from the as-cast and heat-treated conditions were prepared for microstructural characterisation by sectioning with a Buehler AbrasiMet 250, Buehler IsoMet 5000, Struers Labotom-5, and Struers Secotom-20. Samples were then mounted in conduc-

tive bakelite using a Buehler Simplimet 3000 automatic mounting press. Grinding was performed with P400–P2500 SiC paper, followed by polishing with 6–1 μm diamond suspension on a Buehler AutoMet semi-automatic grinder-polisher to achieve a 1 μm surface finish.

2.2 Thermal Analysis Techniques

Thermal analysis of the manufactured alloys in the as-cast state was performed to determine suitable homogenisation heat treatments, taking into account phase transitions and melting temperatures.

2.2.1 Differential Scanning Calorimetry

DSC is a thermal analysis technique that provides information on thermal transitions, such as phase changes, melting, and recrystallisation. The sample and a reference material are exposed to a controlled heating regime and the difference between the two is recorded as the differential heat flow signal. This heat flow is typically shown as a function of temperature. Phase transformations or melting will produce an increase or decrease in the heat flow signal, hence can be used to interpret the solidus, liquidus and phase transition temperatures of the alloy. To determine these transition temperatures, the differential of the heat flow is calculated and the first deviation away from the baseline is taken as the transition temperature [267].

In this study, the DSC analysis was conducted using a TA Instruments SDT Q600, which facilitated two cycles of controlled heating and cooling under an inert Ar atmosphere. Samples were no greater than 5 mm in diameter in any direction to fit within the 6 mm Alumina crucible. First, the sample was heated from room temperature to 1450 °C, employing a heating rate of 20 °C min^{-1} with a 2-minute isothermal hold maintained at the peak temperature. Subsequently, a controlled cooling cycle to 400 °C at the same rate was performed, with an additional 2-minute isothermal hold at the lowest temperature.

2.3 X-Ray Diffraction

X-ray diffraction (XRD) is a non-destructive technique used to obtain crystallographic information about the material, such as the phases present and their associated lattice parameters. In this work, a Panalytical Aeris XRD bench-top diffractometer equipped with a Cu source was used to perform XRD analysis of the sample material. The X-ray source consists of an X-ray tube in which electrons are released from a heated filament via thermionic emission. These electrons are then accelerated from the cathode filament toward a metallic target, or anode, by an applied high voltage. Upon striking the anode, the high-energy electrons may eject inner-shell electrons from the atoms, creating electron vacancies. These vacancies are subsequently filled by electrons from higher energy outer shell electrons, and the resulting energy difference is released in the form of X-ray photons. The energy of these photons is characteristic of the specific electronic transitions within the target material. In addition to this, Bremsstrahlung radiation is also generated. As the incoming electrons approach the positively charged nuclei of the target atoms, they are decelerated and deflected from their original path. This loss of kinetic energy is emitted as a continuous spectrum of X-ray photons. Bremsstrahlung contributes to the background radiation in X-ray spectra and, together with characteristic X-rays, forms the full emission profile of the X-ray source. The X-ray beam is focused onto the sample by a collimator to produce a narrow beam and a monochromator to select a specific wavelength. The X-rays are diffracted by the atoms in the crystal in the crystal lattice according to Bragg's law,

$$n\lambda = 2d\sin\theta, \tag{2.1}$$

where n is an integer representing the diffraction order, λ is the wavelength of the X-rays, d denotes the spacing between the crystal lattice planes and θ is the angle of incidence of the electrons on the sample.

The diffracted X-rays are captured by a detector, measuring their intensity at distinct angles of incidence. As the angle of incidence is varied, constructive and destructive interference of X-rays diffracting from different planes of the crystal lattice yields a characteristic diffraction pattern, with peak positions and intensities relating to the sample's crystallographic structure. For this study, the diffraction patterns were recorded in the

$10\,^\circ < 2\theta < 100\,^\circ$ range in $0.02\,^\circ$ increments. Given the large grain size resulting from arc melting, sample texture poses a significant challenge for data analysis.

Pawley refinement was selected for this analysis as it focuses on accurately fitting the observed diffraction pattern by refining unit cell parameters and peak shapes without relying on structural models to simulate diffraction intensities. Unlike the Rietveld method, which requires detailed crystallographic information, including atomic positions, site occupancies, and phase specific intensity calculations. In contrast, Pawley refinement avoids these assumptions about the precise structure or composition of each phase. This makes it particularly advantageous when analysing systems with unknown or uncertain structures. It also offers a more computationally efficient approach while still providing reliable lattice parameters and enabling the identification of crystalline phases. Thus, all refinements in this study were performed using the full-pattern Pawley fitting procedure [268] in TOPAS-Academic.

However, the use of Pawley refinement limits the extraction of further crystallographic and microstructural information. Key outputs accessible through Rietveld refinement, such as site occupancies, preferred orientation (texture), phase fractions, and microstructural parameters like crystallite size and microstrain estimated through peak broadening, cannot be robustly determined using this method. Despite these limitations, Pawley refinement was deemed the most appropriate choice for this study, as the primary objective was to determine phase formation rather than detailed structural or quantitative analysis.

2.4 Microscopy Analysis

Microscopy techniques have been applied within this work to enable the microstructural characterisation and compositional analysis of the manufactured alloy compositions and complement the crystallographic observations through XRD analysis. This process is critical to enable both the validation of the results of ML predictions as well as assess the suitability of the fabricated alloy compositions for the design case. Software such as ImageJ [269] can be used to analyse the sample microstructure from the resulting microscopy images. Enabling determination of average grain size and phase area fraction calculations.

2.4.1 Optical Microscopy

Two reflected light optical microscopes, a Nikon Eclipse LV150 and Olympus BX51, were used to characterise the samples. Optical microscopy was implemented herein for its ability to efficiently examine large regions of the sample. The sample is illuminated from above by a halogen lamp directed through the objective lens. Reflected light from the sample surface is gathered by the objective lens, magnified, and subsequently captured by a camera or sensor. This digital image is then further magnified and displayed on an associated computer screen.

2.4.2 Scanning Electron Microscopy

Higher resolution microstructural analysis of the fabricated samples was performed using a scanning electron microscope (SEM). In this study, two distinct field emission SEMs housed within the Sorby Centre for Electron Microscopy at the University of Sheffield, namely the Inspect F50 and JEOL JSM-7900F, were employed. Both SEMs use field emission guns to generate an electron beam through the application of a strong electrostatic field to the tip of a sharp W wire. High energy electrons are emitted from the tip of the W wire via quantum tunnelling. This beam of electrons is then focused and converged by condenser lenses within the electron column of the SEM. Deflector coils at the bottom of the electron column raster the electron beam across the surface of the sample. The electrons in the beam interact differently with the different atoms on the surface of the sample, providing information to produce an image or identify the composition of the sample. There are two primary imaging modes for SEMs, secondary electron (SE) and backscattered electron (BSE). SE imaging is the result of electrons being emitted from the sample as a result of the incident high-energy electron beam. These SEs are collected by a detector above the sample surface with the number of electrons determining the intensity of the image. SE imaging provides information on the surface topography as the incidence angle of the electron beam is affected by the uneven sample surface. This surface morphology is displayed in the SE image by differences in contrast. In contrast, in the BSE imaging mode, incident electrons in the beam are reflected back from the sample surface via elastic scattering upon interaction with an atom. The degree of scattering and energy of the BSEs depends on the incident beam energy, atomic number of the atoms they interact with and crystallographic orientation of the material. Hence,

BSE imaging provides compositional information of the sample, with differences in image contrast indicating regions with different elemental composition where brighter contrast indicates regions with compositions corresponding to higher atomic numbers. In all cases within this project a 20 KeV accelerating voltage, spot size of 3.5 and working distance of approximately 10 mm was used.

In addition, energy dispersive X-ray spectroscopy (EDS) measurements were also performed using the SEMs outlined above to determine overall alloy composition, understand elemental distribution of phases within the sample and identify any elemental segregation. The Inspect F50 and JEOL JSM-7900F SEMs in this study were equipped with Oxford Instruments X-Max 80 and Ultim Max 170 EDS detectors respectively. Electrons incident with the sample surface interact with the atoms and if the incident electron energy exceeds the binding energy of an inner-shell electron, it can ionise the atom by ejecting the electron. Consequently, an accelerating voltage of 20 keV was used in this work to ensure sufficient electron energy for effective ionisation. This vacancy in the inner shell is then filled by an outer shell higher energy electron dropping to the lower energy level, accompanied by the emission of an X-ray photon. The energy and number of the emitted X-rays are measured by the solid state detector. The X-rays have a characteristic energy due to the discrete energy levels within the atom and hence constitute a fingerprint for the chemical element present in the sample. Consequently, using analysis tools it is possible to identify the constituent elements present in the sample as well as their distribution within specific phase constituents. Furthermore, the abundance of a specific element within the sample is determined by the number of characteristic X-rays detected enabling quantitative determination of compositions. In this project, large area EDS scans were averaged to give an indication of the overall alloy composition and EDS maps were produced to understand the elemental distribution between the different phases of the samples. The analysis of EDS results obtained in this project was conducted using the Oxford Instruments Aztec software.

2.5 Chemical Compositional Analysis

Inductively coupled plasma optical emission spectroscopy (ICP-OES) was performed to determine the chemical composition of the carbon reinforced samples within this work. The bulk metallic samples are dissolved in acid solutions and then nebulised to form a fine aerosol. The aerosol is then fed into an Ar plasma which is created by passing the inert gas through an induction coil. As the sample solution enters the high temperature Ar plasma, the atoms of the sample are excited to higher energy levels. The excited atoms then return to the ground state by emission of photons with a wavelength characteristic to the element. The emitted photons are collected by a spectrometer and their intensity at the characteristic wavelengths is measured, which can then be compared to known standards to determine the concentration of each element in the sample.

The carbon content in the metallic samples was determined by combustion carbon-sulphur infrared (IR) spectroscopy. The sample is heated to a high temperature in the presence of excess oxygen and during the combustion process the carbon reacts with the oxygen to form carbon dioxide. The carbon dioxide is then exposed to IR radiation which is absorbed at characteristic wavelengths, producing absorption peaks in the IR spectrum. Measuring the absorbance of IR radiation enables the concentration of carbon dioxide and hence carbon content of the sample to be determined by comparison with pure compounds with a known carbon content.

The nitrogen and oxygen content within the samples was also measured through thermoconductivity and IR absorption measurements using an Eltra ONH 2000 Analyser. The sample is heated in a graphite crucible where it releases oxygen in the form of carbon monoxide by reaction with graphite. All carbon monoxide is then oxidised to form carbon dioxide and the oxygen content determined by the IR absorption of the carbon dioxide. The nitrogen content is then measured by thermal-conductivity detection of the gas stream.

All chemical composition analyses were performed externally by the Sheffield Assay Office.

2.6 Hardness Testing

The key mechanical property under investigation in this work was hardness as an indicator of the materials wear resistance.

Vickers hardness measurements are performed by optical measurements of the indent produced by a pyramid shaped diamond tipped indenter after a constant compressive load is applied for a predefined dwell time to the material. The Vickers number is then calculated via,

$$HV = 1.8544 \cdot \frac{F}{d^2}, \tag{2.2}$$

where F denotes the applied force in kilograms-force and d is the average length of the diagonal left by the indenter in millimetres [270]. By optically analysing the indent produced, an indication of material ductility or brittleness can also be obtained qualitatively through the presence of cracks or deformation in the indentation region.

Three types of hardness measurements were collected throughout this project; macro-, micro- and nano-hardness. Macro-hardness analysis was performed at the University of Manchester. A 30 kgf load was applied to the material with a 10 second dwell time for a series of 5 indentations across the sample surface. Micro-hardness measurements were performed at the University of Sheffield using a EMCO-TEST Durascan 70 G5, with a Vickers indenter applying a 1 kgf load with a 15 second dwell time for a series of ten indentations. All measurements were performed in accordance with ASTM E384 [271]. The standard states that the indentations must be spaced greater than $2.5d$ apart and $2.5d$ from the edge of the sample to avoid interference between the indentations and the effects of the edge of the sample. Nano-hardness measurements of the individual phases were performed using a Micro Materials NanoTest Vantage at the Royce Discovery Centre at the University of Sheffield according to the industry standards ISO 14577 [272] and ASTM E2546–07 [273]. Nano-hardness is very similar to the other hardness measurement techniques described above. However, in this case the depth of penetration of the nanometer diamond tip is measured and used to calculate the area of the tip in contact with the material.

Subsequently, the material hardness can be determined via,

$$H = \frac{P_{\max}}{A_r}, \tag{2.3}$$

where, P_{max} is the maximum applied load and A_r is the residual indentation area calculated from the indentation depth. In this study, a depth vs. load hysteresis assessment was performed with a max load of 100 mN and a minimum load of 50 mN. The load was ramped up over a period of 30 s and data was collected post indentation for 60 s to account for any thermal drift.

Error analysis for the indentation measurements was performed by calculating the standard error of the mean,

$$\sigma_{\bar{x}} = \frac{\sigma}{\sqrt{n}}, \tag{2.4}$$

where the standard deviation σ, is divided by the square root of the sample size, n.

2.7 Additive Manufacturing

All additive manufacturing (AM) work undertaken in this study was conducted in the Royce Discovery Centre at the University of Sheffield on the Aconity3D GmbH MINI.

2.7.1 Laser Passes

Laser passes were performed on a flat sample surface ground to a P1200 SiC finish, providing a suitable surface for subsequent imaging while reducing optical reflectivity to minimise laser back reflection. The AconityMINI PBF-LB/M system was configured to disable the powder flow and build plate movement using the laser calibration settings and oxygen content inside the chamber was reduced to below 250 ppm before backfilling with argon. In all cases the laser power was fixed at 130 W and the beam diameter was 80 μm. Additionally, the laser melt tracks were separated by 0.3 mm to avoid interference due to secondary heating between passes of the laser.

Multiple experiments were performed to produce laser melt tracks. In the first case, the speed of the laser passes was varied from 450 mms^{-1} to 850 mms^{-1} in increments of 100 mms^{-1} across all the samples. In the second case, the speed was fixed at 450 mms^{-1}, but the number of passes was increased incrementally from a single pass up to five passes over the same track. These laser power and speed parameters were chosen as they are standard non-extreme parameters typically used in the fabrication of Inconel 718. Inconel 718 was selected over materials such as Ti-6Al-4V because it is more compositionally similar to the HEAs investigated in this work, making it the most appropriate material for comparison in terms of processing behaviour and performance under laser-based fabrication techniques.

The input energy density (IED),

$$\text{IED} = \frac{P}{v \cdot d}, \tag{2.5}$$

with units Jmm^{-2}, describes how much laser energy is delivered to the material per unit volume during the build process [274]. Where P is the laser power, v is the laser scan speed and d denotes the laser beam diameter.

2.8 Machine Learning Model Construction

All ML work conducted in this project was written in Python 3 using the Spyder and Jupyter Notebook integrated development environments and constructed using the SciKit-Learn toolkit [275] and Keras API [276]. A longer and more detailed discussion of the ML construction process and application is included in Sections 3 and 7.

2.9 Thermodynamic Modelling

CALPHAD is a widely used computational modelling technique of the thermodynamics and kinetics of alloy systems. The Thermo-Calc software package [172] was used to perform the required thermodynamic calculations presented in this work and functions by creating a framework through which the global minimisation of the Gibbs free energy can be performed. TC-Python is a software development kit that is used to couple Thermo-

Calc and python to automate calculations [277]. For HEA studies there are several suitable Thermo-Calc databases. Within this work TCNi8, TCNi12, SSOL8, TCHEA6 and TCHEA7 have all been used. All of these databases rely on experimental data for binary and tertiary systems, extrapolating to the higher order HEA systems considered in this work. To support the design process, single point equilibrium phase fractions at multiple temperatures were calculated for a multitude of compositions identified by the machine learning models described in Chapter 3. In addition, phase diagrams of the downselected alloys were produced to evaluate both the general phase formation characteristics and the influence of carbon replacement on the stability of the resulting phases, as discussed in Chapters 4 and 6 respectively.

However, care must be taken when utilising Thermo-Calc for HEA predictions, as many investigated compositions lie outside the assessed compositional space of the underlying thermodynamic databases. These databases are typically built from binary and ternary systems, meaning predictions for complex multicomponent alloys, such as HEAs, may rely on extrapolation and therefore risk reduced accuracy. This is particularly problematic in under-explored regions, where improbable phase predictions or highly sensitive phase diagrams may signal unreliable outputs. As such, CALPHAD results must be interpreted with caution and supported by complementary approaches. In this work, predictions were cross-validated using machine learning models and, where possible, experimental data. This integrated approach is explored further in Chapter 3, with CALPHAD used primarily as a downselection tool to refine the candidate space.

Chapter 3

Coupled Machine Learning and CALPHAD Method for Alloy Design

To accelerate the design process of new alloys for metal forming tooling applications, ML was applied to rapidly search the HEA compositional space to find compositions with suitable properties meeting the design criteria. To address this objective, a supervised RF ML algorithm was trained on experimental data and coupled with CALPHAD thermodynamic simulations, applied post-prediction, to identify promising HEA compositions within a defined compositional search space. The design criteria were informed by the functional requirements of metal forming tooling applications. Accordingly, the aim was to discover compositions that form an FCC phase to ensure sufficient ductility and damage tolerance, while also maximising hardness as a proxy for wear resistance [278].

This methodology, first applying ML and subsequently downselecting using CALPHAD, has a number of key benefits [200]. Additionally, it presents an opportunity for the design and development of novel alloy compositions for a host of different structural and functional applications. Performing CALPHAD analysis on over two million compositions considered by the ML in this study is computationally impractical. Application of ML and filtering by the predictions dramatically reduces the number of compositions that need to be considered and hence, the computational time for the calculations. An additional concern associated with using CALPHAD data as an input to the ML model is the issue of training the model on calculated data. While CALPHAD offers a remarkable tool for

alloy design, it is well documented that calculation accuracies are lower for compositions that deviate away from well-established alloy systems. This limitation arises due to the construction of the thermodynamic databases from experimental assessment of binary and ternary systems, which can often be incompletely characterised across the full compositional space. As a result, the complete behaviour of more complex multicomponent compositions, such as HEAs, may not be fully captured. Thus, extrapolations into this compositional space can lead to inaccurate phase stability calculations. Recognising when CALPHAD is being extrapolated beyond its reliable limits is not straightforward. However, potential warning signs include the appearance of improbable stable phases or phase diagrams that shift dramatically with minor compositional changes. Consequently, when investigating under-explored compositional regions, CALPHAD results should be interpreted with caution. In this work, such predictions were supported by complementary machine learning models and validated experimentally wherever possible. In addition, CALPHAD primarily provides calculations of equilibrium phases, though it can also offer insights into non-equilibrium phases. However, such insights are of limited utility without a clear understanding of the desired outcomes and experimental validation to effectively rationalise the results. Hence, CALPHAD can bias the results against compositions with kinetically sluggish phases that would otherwise be suitable for the application. While this latter point is not applicable herein, the use of ML is envisaged to progressively evolve for increasingly more complicated case studies, where equilibrium, and indeed the use of CALPHAD, may in fact be inadvisable. Therefore, in this case study, CALPHAD was used as a downselection tool only.

The ML architecture proposed herein can predict compositional hardness from experimental data, save significant time over the CALPHAD approach and can be quickly updated with new data, while providing reproducible and accurate predictions. Utilising CALPHAD as a postprocessing tool to interrogate a small subset of the ML predictions provides refined microstructural information for alloy downselection. However, importantly, it retains separation and enables critical interrogation of predictions. In the absence of further experimental data, CALPHAD serves as a robust tool to refine phase predictions obtained from the ML models. It helps guide experimental efforts by highlighting areas of agreement, where immediate technological benefits may be realised, and areas of discrepancy, where targeted experiments can significantly improve model accuracy.

3.1 Dataset Selection

Two independent, published experimental HEA datasets were selected to train and test the initial ML models. The dataset compiled by Gorsse *et al.* [210] contains experimental data on 370 high-entropy and complex concentrated alloys, and was selected due to its unique inclusion of mechanical property information alongside compositional data. A second dataset, compiled by Machaka *et al.* [209], includes 1360 alloy entries with detailed phase formation information. This dataset was chosen because, at the time of this work, it represented the most recent and comprehensive compilation of phase data in the HEA literature, although it lacks corresponding mechanical property information.

Despite these datasets being constructed from papers published in peer reviewed journals and being published in peer reviewed journals themselves they are not free from errors. A corrigendum was published for the Gorsse *et al.* [210] dataset with a new dataset that both corrected errors and included previously omitted data [279]. This updated dataset was utilised in this study. Furthermore, the second dataset by Machaka *et al.* [209] also contains formatting errors, duplicate entries, and entries where the data from the original papers has been copied incorrectly. These errors are mostly eliminated during the data cleaning phase of ML model construction, but it is worth noting the observed low quality of published data within the HEA field. This low quality and quantity of HEA data, with many experimental HEA datasets containing around 1000 or less datapoints, restricts both the insights that can be garnered from the application of ML to HEAs and the ambition of the ML algorithms that can be applied to these systems.

3.2 Data Cleaning and Preprocessing

The Gorsse *et al.* [210] dataset is valuable for its inclusion of both mechanical property data and detailed phase descriptions, though it lacks any processing history. In contrast, the Machaka *et al.* [209] dataset provides limited and inconsistent processing information, omits mechanical property data, and contains a simplified phase classification. Given these limitations, it was deemed appropriate to retain all available data. Ideally, a subset accounting for processing history would be used to train the ML models, but the datasets were not sufficiently complete to allow such a reduction in training data.

Of the 370 compositions included in the dataset collated by Gorsse *et al.* [210], 123 compositions were missing hardness data; however, 95 of these contained yield strength information, allowing partial retention of mechanical property data. Following the approach by Huang *et al.* [201] and Wen *et al.* [280] to maximise the amount of training data available for hardness predictions, an empirical relationship, given by Equation 1.24, was utilised to extrapolate hardness values from the yield strength provided in the dataset. This relationship between yield strength and hardness has been shown to be approximately obeyed by BCC HEAs [201, 280, 281]. However, as this study focuses specifically on FCC HEAs, applying this relationship introduces a limitation, as the correlation between yield strength and hardness in FCC systems is less well established and may not follow the same trend due to differences in deformation mechanisms. For the remaining 28 compositions that did not include either hardness nor yield strength data, the average of the hardness values available in the dataset was imputed. The Machaka *et al.* [209] dataset contained extensive phase formation data for every composition. Data from seventeen compositions were omitted because they fell outside the compositional space defined for the alloy design domain in this study. This approach represents a trade-off between applying a physically informed but imperfect estimate, using statistical imputation methods, or omitting the data entirely. Each option carrying its own limitations in terms of bias, variance, and data completeness.

3.3 Machine Learning Algorithm Selection

Bundela and Rahul [219] evaluated various ML models for predicting mechanical properties using the Gorsse *et al.* [210] dataset, which is also employed in this work. The authors concluded that while artificial neural networks performed well, the XGBoost model delivered the best results. In this study, however, an RF architecture was selected as it outperformed XGBoost, as well as other models, such as linear regression and support vector machines. This discrepancy is likely due to differences in data cleaning approaches and the selected input features. Furthermore, feature based ML, unlike neural networks, is computationally inexpensive and more interpretable for relating the patterns and trends within the data to scientific understanding [188]. Deep learning and neural networks were not selected, due to the limited number of data available being unsuitable for training and validation of these model architectures,[194], increased complexity compared to RF

for little gain in prediction accuracy [239], and limited interpretability [188]. RF was also chosen for its ease of construction, interpretability [187], ability to perform both classification and regression tasks [248], and its previous successful application in material science studies [192, 201, 282]. The capability to perform both classification and regression tasks was crucial within this work to both classifying phase formation of compositions and predicting alloy hardness through regression analysis. RF algorithms combine many individual and uncorrelated decision trees that are constructed and run in parallel with no interaction. Each tree generates a prediction. In regression analysis, the votes of all decision trees are averaged to produce the final result of the model. In classification, the majority vote from all decision trees determines the final output [186, 283].

3.4 Input Features

The training of the ML models and their use in the prediction of hardness and phase formation of new HEA compositions were based upon the physical properties of the constituent elements of the alloys. Selecting suitable features is critical in ML studies, particularly within the materials science domain, to produce meaningful and interpretable predictions. Hence, ten independent features, calculated through an assortment of Hume-Rothery rules, Gibbs free energy rules, and valence electron criteria, such as those discussed in Section 1.5.1 were utilised. These features are detailed in Table 3.1.

As CALPHAD is being used as a downselection method, features derived from CALPHAD calculations, commonly used in ML HEA studies, have been excluded in this work, e.g., the solidus and liquidus temperatures of the alloys [192]. A subset of these features was trialled in different combinations to assess their impact on the predictive capability of the models. However, it was found that utilising the full feature space, detailed in Table 3.1, resulted in improved prediction accuracy, while importantly, multicollinearity analysis did not reveal excessive correlations between features that may result in overfitting.

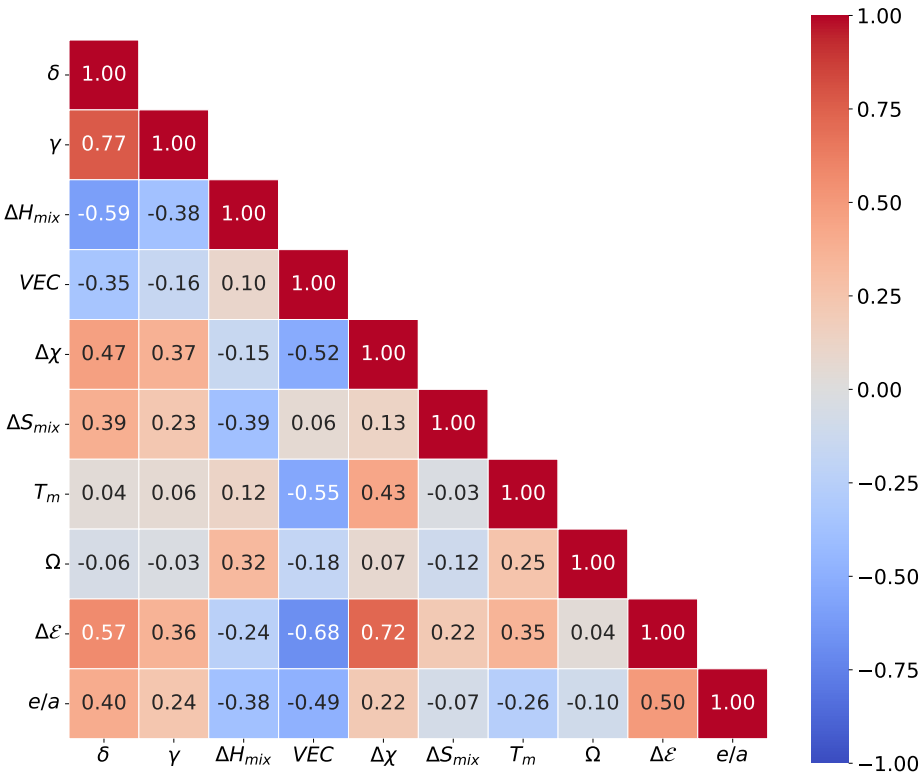
The PCC, defined in Equation 1.25, was calculated for both datasets to measure the linear correlation between any two features, thereby highlighting potential interdependencies. It can be seen from the heat maps in Figure 3.1, that the features used in this study are correlated to varying degrees. In both datasets, one of the strongest feature correlations is observed for the atomic size difference δ and the atomic packing parameter γ, with

Table 3.1: A table of the features used to mathematically describe the alloy compositions, enabling the ML models to make predictions on their phase formation and hardness.

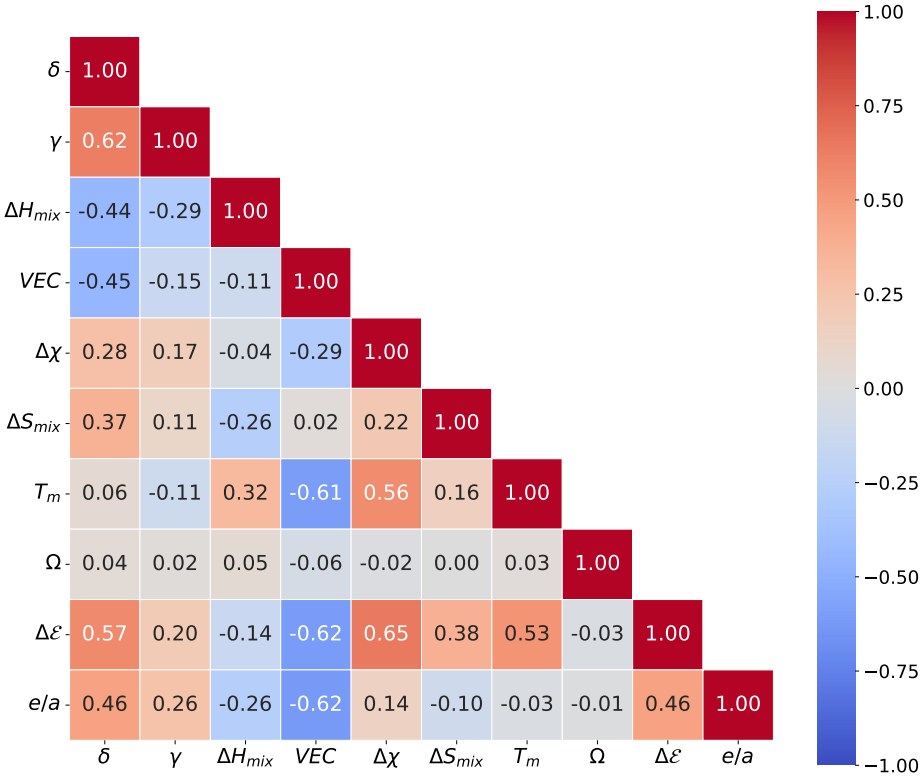
Parameter Symbol	Parameter Name	Equation	Reference
δ	Atomic Size Difference	$\delta = 100\sqrt{\sum_{i=1}^{n} c_i \left(1 - \frac{r_i}{\bar{r}}\right)^2}$	[140–142]
γ	Atomic Packing Parameter	$\gamma = {}^{\omega_S}/_{\omega_L}$ $\omega_x = 1 - \sqrt{\frac{(r_x+\bar{r})^2 - \bar{r}^2}{(r_x+\bar{r})^2}}$	[140]
$\Delta\chi$	Electronegativity Difference	$\Delta\chi = \sqrt{\sum_{i=1}^{n} c_i \left(\chi_i - \bar{\chi}\right)^2}$	[139]
VEC	Valence Electron Concentration	$\mathrm{VEC} = \sum_{i=1}^{n} c_i (VEC)_i$	[146, 147]
e/a	Number of Itinerant Electrons per Atom	$e/a = \sum_{i=1}^{n} c_i (e/a)_i$	[146, 147, 153]
ΔH_{mix}	Enthalpy of Mixing	$\Delta H_{\mathrm{mix}} = 4\sum_{i=1,i<j}^{n} c_i c_j \Omega_{ij}$	[85, 143, 155]
ΔS_{mix}	Entropy of Mixing	$\Delta S_{\mathrm{mix}} = -R\sum_{i=1}^{n} c_i \ln c_i$	[62, 143]
T_m	Weighted Melting Temperature	$T_m = \sum_{i=1}^{n} c_i (T_m)_i$	[156]
Ω	Yang Parameter	$\Omega = \frac{T_m S_{\mathrm{mix}}}{\lvert H_{\mathrm{mix}} \rvert}$	[156]
$\Delta\mathcal{E}$	Young's Modulus Asymmetry	$\Delta\mathcal{E} = \sqrt{\sum_{i=1}^{n} c_i \left(1 - \frac{E_i}{E}\right)^2}$	[160]

Quantities denoted with a bar indicate that it is the average value, while quantities with an i indicate the *i'th* element. c represents the atomic fraction of the element, r denotes the atomic radii and E represents the Youngs modulus. R is the molar gas constant. For γ, ω_x are dimensionless quantities related to the local packing efficiency around atoms with the largest and smallest radii in the alloy, represented by subscript L and S respectively. In ΔH_{mix}, Ω_{ij} is the enthalpy coefficient for elements i and j respectively.

correlations of 0.77 and 0.62 for models based on the datasets by Gorsse *et al.* [210] and Machaka *et al.* [209], respectively. This was anticipated as both features relate to the distribution of atomic radii of the alloys' constituent elements. However, based on the levels of correlation observed it was determined suitable to retain both features for training of the ML model. The electronegativity difference $\Delta\chi$ and Young's modulus asymmetry $\Delta\mathcal{E}$ also showed strong positive associations, with coefficients of 0.72 and 0.65 in the two datasets, respectively. Interestingly, comparing across the literature, a broad range of correlation values have been reported for these features. Huang *et al.* [201] reported a value comparable to this study of 0.71 for the correlation of $\Delta\chi$ and bulk modulus asymmetry (a similar correlation would be expected for the Young's modulus asymmetry $\Delta\mathcal{E}$) [284]. In contrast, Chen *et al.* [202] reported a PCC of 0.11, although this may be the result of considering a single HEA system. The strongest negative correlation occurs between the VEC and $\Delta\mathcal{E}$, -0.68 for the Gorsse *et al.* [210] and -0.62 for the



A



B

Figure 3.1: Correlation heat maps between the ten features used as mathematical descriptors for the ML models. The value in the grid shows the PCC between the different features and the colour intensity is proportional to the magnitude of the PCCs. A) From the Gorsse *et al.* [210] dataset; B) From the Machaka *et al.* [209] dataset.

Machaka *et al.* [209] datasets. This agrees with the negative correlation of -0.71 reported by Chen *et al.* [202] The negative correlation observed between VEC and the number of itinerant electrons per atom *e/a* was unexpected as both features describe electronic structure and hence, would be expected to positively correlate. However, both VEC [146] and *e/a* [153] have been shown to be effective in the prediction of HEA phase formation, thus were both retained within the models inputs. The feature correlations observed in both datasets are comparable, suggesting that these features are likely to exert similar influence on the predictions made by the ML models derived from them. Consequently, as no PCCs ≥ 0.80 were observed, all features detailed in Table 3.1 were retained [244].

3.5 Random Forest Model Training

Three individual RF models were trained from the two available datasets. From the Gorsse *et al.* [210] dataset, a classification model for phase prediction and a regression model for hardness prediction were developed, denoted G-Phase and G-Hard, respectively. From the Machaka *et al.* [209] dataset, another classification model for phase prediction was developed, denoted M-Phase. Based on the available information in the two datasets, G-Phase considers fifteen different phase outcomes, whereas M-Phase considers seven different phase outcomes, as summarised in Table 3.2. The distribution of these phase classes within the dataset is discussed further in Section 5 and shown in Figure 5.2. Unlike a majority of phase prediction models presented in the literature that only consider binary or ternary classification tasks, the models trained herein have an increased number of outcomes. It is therefore anticipated that the classification models from this work will result in lower prediction accuracies in comparison to binary and ternary classification tasks within the literature [192, 201, 203, 239, 248, 285].

Five-fold cross-validation was implemented to enable optimisation of model hyperparameters and provide a more accurate assessment of the performance of the RF models as discussed in Section 1.6.9. This cross-validation was performed with a set random state variable to enable repeats. After cross-validation assessment of the model's performance, the models were retrained using the whole dataset, enabling training on the maximum amount of data available to improve their performance. A voting-based measure of the prediction confidence, developed by Kaufmann *et al.* [192] for RF classification algorithms,

Table 3.2: Possible phase prediction outcomes from the phase classification G-Phase and M-Phase models trained on the Gorsse et. al.[210] and Machaka *et al.* [209] datasets.

Output	**G-Phase**	**M-Phase**
1	N/A	BCC
2	B2 + Im	BCC + Im
3	BCC	FCC
4	BCC + B2	FCC + BCC
5	BCC + HCP	FCC + BCC + Im
6	BCC + Im	FCC + Im
7	FCC	Im
8	FCC + B2 + Im	
9	FCC + BCC	
10	FCC + BCC + B2	
11	FCC + BCC + Im	
12	FCC + HCP	
13	FCC + HCP + Im	
14	FCC + Im	
15	Im	

was applied in this study. The model's confidence in its prediction was calculated as the ratio of the number of decision trees inside the forest that voted for the final phase prediction of that composition, against the total number of trees. Hence, the more trees that vote for a phase, the more confident the model is in its prediction of that phase. This confidence measure was not applied to the hardness prediction model, G-Hard, as it is not suitable for an RF regression model. Instead, the coefficient of determination R^2, MAE and RMSE, defined in Equations 1.27, were used to assess the error and confidence in the regression model.

3.6 Random Forest Hyperparameters Optimisation

Each type of ML algorithm has different hyperparameters that impact the learning process. In the case of RFs, these include the number of decision trees in the forest, how deep each tree is, and the maximum number of features considered when performing a split inside the tree. Optimising model hyperparameters to, for example, control the growth of trees in the forest is particularly useful for small datasets to minimise the likelihood of overfitting. To determine the optimal hyperparameters, a randomised search with five-fold cross-validation was conducted, sampling from a predefined hyperparameter space. The algorithm selects a new combination of hyperparameter values on each iteration to construct the RF. To evaluate the effectiveness of the random hyperparameter search, the best-performing model obtained from the search was compared to the baseline model to assess any improvement in performance. If no improvement in performance is observed, the range of hyperparameters us adjusted and the random search run again. When a satisfactory improvement in performance is found, these hyperparameters are implemented into the final ML algorithm. However, as no significant improvement was found through the random search, the baseline RF model parameters were used.

3.7 Random Forest Performance Assessment

Five-fold cross-validation assessments of the performance of the RF models were conducted to understand how the model would perform on the training data. Accuracy, precision, recall, and F1 scores were all calculated to assess model performance for the phase classification task, the results of which are shown in Table 3.3. Overall performance scores of $> 78\,\%$ and $> 82\,\%$ for classification models G-Phase and M-Phase, respectively, indicate that the models successfully predict phase formation on the validation data from the dataset. Furthermore, the metrics suggest that the models do not suffer from overfitting, enabling potential generalisability to predictions on unseen compositions. The R^2, MAE, and RMSE were utilised to evaluate the error between the predicted values produced by G-Hard and known values of hardness from the dataset. The results of these performance assessments, determined for the hardness predictions of G-Hard, are also displayed in Table 3.3. The results indicate strong agreement and correlation between the model predictions and the experimental data within the training datasets.

Table 3.3: Metrics calculated to assess performance of the classification models at phase prediction and regression model at hardness prediction on unseen data. Models G-Phase and G-Hard were trained on the Gorsse *et al.* [210] dataset, while M-Phase was trained on the Machaka *et al.* [209] dataset.

Performance Metric	**G-Phase**	**M-Phase**	**G-Hard**
Accuracy	78.7 %	82.2 %	–
Precision	80.9 %	82.9 %	–
Recall	78.7 %	82.2 %	–
F_1 Score	76.9 %	81.8 %	–
Coefficient of Determination	–	–	73.7 %
Mean Absolute Error	–	–	66.1 HV
Root Mean Squared Error	–	–	92.6 HV

Figure 3.2 depicts the correlation between the predicted hardness and dataset hardness in the testing dataset. The majority of points lie close to the diagonal black dashed line representing perfect agreement, again showing the good correlation between predicted and dataset hardness values. A linear fit of the predicted hardness against the dataset hardness is denoted by the red solid line. The closer the diagonal black dashed line is to the linear fit of the red solid line, the lower the systematic error of the model. While the alignment is generally good, a degree of systematic deviation can still be observed, suggesting that the model may not fully capture all underlying physical relationships.

To interpret and understand the ML outputs, permutation feature importance analysis was utilised to highlight the key features influencing phase and hardness predictions. The results of the permutation feature importance assessment in this study are shown in Figure 3.3. VEC is considered the most important feature for phase prediction in both classification models. In addition, VEC is also an important feature for hardness predictions, an encouraging result due to the dependence of hardness on underlying phase constitution. This agrees strongly with literature, with several reports finding VEC to be the most important feature in the determination of phase formation in HEAs [203, 241, 248, 280]. The importance of VEC in phase formation was established by Hume-Rothery, who found that similar crystal structures form when intermetallic compounds have comparable VECs [86, 110]. Guo *et al.* [146] further demonstrated that higher VEC values tend to promote FCC formation, while lower values favour BCC phases.

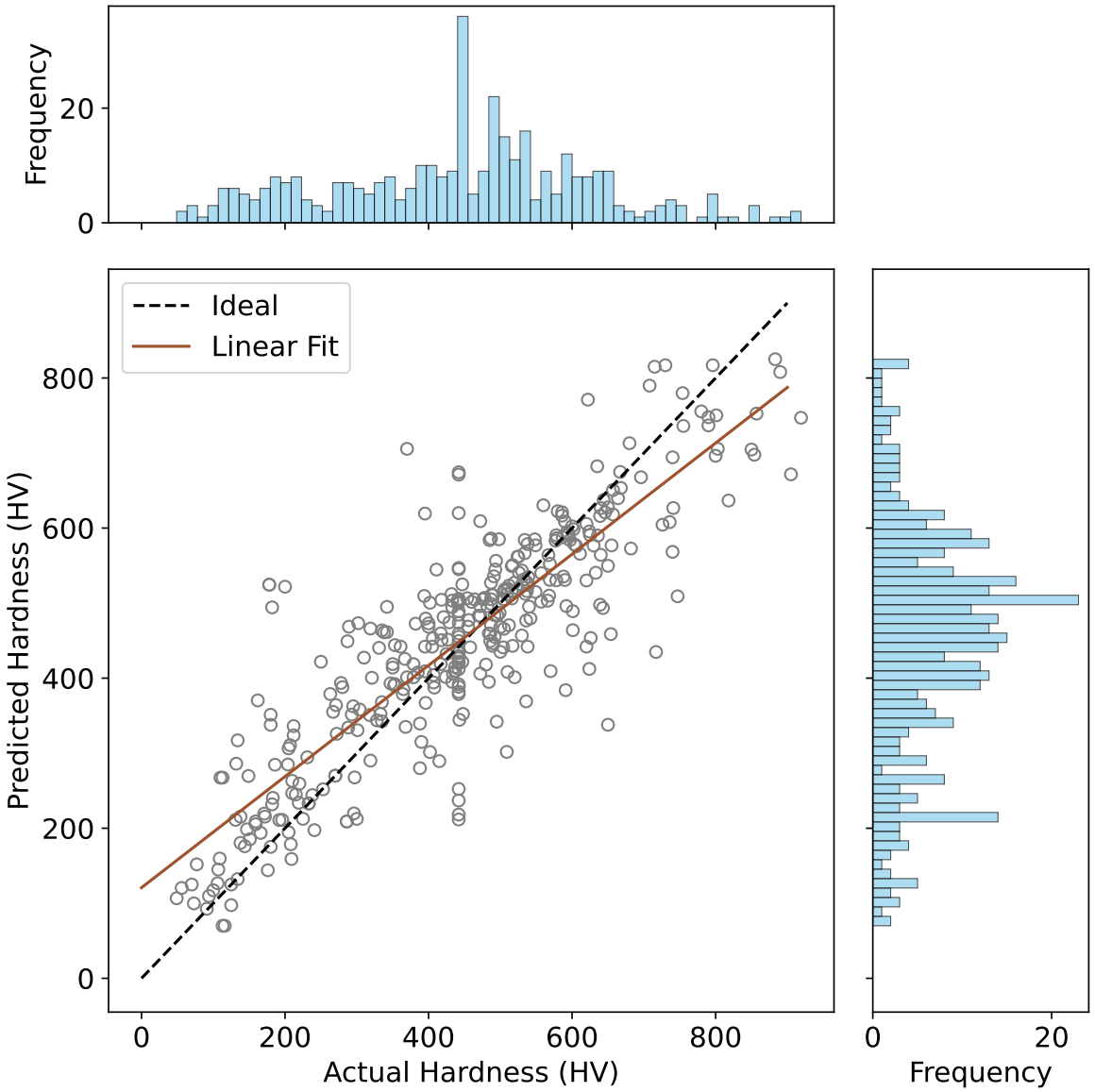


Figure 3.2: Comparison of predicted alloy hardness from G-Hard with known alloy hardness values from the Gorsse *et al.* [210] dataset across all folds of the cross-validation testing. The dashed black line represents the ideal parity between predicted and true values, while the solid red line shows the linear regression fit. Marginal histograms display the distributions of the predicted and known hardness values from the dataset.

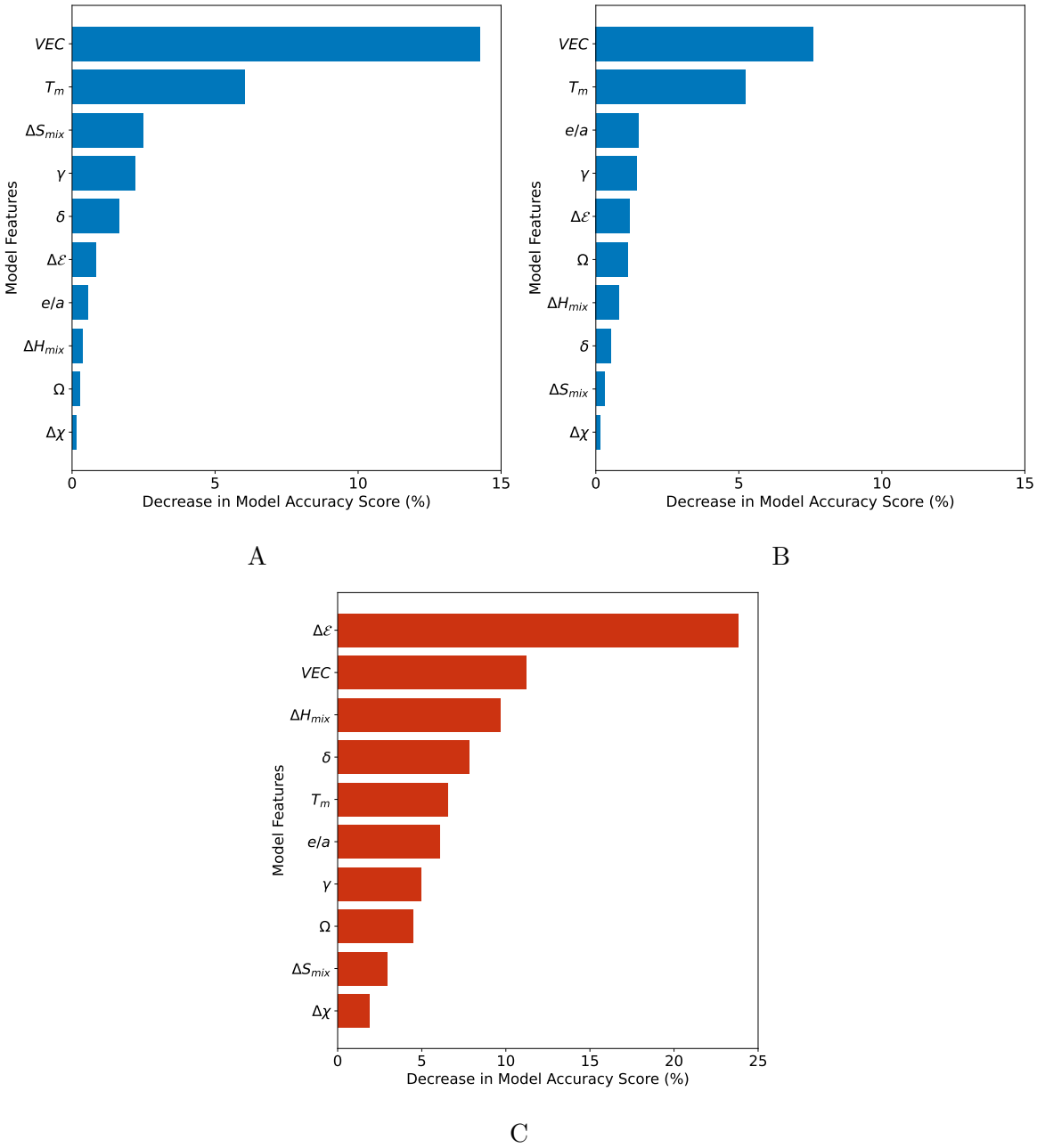


Figure 3.3: Permutation feature importance for the ten features used as mathematical descriptors in the ML models. A) classification model G-Phase; B) classification model M-Phase; C) regression model G-Hard.

Notably, G-Phase is found to be more strongly affected by VEC than M-Phase, likely reflecting differences in the experimental datasets used. The Gorsse *et al.* [210] dataset used for model G-Phase contains more detailed and complete phase information, allowing clearer relationships between features such as VEC and phase type to be learned. In contrast, the Machaka *et al.* [209] dataset used for model M-Phase, applies a more simplified classification scheme, grouping intermetallic phases and HCP solid solutions together into broader phase classes, as described in Table 3.2. This reduction in phase resolution likely obscures more subtle feature–phase relationships, thereby diminishing the apparent influence of VEC on model predictions. Furthermore, the relative size of the datasets may also contribute to the observed differences, with the Machaka *et al.* [209] dataset being significantly larger than the Gorsse *et al.* [210] dataset. The greater volume of training data in the former may reduce the model's reliance on any single feature, such as VEC, by distributing importance across a broader feature space. In contrast to VEC, $\Delta\chi$ is found to have little impact on the predictions of all three models, shown last in all permutation feature importance assessments. In the hardness regression model G-Hard, $\Delta\mathcal{E}$ emerges as the most influential feature. However, this parameter holds little importance in the two-phase classification models G-Phase and M-Phase, highlighting a divergence in feature relevance between the regression and classification tasks.

SHAP is a local interpretation method that explains individual predictions by quantifying the contribution of each feature [286]. SHAP summary plots, which combine feature importance and feature effects [186], are presented in Figure 3.4 for each model. These plots lead to conclusions similar to those drawn from the PCC and permutation importance analysis shown in Figures 3.1 and 3.3, respectively. All three models assign high importance to VEC. Large VEC values result in significant positive SHAP values for FCC phase prediction and large negative SHAP values for hardness prediction. This indicates that compositions with higher VEC are more likely to favour FCC phase formation and exhibit lower hardness values. This trend aligns with established observations that higher VEC promotes formation of ductile FCC phases, while suppressing harder BCC and intermetallic phases, thereby reducing overall hardness [141, 146, 233, 239].

The models demonstrate sensible dependencies consistent with established empirical observations and physical principles, supporting the reliability of their outputs. Notably, ΔS_{mix} ranks among the least influential features across all three SHAP summary plots.

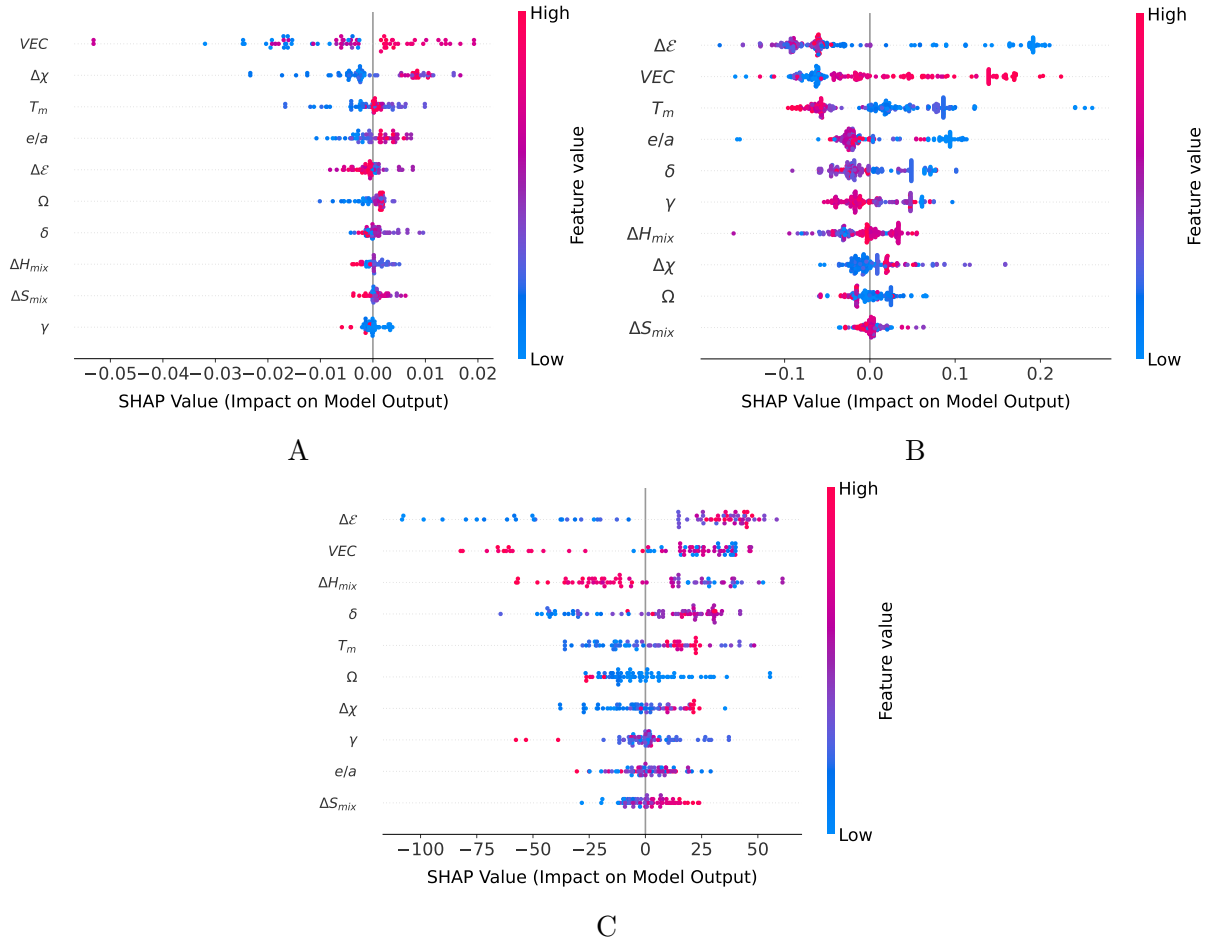


Figure 3.4: SHAP value distribution plots illustrating the importance and effects of different features for various compositions: A) G-Phase for FCC phase formation, B) M-Phase for FCC phase formation, and C) G-Hard for hardness predictions.

In the G-Hard model, it plays a minimal role in predicting hardness, with only a 0.30 % drop in performance when removed, as shown in Figure 3.3c. For G-Phase and M-Phase, it has a slightly greater but similar impact, with 2.47 % and 2.94 % decrease in performance, shown in Figures 3.3a and 3.3b, respectively. Both datasets [209, 210] used in this study contain a comparable proportion of solid-solution-forming compositions, approximately 60 %. In Equation 1.11, the configurational or mixing entropy is calculated assuming ideal, randomly distributed solid solutions, and does not reflect the total entropy. Additional contributions from excess vibrational, magnetic, and electronic effects can significantly influence thermodynamic stability and phase selection within HEAs [49]. Thus, this limited representation may explain why the ML models assign relatively low importance to entropy-related features, as they do not fully capture the entropy complexity in real alloy systems.

3.8 Generation of Virtual Candidate Search Space

This work employed a forward design methodology. Following model training, a virtual candidate search space was constructed for the ML models to predict phase formation and hardness across a wide range of HEA compositions. Element selection was guided by the available datasets and domain knowledge to promote FCC phase formation, as specified by the design criteria, illustrated in Figure 3.5. To improve practicality, selections also aimed to minimise cost and maximise elemental abundance, excluding recycled sources, using public data on commodity prices and availability [9]. Broader supply risk indicators, such as Herfindahl-Hirschman Index (HHI) values reflecting production or reserve concentration, were qualitatively considered during downselection [287]. The search space was generated following the sequence below:

1. Definition of key elements relevant to the case study and design application: Fe, Ni, Co, Al, Ti, W, Cr, Mn, Hf, Nb, Mo, and Ta.
2. Consideration of every possible equiatomic permutation of these elements in a five-element system without repetition, for a total of 792 compositions.
3. Creation of every possible compositional permutation of these five element systems between a minimum of 5 at.% and a maximum of 45 at.% elemental weighting, with a granularity of 5 at.%, yielding a total of 2 238 193 compositions.

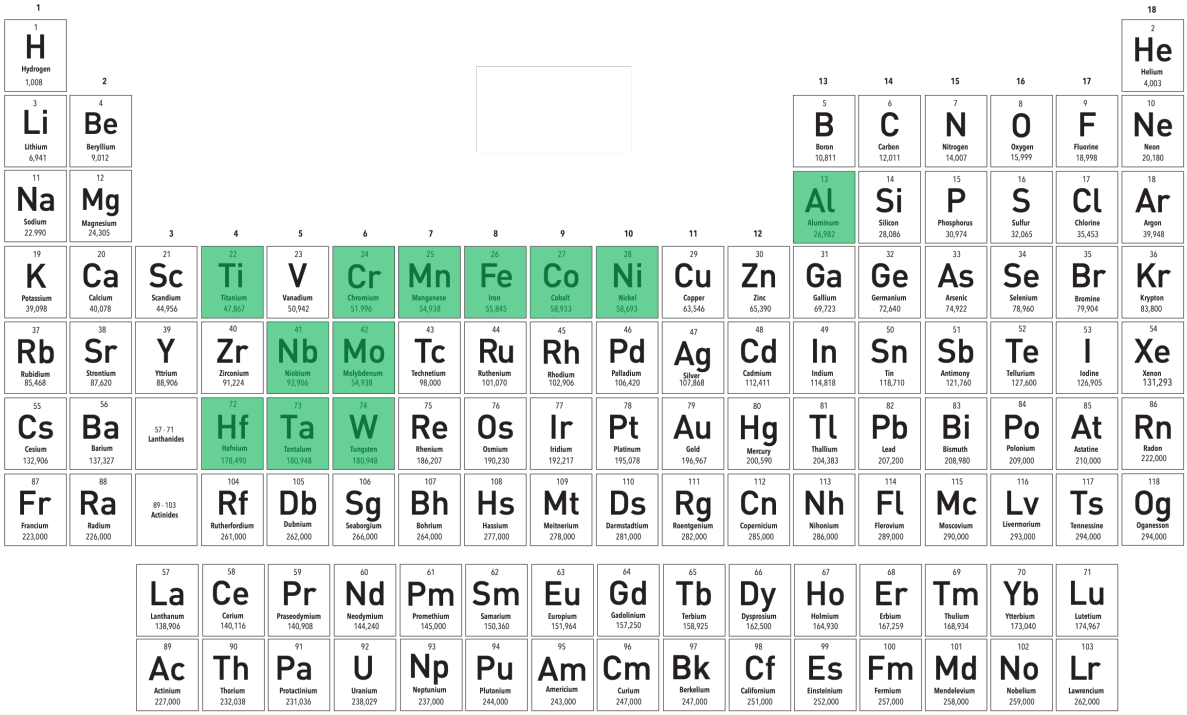


Figure 3.5: Periodic table with highlighted elements indicating those used to create the virtual candidate search space for ML predictions on unseen data.

3.9 High-throughput Machine Learning Predictions and CALPHAD Analysis

All three RF models were used to make high-throughput predictions on the phase and hardness of a series of unseen HEA compositions, with the goal of downselecting a small sample of compositions for experimental testing, to further validate and refine the models. The results of the high-throughput predictions were compiled and then systematically abridged for further analysis. CALPHAD analysis was subsequently employed to enable further downselection of alloys for experimental fabrication from the ML outputs. To meet the design criteria of the chosen case study, as a first step, all compositions where classification models G-Phase and M-Phase did not both predict FCC phase formation were eliminated. A total of 24,613 HEA compositions were predicted to form an FCC phase by both G-Phase and M-Phase. CALPHAD calculations of the equilibrium phase formation of the remaining HEA compositions at 800 °C, 900 °C and 1000 °C were performed using the TCNI8 and SSOL4 databases within the Thermo-Calc software package and automated using TQ-Fortran. CALPHAD calculations are known to be less accurate at "low" temperatures, often predicting kinetically inhibited or unrealistic intermetallic

phase formation. In addition, calculations at temperatures over 1000 °C may eliminate a number of compositions if the solidus temperature of the material is low. Thus, 1000 °C was selected as a compromise temperature between accuracy of CALPHAD predictions and practicability of the chosen case study, with 1000 °C representing a sensible operating limit. TCNI8 was utilised in this study as an FCC crystal structure was targeted and hence it was considered to be the most relevant database, providing more holistic information for the systems under consideration. Compositions were sorted by FCC phase fraction formation and subsequently, ML-predicted hardness. Figure 3.6 shows the phase diagrams of the nine downselected compositions as a result of the ML and CALPHAD outputs for the virtual candidate search space.

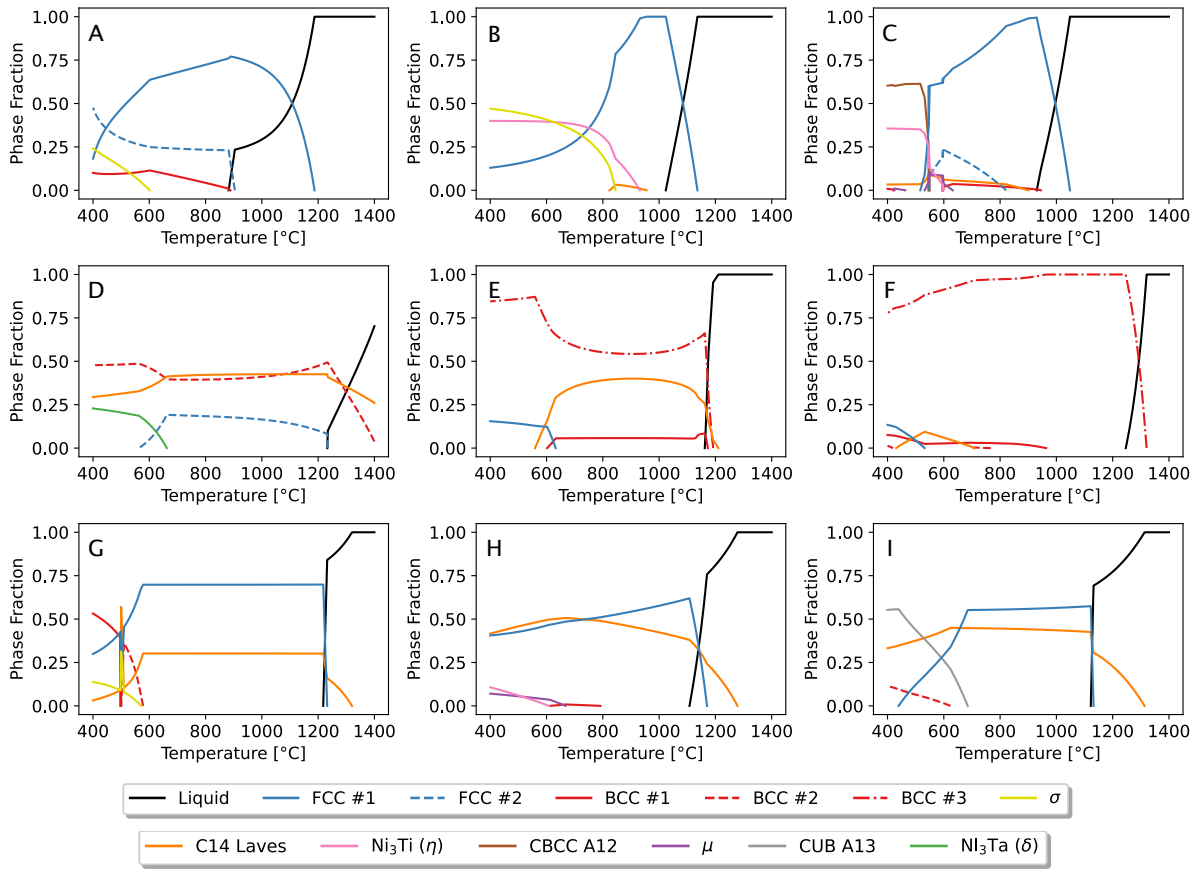


Figure 3.6: Phase diagram plots of the nine alloys downselected in this work for experimental evaluation, through CALPHAD using Thermo-Calc and the TCNI8 database. The notation A–I corresponds to the alloy compositions in Tables 3.4–3.6. CBCC A12 corresponds to the α-Mn phase and CUB A13 corresponds to the β-Mn phase.

The twelve hardest FCC-predicted compositions (by all models and CALPHAD) are shown in Table 3.4. Due to compositional similarities, the compositions highlighted in bold in Table 3.4 and labelled A–C, were chosen as the most interesting to experimentally investigate. In addition, the three highest hardness alloys, as shown in Table 3.5 and labelled D–F, irrespective of CALPHAD-predicted phase formation, were selected for experimental testing to enable an improved understanding of the performance of the regression model constructed. It is worth noting that the higher hardness as predicted by G-Hard in Table 3.5 is likely due to the alloys not being FCC based, as indicated by the CALPHAD predictions, despite being projected to form a single-phase solid solution FCC by G-Phase and M-Phase. Furthermore, the three hardest compositions predicted to form a primary FCC phase by the ML and a secondary C14 Laves phase by CALPHAD thermodynamic simulations were also downselected, shown in Table 3.6 and labelled G–I respectively. After selecting the appropriate alloy compositions, they were experimentally fabricated and analysed using the methodologies outlined in Chapter 2.

Table 3.4: The hardest alloy compositions according to model G-Hard, also predicted to exhibit single-phase FCC formation by models G-Phase, M-Phase and CALPHAD equilibrium phase fraction calculations. Compositions highlighted in bold and labelled A–C were identified as the most promising candidates for experimental investigation.

Sample Index	**Alloy**	**ML Confidence G-Phase (%)**	**ML Confidence M-Phase (%)**	**ML Hardness G-Hard (HV)**
A	**$Cr_{20}Mn_{20}Fe_{10}Ni_{45}Hf_5$**	47.0	41.5	483
–	$Cr_{20}Mn_{15}Fe_{15}Ni_{45}Hf_5$	43.0	42.5	479
B	**$Ti_{10}Cr_{10}Mn_{25}Fe_{20}Ni_{35}$**	57.0	37.4	476
–	$Ti_{20}Mn_{20}Fe_5Co_{10}Ni_{45}$	43.0	38.6	474
–	$Ti_{20}Mn_{25}Fe_5Co_5Ni_{45}$	39.0	39.5	473
–	$Cr_{15}Mn_{20}Fe_{15}Ni_{45}Hf_5$	49.0	41.6	471
–	$Cr_{15}Mn_{25}Fe_{10}Ni_{45}Hf_5$	48.0	45.5	471
–	$Cr_{15}Mn_{15}Fe_{20}Ni_{45}Hf_5$	48.0	41.6	468
–	$Cr_{20}Mn_{10}Fe_{20}Ni_{45}Hf_5$	45.0	40.5	461
–	$Cr_{10}Mn_{25}Fe_{15}Ni_{45}Hf_5$	50.0	46.4	460
–	$Cr_{10}Mn_{20}Fe_{20}Ni_{45}Hf_5$	50.0	46.9	452
C	**$Ti_{10}Mn_{45}Fe_{15}Ni_{25}Mo_5$**	32.0	37.5	451

Table 3.5: The hardest alloy compositions according to ML model G-Hard, also predicted to exhibit single-phase FCC formation according to G-Phase and M-Phase, irrespective of CALPHAD equilibrium phase fraction calculations.

Sample Index	Alloy	ML Confidence G-Phase (%)	ML Confidence M-Phase (%)	ML Hardness G-Hard (HV)	CALPHAD Phase	CALPHAD Phase Fraction (%)
D	$\mathbf{Al_{20}Ti_5Co_{30}Ni_{30}Nb_{15}}$	26.0	26.0	587	C14 Laves, BCC, and FCC	42.5, 41.0, and 16.5
E	$\mathbf{Al_{30}Ti_{20}Fe_{30}Ni_{15}Mo_5}$	40.0	39.0	584	BCC and C14 Laves	60.8 and 39.2
F	$\mathbf{Al_{30}Ti_{20}Cr_{10}Fe_5Ni_{35}}$	47.0	41.0	583	BCC	100.0

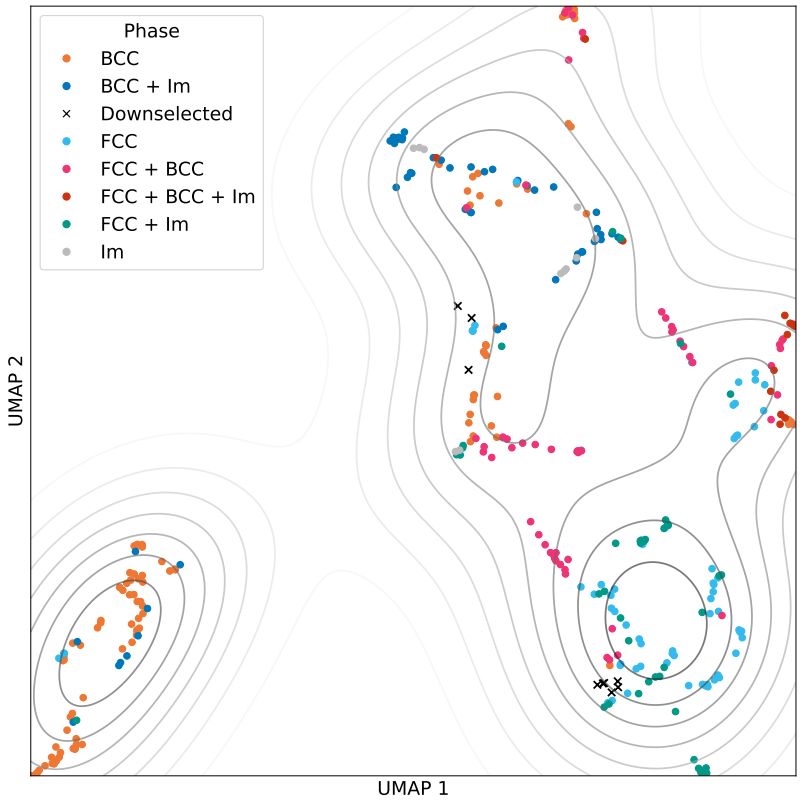
Table 3.6: The hardest alloy compositions according to model G-Hard, also predicted to form single-phase FCC structures by models G-Phase and M-Phase, with an additional secondary C14 Laves phase identified by CALPHAD equilibrium phase fraction calculations.

Sample Index	Alloy	ML Confidence G-Phase (%)	ML Confidence M-Phase (%)	ML Hardness G-Hard (HV)	CALPHAD Phase	CALPHAD Phase Fraction (%)
G	$\mathbf{Fe_{20}Co_{45}Cr_5Mn_{20}Hf_{10}}$	39.0	44.52	552	FCC and C14 Laves	69.8, and 30.2
H	$\mathbf{Fe_{45}Ni_{15}Ti_{15}Mn_{20}Mo_5}$	41.0	48.1	541	FCC and C14 Laves	57.7 and 42.3
I	$\mathbf{Fe_{15}Co_{30}Mn_{40}Hf_5Nb_{10}}$	31.0	53.4	540	FCC and C14 Laves	56.4 and 43.6

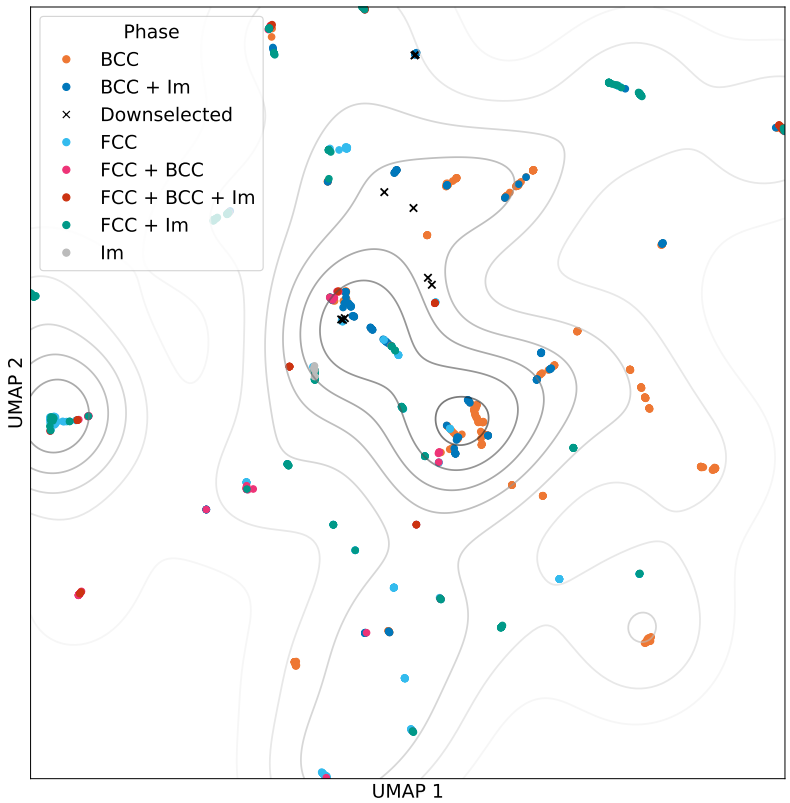
3.10 Distribution of Downselected Alloys in Embedded Training Data Space

To assess the dataset distribution, the compositional uniqueness of the downselected alloys, and their proximity to clusters within the training data, Uniform Manifold Approximation and Projection (UMAP) embedding [288] was applied. UMAP is a dimensionality reduction technique, comparable to Principal Component Analysis (PCA) and t-distributed Stochastic Neighbour Embedding (t-SNE), that projects high-dimensional data, such as the feature space used in ML training, into a lower-dimensional space, typically two dimensions. UMAP preserves both local and global data structure, thereby revealing underlying patterns, groupings, or separations. The resulting embeddings of the training datasets and downselected alloys are shown in Figures 3.7 and 3.8 where colour denotes phase or hardness and black crosses indicate the downselected alloys. Overlaid on these embeddings are kernel density estimate (KDE) contour plots, which visualise the density of training data points within the embedded space. Closely spaced contours indicate regions of high data concentration, whereas widely spaced or absent contours reflect sparsely populated areas of the training datasets. While UMAP visualisation can highlight alloys lying on the fringes or outside dense clusters, which are more likely to be compositionally distinct from the training data, such separation in the embedding does not in itself confirm novelty in the full feature space.

The UMAP embeddings presented in Figures 3.7 and 3.8 reveal notable clustering within the Gorsse *et al.* [210] dataset, suggesting an almost bimodal distribution. A distinct cluster of compositions exhibiting BCC phase formation is observed in the bottom-left region of the plot, separated from the rest of the data. This separation likely reflects the dataset's inclusion of two compositionally distinct alloy families: CrMnFeCoNi-based HEAs and refractory HEAs, the latter of which typically form BCC phases. Furthermore, the second, larger cluster appears to nearly divide into two sub-clusters, as indicated by the KDE contours: one predominantly comprising FCC and FCC + Im compositions, and the other containing a mixture of BCC, BCC + Im, and Im compositions. These phase-formation clusters are also clearly reflected in the hardness UMAP in Figure 3.8, with FCC regions aligning with lower hardness values, BCC regions with higher hardness, and BCC + Im regions with the highest hardness.



(a) *Gorsse et al.* [210] dataset feature space.



(b) *Machaka et al.* [209] dataset feature space.

Figure 3.7: UMAP embeddings of feature spaces used to train the ML models, coloured by phase classification. Downselected alloys are marked with black crosses, and KDE contours highlight the distribution and clustering of the training data.

The downselected alloy compositions occupy regions of the UMAP space distinct from much of the training data but are all embedded within the main cluster, indicating a stronger likelihood of FCC phase formation. Six lie within high-density regions, as shown by the KDE contours, while three are located near the periphery. These peripheral alloys correspond to those selected for their high predicted hardness within the FCC phase domain, irrespective of CALPHAD predictions, and may therefore carry greater uncertainty in phase formation.

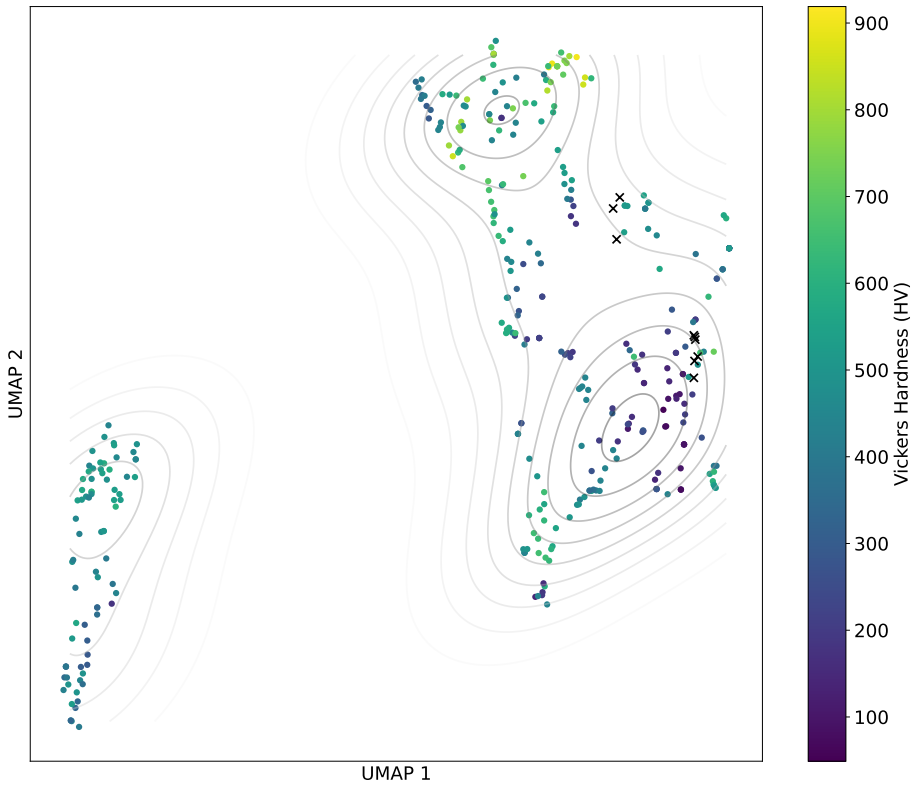


Figure 3.8: UMAP embeddings of the Gorsse *et al.* [210] feature space used to train the ML models, coloured by measured hardness. Downselected alloys are marked with black crosses, and KDE contours highlight the distribution and clustering of the training data.

In contrast, the Machaka *et al.* [209] dataset exhibits notably weaker clustering in Figure 3.7b. Nonetheless, the KDE contour analysis still reveals a subtle indication of bimodality. Three of the downselected alloys are embedded at the very centre of one of the densest regions of this dataset, suggesting a high degree of model confidence in their predictions. In contrast, the remaining alloys lie on the fringes of the KDE contours, well separated from the bulk of the training data, and one appears as a pronounced outlier. These positions indicate reduced model confidence and underscore the compositional uniqueness of these candidates.

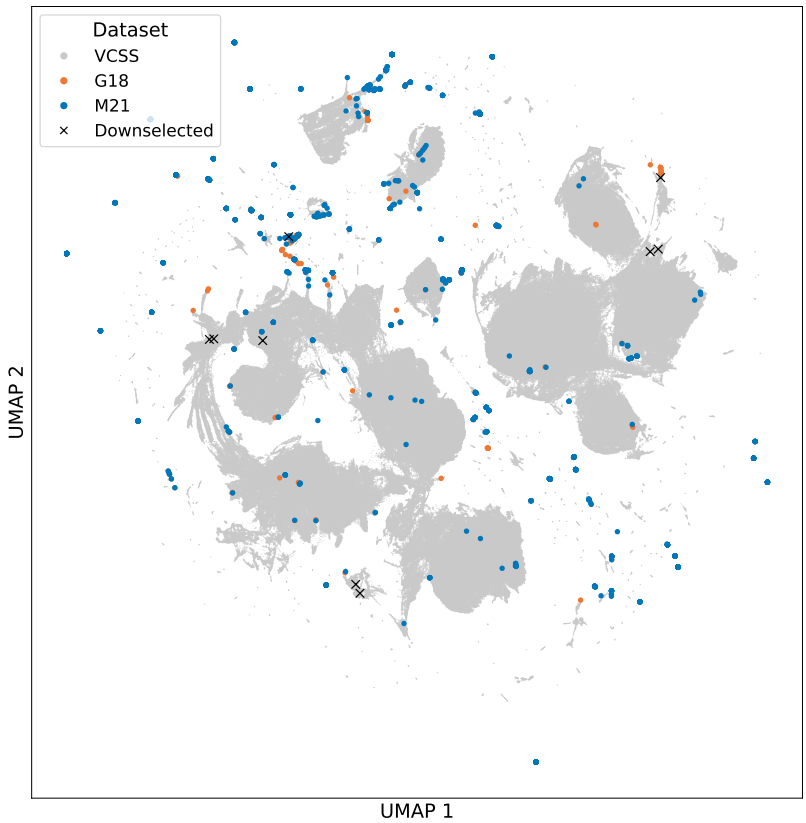


Figure 3.9: UMAP embeddings of the virtual candidate search space (VCSS) overlaid with the Gorsse *et al.* [210] and Machaka *et al.* [209] datasets, with downselected alloys marked by black crosses, illustrating their distribution within the broader design space.

Overlaying the UMAP embeddings of the Gorsse *et al.* [210] and Machaka *et al.* [209] datasets, together with the downselected alloy compositions, onto the virtual candidate search space in Figure 3.9 illustrates the relationship between the training data, the broader design space, and the selected alloys. Data from the Machaka *et al.* [209] dataset exhibits wide coverage across the entire search space, extending into and beyond the peripheral regions while maintaining areas of high density. In contrast, the Gorsse *et al.* [210] dataset covers a smaller portion of the search space, reflecting its more limited size, but does form some dense clusters in specific regions. Together, the two datasets provide complementary coverage of the candidate space. The downselected alloys are distributed across multiple regions of the search space, including both densely populated and sparsely sampled areas, with some overlap with the training datasets. This positioning suggests that the selected alloys are likely compositionally distinct from much of the training data while collectively spanning a diverse portion of the design space. Alloys located in sparsely populated areas may have higher prediction uncertainty, but also present greater potential for discovering compositions with novel property combinations.

3.11 Summary

The methodology employed in this study, which involves initially applying ML followed by downselection using CALPHAD, offers several key advantages. Primarily, CALPHAD is a time-consuming process, as each evaluation takes a non-trivial amount of time and must typically be performed sequentially for each composition of interest. Therefore, it is impractical for exploring the compositional space of HEAs at the scale proposed in this study. Additionally, CALPHAD calculations can become unreliable when applied to compositional regions lacking complete characterisation in the thermodynamic database. Furthermore, CALPHAD was not utilised to provide data or input features to train the ML models, as doing so would have introduced simulated data into a framework designed to prioritise experimentally validated data. On the other hand, ML enables rapid and efficient predictions across the HEA compositional space. Its expediency allows for continuous updates with new experimental data, fostering iterative improvements to the model's accuracy and reliability. This cyclic feedback loop between prediction and experimental validation is critical to accelerate the alloy discovery process while maintaining a strong foundation in experimentally validated insights.

To that end, three RF models were trained on openly available experimental HEA data, achieving an average predictive accuracy of 80.5 % for phase formation and an R^2 score of 73.7 % for predicting the hardness of unseen HEA compositions respectively. Further interrogation of the models highlighted the significance of features such as VEC and T_m in phase predictions, as well as $\Delta\mathcal{E}$ and VEC in hardness predictions. These findings show strong alignment with prior ML-based HEA studies and earlier parametric approaches to phase prediction, as discussed in Section 1.5.2.

Building on this, a virtual candidate search space comprising over two million HEA compositions was created, enabling the ML models to predict and significantly narrow the pool of potential HEA candidates. The integration of CALPHAD as a post-processing tool proved successful in providing deeper insights into HEA phase formation and facilitating the downselection to a more manageable subset of compositions. This approach reduced the over 24 000 FCC forming compositions proposed by the ML to nine novel and potentially promising HEAs, while also identifying three of these as forming an FCC + C14 Laves microstructure. These Laves phase-forming compositions are particularly inter-

esting for experimental investigation in the selected case study and highlight one of the limitations of applying ML independently, given its constraints in phase classification due to the available training data.

Consequently, the combined application of ML and CALPHAD in this manner not only facilitates the identification of suitable compositions for the target application, but also identifies areas of discrepancy where additional experimental data could significantly enhance future ML predictions and thermodynamic models. Building on this approach, nine HEA compositions identified through the methodology were experimentally fabricated to validate the ML predictions and assess their suitability for tooling applications, specifically targeting high hardness for wear resistance and sufficient ductility for damage tolerance.

Chapter 4

Experimental Assessment of Downselected Alloys

To validate the performance of the ML model and evaluate its suitability for the design use case of the downselected alloy compositions presented in Chapter 3 (Tables 3.4, 3.5, and 3.6), the selected HEA systems were synthesised via arc melting under an inert Ar atmosphere. For each composition, 30 g button ingots were produced using high-purity ($>$ 99.5 % by mass) bulk raw elements.

4.1 Compositional Analysis

The bulk elemental compositions after arc-melting were confirmed by averaging five large-area EDX scans, with results compared to nominal compositions in Table 4.1. Most bulk compositions were within $\pm$ 4 % of the target concentrations for each element. However, significant deviations were observed for Mo, Cr, and Mn. These are attributed to the high melting points of Mo and Cr, which can lead to incomplete melting, and the low evaporation temperature of Mn, which can result in elemental loss during processing. Despite these variations, phase formation in the fabricated compositions, evaluated using both ML and CALPHAD, aligned with predictions based on the nominal compositions. Thus, these alloys were deemed suitable for further experimental evaluation to assess model fidelity.

Table 4.1: Comparison of the downselected alloy nominal compositions and the experimentally fabricated compositions.

Sample Index	Nominal Alloy Composition	Experimental Alloy Composition	ML Confidence Model X (%)	ML Confidence Model Z (%)	ML Hardness Model Y (HV)
A	$Cr_{20}Mn_{20}Fe_{10}Ni_{45}Hf_{5}$	$Cr_{22.3}Mn_{17.9}Fe_{10.2}Ni_{44.8}Hf_{4.8}$	42.0	41.5	477
B	$Ti_{10}Cr_{10}Mn_{25}Fe_{20}Ni_{35}$	$Ti_{10.0}Cr_{9.6}Mn_{27.0}Fe_{19.6}Ni_{33.8}$	60.0	43.5	478
C	$Ti_{10}Mn_{45}Fe_{15}Ni_{25}Mo_{2.5}$	$Ti_{10.3}Mn_{45.9}Fe_{15.5}Ni_{26.0}Mo_{2.3}$	37.0	43.5	429
D	$Al_{20}Ti_{5}Co_{30}Ni_{30}Nb_{15}$	$Al_{19.9}Ti_{5.0}Co_{30.4}Ni_{30.1}Nb_{14.6}$	24.9	30.9	586
E	$Al_{30}Ti_{20}Fe_{30}Ni_{15}Mo_{5}$	$Al_{29.7}Ti_{20.6}Fe_{30.3}Ni_{14.6}Mo_{4.8}$	40.7	40.0	586
F	$Al_{30}Ti_{20}Cr_{10}Fe_{5}Ni_{35}$	$Al_{29.6}Ti_{20.5}Cr_{11.4}Fe_{5.2}Ni_{33.3}$	42.7	41.0	590
G	$Fe_{20}Co_{45}Cr_{5}Mn_{20}Hf_{10}$	$Fe_{20.3}Co_{43.7}Cr_{5.7}Mn_{21.4}Hf_{8.9}$	56.0	32.8	543
H	$Fe_{45}Ni_{15}Ti_{15}Mn_{20}Mo_{5}$	$Fe_{41.8}Ni_{15.2}Ti_{15.6}Mn_{26.1}Mo_{1.3}$	54.0	42.8	513
I	$Fe_{15}Co_{30}Mn_{40}Hf_{5}Nb_{10}$	$Fe_{16.1}Co_{31.4}Mn_{37.8}Hf_{4.9}Nb_{9.8}$	55.0	35.4	535

ML confidence and hardness predictions shown were derived using the experimental alloy compositions.

4.2 Differential Scanning Calorimetry Analysis

DSC analysis and homogenisation heat treatments were performed on the samples prior to material preparation, microstructural characterisation, and hardness testing, following the equipment and procedures outlined in Chapter 2. The DSC results for all nine samples are shown in Figure 4.1, with heat flow measurements normalised by mass for direct comparison. Two homogenisation regimes were established by analysing the differentiated heat flow curves to identify inflection points, corresponding to phase changes or the solidus temperature of the alloys. The relative complexity of the DSC thermograms suggests that the phase equilibria in these alloys are more intricate than might be expected for single-phase materials. This complexity likely reflects the multiphase nature of the alloys and elemental segregation, which influence the thermal events observed during heating. Samples A, B, C, and H were heated to 1000 °C for 48 hours, while samples D, E, F, G, and I were heated to 1150 °C for 48 hours, followed by air cooling. These temperatures were selected to approach the alloys' solidus temperature without risking incipient melting. The extended 48-hour homogenisation period aimed to try and approach equilibrium conditions, facilitating the diffusion of lower diffusion rate elements, such as Hf and Mo, throughout the HEA systems [92].

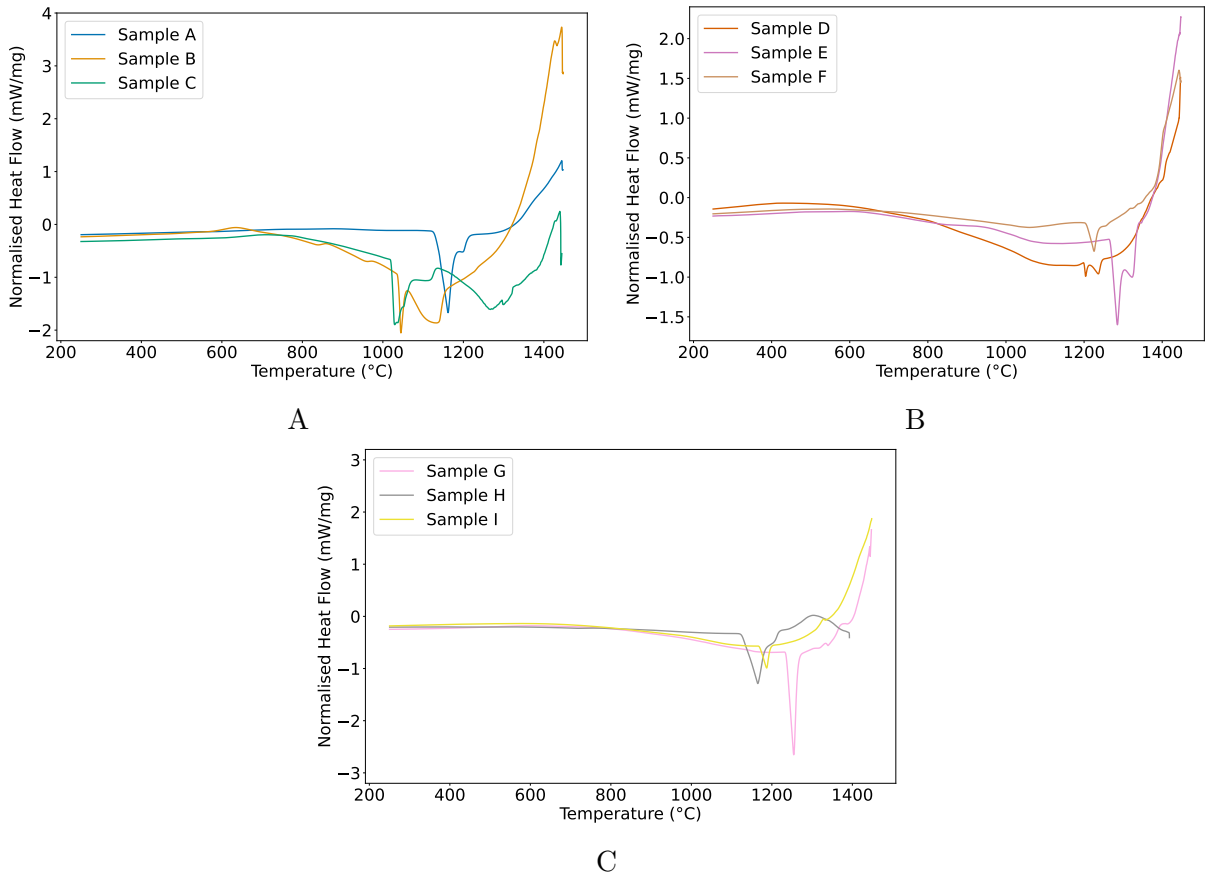


Figure 4.1: DSC results showing the mass normalised heat flow against the temperature. Microstructural phase changes and melting points can be inferred from significant deviations in the gradient of the line plots.

4.3 Microstructural Analysis of As-Cast and Homogenised Material

Microstructural analysis of the alloy compositions was conducted using a combination of SEM and EDS to identify the phases present and their relative chemistry. BSE micrographs and EDS maps of the as-cast alloys are shown in Figures 4.2–4.4. Following rapid solidification during the arc-melting process, all alloys exhibited a coarse-grained microstructure with strong contrast arising from variations in both crystal orientation and composition. The EDS maps reveal clear elemental segregation within the grains, consistent with dendritic solidification in all alloys. No evidence of single-phase solid-solution formation was observed; instead, all alloys exhibited a multiphase microstructure.

The resulting BSE SEM micrographs and EDS maps of the alloys in the homogenised condition following the homogenisation treatments outlined above in Section 4.2 are presented in Figures 4.5–4.7. These SEM-based EDS maps highlight clear elemental segregation within the grains between the matrix and precipitating phases. As in the as-cast state, there is no evidence of single-phase solid solution formation in any of the fabricated compositions. However, there is a distinct evolution in microstructure due to the homogenisation process for all alloys. In all cases, the homogenisation process was sufficient to minimise and in some cases remove elemental segregation within the solidifying phases and ensure chemical equilibration of the composition of each phase. The skeletal interdendritic solidification observed in alloys in the as-cast state was observed to break down in most cases in the homogenised samples in favour of discrete particles, most visibly in Sample B, Figures 4.2b and 4.5b respectively. Importantly, all compositions were found to be multiphase even after the homogenisation heat treatments.

Following observation of the alloy microstructure by SEM analysis and elemental partitioning by EDS mapping, XRD analysis was performed according to the methodology detailed in Section 2.3 to identify the crystallographic nature of the phases forming within the alloys. The resulting XRD patterns, full-pattern Pawley fits, and the differences between the raw data and fits for both the as-cast and homogenised samples are shown in Figures 4.8–4.16. In most cases, a change in the phase composition from the as-cast to homogenised state is detected in the XRD patterns. However, a reliable XRD pattern could not be obtained for Sample B in the as-cast condition due to significant texturing effects, which hindered accurate phase identification. This highlights the limitations of XRD when dealing with textured samples, where diffraction peaks may not accurately reflect the bulk phase composition. Therefore, multiple complementary methods, including SEM and EDS discussed prior, were utilised to improve confidence in the experimental results and reduce over-reliance on a single characterisation technique.

A summary of the data extracted from the EDS and XRD analysis is provided in Table 4.2.

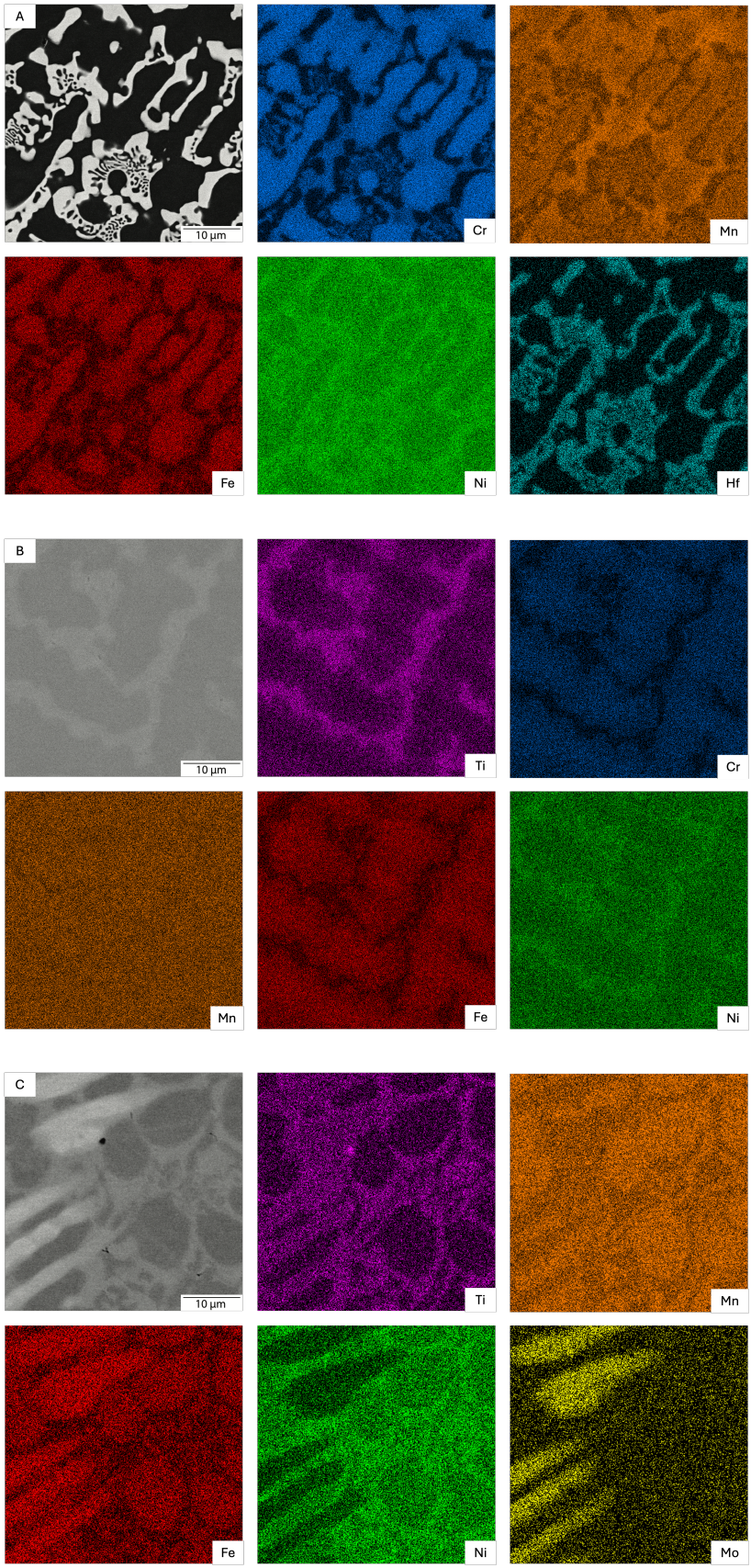


Figure 4.2: BSE micrographs and EDS elemental maps of alloy compositions A–C, ($Cr_{22.3}Mn_{17.9}Fe_{10.2}Ni_{44.8}Hf_{4.8}$, $Ti_{10.0}Cr_{9.6}Mn_{27.0}Fe_{19.6}Ni_{33.8}$, $Ti_{10.3}Mn_{45.9}Fe_{15.5}Ni_{26.0}Mo_{2.3}$) in the as-cast condition.

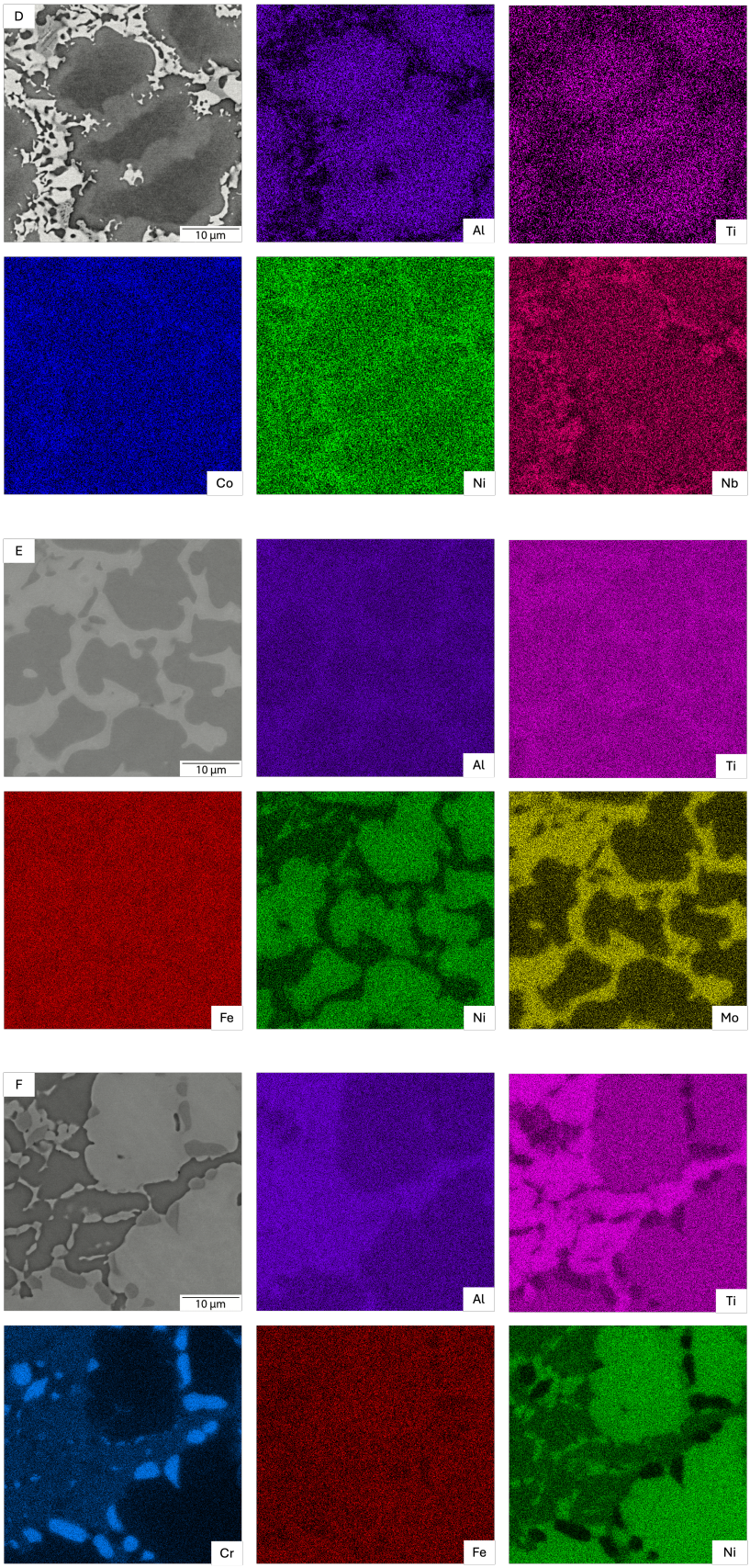


Figure 4.3: BSE micrographs and EDS elemental maps of alloy compositions D–F, ($Al_{19.9}Ti_{5.0}Co_{30.4}Ni_{30.1}Nb_{14.6}$, $Al_{29.7}Ti_{20.6}Fe_{30.3}Ni_{14.6}Mo_{4.8}$, $Al_{29.6}Ti_{20.5}Cr_{11.4}Fe_{5.2}Ni_{33.3}$) in the as-cast condition.

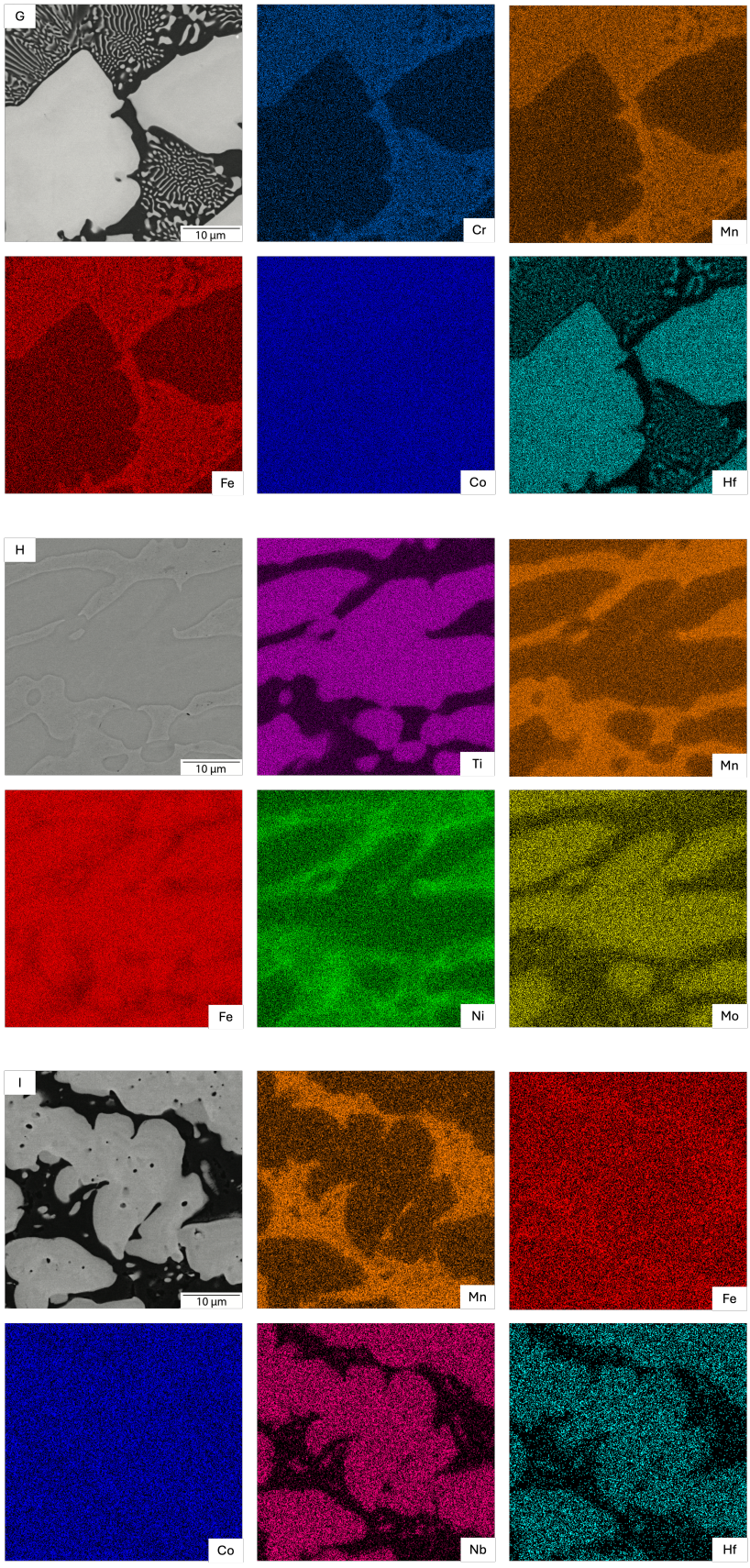


Figure 4.4: BSE micrographs and EDS elemental maps of alloy compositions G–I, ($Fe_{20.3}Co_{43.7}Cr_{5.7}Mn_{21.4}Hf_{8.9}$, $Fe_{41.8}Ni_{15.2}Ti_{15.6}Mn_{26.1}Mo_{1.3}$, $Fe_{16.1}Co_{31.4}Mn_{37.8}Hf_{4.9}Nb_{9.8}$) in the as-cast condition.

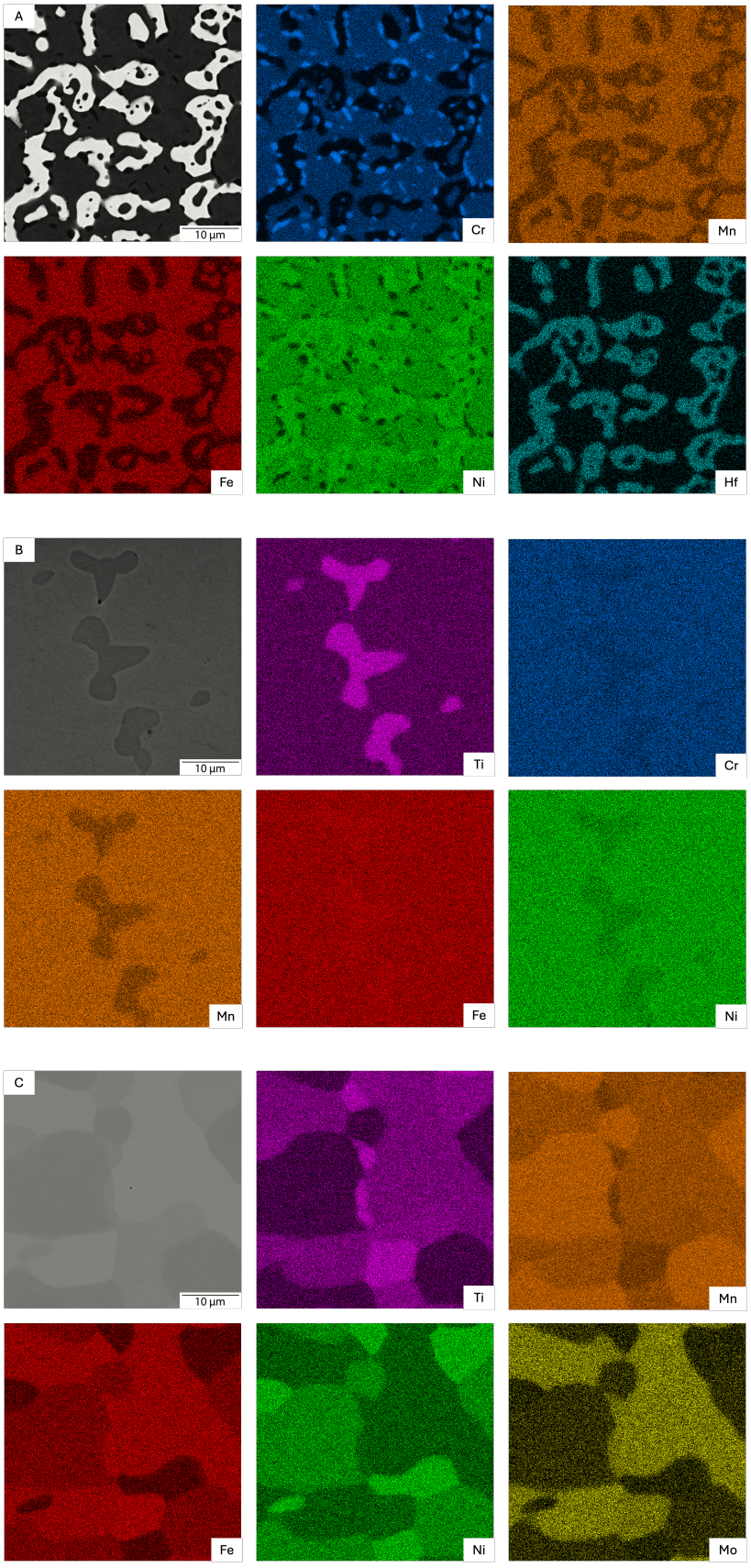


Figure 4.5: BSE micrographs and EDS elemental maps of alloy compositions A–C, ($Cr_{22.3}Mn_{17.9}Fe_{10.2}Ni_{44.8}Hf_{4.8}$, $Ti_{10.0}Cr_{9.6}Mn_{27.0}Fe_{19.6}Ni_{33.8}$, $Ti_{10.3}Mn_{45.9}Fe_{15.5}Ni_{26.0}Mo_{2.3}$) in the homogenised condition.

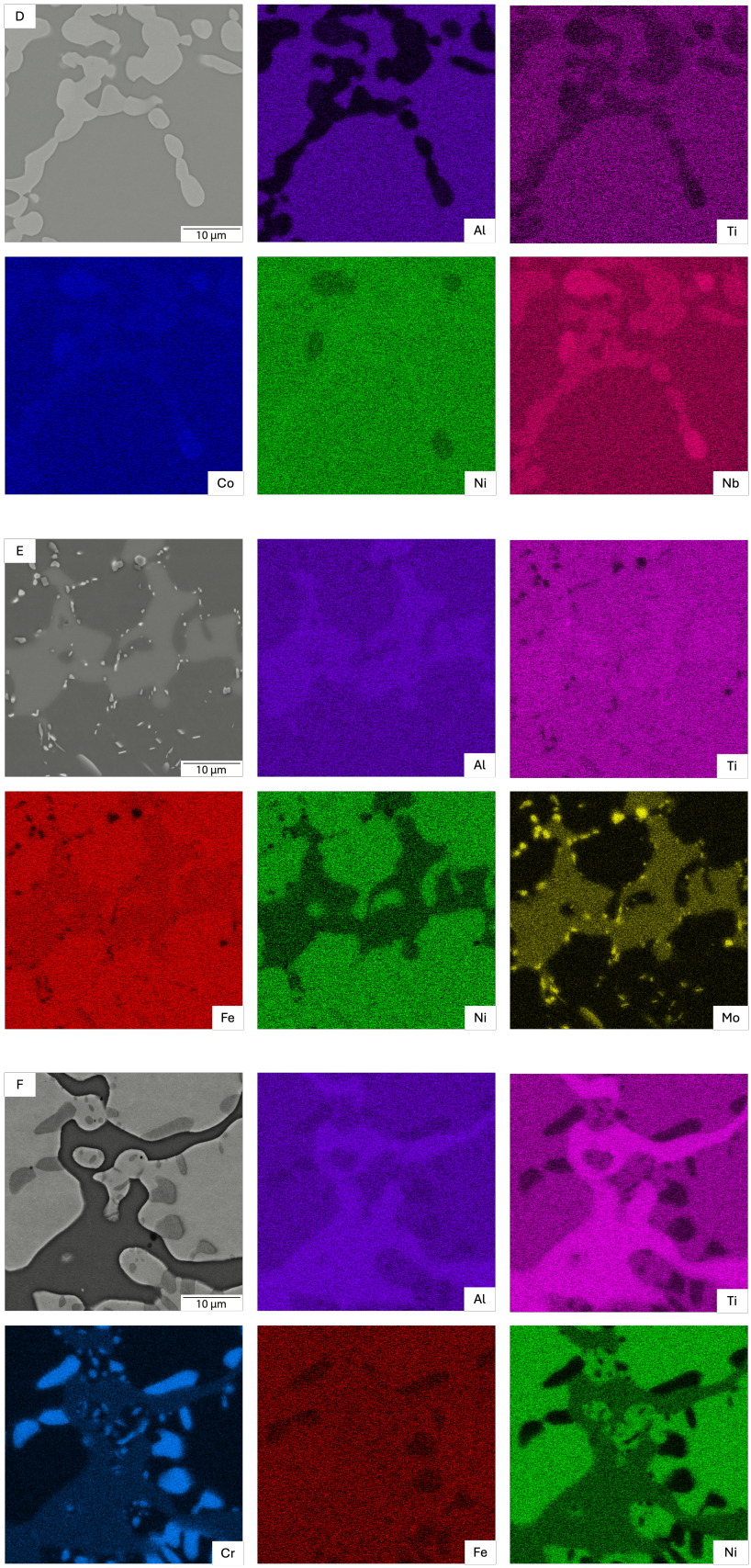


Figure 4.6: BSE micrographs and EDS elemental maps of alloy compositions D–F, ($Al_{19.9}Ti_{5.0}Co_{30.4}Ni_{30.1}Nb_{14.6}$, $Al_{29.7}Ti_{20.6}Fe_{30.3}Ni_{14.6}Mo_{4.8}$, $Al_{29.6}Ti_{20.5}Cr_{11.4}Fe_{5.2}Ni_{33.3}$) in the homogenised condition.

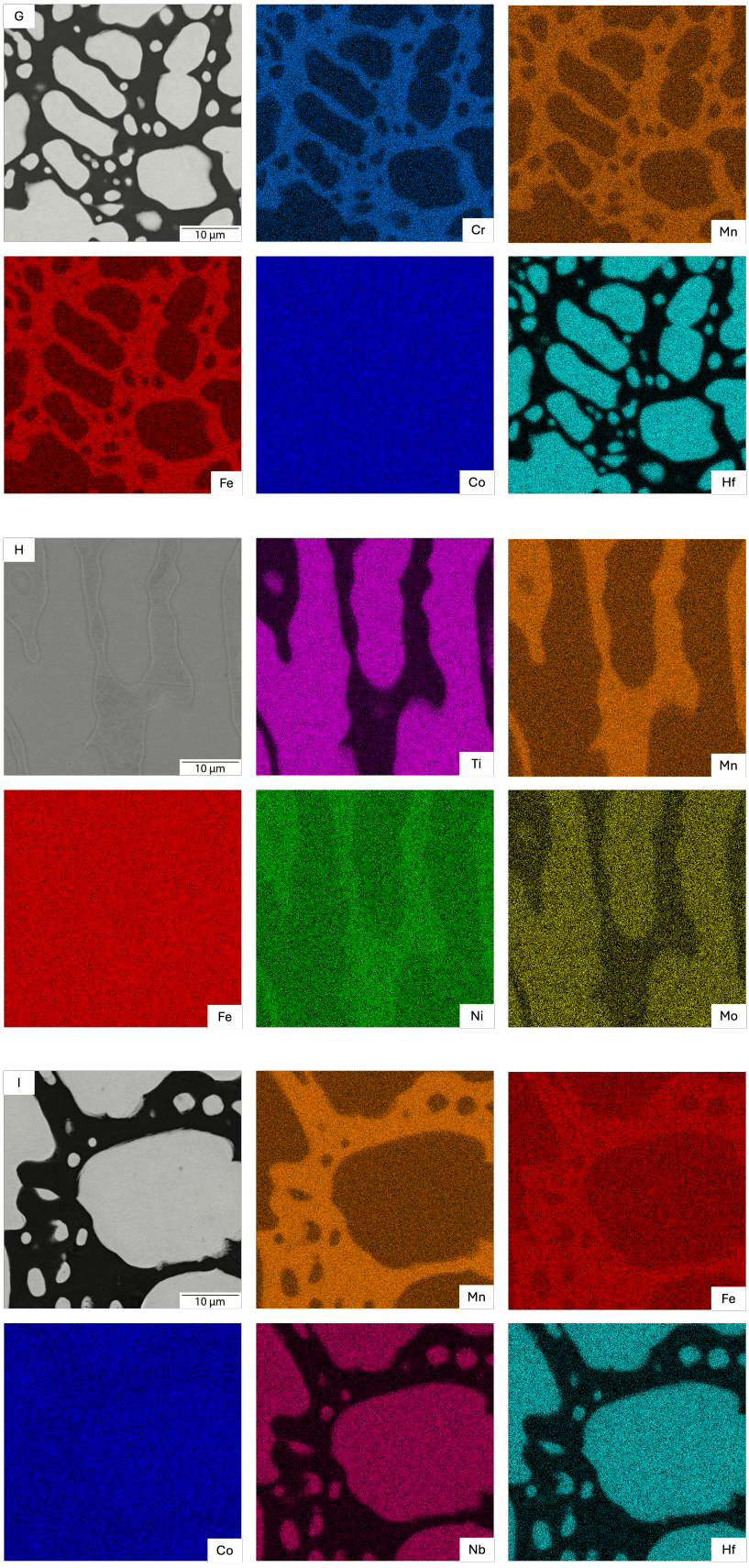


Figure 4.7: BSE micrographs and EDS elemental maps of alloy compositions G–I, ($Fe_{20.3}Co_{43.7}Cr_{5.7}Mn_{21.4}Hf_{8.9}$, $Fe_{41.8}Ni_{15.2}Ti_{15.6}Mn_{26.1}Mo_{1.3}$, $Fe_{16.1}Co_{31.4}Mn_{37.8}Hf_{4.9}Nb_{9.8}$) in the homogenised condition.

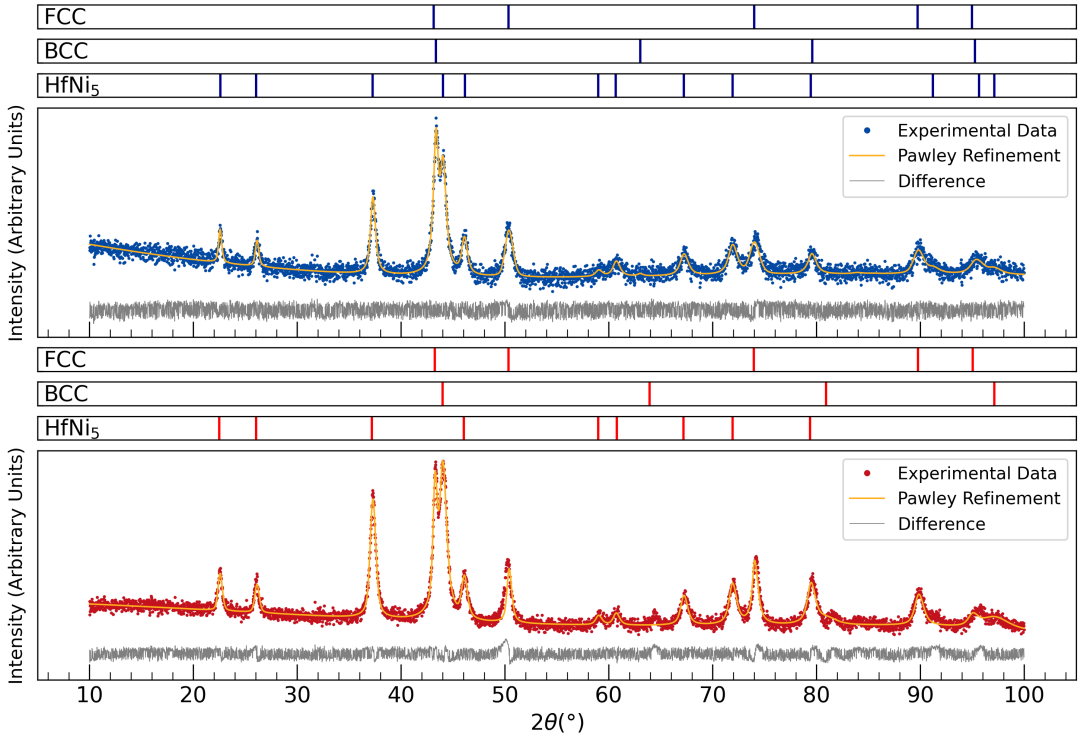


Figure 4.8: XRD patterns overlaid with Pawley refinement fits for alloy composition A ($Cr_{22.3}Mn_{17.9}Fe_{10.2}Ni_{44.8}Hf_{4.8}$) in the as-cast (top) and heat-treated (bottom) conditions.

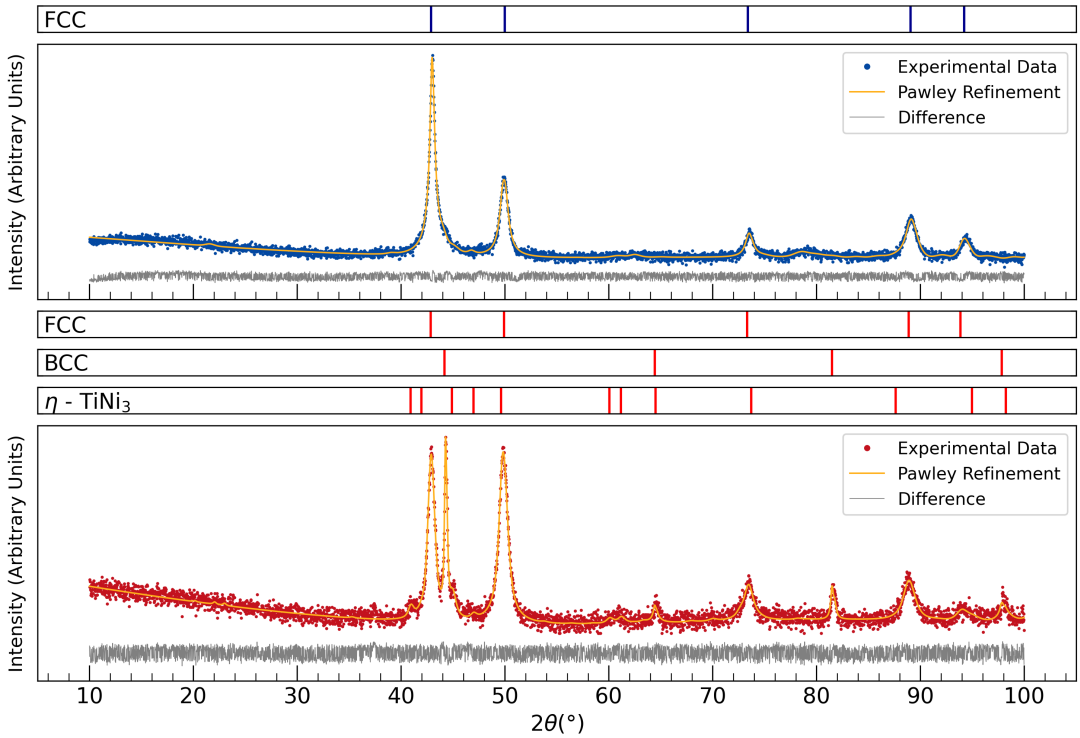


Figure 4.9: XRD patterns overlaid with Pawley refinement fits for alloy composition B ($Ti_{10.0}Cr_{9.6}Mn_{27.0}Fe_{19.6}Ni_{33.8}$) in the as-cast (top) and heat-treated (bottom) conditions.

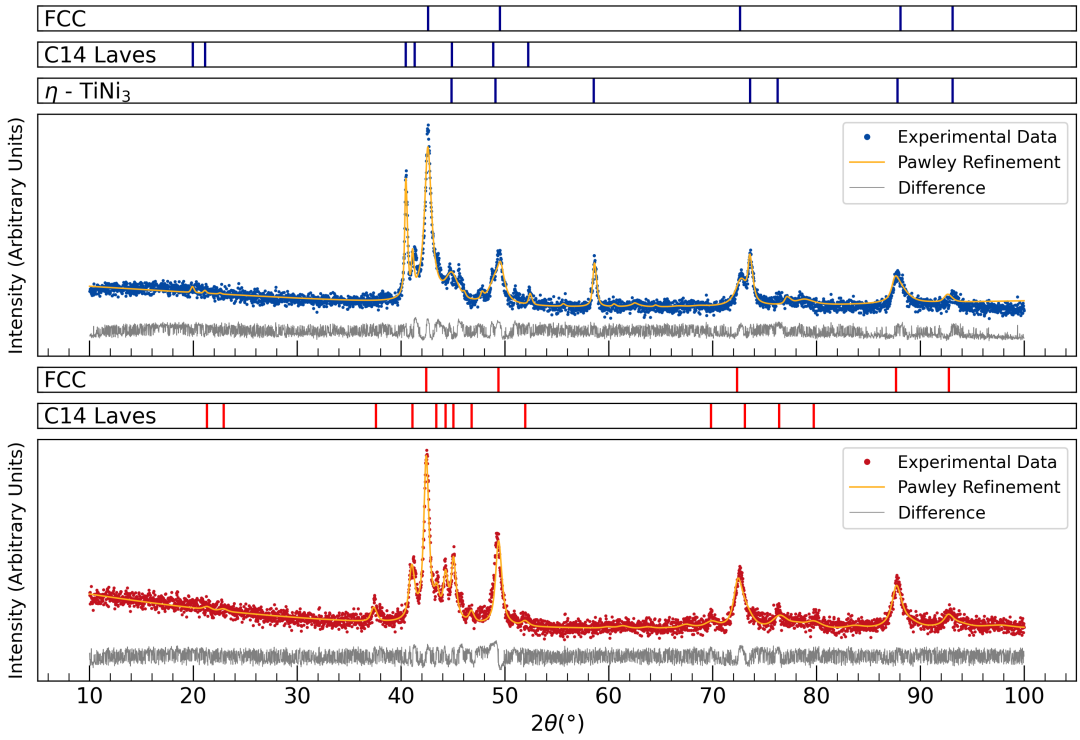


Figure 4.10: XRD patterns overlaid with Pawley refinement fits for alloy composition C ($Ti_{10.3}Mn_{45.9}Fe_{15.5}Ni_{26.0}Mo_{2.3}$) in the as-cast (top) and heat-treated (bottom) conditions.

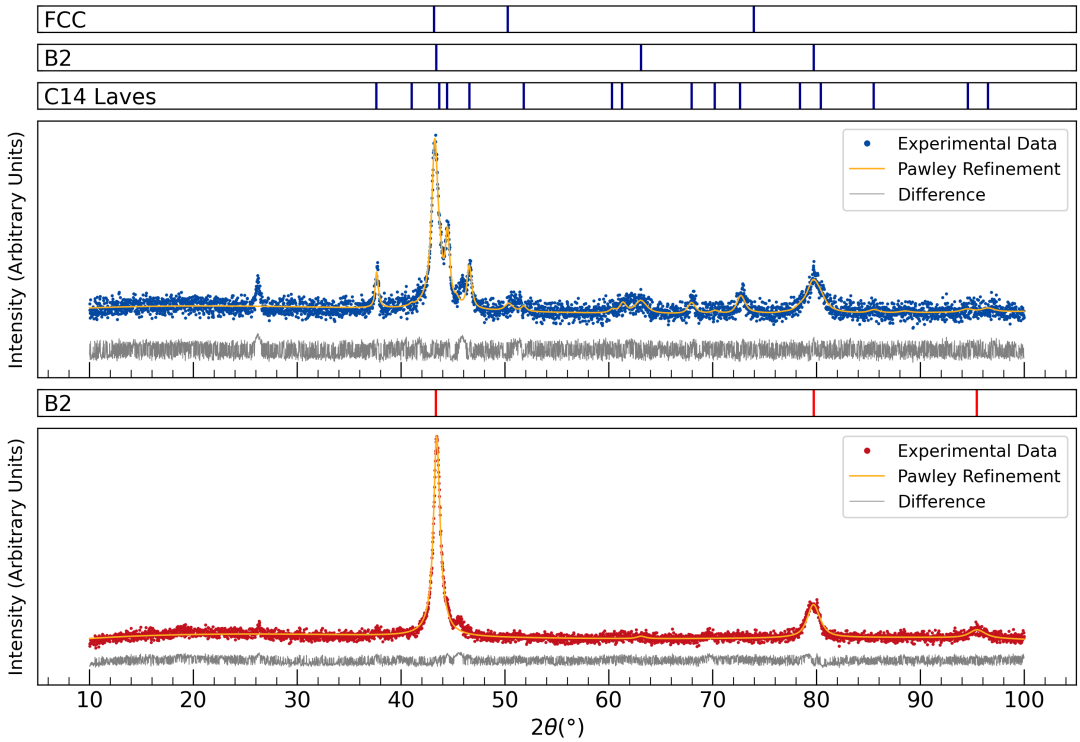


Figure 4.11: XRD patterns overlaid with Pawley refinement fits for alloy composition D ($Al_{19.9}Ti_{5.0}Co_{30.4}Ni_{30.1}Nb_{14.6}$) in the as-cast (top) and heat-treated (bottom) conditions.

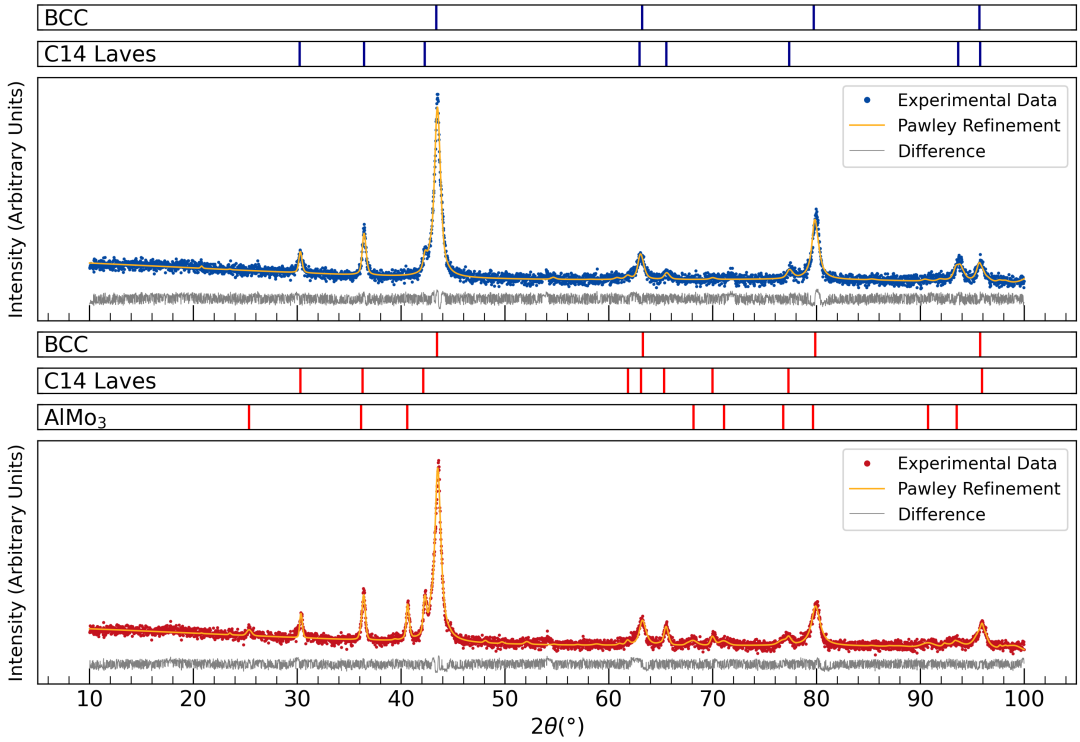


Figure 4.12: XRD patterns overlaid with Pawley refinement fits for alloy composition E ($Al_{29.7}Ti_{20.6}Fe_{30.3}Ni_{14.6}Mo_{4.8}$) in the as-cast (top) and heat-treated (bottom) conditions.

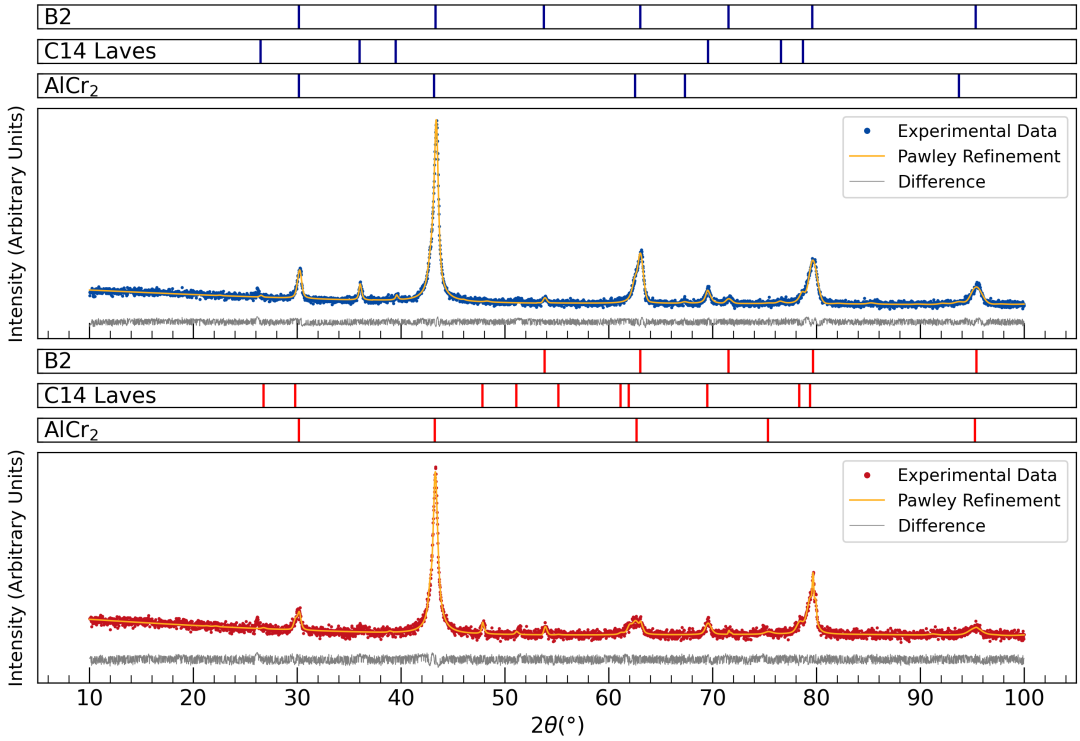


Figure 4.13: XRD patterns overlaid with Pawley refinement fits for alloy composition F ($Al_{29.6}Ti_{20.5}Cr_{11.4}Fe_{5.2}Ni_{33.3}$) in the as-cast (top) and heat-treated (bottom) conditions.

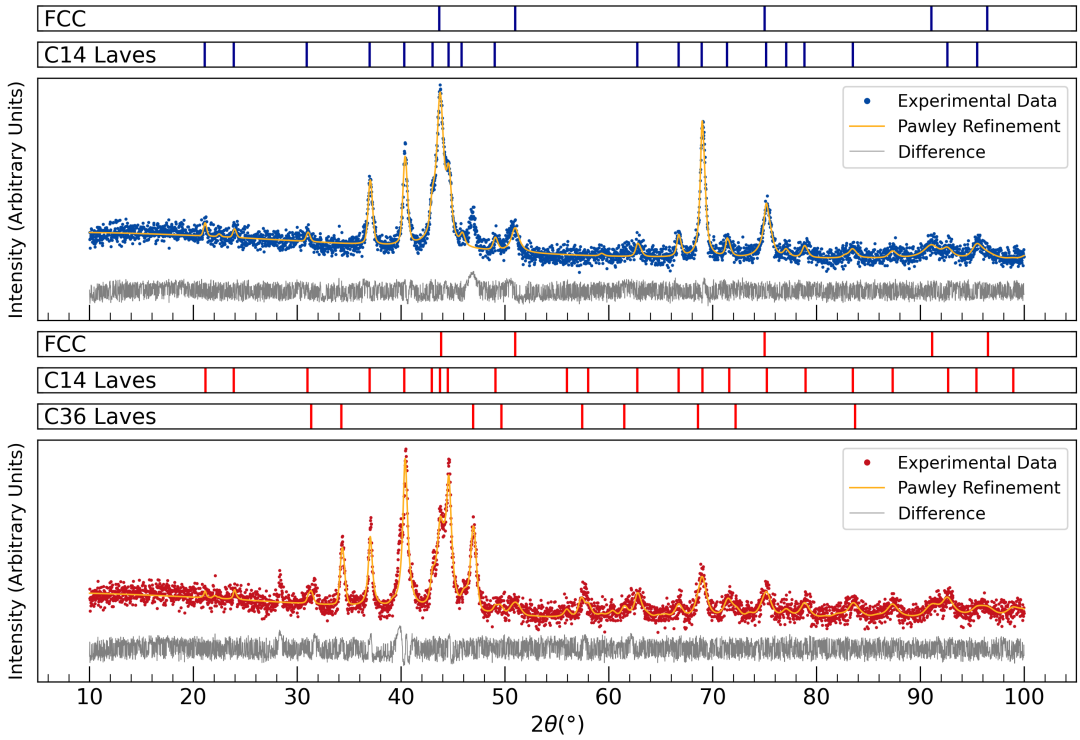


Figure 4.14: XRD patterns overlaid with Pawley refinement fits for alloy composition G ($Fe_{20.3}Co_{43.7}Cr_{5.7}Mn_{21.4}Hf_{8.9}$) in the as-cast (top) and heat-treated (bottom) conditions.

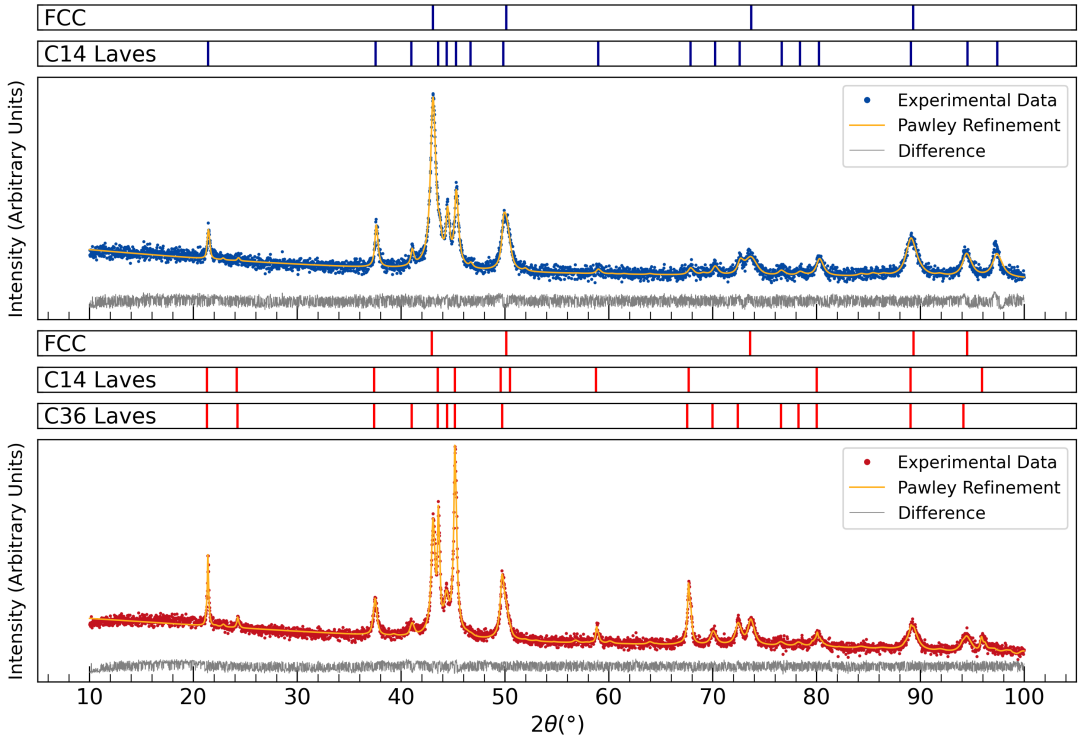


Figure 4.15: XRD patterns overlaid with Pawley refinement fits for alloy composition H ($Fe_{41.8}Ni_{15.2}Ti_{15.6}Mn_{26.1}Mo_{1.3}$) in the as-cast (top) and heat-treated (bottom) conditions.

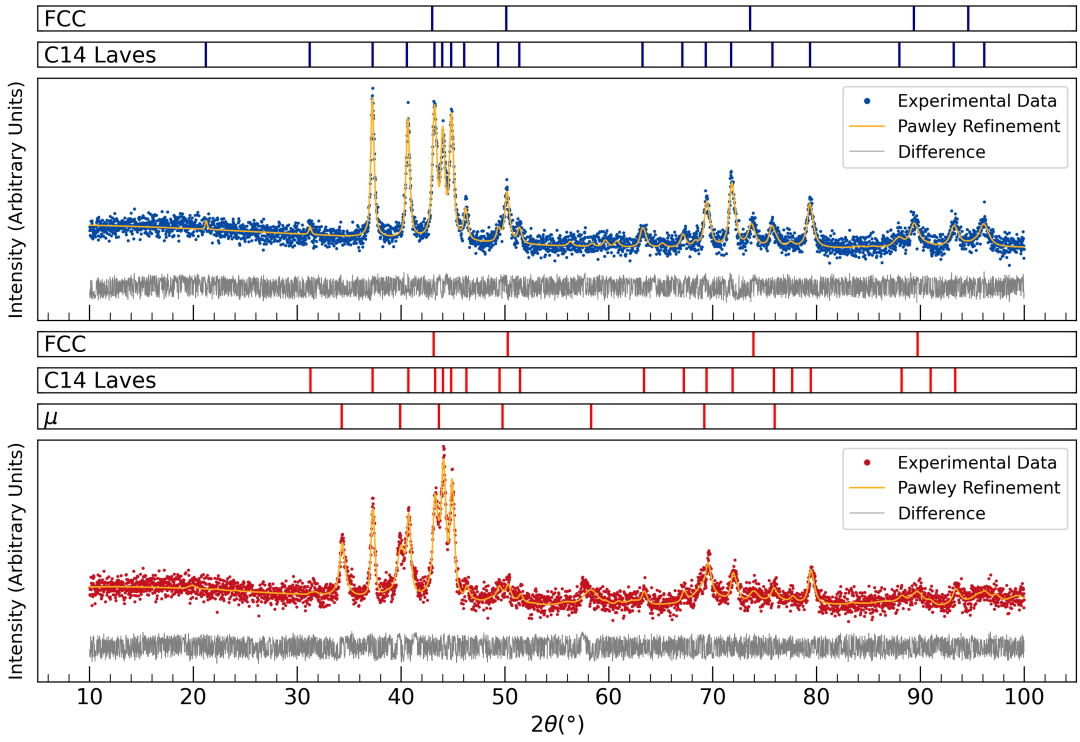


Figure 4.16: XRD patterns overlaid with Pawley refinement fits for alloy composition I ($Fe_{16.1}Co_{31.4}Mn_{37.8}Hf_{4.9}Nb_{9.8}$) in the as-cast (top) and heat-treated (bottom) conditions.

Table 4.2: Summary of the microstructural information extracted from the EDS and XRD analysis of the alloy compositions in the as-cast and homogenised state.

Sample Index	**Experimental Alloy Composition**	**As-Cast Phase Fomation**	**Homogenised Phase Formation**
A	$Cr_{22.3}Mn_{17.9}Fe_{10.2}Ni_{44.8}Hf_{4.8}$	FCC + BCC + $HfNi_5$	FCC + BCC + $HfNi_5$
B	$Ti_{10.0}Cr_{9.6}Mn_{27.0}Fe_{19.6}Ni_{33.8}$	FCC	FCC + BCC + η
C	$Ti_{10.3}Mn_{45.9}Fe_{15.5}Ni_{26.0}Mo_{2.3}$	FCC + C14 Laves + η	FCC + C14 Laves
D	$Al_{19.9}Ti_{5.0}Co_{30.4}Ni_{30.1}Nb_{14.6}$	FCC + B2 + C14 Laves	B2
E	$Al_{29.7}Ti_{20.6}Fe_{30.3}Ni_{14.6}Mo_{4.8}$	BCC/B2 + C14 Laves	BCC/B2 + C14 Laves + $AlMo_3$
F	$Al_{29.6}Ti_{20.5}Cr_{11.4}Fe_{5.2}Ni_{33.3}$	BCC/B2 + C14 Laves + $AlCr_2$	BCC/B2 + C14 Laves + $AlCr_2$
G	$Fe_{20.3}Co_{43.7}Cr_{5.7}Mn_{21.4}Hf_{8.9}$	FCC + C14 Laves	FCC + C14 Laves + C36 Laves
H	$Fe_{41.8}Ni_{15.2}Ti_{15.6}Mn_{26.1}Mo_{1.3}$	FCC + C14 Laves	FCC + C14 Laves + C36 Laves
I	$Fe_{16.1}Co_{31.4}Mn_{37.8}Hf_{4.9}Nb_{9.8}$	FCC + C14 Laves	FCC + C14 Laves + μ

For Samples E and F, BCC and B2 phases could not be distinguished due to their similar peak positions and the limitations of Pawley refinement, which does not consider atomic ordering.

4.4 Hardness Analysis of As-Cast and Homogenised Material

The hardness of the alloys was assessed by microindentation hardness testing, as outlined in Section 2.6. Results of the microindentation hardness assessments of all alloys in both the as-cast and homogenised condition are presented in Figure 4.17. For alloys A–C, the ML-predicted hardness is significantly higher than that of both the as-cast and homogenised conditions. However some agreement within the range of uncertainty of the experimentally determined values was observed. In contrast, a significant increase in hardness compared to ML predictions is observed for alloys D–F; alloys G–I show both increases and reductions in hardness when compared to the ML predicted values. The only notable change in measured hardness from the as-cast to the homogenised condition occurs for alloy composition B ($Ti_{10.0}Cr_{9.6}Mn_{27.0}Fe_{19.6}Ni_{33.8}$), where a significant increase is measured, consistent with the changes observed in the microstructure in Figures 4.2b and 4.5b. All the remaining alloy compositions measured hardness values in the as-cast and homogenised state are within errors.

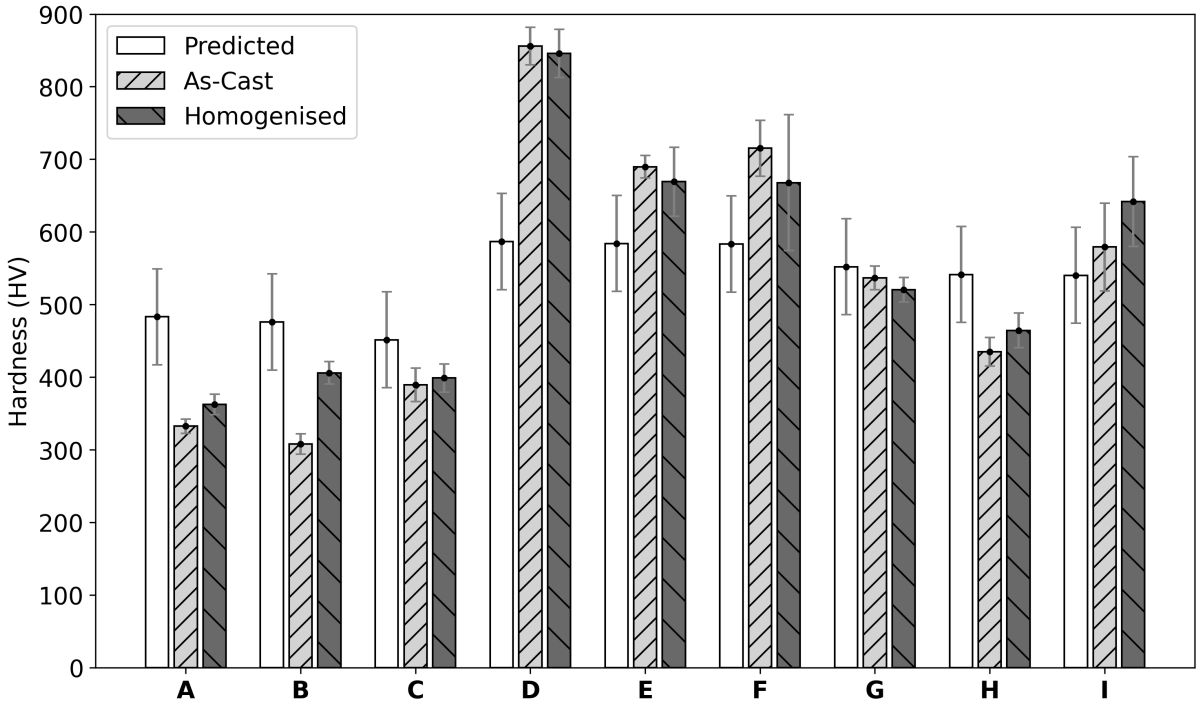


Figure 4.17: Comparison of ML-predicted, as-cast, and homogenised microindentation hardness (HV) for the nine alloys fabricated in this study. Error bars for predicted hardness indicate the ML regression model's MAE, while those for the experimentally measured as-cast and homogenised samples represent the standard error.

Table 4.3: Experimentally determined microindentation hardness measured by applying a 1 kgf load with a 15 second dwell time for a series of ten indentations in accordance with ASTM E384 [271]. Typical hardness values for industrially relevant WC-Co compositions range from 700–2300 HV 10 [289].

Sample Index	Experimental Alloy Composition	ML Hardness Model Y (HV)	Experimental Hardness As-Cast (HV)	Experimental Hardness Homogenised (HV)
A	$Cr_{22.3}Mn_{17.9}Fe_{10.2}Ni_{44.8}Hf_{4.8}$	477	332.4 ± 6.8	362.2 ± 8.9
B	$Ti_{10.0}Cr_{9.6}Mn_{27.0}Fe_{19.6}Ni_{33.8}$	478	307.7 ± 8.7	405.8 ± 11.6
C	$Ti_{10.3}Mn_{45.9}Fe_{15.5}Ni_{26.0}Mo_{2.3}$	429	389.5 ± 15.4	398.0 ± 12.2
D	$Al_{19.9}Ti_{5.0}Co_{30.4}Ni_{30.1}Nb_{14.6}$	586	855.8 ± 15.4	845.7 ± 21.8
E	$Al_{29.7}Ti_{20.6}Fe_{30.3}Ni_{14.6}Mo_{4.8}$	586	689.6 ± 11.6	669.2 ± 30.5
F	$Al_{29.6}Ti_{20.5}Cr_{11.4}Fe_{5.2}Ni_{33.3}$	590	715.2 ± 23.0	667.7 ± 71.7
G	$Fe_{20.3}Co_{43.7}Cr_{5.7}Mn_{21.4}Hf_{8.9}$	552	536.7 ± 16.5	552.0 ± 17
H	$Fe_{41.8}Ni_{15.2}Ti_{15.6}Mn_{26.1}Mo_{1.3}$	541	435.0 ± 19.5	464.3 ± 24
I	$Fe_{16.1}Co_{31.4}Mn_{37.8}Hf_{4.9}Nb_{9.8}$	540	579.1 ± 60.5	641.7 ± 62

Optical images were taken of representative indents from each of the nine samples in both the as-cast and homogenised conditions using an optical microscope. These images enabled evaluation and comparison of the hardness and mechanical response of the material between the different processing conditions. By measuring the diagonals of the Vickers indentations, the hardness values of the samples can be calculated, as recorded in Table 4.3, providing quantitative data on their mechanical properties. Larger indentations generally correspond to softer materials, while smaller ones indicate harder materials. Additionally, the images allow for qualitative analysis of surface features, such as the presence of cracking or plastic deformation around the indentations, which can indicate the material's brittleness or ductility. The overall shape and symmetry of the indentations also provides insights into the homogeneity of the material, highlighting any variations in microstructure that may arise from differences in processing as well as the impact of grain boundaries on the indentations. Optical images of representative indents for the nine samples in both as-cast and homogenised conditions are shown in Figures 4.18 and 4.19, respectively. These images reveal significant variations in the microhardness indentations across the samples. Most samples exhibit cracking, indicative of localised brittleness, while some display pronounced asymmetry. This asymmetry aligns with the larger errors measured for these samples in Figure 4.17 and Table 4.3, reflecting greater variability in their hardness measurements. Notably, Sample B shows no cracking but distinct slip bands on its surface. Some samples, such as alloy compositions E and F, exhibit straight

cracks originating from the corners of the indentations, propagating through the material. Sample D stands out as exhibiting the highest hardness of all alloys tested, yet shows no obvious cracking in the micrographs, suggesting a favourable combination of strength and damage tolerance. In contrast, Sample H shows cracking around the entire indentation, seemingly following phase boundaries and confined to a single phase. Comparing as-cast to homogenised samples reveals that those without cracking in the as-cast condition remain crack-free after homogenisation. However, for other samples, cracking becomes more pronounced after homogenisation, with Sample B also showing increased plastic deformation.

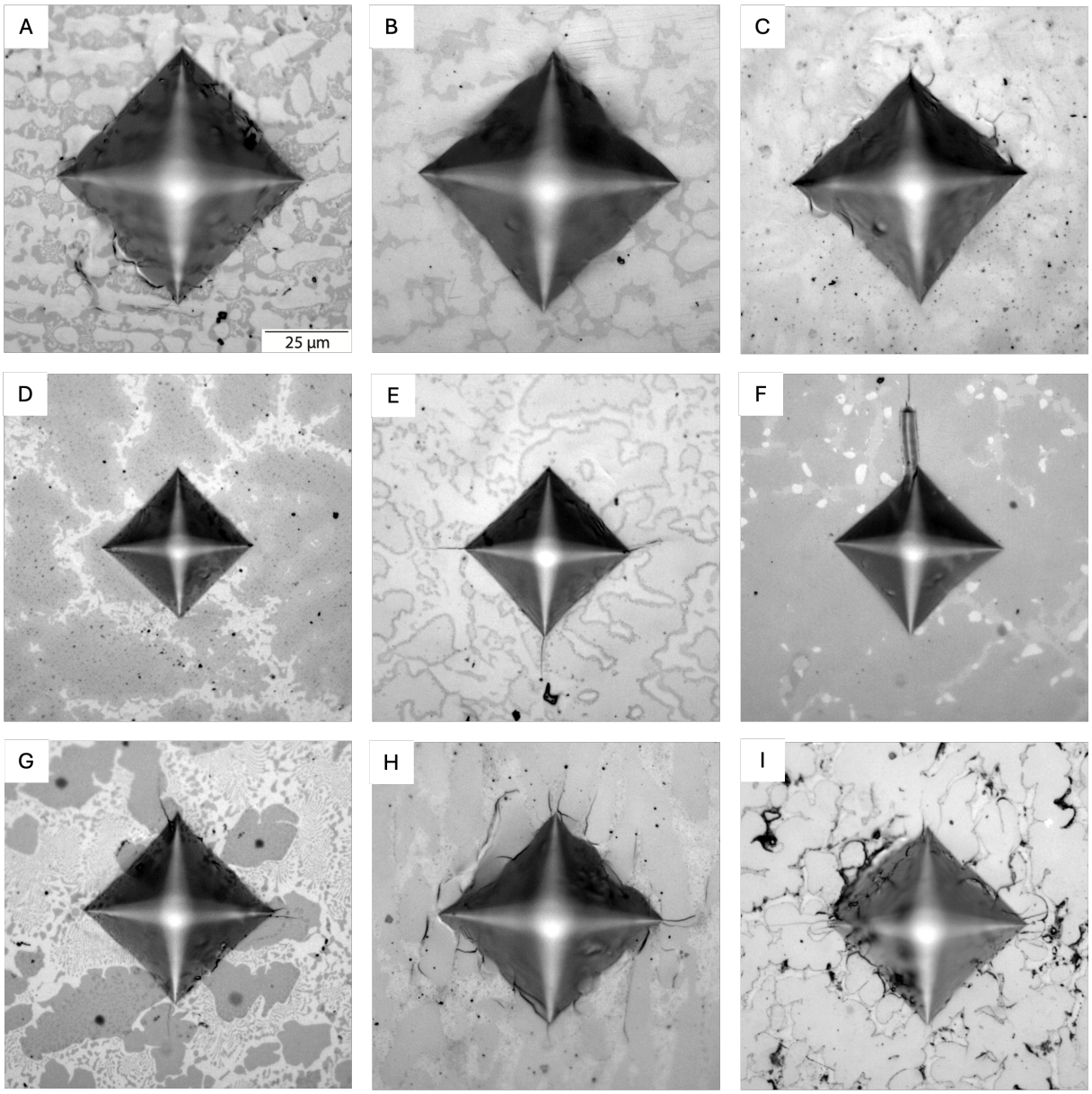


Figure 4.18: Optical images of microhardness indentations across the nine different samples in the as-cast condition. Each subfigure shows the characteristic square-shaped indent produced by the Vickers indenter under a fixed load of 1 kgf. The size and shape of the indentations vary due to differences in material hardness across the samples. Measurements of the diagonal lengths were taken from these indentations to calculate Vickers hardness values for comparative analysis.

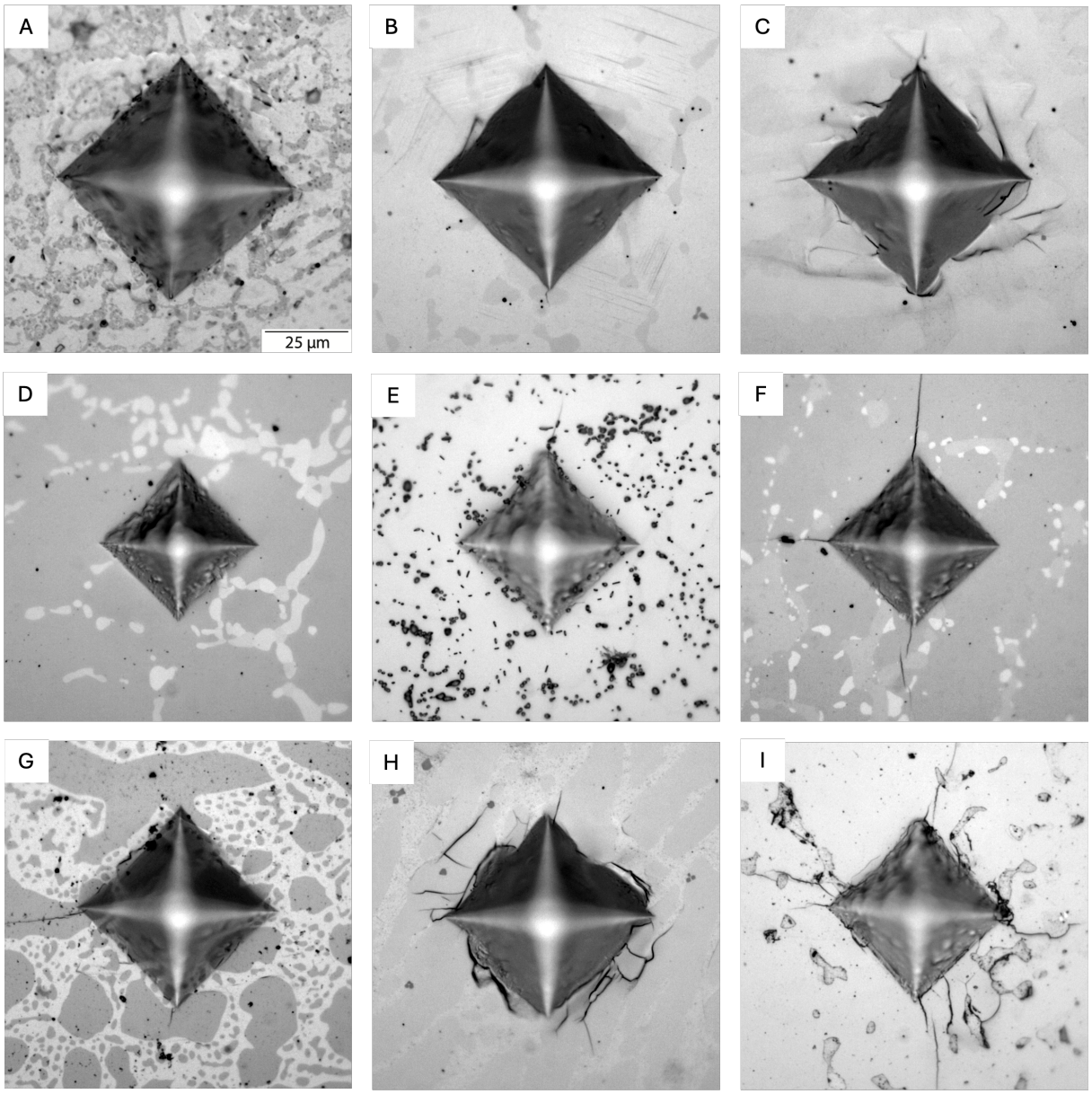


Figure 4.19: Optical images of microhardness indentations across the nine different samples in the homogenised condition. Each subfigure shows the characteristic square-shaped indent produced by the Vickers indenter under a fixed load. The size and shape of the indentations vary due to differences in material hardness across the samples. Measurements of the diagonal lengths were taken from these indentations to calculate Vickers hardness values for comparative analysis

4.5 Summary

Nine novel HEA compositions, downselected using the coupled ML and CALPHAD approach described in Chapter 3, were successfully fabricated via vacuum arc melting. These alloys were then characterised using a range of techniques: SEM, EDS, and XRD were used to identify phases and examine microstructures, while microindentation and optical microscopy assessed hardness and post-indentation deformation and cracking behaviour. The results of these experimental investigations are presented in this chapter.

Although most alloys exhibit an FCC solid solution phase, all alloys also display intermetallic phase formation, with phases such as η and C14 Laves observed across the compositions (Table 4.2). These intermetallic phases persist despite microstructural evolution following homogenisation treatments. Secondary phases remain evident post-homogenisation, reflecting the stability of the intermetallic components. Hardness measurements align with these observations, with alloys containing higher fractions of intermetallic phases exhibiting increased hardness. These findings provide insights into the interplay between phase composition, microstructure, and mechanical properties within these HEAs. A combined discussion of the predictions from the coupled ML and CALPHAD methodologies and the experimental characterisation of the fabricated HEAs is presented in the following chapter.

Chapter 5

Integrated Machine Learning and Experimental Findings Discussion

Building on the findings presented in Chapters 3 and 4, this chapter provides a critical discussion and interpretation of the results and their broader implications. The discussion is divided into two main sections: an evaluation of the microstructural predictions and experimental observations, and an assessment of the mechanical property predictions relative to the experimental measurements.

From the RF ML models constructed and trained on the publicly available experimental datasets [209, 210], predictions for phase and hardness properties of HEAs were performed in unexplored compositional spaces. In contrast to the majority of literature, CALPHAD was not used to supplement data or as an input to the models. Instead, CALPHAD was used to provide additional insights into the predicted microstructures constitution and assist in downselecting suitable alloys for experimental analysis. Based on these predictions, nine alloy compositions were fabricated and their microstructural and hardness properties examined to evaluate their potential to meet the design criteria and to assess the performance of the ML predictions. These nine compositions represented three distinct alloy clusters: the three compositions predicted by both ML and CALPHAD to be the hardest while forming a single-phase FCC microstructure; the three hardest single-phase FCC alloys predicted by ML, irrespective of CALPHAD predictions; and the three hardest single-phase FCC alloys predicted by ML, which CALPHAD indicated would form

a dual-phase FCC and C14 Laves microstructure. Although none of the experimentally evaluated alloys exhibited a single-phase FCC structure, three were found to possess an FCC matrix. The alloys predicted to form dual FCC and C14 Laves phases were confirmed to display this microstructure in the as-cast condition, with additional C36 Laves phase formation observed after homogenisation. For the hardness predictions, there is some agreement between the results, but in general there is an over prediction of the hardness for FCC alloys, discussed later in Section 5.2.

Critically, despite the discrepancies between predictions and experimental measurements, the methodology employed identified compositions that are suitable for further experimental evaluation toward the intended use case. Furthermore, the construction of the models and their rigorous analysis have revealed several areas for improvement for both the ML architectures; highlighted the need for reliable, extensive, and expansive datasets.

5.1 Phase Formation and Microstructural Analysis

It is clear from the experimental results, shown in the BSE micrographs within Chapter 4 Figures 4.2 through to 4.7, that none of the fabricated alloys exhibited a fully single-phase FCC solid solution in either the as-cast or homogenised condition. Instead, varying degrees of intermetallic phase formation were observed across all samples. Notably, seven of the nine compositions contained an FCC phase, while the remaining two formed BCC or B2 matrix phases. These results highlight the challenges associated with phase prediction in complex compositional spaces and the limitations of the current ML classification models.

5.1.1 Impact of Training Data Bias on Alloy Downselection

This discrepancy between experiment and prediction primarily originates from the datasets used in the ML training. The imbalanced data contained within the datasets, illustrated in Figures 5.1 and 5.2, coupled with the bias of FCC compositions toward the CrMnFeCoNi system, resulted in the predictions herein having reduced confidence indicators when increased hardness was prioritised. Across the predictions of the two models for the nine downselected alloys an average prediction confidence of 42.4 % was recorded. Achieving higher hardness alloys, such as alloys A–C, was prioritised over those more likely to produce a single-phase FCC solid-solution, but at a significantly reduced hardness.

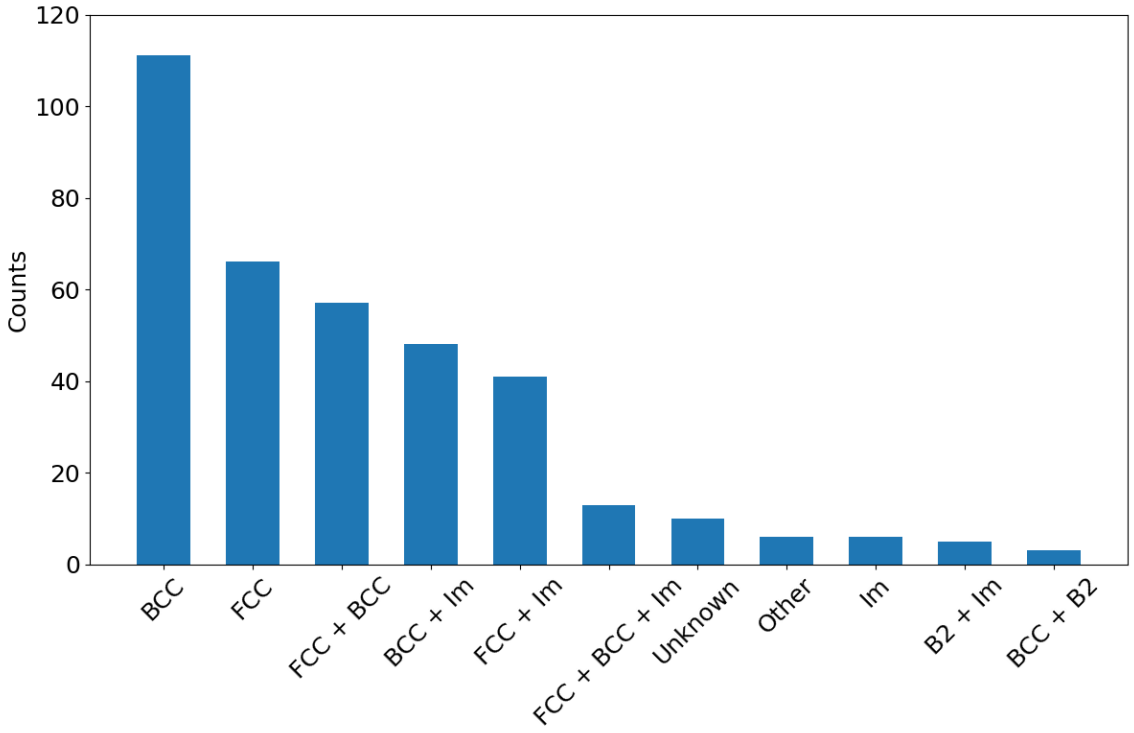


Figure 5.1: Phase distribution of HEA compositions from the dataset constructed by Gorsse *et al.* [210]. The category labelled "Other" aggregates the occurrences of FCC + B2 + Im, FCC + BCC + B2, FCC + HCP, FCC + HCP + Im, and BCC + HCP phases. The "Unknown" category represents HEA compositions in the dataset with no reported phase information.

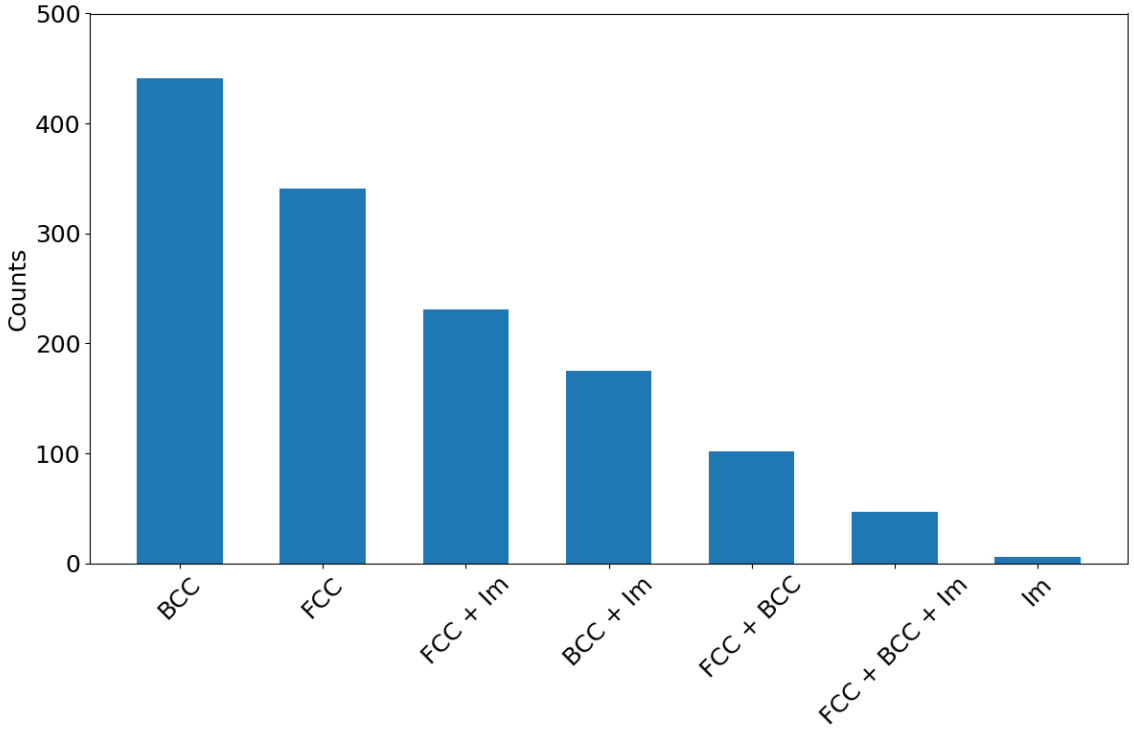


Figure 5.2: Phase distribution of HEA compositions from the dataset constructed by Machaka *et al.* [209].

For example, restricting the selection to only those compositions predicted to form an FCC phase with confidence $\geq$ 90 % by both G-Phase and M-Phase reduces the set of 24,613 ML-predicted FCC-forming alloys to just 443, all of which are also predicted by CALPHAD to form a single FCC phase. Furthermore, all 443 of these alloys are some minor compositional variation of CrMnFeCoNi, as expected, as this system dominates the literature with respect to FCC HEAs. Furthermore, these compositions exhibit significantly lower hardness values predicted by the ML, averaging only 105 HV, compared to the microhardness of pure Co (106 HV) and Ni (65 HV) [290]. Such compositions would not offer any advantage, even as replacements for the binder material. Consequently, priority was given to compositions predicted to have high hardness, even at the expense of high confidence in forming a single-phase FCC solid solution, to enable broader exploration of the HEA compositional space. Hence, high-hardness-predicted compositions were prioritised, at the expense of high confidence in prediction of a single-phase FCC solid-solution, to enable further exploration of HEA compositional space.

5.1.2 Microstructural Characterisation and Observations

The phase area fractions of the alloy compositions fabricated in this study, determined through ImageJ analysis of BSE-SEM micrographs, are provided in Tables 5.1 and 5.2 for the as-cast and heat-treated conditions, respectively.

SEM analysis (Figure 4.2a) reveals that Sample A comprises two phases: an FCC matrix and an $HfNi_5$ phase. After homogenisation, a Cr-rich minority phase constituting approximately (5$\pm$ 1)% of the microstructure precipitates from the FCC matrix (Figure 4.5a). This phase corresponds to the Cr-based BCC phase identified in both the as-cast and homogenised XRD patterns (Figure 4.8). These observations underscore the importance of assessing post-processing effects, as the as-cast condition may not accurately reflect equilibrium or industrially relevant microstructures.

Of the alloys predicted to form single-phase FCC by both ML and CALPHAD, Alloy B exhibits the lowest intermetallic fraction, (25 $\pm$ 1)% in the heat-treated condition, reduced from 45 % in the as-cast state. This aligns with its high FCC phase prediction confidence, averaging 51.8 % across the two models, one of the highest among the downselected alloys. A reliable XRD pattern could not be obtained for the as-cast sample due to pronounced texturing, and only an FCC phase could be identified (Figure 4.9). In the homogenised

condition (Figure 4.5b), EDS mapping indicates a two-phase microstructure, with a Ni- and Ti-rich (Ni_3Ti) η phase that spheroidises during heat treatment. XRD analysis also reveals a third phase corresponding to a BCC structure. The presence of the η phase and its spheroidisation upon homogenisation make this alloy an excellent candidate for carbon reinforcement, discussed further in Chapter 6.

In the as-cast condition, Sample C exhibits a multi-phase microstructure, with phase area fraction measurements indicating a primary FCC phase at (46 ± 2)%, a secondary Ni3Ti-based η phase at (34 ± 2)%, and a ternary Fe2Mo C14 Laves phase at (20 ± 2)%. As shown in the EDS maps in Figure 4.2c, the C14 Laves phase forms in a finger-like morphology, while the η phase is more evenly distributed within the FCC matrix, consistent with the XRD analysis in Figure 4.10. However, following homogenisation, the microstructure transitions to a more platelet-like morphology, and the η phase is no longer detected in the XRD pattern. Combined with phase fraction analysis of the SEM micrographs, this suggests that the η phase decomposes, giving rise to additional FCC and C14 Laves phases of similar composition. In the homogenised condition, shown in Figure 4.5c, the lighter Fe- and Mo-rich regions correspond to the C14 Laves phase, while the darker Mn- and Ni-rich areas are likely FCC. EDS mapping also reveals the presence of at least two further phases, including one Ti-rich phase, reflecting the presence of multiple FCC or C14 Laves variants overlapping in the XRD pattern. This overlap of phases with similar compositions and morphologies makes accurate phase fraction analysis of the homogenised condition particularly challenging.

Samples D–F were selected as they were the hardest FCC alloys predicted by the ML models, irrespective of CALPHAD assessment. However, only one of these compositions, Alloy D, actually forms an FCC phase, which subsequently disappears from the XRD pattern after heat-treatment. In these systems, BCC/B2 primary phase formation dominates, accompanied by substantial intermetallic formation driven by the presence of high Al content, 20–30 at.%. This promotes the formation of Ni(TiAl) B2, and Mo_3Al and Cr_2Al intermetallic phases. The absence of an FCC matrix, combined with the prevalence of these intermetallics, renders these alloys extremely brittle. Macroscopic cracking occurs in these alloys both during arc-melting and under mechanical loading, as discussed in Section 5.2.

Sample D exhibits a notable microstructural transformation following homogenisation. As shown in Figures 4.3a and 4.6a, the original three-phase skeletal structure observed in the as-cast condition coalesces into a two-phase microstructure, with Co- and Nb-rich precipitates forming throughout. Phase fraction analysis shows the primary FCC phase decreases dramatically from (43 ± 1)% in the as-cast state to complete absence after heat treatment, while the B2 phase increases to (77 ± 4)%. This represents the largest change between as-cast and homogenised conditions for any alloy composition investigated. XRD analysis of Figure 4.11, identifies the as-cast phases as FCC, a Ni(TiAl)-based B2 phase, and a $(CoNi)_2Nb$-based C14 Laves phase. In the homogenised condition, strong texturing prevents acquisition of a reliable pattern, thus only a B2 phase is clearly identifiable. An additional peak to the right of the main 43 ° peak suggests the presence of another phase, though no definitive conclusion can be drawn from this single feature.

XRD analysis (Figure 4.11) identifies the as-cast phases as FCC, a Ni(TiAl)-based B2 phase, and a $(CoNi)_2Nb$-based C14 Laves phase. In the homogenised condition, strong texturing prevents a reliable pattern, with only a B2 phase clearly identifiable. A peak to the right of the main 43,° peak suggests another phase, though no definitive conclusion can be drawn from this single feature.

Good agreement is observed between the EDS maps and XRD analysis for Alloy E. In the as-cast condition, the EDS maps display a skeletal two-phase microstructure, with Ni- and Mo-rich phases, as shown in Figure 4.3b. This is corroborated by the XRD analysis in Figure 4.12, which produces a good fit for a dual BCC or B2 phase and a C14 Laves phase. It is not possible, with the available information, to make a clear distinction as to whether a BCC or B2 phase is present, and the C14 Laves phase could adopt either a Fe_2Mo-type or Fe_2Ti-type structure. Following the homogenisation process shown in Figure 4.6b, the area fraction of BCC or B2 phase increases significantly from (65 ± 2)% to (73 ± 3)%, while the C14 Laves content decreases from (35 ± 1)% to (24 ± 3)%. In addition, a third minority phase is observed to precipitate from the C14 Laves phase, forming small Mo-rich precipitates identified by XRD as the brittle intermetallic $AlMo_3$.

In the as-cast condition, Sample F exhibits a three-phase microstructure, Figure 4.3c, consistent with the XRD pattern in Figure 4.13, which fits well to BCC or B2, C14 Laves, and an $AlCr_2$ phase. As with Alloy E, the available evidence does not allow a definitive distinction between BCC and B2, although the EDS maps clearly identify the C14 Laves

phase as $Ti(Cr,Al)_2$. Following homogenisation, Figure 4.6c, the same three phases are retained, and the measured area fractions remain unchanged. The most notable effect of heat treatment is a reduction in elemental segregation, with each phase exhibiting sharper compositional partitioning. For example, the Cr-rich phase shows increased Cr enrichment and correspondingly lower concentrations of Ti, Fe, and Ni.

Samples G–I were selected as the hardest alloys predicted by the ML models to form a single-phase FCC microstructure, with CALPHAD calculations also indicating the presence of a secondary C14 Laves phase. Alloys with a predicted secondary C14 Laves phase were prioritised for their potential suitability for carbon reinforcement strategies, discussed in Chapter 6, aimed at suppressing secondary intermetallic phase formation while enhancing mechanical properties. Although Laves phases can offer high strength, their inherent brittleness severely limits practical application. Consequently, they are often combined with more ductile phases to improve toughness [291]. As anticipated, all three alloys exhibited both an FCC phase and a C14 Laves phase in the as-cast condition. Laves phases typically occur in three polytypes: cubic C15, and hexagonal C14 and C36, which often share very similar compositions. The C14 polytype generally adopts an $A(B,C)_2$ composition, whereas C36 follows a $(A,B)C_2$ composition [292]. These similarities make it impossible to distinguish the different polytypes using EDS alone, as similar elemental enrichments are likely to be detected. While XRD can, in theory, differentiate between these structures, determining the precise crystallographic nature is challenging in practice, particularly when multiple Laves phases coexist with similar diffraction signatures [291]. Previous studies have attempted to predict Laves phases formation using the same atomic size, electronegativity and VEC features utilised in this study [291–293]. However, transitions between the three polytypes can occur, highly dependent on temperature and composition, as well as being stress induced [294]. The stability of the different Laves structures depends heavily on which elements are present within the alloy, with deviation from the stoichiometry and different alloying elements influencing the stability of the different polytypes [293]. For all Alloys G–I, area phase fractions remain largely unchanged after heat treatment, with a slight decrease in FCC content accompanied by a corresponding increase in C14 Laves phase.

From the EDS maps taken for Sample G, a two phase microstructure is observed in both the as-cast and homogenised case, shown in Figures 4.4a and 4.7a respectively. Following the homogenisation regime, the eutectic microstructure of the C14 Laves within the FCC matrix has disappeared and the large Hf-rich precipitates have been broken up into much smaller precipitates. In contrast, the XRD pattern for Sample G, Figure 4.14, indicates a dual-phase microstructure comprising FCC and C14 Laves phases in the as-cast condition, with the emergence of a C36 Laves phase following homogenisation. This suggests a partial transformation from the C14 to C36 structure during heat treatment, although insufficient time at temperature may have prevented the transformation from reaching completion. As discussed earlier, the C14 and C36 Laves phases share similar hexagonal structures and chemical compositions, leading to overlap in the EDS maps. However, they can be readily distinguished by XRD due to differences in their diffraction patterns. Notably, an unidentified peak appears at approximately 47 ° in the as-cast XRD pattern. One possible explanation is an orientation relationship between the FCC (111) plane and the C14 Laves phase, which may enhance diffraction intensity at this position. Alternatively, this peak could correspond to the presence of a minor amount of the C36 Laves phase, which becomes more prominent after homogenisation. Nevertheless, a definitive conclusion cannot be drawn based on a single unidentified peak. In the EDS maps of Sample G, the C14 Laves phase appears in a Hf- and Co- rich region. Thus, it would be anticipated that a HfCo based Laves phase would form, the most common of which is Co_2Hf, stoichiometrically a cubic C15 Laves phase. This C15 polytype is reported in the majority of literature [295, 296], except in the case of a single theoretical simulation suggesting C14 formation [297], and in the case of Wang *et al.* [293], where it was found to stabilise a C36 hexagonal structure within a Co-based superalloy. In this case, the XRD fit in Figure 4.14 clearly shows the presence of a C14 Laves structure and an additional C36 Laves structure following the homogenisation regime. Within the system of Alloy G, FeCoCrMnHf, a range of potential binary and ternary Laves phases exist [298]. The substitution of Fe, Mn, and Cr onto the Co sublattice produces a phase that deviates from pure Co_2Hf, initially stabilising the C14 Laves structure before transitioning to the C36 polytype during homogenisation as elemental segregation advances. CALPHAD analysis was performed to determine individual phase compositions, but due to the complex nature of the different Laves polytypes and their transformations, no conclusive results as to the phase composition could be ascertained.

The microstructure for Sample H remains unchanged across the as-cast and homogenised conditions, as evidenced by Figures 4.4b and 4.7b. Despite this consistency in the EDS maps, the XRD pattern in Figure 4.15 reveals a similar phase evolution to that observed in Alloy G. In the as-cast condition, a good fit for a dual-phase FCC and C14 Laves microstructure is obtained, while in the homogenised condition, the emergence of a C36 Laves phase is detected in the XRD pattern. Based on the similarity of the XRD patterns across the two conditions, it is possible that the C36 Laves phase is also present in the as-cast state, but in a volume fraction too low to be detected or resolved in the refinement. As with the previous discussion of Sample G, these C14 and C36 Laves phases both have hexagonal structures and the same composition, thus overlap within the EDS maps, but are clearly differentiated within the analysis of the XRD pattern.

Finally, Sample I again follows the same trend as Samples G and H. A dual-phase FCC and C14 Laves microstructure is observed in the EDS map in Figure 4.4c, with the C14 Laves phase again corresponding to the lighter region rich in both Hf and Nb. This is verified by the XRD analysis in Figure 4.16, showing a good fit for a dual phase FCC and C14 Laves structure. However, instead of the C36 Laves phase forming following subsequent heat treatment, in this case a μ phase is observed in the XRD fit. This phase is not visible on the EDS map in Figure 4.7c, but must form from the $Nb(Fe,Co)_2$ based C14 Laves phase, which have demonstrated precipitation of a Nb-rich μ phase upon cooling from elevated temperatures [299, 300].

Table 5.1: Phase area fractions determined by ImageJ analysis of multiple wide-area BSE-SEM micrographs for the nine alloy compositions in the as-cast condition.

Sample Index	Primary Phase	Area Fraction (%)	Secondary Phase	Area Fraction (%)	Ternary Phase	Area Fraction (%)
A	FCC	66 ± 1	$HfNi_5$	34 ± 1	-	-
B	FCC	54 ± 2	η	46 ± 2	-	-
C	FCC	46 ± 2	η	34 ± 2	C14 Laves	20 ± 2
D	FCC	43 ± 1	B2	38 ± 1	C14 Laves	18 ± 1
E	BCC/B2	65 ± 2	C14 Laves	35 ± 1	-	-
F	BCC/B2	67 ± 4	C14 Laves	19 ± 3	$AlCr_2$	14 ± 1
G	C14 Laves	54 ± 2	FCC	46 ± 2	-	-
H	FCC	56 ± 2	C14 Laves	44 ± 1	-	-
I	C14 Laves	69 ± 1	FCC	31 ± 1	-	-

Table 5.2: Phase area fractions determined by ImageJ analysis of multiple wide-area BSE-SEM micrographs for the nine alloy compositions in the heat-treated condition.

Sample Index	Primary Phase	Area Fraction (%)	Secondary Phase	Area Fraction (%)	Ternary Phase	Area Fraction (%)
A	FCC	60 ± 1	$HfNi_5$	35 ± 1	BCC	5 ± 1
B	FCC	75 ± 1	η	25 ± 1	-	-
***C**	-	-	-	-	-	-
D	B2	77 ± 4	C14 Laves	23 ± 4	-	-
E	BCC/B2	73 ± 3	C14 Laves	24 ± 3	$AlMo_3$	3 ± 1
F	BCC/B2	66 ± 3	C14 Laves	21 ± 3	$AlCr_2$	13 ± 1
G	C14 Laves	60 ± 1	FCC	40 ± 1	-	-
H	FCC	51 ± 1	C14 Laves	49 ± 1	-	-
I	C14 Laves	76 ± 1	FCC	24 ± 1	-	-

*BSE micrographs reveal multiple phases of similar contrast, making them difficult to distinguish and rendering the results unrepresentative of the true phase structure. From the EDS and XRD analysis it is likely that the η phase has decomposed into additional compositionally similar FCC and C14 Laves phases.

5.1.3 Comparison of CALPHAD and Experimental Microstructures

To assist in the alloy downselection process, equilibrium phase fraction calculations at 1000 °C were performed using CALPHAD and the TCNi8 database on the compositions predicted to form single-phase FCC by both G-Phase and M-Phase. To enable effective comparisons between the experimentally fabricated alloys and CALPHAD, a long duration exposure at 1000 °C and subsequent quench would be required. However, CALPHAD predictions of the same alloy systems as a function of temperature still do not correctly identify the microstructure of the alloy compositions, as described in Table 4.2, and in most cases predict more complex intermetallic phases not observed in the microstructure. The observed microstructure, such as the Laves phases in Samples G–I, suggest that the alloys have still yet to reach equilibrium conditions as calculated by CALPHAD.

5.2 Mechanical Property Analysis

Overall, the hardness ML model does not accurately predict the measured values for the experimentally fabricated alloys, although some predictions fall within the margin of error, as shown in Figure 4.17, Chapter 4. On average, the percentage difference between predicted and experimental values is (21 ±13) % for the as-cast condition and (16± 13) % for the heat-treated condition, indicating a consistent deviation in the model's performance. Further scrutiny of Figure 4.17 reveals distinct patterns and systematic errors in the ML hardness predictions across the three categories of downselected alloy systems. The hardness values for Alloys A-–C are found to be systematically overpredicted. In contrast, for Alloys D—F, there is significant underprediction of the hardness compared to the experimentally measured values in both the as-cast and homogenised states. Better agreement with the predictions is obtained for Alloys G–I within the range of errors, although discrepancies persist. The relative overprediction of the hardness for Alloys A-–C is less pronounced when compared to the underprediction for Alloys D-–F. Importantly, the hardness model did accurately capture the correct trends, with the alloys experimentally determined to display an FCC matrix phase and a secondary intermetallic phase predicted to be a lower hardness than those observed to form BCC and B2 intermetallic-based microstructures.

5.2.1 Micro-Indentation Hardness Measurement Analysis

The discrepancies in prediction of the hardness values from the ML regression G-Hard compared to the measured values, are believed to be in part due to the experimental HEA mechanical properties dataset used to train the model [210]. The dataset contains only 366 data points, including 95 values calculated through an empirical relationship with yield strength, Equation 1.24, and 28 imputed values. The distribution of all the hardness data utilised within the training of the ML model, is shown in Figure 5.3. Of the entries in the dataset, there are significantly more BCC-forming compositions than FCC, constituting 30.3 % and 18.0 % of the dataset respectively. This disparity between the different phases representation in the dataset is highlighted in Figure 5.1.

Of the 66 FCC-labelled compositions, 20 do not include a value for hardness, and of these, 8 also do not include a yield strength value. Furthermore, the empirical relationship in Equation 1.24, used to convert yield strength to hardness, is more applicable to BCC-structured alloys than to those with an FCC structure [98]. Consequently, the "FCC" phase has the highest number of imputed values, followed by the "FCC + Im" phase with 6 imputed entries, out of the 28 total imputed hardness values across the entirety of the dataset. This imputation of the average value of hardness, 442 HV, for missing entries is clearly evidenced by the cluster of points along the median line shown on Figure 5.3, as following the imputation process the mean and median of the dataset are equal. The minimum hardness value is 49 HV, the maximum is 919 HV and the upper and lower quartiles are 320 HV and 557 HV respectively. While ML algorithms have the capability for extrapolation as well as interpolation, the maximum hardness predicted for any HEA composition would not be expected to significantly exceed the maximum value of 919 HV.

Further analysis of the 66 FCC-labelled compositions, following data cleaning, revealed a hardness distribution with a mean of 237 HV, a median of 189 HV, a lower quartile of 132 HV, and an upper quartile of 295 HV. This distribution is visualised in Figure 5.4.

The highest value of hardness for a single-phase FCC composition was 537 HV and of the 66 FCC-labelled compositions, only 15 were found to be quoted as having a hardness of $\geq$ 400 HV. Additionally, there is an absence of data in the region $320 < \text{HV} < 420$. However, the key trend identified in the FCC-labelled compositions hardness distribution is the cluster of 8 points at exactly 442 HV, the imputed average value. As stated, there

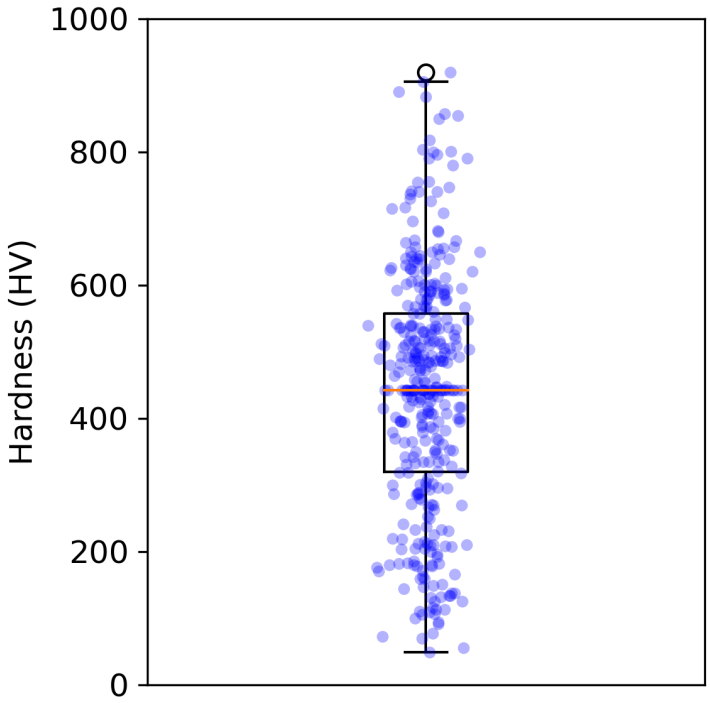


Figure 5.3: Box plot with overlaid scatter points showing the distribution of hardness data used to train the ML model. Scatter points are horizontally jittered along the x-axis to visualise the relative spread at specific hardness values.

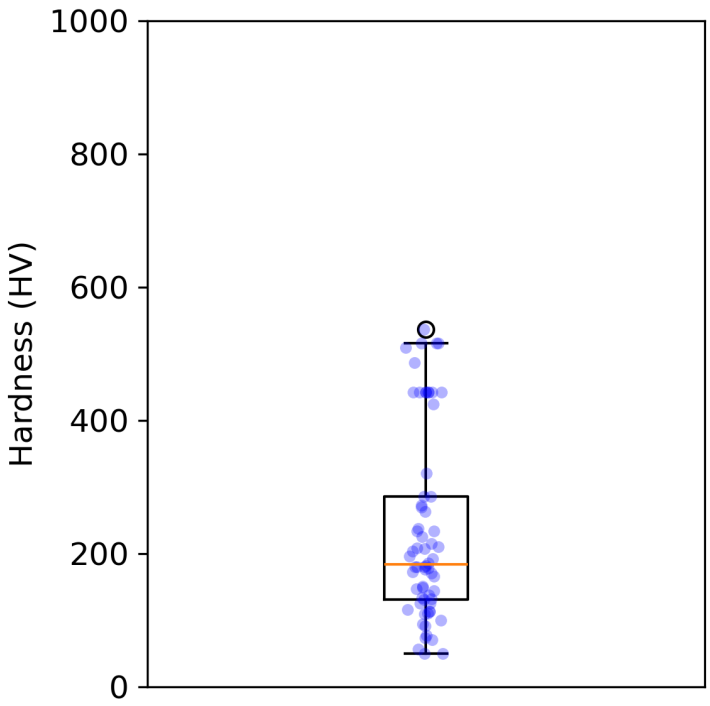


Figure 5.4: Box plot with overlaid scatter points showing the distribution of hardness data for compositions with single-phase FCC formation used to train the ML model. Scatter points are horizontally jittered along the x-axis to visualise the relative spread at specific hardness values.

are only 15 FCC compositions with hardness $\geq$ 400 HV, with more than half of these corresponding to imputed values as no data was present within the dataset. Interestingly, the other 7 values for FCC-labelled compositions exceeding 400 HV were taken as the hardness directly from the dataset and were not calculated using the empirical relation in Equation 1.24. This could potentially indicate that the compositions with higher hardness were mislabelled as single-phase FCC in their respective publications and may have instead exhibited the formation of secondary or intermetallic phases. The overprediction observed for Alloys A-–C is in contrast to the experimentally observed microstructure of the alloy. It would be expected that as the model predicts single-phase FCC formation, the presence of secondary intermetallics, seen in the BSE micrographs in Figures 4.2 and 4.5, would lead to an increase in alloy hardness over the predictions. Instead, the opposite trend is observed. This is further reinforced by the hardness measurements of Samples G–I which form a FCC and C14 Laves microstructure with hardness values in the range of 400–600 HV and most closely correspond to the ML predictions.

The disparity between the ML hardness and measured hardness for alloys D-–F occurs because these alloys have been downselected as they were predicted to be the highest hardness alloys to form a single-phase FCC solid solution. As highlighted by the permutation feature importance plots in Figure 3.3 and the SHAP summary plots in Figure 3.4, all models place a very high importance on VEC and both G-Hard and M-Phase place very high importance on the Young's modulus asymmetry ($\Delta\mathcal{E}$). It is expected that $\Delta\mathcal{E}$ would be related to alloy hardness and indeed the SHAP summary plots show that larger values of $\Delta\mathcal{E}$ lead to the model predicting higher values of hardness. Similarly, in M-Phase, smaller values of $\Delta\mathcal{E}$ are less likely to predict FCC phase formation. Furthermore, larger values of VEC are shown to be more likely to predict FCC phase formation and a lower alloy hardness. Thus, despite the classification and regression models not being coupled, the model interpretation metrics discussed in Chapter 3, reveal that similar emphasis is placed on input features across all models. Therefore, it would be expected that if the classification ML model predicts a single-phase FCC solid solution, then the parallel regression ML model would also predict a lower hardness. This lends credence to the future application of a nested model where phase predictions are used as an input to predict alloy hardness. Consequently, as the alloys are not in fact single-phase FCC solid solutions and are in some cases not based on an FCC matrix at all, it would be expected

that they would display a significantly higher hardness than that predicted by the ML model. The maximum single-phase FCC hardness recorded in the training dataset was 537 HV. Thus, the ML model would not be expected to extrapolate much beyond this maximum value and certainly would not predict hardness values in excess of 650 HV, such as those exhibited experimentally for alloys D-–F.

5.2.2 As-Cast vs. Homogenised Material

Despite the pronounced microstructural evolution observed from the as-cast to homogenised states, the hardness values for most alloys remain comparable within the bounds of measurement error. A notable exception is Alloy B, where the spherodisation of the Ni_3Ti-based η phase significantly increases hardness following homogenisation. However, the overall variation in hardness between the as-cast and homogenised conditions was not substantial enough to justify further investigation, particularly given the measurement uncertainties. This consistency is reassuring, as the dataset used does not account for manufacturing methods or post-manufacturing processing in its hardness values.

5.2.3 Optical Analysis of Micro-Indentations

By optically inspecting the hardness indentations, qualitative inferences about the samples ductility and damage tolerance or response to deformation can be made. As expected from the calculations of hardness using Equation 2.2, smaller indents indicate a harder material. Optical microscopy images in Figure 4.18 (Chapter 4) show representative indents made in the as-cast material. These reveal that the majority of samples exhibited some form of cracking or plastic deformation. This cracking arises from material inhomogeneity and the brittle nature of certain phases, which possess limited ductility and a reduced ability to accommodate plastic deformation. Radial or Palmqvist cracks originating either from the corners of the indentations, or distortion of the sample surface through shear bands caused by plastic deformation are observed following the hardness indentations. In the as-cast condition, Sample D is the only sample that does not display any form of cracking or visible slip bands. Sample B displays no cracking, instead forming slip bands on the sample surface as the material deforms plastically upon the indentation load. In contrast to the behaviour seen in other samples, Alloys E–I all display radial cracks originating from the corners of the indentations, indicative of brittle behaviour and low fracture toughness.

Meanwhile, Alloys A, C, H, and I exhibit smaller cracks that initiate at the edges of the indentations or in the surrounding material, rather than from the corners. In Samples C, H, and I, the cracks follow but do not cross the phase boundaries. This suggests that one of the phases is significantly tougher than the other, or that there is a substantial degree of crystallographic mismatch between the two. As a result, the crack is deflected along the boundary, unable to propagate into the adjacent phase. From the composition of Alloy C, it is difficult to ascertain the exact phase through which the cracks propagate. In Sample H, cracks propagate through the Laves phase before continuing along the interface with the FCC phase. Alternatively, in Sample I, the cracks propagate through the Laves phase but arrest at the interface without continuing along it, unlike the behaviour observed in Sample H.

The indentations made in the homogenised material are shown in Figure 4.19. As in the as-cast case, Sample D is the only one not to display any form of cracking or plastic deformation. Notably, it also recorded the highest hardness value of all samples by a substantial margin, indicating a unique combination of strength and resistance to damage. In the majority of cases, the radial cracking from the corners of the indentations in the homogenised samples is more extreme, despite the load and dwell time of the indentation remaining the same. This indicates that the precipitation of additional intermetallic phases, such as C36 Laves and μ in Samples G–I, has contributed to increased brittleness. Furthermore, the slip bands resulting from plastic deformation in Sample B are more pronounced, believed to be due to the complete change in microstructure from a skeletal η phase, to a more particulate η phase. As with the as-cast case, the cracking originating from the edges of the indentations and material surrounding the indents in alloys C, H, and I do not cross the phase boundaries, instead being deflected and following the phase boundary until the crack arrests.

5.3 Summary

The primary goal of this research was to apply ML methodologies to accelerate the design of HEA hardmetal matrix compositions tailored for metal-forming tooling applications. This objective was distilled into two key design criteria: achieving high hardness and ensuring a single-phase FCC microstructure, which serve as a proxy for wear resistance, and ductility and toughness respectively. To this end, a series of RF ML models were developed and trained using experimentally determined public datasets on HEA phase formation and hardness. The models were used to predict the target properties across the vast HEA compositional space. Unlike most studies in the literature, this work did not rely on CALPHAD to supplement data or provide features for direct input to the ML models. Instead, CALPHAD was employed post-ML analysis to perform further microstructural investigations and aid in the downselection of promising alloy compositions for experimental validation.

Nine compositions were selected for fabrication and subjected to microstructural and mechanical property evaluations to assess their alignment with the design criteria and the predictive accuracy of the ML models. These compositions included three unique alloy systems predicted by the ML to exhibit the highest hardness with a single-phase FCC structure irrespective of CALPHAD phase prediction, three systems predicted by both the ML and CALPHAD to form the hardest single-phase FCC microstructures, and three systems predicted by the ML to form the hardest single-phase FCC microstructures, with CALPHAD identifying an additional secondary C14 Laves phase.

The experimental validation of the ML and CALPHAD predictions revealed important insights and challenges. None of the alloys fabricated produced a single-phase FCC microstructure as predicted by the ML models in either the as-cast or homogenised state. The three hardest FCC alloys predicted, irrespective of CALPHAD phase formation results, were found to primarily form BCC and B2 phases. In contrast, those predicted as the hardest FCC alloys by both ML and CALPHAD successfully developed a primary FCC solid solution phase, but also displayed additional undesirable intermetallic phases. The alloys predicted by ML to form FCC with secondary C14 Laves phases, as indicated by CALPHAD, exhibited this microstructure upon fabrication. However, after heat treatment, further evolution was observed with the emergence of C36 and μ phases.

Overall, the accuracy of alloy hardness predictions was limited, though some agreement was observed within the margin of error. The average percentage difference between predicted and experimental hardness values was (21 ± 13) % for as-cast measurements and (16 ± 13) % for heat-treated measurements, indicating a consistent deviation in the ML model predictions.

Issues with ML phase predictions are directly linked to the insufficient quantity of data and the limited availability and integration of manufacturing and processing conditions into the model. These factors play a critical role in microstructural formation and evolution, as evidenced by the formation of additional C36 Laves and μ phases in Samples G–I after homogenisation. The observed phase formation discrepancies between experimental results and ML predictions were not entirely unexpected, as regions of low-confidence FCC phase predictions were intentionally explored to prioritise alloy hardness. This approach enabled investigations beyond traditional FCC forming HEA compositional spaces, where the models demonstrated significantly higher confidence, but hardness was much lower. Hardness prediction inaccuracies also arose from the limited data and were further exacerbated by the reliance on empirical calculations and imputed values, with imputed FCC hardness values disproportionately influencing the predictions. These findings highlight the importance of expanding datasets to improve ML model accuracy while demonstrating the potential of ML to accelerate, innovate and drive the alloy design process, particularly within the HEA space.

Despite the limitations in ML phase prediction accuracy, the combination of ML with CALPHAD in this study has successfully accelerated the alloy design process. Compared to alternative approaches, such as exhaustive CALPHAD screening, DFT-based simulations, or parametric mapping using empirical descriptors, this hybrid strategy offers significant efficiency gains. CALPHAD alone, while providing more in depth thermodynamic insights, is too time consuming to apply exhaustively across the vast HEA compositional space. First principles methods like DFT offer high fidelity insights into phase stability and electronic structure, but are computationally prohibitive for high-throughput exploration. Similarly, empirical parametric plots (e.g., based on δ, ΔH_{mix}, or VEC) offer qualitative guidance, but lack the predictive power and scalability of ML models. In contrast, the combined ML and CALPHAD approach enables rapid screening of thousands of compositions to identify a downselected subset for thermodynamic vali-

dation and experimental synthesis. The resulting alloys display complex and potentially application-relevant microstructures, underscoring the value of integrating data driven models with established thermodynamic tools to streamline alloy discovery.

In the following chapter, these compositions will be further explored through carbon reinforcement to enhance mechanical properties and refine microstructures. The addition of carbon is intended to promote favourable phases while leveraging the unique characteristics identified by the combined ML and CALPHAD approach. This strategy brings the development of optimised HEAs for metal-forming tooling applications a step closer.

Chapter 6

Carbon Reinforcement and Laser Passes

The reinforcement of FCC HEAs by the addition of interstitial elements, presents an opportunity to maintain the high ductility provided by the base FCC crystal structure, while enhancing the mechanical properties of the alloys [52, 301, 302]. Precipitation strengthening by a reinforcing MC carbide phase formed *in situ*, i.e. simultaneously with the matrix phase [303], is an effective method to strengthen HEAs at both low and high temperatures [304]. This strategy is particularly advantageous for AM processes, where *in situ* phase formation can enhance mechanical properties during rapid solidification and repeated thermal cycling. Increases in both yield strength and ductility have been observed with increasing carbon content in studies performed on the CrMnFeCoNi-C alloy due of the effect of precipitation hardening [301]. In addition, it has been demonstrated that carbon addition can be helpful in reducing the formation of solidification defects and oxide inclusions [305]. Importantly, carbon reinforcement can suppress the formation of intermetallic phases, such as Laves phases, in HEAs [305], by depleting the alloy matrix of intermetallic-forming elements through their incorporation into MC carbides [306]. There are three types of Laves phases: hexagonal C14, cubic C15 and hexagonal C36 [52]. Of these, the C14 Laves phase is the most frequently formed intermetallic phase in HEAs [307, 308]. The C14 Laves phase has a hexagonal crystal structure, with very high hardness and wear resistance, but limited ductility [309]. Hence, as displayed in Chapter 5,

formation of the hard but brittle C14 Laves phase increases the hardness and strength of the material, but reduces the toughness [302, 306]. Therefore, it is desirable to replace the hard, but brittle Laves phase with suitable reinforcing phases to maintain the high hardness while improving toughness [306]. Heat treatment at temperatures exceeding the dissolution point of the Laves phase can reduce its volume fraction within the alloy. However, as demonstrated in Chapter 4, extended exposure to elevated temperatures may also promote the formation of additional Laves phases through solid-state transformations. As previously noted, the introduction of carbon can suppress Laves phase formation [308]. Elements such as Ti and Nb are known to promote Laves phase formation in HEAs [306, 310], but they also play a critical role in forming MC-type carbides. The formation of these carbides consumes a significant portion of Ti and Nb, reducing their availability for Laves phase formation and thereby limiting elemental segregation in the bulk. This suppression of the Laves phase may enhance ductility [305, 306]. While a lower Laves phase fraction reduces obstacles to dislocation motion, potentially decreasing the alloy's yield strength [310], the presence of MC carbides can provide additional strengthening by impeding dislocation motion, partially offsetting the strength loss caused by Laves phase suppression [306]. The formation of MC carbides occurs in the melt, consuming key elements and thereby reducing interdendritic segregation, which suppresses the formation of Laves phases [305]. Compared to Laves phases, MC carbides are more effective at enhancing wear resistance, making them particularly critical for tooling applications where durability and surface performance are essential. Accordingly, the use of *in situ* carbon reinforcement presents an opportunity to investigate HEAs that would normally form undesirable intermetallic Laves phases, while simultaneously improving mechanical performance for tooling applications. *In situ* MC carbide formation, such as TiC, has been shown to produce a better interface with the alloy matrix in comparison to *ex situ* formation of TiC in the same HEA. This enhanced interface is beneficial to the wear performance of the HEA as it minimises the risk of detachment of the MC carbide from the matrix [306]. Therefore, to investigate the simultaneous mitigation of Laves phase formation and mechanical property enhancement of carbon reinforcement within HEAs, Samples G–I, as discussed in Chapter 4 were chosen to be re-fabricated with carbon reinforcement. Additionally, Sample B was also selected for carbon reinforcement testing as it was hypothesised that the Ni_3Ti-based η phase could also be mitigated by the addition of carbon due to the extraction of Ti from the matrix.

6.1 Thermodynamic Analysis of Carbon Additions to High Entropy Alloys

Before fabrication of the carbon reinforced samples, thermodynamic analysis was conducted utilising CALPHAD. This provides insights into the potential phase formation and phase fractions of the alloys following the addition of carbon. It can also provide an estimate of the required carbon content needed for each alloy to suppress the formation of secondary phases outside of the FCC matrix and MC carbide phase. Two approaches to carbon addition were thermodynamically investigated: replacing solely the balance element with carbon and replacing all elements equally, preserving the composition's original elemental proportions. Based on the analysis, the latter approach, distributing carbon equally while preserving the original elemental fractions, was determined to be the most effective. Furthermore, the quantity of carbon additions were informed by domain knowledge, considering which elements in the alloy compositions are most likely to form carbide phases and the respective stoichiometric ratios associated with these phases [311]. This accounts for the tendency of specific elements in the alloy, such as Ti and Hf, to preferentially bond with the carbon additions to form MC carbides and the lack of interaction with the "balance" elements such as Fe and Ni, in these HEAs. This maintains the compositional ratios of the original HEA following the carbon reinforcement, such that the FCC matrix microstructure is retained and suppression of the secondary intermetallic phases is achieved. Phase diagrams illustrating the evolution of phase composition with increasing carbon content were calculated using the CALPHAD method in Thermo-Calc with the SSOL8 thermodynamic database. These calculations were based on the experimentally measured compositions of the non-carbon-reinforced alloys listed in Table 6.1 and are presented in Figure 6.1.

Carbon additions of 10 at.%, 7.5 at.%, 10 at.% and 12 at.% for alloy compositions B and G–I respectively were deemed appropriate following the thermodynamic calculations. In all cases, the thermodynamic analysis shows a reduction in secondary intermetallic phase formation as a secondary FCC-based mono-carbide phase forms. With further increases in carbon content, this is followed by the formation of more complex carbide phases such as M_7C_3, as well as cementite, or graphite. Further thermodynamic analysis was conducted at 1000 °C to assess the individual phase formation and composition of

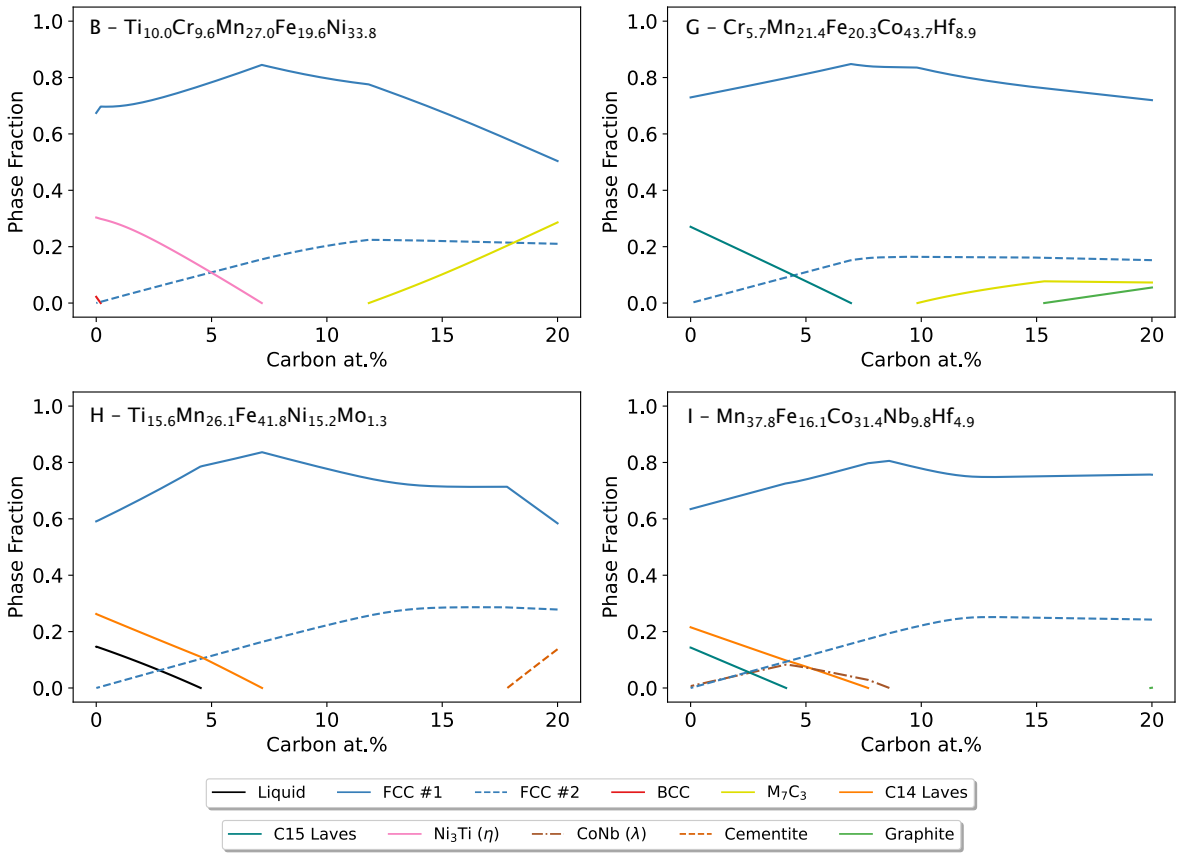


Figure 6.1: Phase diagram plots of the four alloys selected for carbon reinforcement, generated through CALPHAD using Thermo-Calc and the SSOL8 database. The compositions input into Thermo-Calc correspond to the experimentally determined values from the large-area EDS scans provided in Table 4.1. In these plots, FCC #2 represents the FCC-structured MC carbide phase.

the phases. Table 6.1 presents the results of the thermodynamic analysis, highlighting the appropriate carbon additions and the resulting phase fractions. Following carbon addition, the η phase in Sample B is suppressed and a secondary FCC-based MC carbide phase forms. The primary FCC phase, comprising 79.7 % of the material, is primarily composed of Ni, Mn, and Fe, while the secondary MC carbide phase accounts for the remaining 20.3 % and consists mainly of Ti and carbon. Cr is predicted to be dispersed in both phases, substitutionaly occupying the same sublattice as NiMnFe and the Ti atoms of the carbide phase respectively. Thermodynamic analysis of Sample G, shows suppression of Laves phase formation with a secondary FCC-based carbide phase forming. With a 7.5 at.% carbon addition, CALPHAD predicts that 84.2 % of the alloy microstructure consists of a primary FCC phase composed of Co, Mn, Fe, and Cr, while the remaining 15.8 % forms a secondary HfC-type FCC carbide phase. In Sample H, increasing the carbon content to 10 at.% results in a dual FCC phase microstructure. The primary

phase, comprising 77.9 % of the microstructure, is rich in Fe, Mn, and Ni. The secondary phase, accounting for 22.1 %, is an FCC carbide consisting mainly of Ti and carbon, with a minor substitution of Mo on the Ti sublattice. Finally, in Sample I, a carbon addition of 12 at.% is sufficient to suppress the formation of other intermetallic phases, again resulting in a dual FCC phase structure. The primary FCC phase, composed of Mn, Co, and Fe, constitutes 75.1 % of the microstructure, while the secondary FCC-based carbide phase (24.9 %) contains Nb and Hf substituting on the same sublattice, with a Nb:Hf ratio of approximately 2:1, consistent with the overall alloy composition.

Table 6.1: Comparison of non-carbon-reinforced HEA compositions with nominally proposed carbon-reinforced variants, based on CALPHAD assessments. The associated phase fractions of the matrix FCC phase and MC carbide precipitate phases, as predicted by CALPHAD, are also presented.

Sample Index	**Non-Carbon-Reinforced Alloy Composition**	**Nominal Carbon Reinforced Alloy Composition**	**CALPHAD FCC Phase Fraction (%)**	**CALPHAD MC Phase Fraction (%)**
B	$Ti_{10.0}Cr_{9.6}Mn_{27.0}Fe_{19.6}Ni_{33.8}$	$Ti_{9.0}Cr_{8.7}Mn_{24.2}Fe_{17.7}Ni_{30.4}C_{10.0}$	79.7	20.3
G	$Cr_{5.7}Mn_{21.4}Fe_{20.3}Co_{43.7}Hf_{8.9}$	$Cr_{5.3}Mn_{19.8}Fe_{18.7}Co_{40.4}Hf_{8.3}C_{7.5}$	84.2	15.8
H	$Ti_{15.6}Mn_{26.1}Fe_{41.8}Ni_{15.2}Mo_{1.3}$	$Ti_{14.0}Mn_{20.5}Fe_{38.7}Ni_{14.5}Mo_{2.3}C_{10}$	77.9	22.1
I	$Mn_{37.8}Fe_{16.1}Co_{31.4}Nb_{9.8}Hf_{4.9}$	$Mn_{33.2}Fe_{14.2}Co_{27.6}Nb_{8.7}Hf_{4.3}C_{12.0}$	75.1	24.9

The formation of these secondary FCC-based MC phases is expected to enhance the ductility of the alloys by suppressing the more brittle intermetallic phases present prior to carbon addition. At the same time, these carbides can also improve mechanical properties such as hardness and wear resistance. These proposed carbon additions are substantial in contrast to other metallic alloys, such as high carbon steels which typically contain only up to 1 at.% of carbon. However, this carbon content is relatively low by comparison to compounds such as WC cermets and HECs, which typically contain around 50 at.% carbon.

6.2 Carbon Reinforcement

The carbon reinforced samples were fabricated using the same arc melting methodology as the standard HEA samples outlined in Section 2.1.1. Mn was present in all the alloys chosen to be re-fabricated with carbon additions and the issue of Mn evaporation that was present in the initial alloy fabrication was exacerbated here by the presence of carbon. Due to its exceptionally high melting point of 3600 °C, carbon does not melt during the arc melting process and must instead dissolve into the molten charge. To facilitate this, 99.9 % pure graphite was ground into a fine powder prior to addition, increasing its surface area and promoting dissolution during melting. Initial attempts to manufacture the alloys via arc melting were unsuccessful, as the carbon did not adequately dissolve homogeneously into the melt. To address this, a two-step master alloy approach was adopted. First, a master alloy ingot was created by arc melting all elements except Mn and carbon, ensuring thorough mixing and homogenisation. This master ingot was then remelted with Mn plate and graphite powder added directly to the crucible. The simultaneous addition of Mn and carbon was intended to improve carbon dissolution and reduce manganese loss. By introducing them together, carbon could dissolve more effectively into the melt, potentially aided by early interaction with molten Mn, while also limiting the extent of Mn evaporation. This approach enabled more controlled incorporation of both Mn and carbon into the final alloy composition. Carbon was added in the form of graphite powder to aid dissolution into the molten Mn. While fine graphite powder can disperse within the arc melting chamber due to the high-energy environment, potentially affecting compositional control, this risk was mitigated by careful powder handling and placement within the crucible prior to melting. Furthermore, ICP-OES analysis was performed on the final alloys to verify that the target compositions had been achieved and to ensure successful carbon incorporation. As in the standard methodology, the alloy was repeatedly remelted an additional three times to try to attain alloy homogeneity. This reduced number of remelts compared to the original methodology for the non-carbide samples is due to the substantial amount of Mn evaporation during the casting of the second melting stage, where the master alloy is melted in combination with Mn and carbon powder. The evaporation resulted in a significant layer of soot obscuring the view-port and making remelting almost impossible.

6.3 Chemical Composition Analysis

Due to the high carbon content of these alloys, accurate compositional analysis by EDS was not possible. Thus, ICP-OES was used to determine the manufactured alloys compositions, as outlined in Section 2.5. These fabricated compositions, as well as the target nominal alloy compositions are detailed in Table 6.2. For Samples B and G, the experimental compositions closely matched the target nominal compositions. The ratio between carbon and the element in at.% most likely to form the MC carbide, Ti and Hf in Samples B and G respectively, is close to one. In contrast, the experimental compositions of Alloys H and I, exhibit a larger deviation from the target nominal alloy compositions. For Sample H the largest disparity originates in the quantity of Mn and carbon. The percentage differences between the target and manufactured compositions are 56.2 % and 34.7 % for the Mn and carbon respectively. This difference is due to the addition of high melting temperature elements such as Mo to the master alloy. During the secondary melting phase combining the master alloy and Mn_3C, a 6.61 % loss of material due to evaporation was observed. However, mitigating material losses further during this melting process was challenging due to the additions of Mo resulting in a master alloy with higher melting temperature. The observed losses are significantly more than the 20 % of additional Mn added to the system to counteract this evaporation process. Unlike Samples B and G, because of the ratio of both Ti and Mo to carbon, which would be likely to form TiC and Mo_2C, it would be anticipated that not all of the intermetallic Laves phase would be suppressed. Consequently, this results in a microstructure containing an FCC matrix, a secondary intermetallic phase and a third MC carbide phase. Sample I is the alloy system with the greatest disparity between the target nominal composition and the manufactured composition. Due to the large quantity of high melting point refractory elements and Mn in this alloy composition, it was difficult to integrate the master alloy with the Mn and carbon without encountering significant evaporation. This results in a substantially lower Mn and carbon content than expected, and concomitantly higher concentrations of the remaining elements. A material loss of 6.61 % was measured for the melting process of Mn and carbon containing alloy, compared to a 0.38 % material loss during the melting of the master alloy alone. Additionally, during the vacuum arc melting process, significant cracking of this sample was observed, especially during the subsequent cooling. This

cracking was most likely caused by residual brittleness associated with the formation of NbC precipitates, which, while intended to replace more brittle intermetallic phases, may still exhibit limited toughness depending on their morphology and distribution. Therefore, due to the significant limitations to the manufacturability of this sample, further research into this composition was discontinued.

Table 6.2: Comparison of the target nominal carbon reinforced compositions to the experimentally fabricated compositions utilising the master alloy and Mn-C dissolution methodology and measured using ICP-OES chemical analysis techniques. Values provided are in atomic percent.

Sample Index	Nominal Alloy Composition	Experimental Alloy Composition
B	$Ti_{9.0}Cr_{8.7}Mn_{24.2}Fe_{17.7}Ni_{30.4}C_{10.0}$	$Ti_{9.3}Cr_{8.8}Mn_{23.3}Fe_{17.8}Ni_{31.1}C_{9.7}$
G	$Cr_{5.3}Mn_{19.8}Fe_{18.7}Co_{40.4}Hf_{8.3}C_{7.5}$	$Cr_{5.2}Mn_{18.9}Fe_{16.2}Co_{41.3}Hf_{7.1}C_{6.8}$
H	$Ti_{14.0}Mn_{20.5}Fe_{38.7}Ni_{14.5}Mo_{2.3}C_{10}$	$Ti_{18.1}Mn_{11.5}Fe_{38.9}Ni_{14.8}Mo_{2.4}C_{14.2}$
I	$Mn_{33.2}Fe_{14.2}Co_{27.6}Nb_{8.7}Hf_{4.3}C_{12.0}$	$Mn_{21.76}Fe_{19.1}Co_{37.4}Nb_{12.1}Hf_{5.4}C_{4.2}$

6.4 Microstructural Analysis

As with the as-cast and homogenised non-carbon reinforced samples discussed earlier, microstructural analysis of the alloy compositions was conducted by a combination of SEM and EDS analysis to determine the phases present and their relative chemistry. BSE micrographs and EDS maps of the carbon reinforced alloy compositions are presented in Figures 6.2–6.6. Additionally, the area phase fractions of the alloy compositions fabricated in this study, determined through ImageJ analysis of BSE-SEM micrographs, are provided in Table 6.3. Images from two different locations within Sample G are presented due to a difference in microstructure observed within the bulk of the as-cast ingot, indicating a non-homogeneous elemental distribution within the alloy.

Sample B, Figure 6.2, shows a marked change in microstructure compared with the non-carbon-containing alloy presented in Chapter 4. The Ni_3Ti η phase present in both the as-cast and homogenised conditions is entirely replaced by an FCC TiC phase precipitating within the matrix. Area phase fraction analysis confirms that the FCC phase content

increases from 60–66 % to 82 % following carbon reinforcement. EDS maps reveal Ti enrichment within these precipitates, indicating that the carbon addition was sufficient to suppress the secondary intermetallic η phase, as predicted by thermodynamic analysis. Within the FCC matrix, Mn, Fe, and Cr distributions remain somewhat heterogeneous, with certain regions enriched relative to others. However, the BSE micrograph shows no evidence of secondary phase formation within the matrix, suggesting that the observed contrast arises from elemental segregation, which may be reduced through additional heat treatment.

Sample G develops two distinct microstructures within the bulk alloy following carbon addition. In the first, shown in Figure 6.3, a dual-phase structure of an FCC matrix and secondary HfC FCC phase is observed. Area phase fraction analysis shows that in this two-phase carbide region, the C14 Laves phase is completely suppressed, with FCC becoming the primary phase and increasing from 40–46 % to 75 % following carbon reinforcement. This aligns with the thermodynamic predictions in Figure 6.1, where suppression of the (predicted C15 but experimentally observed C14) Laves phase allows formation of a secondary FCC carbide phase by addition of sufficient carbon.

In contrast, the second microstructure, shown in Figure 6.4, also exhibits a eutectic-like structure of FCC matrix and a Cr-, Fe-, and Hf-rich phase. This suggests that not all Hf has been incorporated into the FCC carbide, leaving sufficient Hf to form a residual intermetallic, most likely C14 Laves. ICP-OES analysis supports this interpretation, showing the alloy contains 7.1 at.% Hf and 6.8 at.% C, insufficient to fully stabilise the HfC monocarbide, with thermodynamic modelling predicting 7.5 at.% C would be required to achieve a purely FCC–HfC microstructure. In this three-phase carbide region, area phase fraction analysis indicates that the C14 Laves phase is reduced from 54–60 % to 24 %, with FCC again becoming the primary phase. The proportion of HfC remains similar between the two regions, at around 25 %. Increasing carbon content and/or applying additional heat treatment could therefore eliminate the residual Laves phase and produce the desired FCC–MC microstructure.

The BSE micrograph and EDS maps for Sample H in Figure 6.5 reveal a three-phase microstructure. Area phase fraction analysis shows that carbon reinforcement suppresses the C14 Laves phase from 44–49 % to 15 %, with a corresponding increase in FCC content and the precipitation of a TiC phase. Unlike Samples B and G in Figures 6.2 and 6.3

respectively, where carbide-forming elements are concentrated entirely within the carbide phase, Sample H shows Ti and Mo distributed throughout the microstructure. Regions enriched in these elements correspond to the carbide precipitates, suggesting the formation of a (Ti,Mo)C crystal structure. The remaining elements form a two-phase matrix enveloping the carbides. As with Sample G, this indicates incomplete suppression of intermetallic phases. However, ICP-OES analysis suggests the limitation is not due to a lack of carbon, but rather a deficiency in Mn and an excess of Ti within the composition. The high Mo content significantly raises the melting temperature, promoting Mn evaporation during processing and making it difficult to incorporate the required Mn. With improved manufacturability and composition control, this alloy could potentially achieve the targeted dual FCC–MC microstructure.

As with the previous alloy, Sample I also exhibits a three-phase microstructure; however, unlike every other alloy in this study, carbon reinforcement did not suppress C14 Laves phase formation. Area phase fraction analysis revealed that carbon addition increased the C14 Laves content from 69–76 % to 81 %, reduced the FCC content from 24–31 % to 13 %, and precipitated a small 6 % fraction of HfC. Thermodynamic analysis had predicted the formation of an FCC carbide phase in which Nb and Hf substitute on the same sublattice. However, ICP-OES measurements in Table 6.2, indicate that the carbon content was insufficient to fully form (Hf,Nb)C. Consequently, the excess Hf and Nb were instead available to form an intermetallic phase, identified by XRD in Section 6.5 as the C14 Laves phase. The absence of significant carbide formation in the BSE micrograph supports this, and is likely a consequence of manufacturing challenges posed by the high refractory element content, which caused substantial Mn evaporation and limited carbon incorporation. In this case, the C14 Laves phase forms the primary matrix, $(Mn,Fe,Co)_2Hf$ and $(Mn,Fe,Co)_2Nb$, while the FCC phase appears as a secondary eutectic phase enriched in Fe and Co, as shown in the EDS maps.

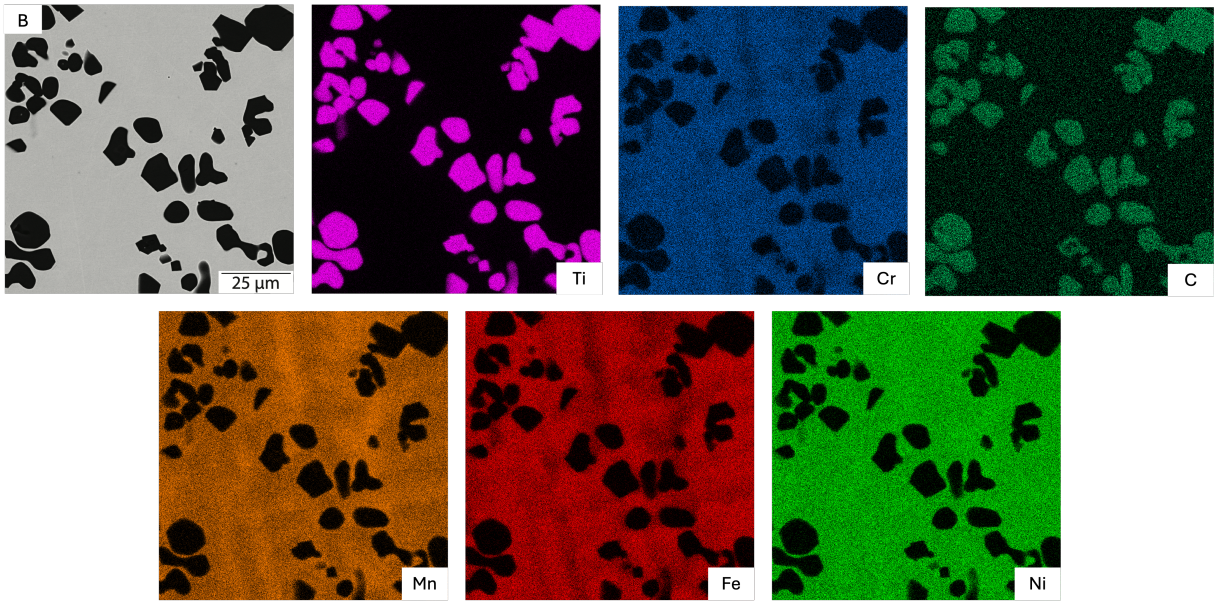


Figure 6.2: BSE image and EDS elemental maps of Sample B ($Ti_{9.3}Cr_{8.8}Mn_{23.3}Fe_{17.8}Ni_{31.1}C_{9.7}$) following alloying with carbon in the as-cast condition.

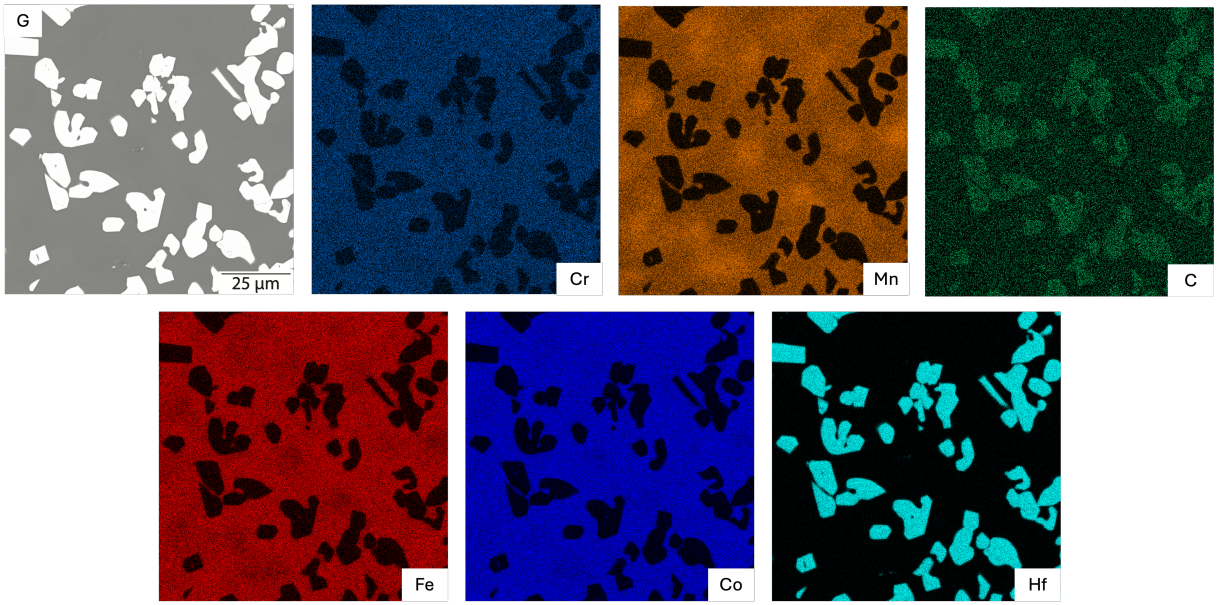


Figure 6.3: BSE image and EDS elemental maps of Sample G ($Cr_{5.2}Mn_{18.9}Fe_{16.2}Co_{41.3}Hf_{7.1}C_{6.8}$) following alloying with carbon in the as-cast condition.

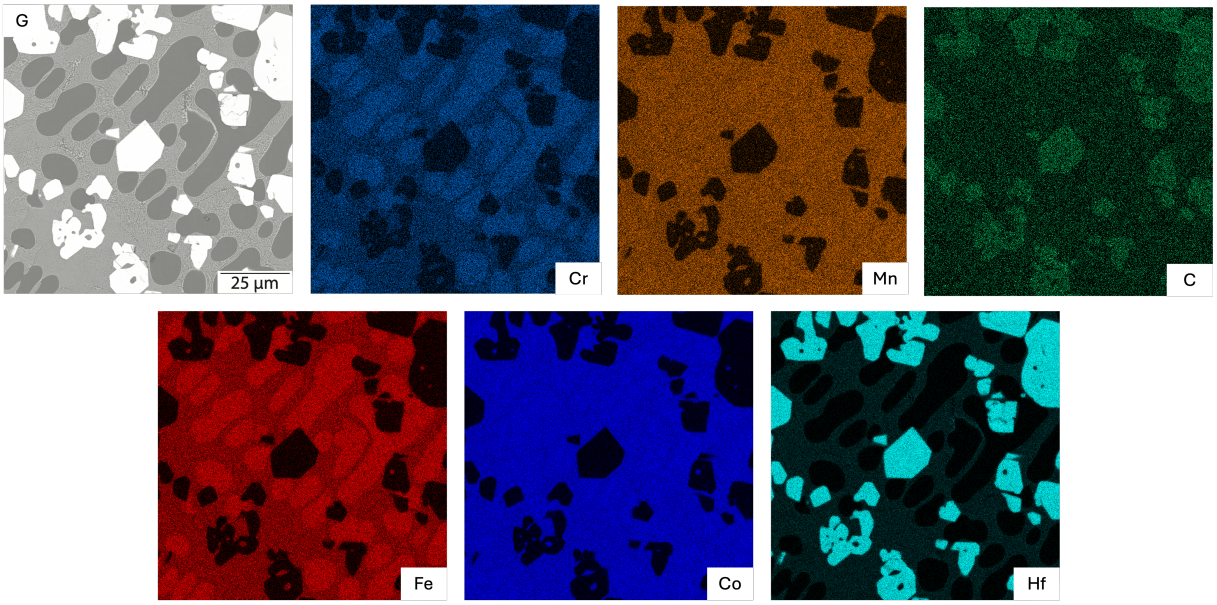


Figure 6.4: BSE image and EDS elemental maps of Sample G ($Cr_{5.2}Mn_{18.9}Fe_{16.2}Co_{41.3}Hf_{7.1}C_{6.8}$) at a secondary location within the bulk of the ingot following alloying with carbon in the as-cast condition.

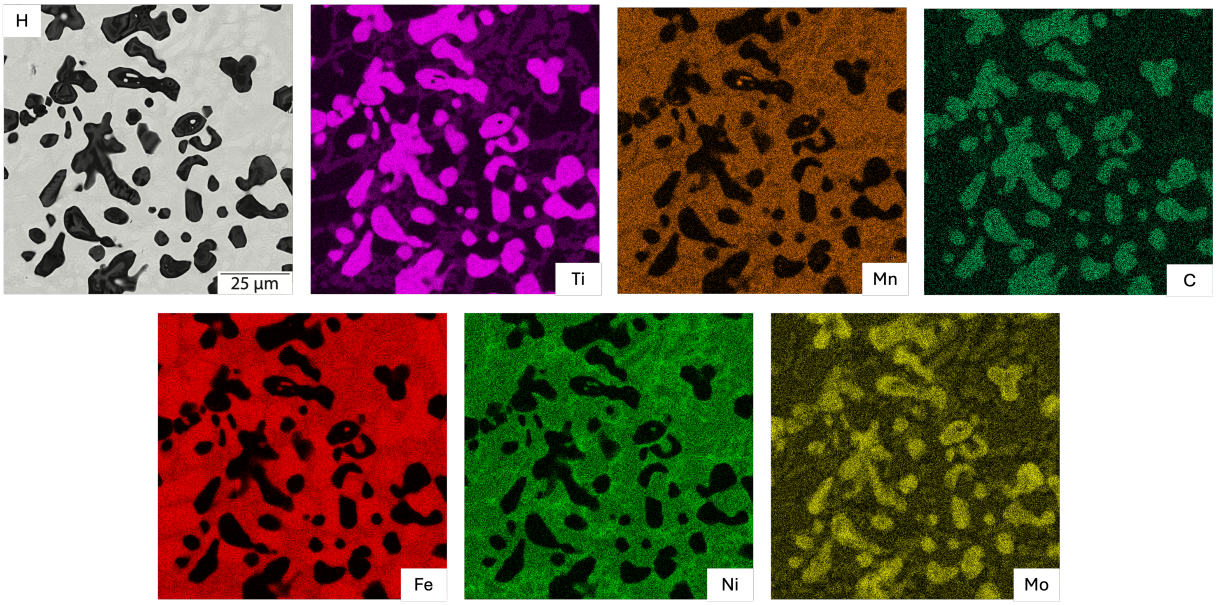


Figure 6.5: BSE image and EDS elemental maps of Sample H ($Ti_{18.1}Mn_{11.5}Fe_{38.9}Ni_{14.8}Mo_{2.4}C_{14.2}$) following alloying with carbon in the as-cast condition.

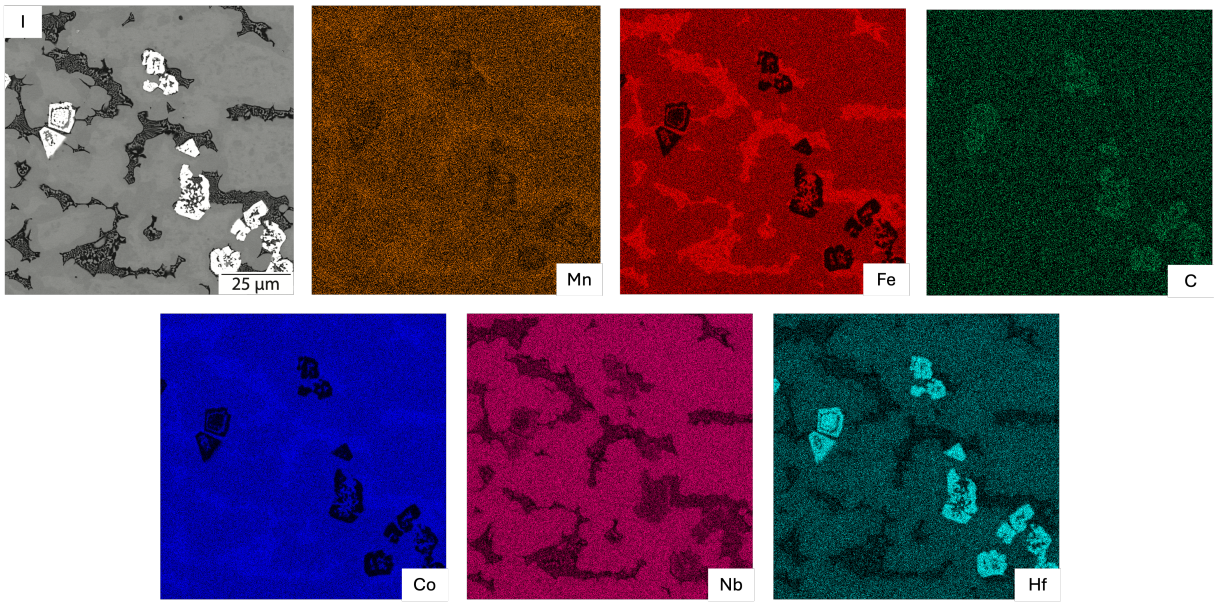


Figure 6.6: BSE image and EDS elemental maps of Sample I ($Mn_{21.76}Fe_{19.1}Co_{37.4}Nb_{12.1}Hf_{5.4}C_{4.2}$) following alloying with carbon in the as-cast condition.

Table 6.3: Phase area fractions determined by ImageJ analysis of multiple wide-area BSE-SEM micrographs for the four alloy compositions after *in situ* carbon reinforcement. Sample G was analysed twice to account for microstructural inhomogeneity.

Sample	**Primary**		**Secondary**		**Ternary**	
Index	**Phase**	**Area Fraction (%)**	**Phase**	**Area Fraction (%)**	**Phase**	**Area Fraction (%)**
B	FCC	82 ± 1	TiC	18 ± 1	-	-
G	FCC	75 ± 2	HfC	25 ± 2	-	-
G	FCC	52 ± 3	C14 Laves	24 ± 1	HfC	24 ± 2
H	FCC	72 ± 1	C14 Laves	15 ± 1	TiC	13 ± 1
I	C14	81 ± 2	FCC	13 ± 2	HfC	6 ± 1

6.5 X-Ray Diffraction Analysis

Following the EDS investigation, XRD analysis was conducted in accordance with the methodology outlined in Section 2.3 to identify the phases present within the alloys and to verify the suppression of secondary intermetallic phases previously indicated by EDS analysis in selected samples. The resulting XRD patterns, full-pattern Pawley fits and difference between the raw data and fits for the carbon reinforced samples can be seen in Figures 6.7–6.10.

The Pawley refinement for Sample B in Figure 6.7 shows a very good fit with a dual FCC microstructure where one of the FCC phases is a TiC-based FCC carbide phase. This fit correlates very well with the EDS analysis of this sample where the η phase that was present in the as-cast and homogenised microstructure (Figure 4.2b and 4.5b) has been completely suppressed by the carbon addition.

Likewise, the XRD pattern for Sample G in Figure 6.8 indicates the presence of a dual FCC phase microstructure following carbon reinforcement. This observation is consistent with the microstructure in Figure 6.3, which reveals two distinct phases: an FCC matrix and FCC carbide precipitates. However, the secondary microstructure in Figure 6.4 shows the presence of a third eutectic phase within the matrix. The absence of this phase in the XRD pattern suggests that it constitutes a minor fraction of the material and is not representative of the bulk sample. As previously discussed, a slight increase in carbon content or the application of an appropriate heat treatment regime could promote homogenisation and eliminate this residual eutectic phase.

For Sample H, good agreement is observed between the BSE micrograph, EDS maps, and XRD fits shown in Figure 6.5. The XRD fit in Figure 6.9 reveals the presence of two FCC phases along with a third phase, identified as C14 Laves. A key indicator of the C14 phase in the XRD data is the trio of peaks between $20\,^\circ < 2\theta < 25\,^\circ$, which is notably absent in Figure 6.8. As previously discussed, the primary phase appears to be C14 Laves; however, it could also correspond to the C36 Laves phase due to the compositional and crystallographic similarities between the two. Since the primary peaks for both C14 and C36 are present in the XRD pattern, further confirmation via transmission electron microscopy would be necessary to resolve the atomic planes and differentiate between these phases.

Thermodynamically, TiC is the most stable MC carbide phase in this composition and is expected to form initially due to the sluggish diffusion of Mo. Although the orthorhombic Mo_2C phase is typically the most stable Mo-based carbide, its formation is suppressed by the combination of insufficient carbon content and high processing temperatures. Instead, Mo is likely incorporated into a (Ti,Mo)C structure, substituting for Ti within the same sublattice. This behaviour aligns with the slow diffusion of Mo and is further supported by the observed overlap of Ti and Mo in the EDS maps in Figure 6.5.

Finally, the XRD analysis of Sample I after carbon alloying reveals a three-phase microstructure, consistent with the EDS maps. As expected, the FCC and HfC phases are present; however, a C14 Laves phase is also detected. Compared to the XRD patterns of other samples, the intensity of the peaks is significantly lower relative to the background noise. This reduced signal is likely attributable to fluorescence caused by the higher combined quantities of Co and Fe in this composition. Additionally, the extensive surface cracking observed in the sample may contribute to diminished diffraction of the x-rays. The reduced peak intensity lowers the signal-to-noise ratio, complicating accurate peak identification and, consequently, phase determination. Nevertheless, thermodynamic analysis, along with the EDS maps and XRD results from the non-carbon-containing sample in both the as-cast and homogenised states, supports the presence of two FCC phases and a third C14 Laves phase. Furthermore, the Pawley refinement shown in Figure 6.10 demonstrates a good fit despite the challenges posed by the reduced signal-to-noise ratio.

From the Pawley refinements of the obtained XRD patterns, lattice parameters of the individual phases can be determined [268]. From these lattice parameters the lattice misfit f of the individual phases within the microstructure can be calculated as a percentage assuming cubic precipitates [312],

$$f(\%) = \frac{|a_p - a_m|}{a_m} \times 100, \tag{6.1}$$

where a_p and a_m denote the lattice parameters of the precipitate and matrix phases respectively. This lattice misfit determines the coherency of the different phases forming within the alloy microstructure. Strain free coherent interfaces can form between phases with identical lattice parameters even if they have different chemical compositions and/or crystal lattice structures [312]. However, when the distance between the atoms in the

interface is not identical it is still possible to maintain coherency by straining one or both of the two lattices, with lattice mismatch < 10 % reported to be required between the phases for this to occur. In the ideal case, where the crystal structures perfectly match, the dislocations can transition into and cut through the precipitate. Thus, the strengthening effect depends on the crystal structure of the precipitate, which may also likely be ordered, as the dislocation attempts to pass through it. However, away from the ideal case, these coherent interfaces generate a strain field due to the small amount of misfit and lattice distortion. This strain field interacts with the dislocations, either attracting or repulsing them, impeding the motion of dislocations and strengthening the material [312, 313]. The less coherent the interphase boundary, the higher interfacial strain and thus the greater the resistance to dislocation motion. For a lattice misfit, $10\ \% < f < 20\ \%$, it becomes energetically favourable for a semicoherent interface to form where the disregistry is periodically taken up by a series of dislocations. The dislocations present at this interface, in addition to the strain fields, impede the motion of further dislocations, resulting in additional strengthening of the material. Semicoherent interfaces may be coherent in one plane and incoherent on another, such as FCC and HCP which are coherent in the basal plane and often incoherent along the crystallographic c-axis of the HCP structure. In semi-coherent structures, the lattice strain and dislocations at the interface can restrict dislocation motion as coherent planes will allow dislocation glide, whereas, where incoherency is highest, no dislocations will be able to transition into the secondary phase lattice. When substantial lattice misfit is present between the two phases, $f > 20$ %, a completely incoherent interface forms [312, 314]. Incoherent interfaces cause dislocation pileups as the dislocations cannot cross the interphase boundary, having to bow around the precipitate via a mechanism known as Orowan looping.

Typically, a precipitate forms with a coherent or semicoherent interface, which may lose coherency over time as the precipitate grows or undergoes phase transitions. In some cases, the thermodynamically stable precipitate phase is inherently incoherent with the matrix. However, incoherent precipitates can be artificially installed into the microstructure through processes such as oxide dispersion strengthening. The carbide precipitates forming in the alloys investigated in this work are likely semicoherent. Initially forming coherently with the matrix but becoming semicoherent as they grow, with the formation of geometrically necessary dislocations to accommodate the associated strain.

Table 6.4 presents the lattice parameters of the carbon-reinforced compositions, as determined from Pawley refinements of the XRD patterns. For Alloy B, the lattice parameters were determined to be (3.64 ± 0.01) Å and (4.33 ± 0.01) Å for the FCC and TiC phases respectively. This equates to a lattice misfit of (19.00 ± 0.01) %, indicating that a semi-coherent interphase boundary exists between the two phases. The lattice parameter calculated for the TiC precipitate is in agreement with the expected lattice parameter of 4.33 Å [216] for pure TiC. For Alloy G, the lattice parameters were calculated as (3.59 ± 0.01) Å and (4.64 ± 0.01) Å for the FCC matrix and HfC respectively. Equating to a lattice misfit of (29.17 ± 0.01) %. However, it is more likely that a semicoherent interface forms with a significant amount of geometrically necessary dislocations forming to accommodate the large amount of disregistry. As with the TiC phase in Sample B, the lattice parameter of the HfC is very close to the expected value of stoichiometric HfC, 4.63 Å [315, 316]. Sample H has lattice parameters of (3.63 ± 0.01) Å and (4.33 ± 0.01) Å for the FCC matrix and TiC phases respectively, resulting in a lattice misfit of (19.35 ± 0.01) %. The lattice parameter of TiC is in good agreement with the expected lattice parameter, suggesting that little Mo is present in the sample. Finally, Sample I forms an FCC matrix and HfC precipitate phase with lattice parameters of (3.58 ± 0.01) Å and (4.57 ± 0.01) Å respectively; a lattice misfit of (27.56 ± 0.06) %.

Table 6.4: Lattice parameters of the FCC matrix and MC carbide precipitates for the carbon-reinforced HEA compositions, determined via Pawley refinement of the XRD patterns in Figures 6.7–6.10. Also presented is the lattice misfit percentage between the FCC matrix and MC carbide phases.

Sample	**Nominal Carbon Reinforced**	**FCC Matrix**	**MC Precipitate**	**Lattice Misfit (%)**
Index	**Alloy Composition**	**Lattice Parameter (Å)**	**Lattice Parameter (Å)**	
B	$Ti_{9.0}Cr_{8.7}Mn_{24.2}Fe_{17.7}Ni_{30.4}C_{10.0}$	3.64 ± 0.01	4.33 ± 0.01	19.00 ± 0.01
G	$Cr_{5.3}Mn_{19.8}Fe_{18.7}Co_{40.4}Hf_{8.3}C_{7.5}$	3.59 ± 0.01	4.64 ± 0.01	29.17 ± 0.01
H	$Ti_{14.0}Mn_{20.5}Fe_{38.7}Ni_{14.5}Mo_{2.3}C_{10}$	3.63 ± 0.01	4.33 ± 0.01	19.35 ± 0.01
I	$Mn_{33.2}Fe_{14.2}Co_{27.6}Nb_{8.7}Hf_{4.3}C_{12.0}$	3.58 ± 0.01	4.57 ± 0.01	27.56 ± 0.06

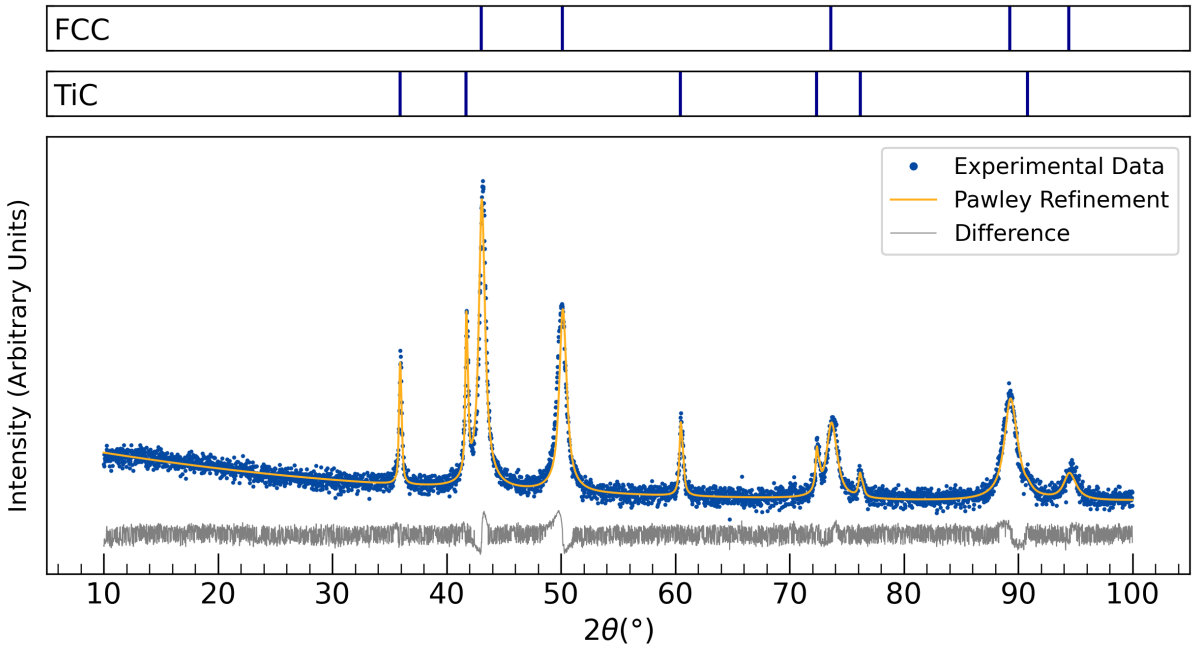


Figure 6.7: XRD patterns overlaid with Pawley refinement fits and their respective difference for Sample B ($Ti_{9.3}Cr_{8.8}Mn_{23.3}Fe_{17.8}Ni_{31.1}C_{9.7}$) following alloying with carbon in the as-cast condition.

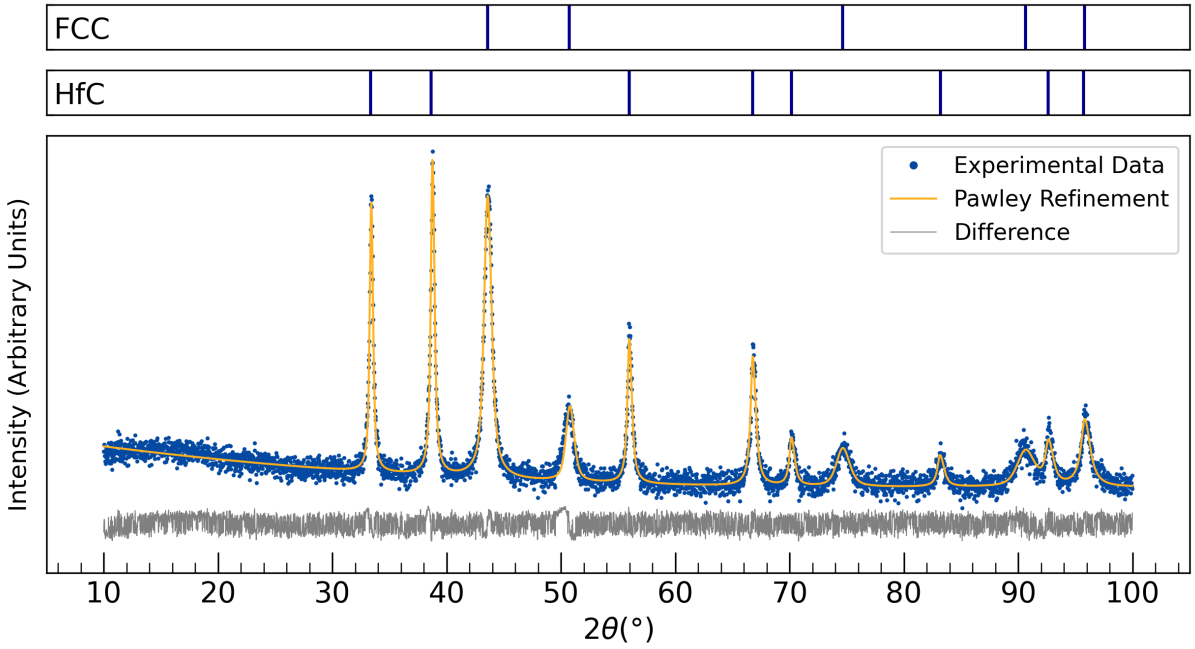


Figure 6.8: XRD patterns overlaid with Pawley refinement fits and their respective difference for Sample G ($Cr_{5.2}Mn_{18.9}Fe_{16.2}Co_{41.3}Hf_{7.1}C_{6.8}$) following alloying with carbon in the as-cast condition.

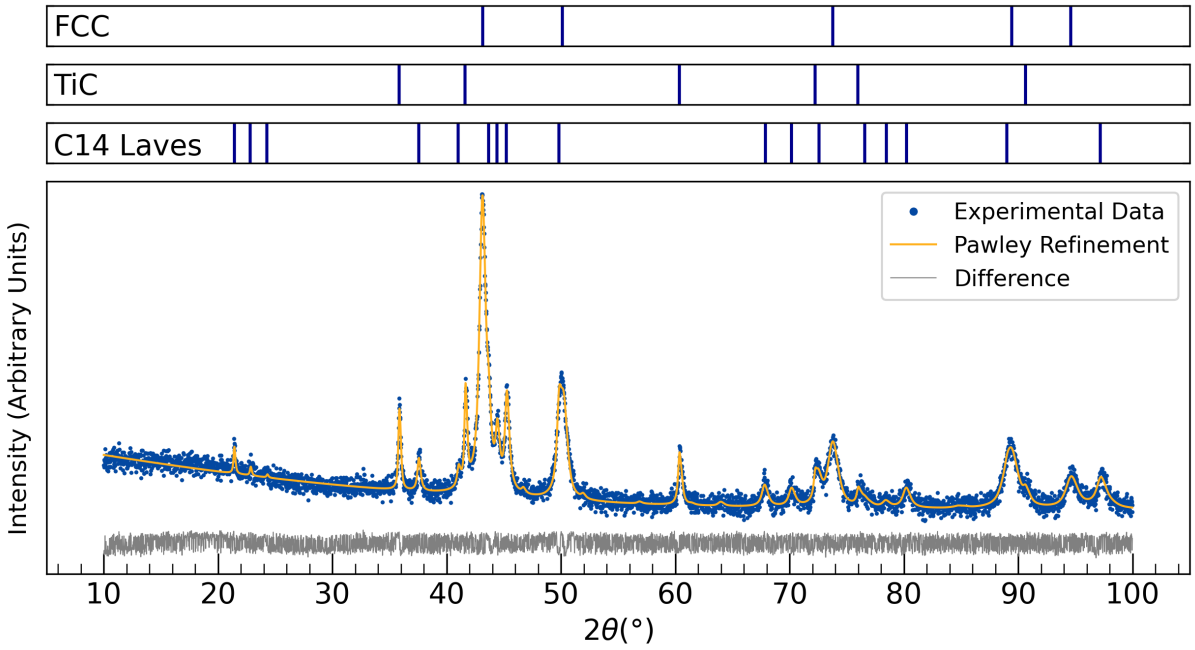


Figure 6.9: XRD patterns overlaid with Pawley refinement fits and their respective difference for Sample H ($Ti_{18.1}Mn_{11.5}Fe_{38.9}Ni_{14.8}Mo_{2.4}C_{14.2}$) following alloying with carbon in the as-cast condition.

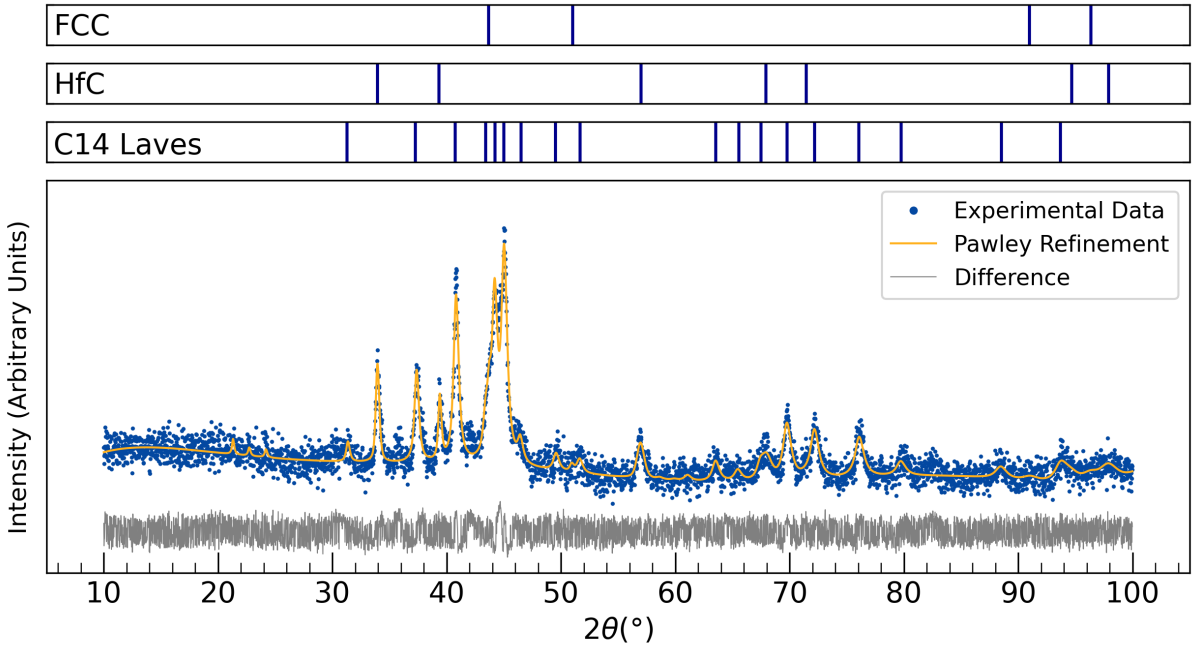


Figure 6.10: XRD patterns overlaid with Pawley refinement fits and their respective difference for Sample I ($Mn_{21.76}Fe_{19.1}Co_{37.4}Nb_{12.1}Hf_{5.4}C_{4.2}$) following alloying with carbon in the as-cast condition.

6.6 Mechanical Property Analysis

The hardness of the carbon reinforced alloy compositions was assessed according to the same methodology outlined in Section 2.6. The results of the micro-indentation hardness tests are shown in Figure 6.11.

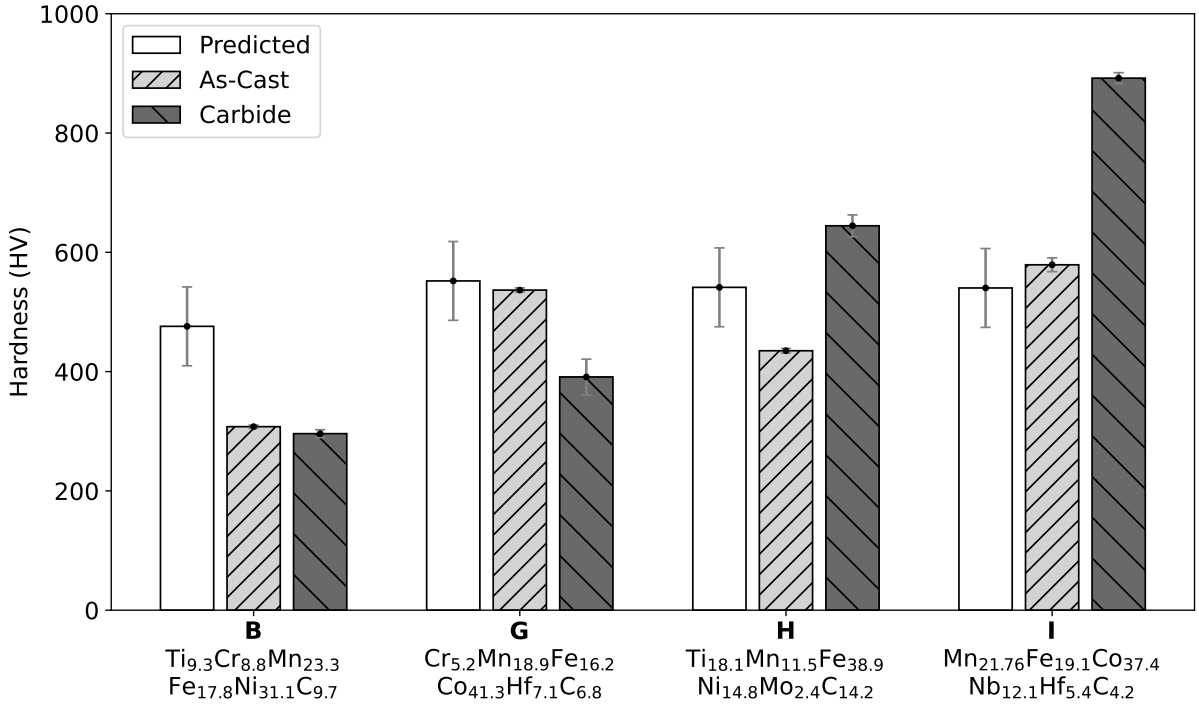


Figure 6.11: Bar chart enabling comparison between the ML-predicted, as-cast, and carbon reinforced microindentation hardness in HV of the four alloys selected to be carbon reinforced in this study. Error bars on the predicted hardness values represent the MAE score of the ML regression model. The error bars on the experimentally measured as-cast and carbon reinforced samples represent the standard error.

The results of the micro-hardness indentation tests clearly show a maintained hardness for Sample B despite the shift in microstructure from a Ni_3Ti η phase to a secondary TiC FCC phase. The standard error on these measurements is also very low as the alloy microstructure is very homogeneous. In contrast, Sample G displays a significant reduction in hardness from (536.7 $\pm$ 3.6) HV to (391.0 $\pm$ 29.9) HV. This correlates with the microstructure observed for the carbon reinforced Sample G in Figures 6.3 and 6.4, where in some regions the secondary intermetallic phase remains, producing a three phase microstructure. However, this was not picked up by the XRD analysis which only portrayed a dual FCC microstructure, one of which was a HfC structure. This secondary intermetallic phase, is suppressed by the introduction of carbon and formation of a HfC

phase provides a greater reinforcing effect than the carbide precipitates due to the eutectic microstructure, but is likely detrimental to the ductility. The maintained hardness in Sample B and the reduction observed in Sample G following carbon addition are likely due to differences in the mechanical response of their constituent phases during microindentation. It appears that only the ductile FCC matrix is effectively indented, deforming to accommodate the applied load. This interpretation aligns with anecdotal observations during sample preparation, where both samples were significantly harder to section, suggesting that the carbides provide substantial resistance to the cutting instrument. This resistance indicates increased wear resistance imparted by the carbides, while the FCC matrix enables deformation and damage tolerance during indentation.

Both Samples H and I display a substantial increase in hardness following the addition of carbon. However, both still prominently feature a secondary intermetallic phase as well as the primary FCC phase and newly formed carbide phase. The respective XRD analysis in Figures 6.5 and 6.6, both demonstrate that the initial C14 Laves phase has not been fully suppressed by the addition of carbon. In the case of Sample H, this could likely be mitigated by the addition of a subsequent heat treatment in order to remove the last of the secondary C14 Laves phase. However, in the case of Sample I, it is more likely that there is insufficient carbon in the alloy composition, as highlighted in Table 6.2, to form enough carbide phase to suppress the C14 Laves phase. This eutectic microstructure of the FCC matrix phase and Laves phase produces a strong strengthening effect within the alloy resulting in an enhanced hardness, supplemented by the addition of an incredibly hard carbide phase. The standard error of the micro-hardness measurements for Samples H and I after carbon addition are smaller than Sample G, indicating that even though a three phase microstructure is formed, the alloy microstructure is homogeneous.

Macro-indentation hardness investigations were conducted according to the methodology outlined in Section 2.6 to try to provide further insight into the role played by the FCC matrix and carbide precipitates during the indentation process. The results of this macro-hardness assessment are displayed in Figure 6.12 alongside the results of the micro-hardness investigation. However, these macro-hardness tests were ultimately inconclusive, displaying the same effect as the micro-indentations, where the indentation sinks into the soft FCC matrix and follows the boundary of the carbide precipitates with no macro-cracking into the matrix and only a few occurrences of cracking of the carbides. Carbide

precipitates are also observed to sit on the faces inside the indents. Suggesting that during the indentation process the carbide precipitates do not play a substantial role in increasing the hardness as the significantly softer FCC matrix deforms around them. Therefore, nano-indentation hardness analysis was performed to get an accurate measurement of the individual matrix and carbide precipitate hardness respectively.

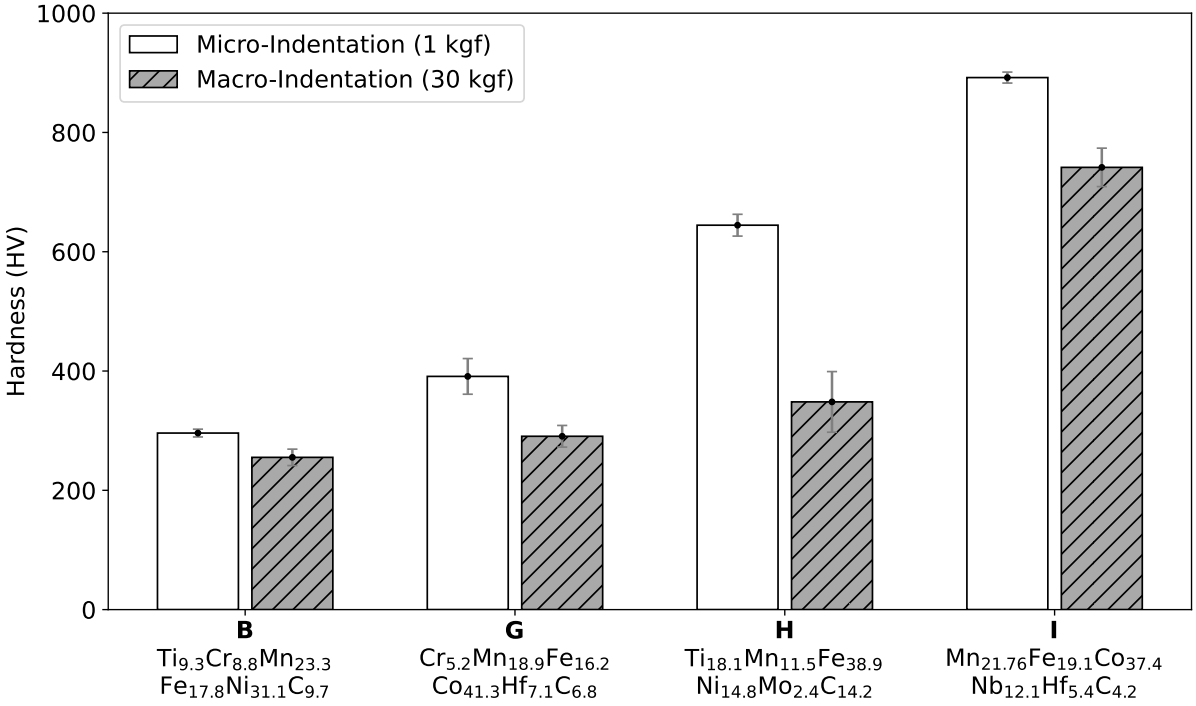


Figure 6.12: Bar chart showing the results of the macro-hardness indentation analysis and enabling comparison to the micro-hardness assessments. Error bars represent the standard error of the measurements.

The results of the subsequent nano-hardness indentation investigations, performed as described in Section 2.6 are presented in Figure 6.13. Additionally, rule of mixtures analysis was performed according to,

$$HV = fHV_{\text{carbide}} + (1 - f)HV_{\text{matrix}}, \tag{6.2}$$

where f denotes the carbide phase area fraction and $HV_{\text{carbide/matrix}}$ denotes the nano-hardness of the carbide and matrix phases respectively. The carbide phase fractions were determined from both CALPHAD predictions and experimental area fraction observations using an optical microscope. ImageJ image processing software [269] was used to calculate the area fraction of the carbide precipitates, averaged over 25 images taken across the surface of the samples. The results of the area fraction analysis are as follows: Sample

B contained (18.0 ± 1.3) % carbide precipitate, Sample G (27.8 ± 1.0) %, Sample H (15.4 ± 0.8) %, and Sample I (4.5 ± 0.4) %. As expected from the EDS maps in Figures 6.2–6.6, Samples B and G contain comparable amounts of carbon to those predicted by CALPHAD, resulting in the formation of a dual phase FCC matrix and FCC carbide microstructure. However, Sample H and in particular Sample I contain a substantially lower carbide fraction than that predicted by CALPHAD, leading to intermetallic Laves phases remaining present within the alloy microstructure.

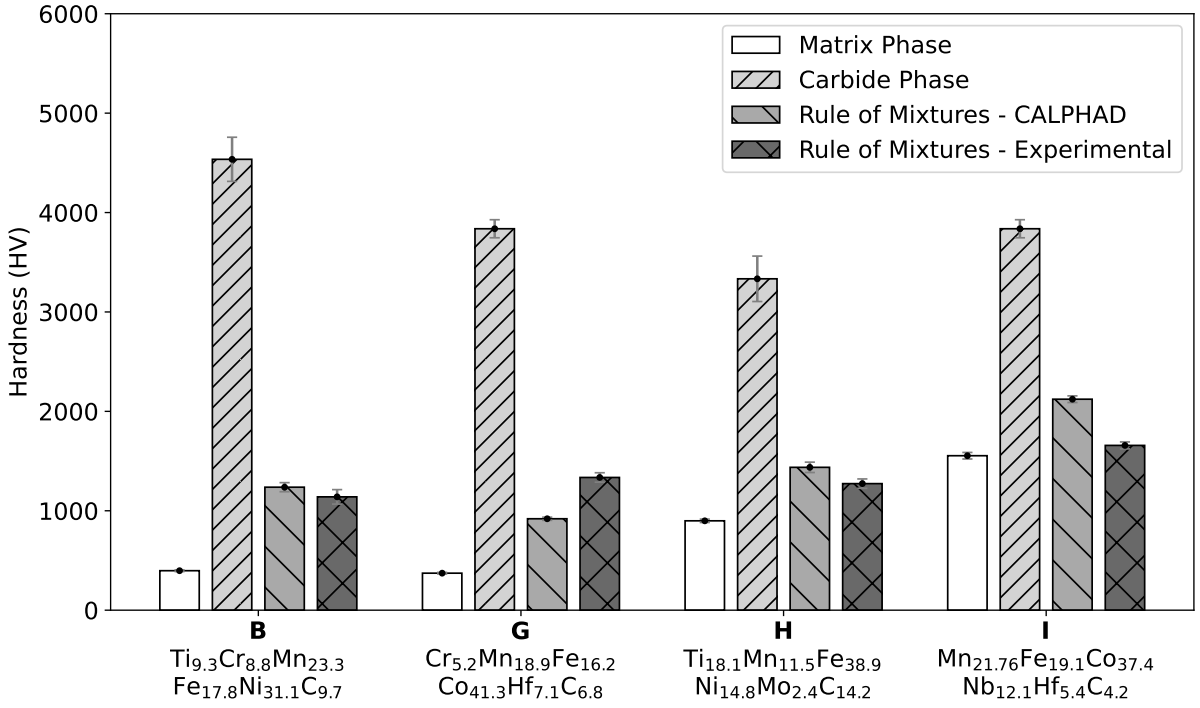


Figure 6.13: Bar chart showing the results of the nano-hardness indentation analysis for the matrix and carbide precipitates respectively. The rule of mixtures hardness has also been calculated from CALPHAD prediction of phase volume fraction and experimental area fractions obtained from optical microscopy assessments. Error bars represent the standard error of the measurements and have been calculated through error propagation analysis [317] for the rule of mixtures. No error is provided by Thermo-Calc for the CALPHAD assessments of volume fraction so these values have been treated as constants.

Nano-indentation results confirm that, as anticipated, the matrix phase is significantly softer in Samples B and G, where no additional intermetallic phase is present. In contrast, the presence of the C14 Laves phase in Samples H and I increases resistance to indentation, indicating a harder microstructure. As expected, the carbide phases exhibit very high hardness, with the HfC phases in Samples G and I showing good agreement in measured values. However, a reduction in the hardness of the TiC phase is seen from Sample B to I, likely caused by the presence of Mo forming Mo_2C or substituting onto the same sublattice

as Ti within the carbides. However, the rule of mixtures calculations suggest that the addition of carbon should have a large strengthening effect leading to a significant increase in hardness, especially in the case of Samples B and G where a reduction in hardness is actually observed from the addition of carbon, Figure 6.11. This reduction in hardness, despite the addition of a significantly harder carbide precipitate phase, is due to the reduction of phase boundaries and incoherence of the matrix and carbide precipitates. The eutectic alloy microstructure of the alloys before carbon reinforcement results in the presence of a large number of phase boundaries in comparison to the microstructure in Figure 6.2, where large carbide precipitates form within the matrix. These phase boundaries impede dislocation motion resulting in a strengthening effect.

While the carbides provide excellent wear resistance for the alloy due to their extreme hardness seen in Figure 6.13, they do not provide a significant improvement to the overall strength of the alloy. Instead, the enhanced hardness seen in Samples H and I in Figure 6.11 is a result of the presence of an additional intermetallic C14 Laves phase. This forms a eutectic microstructure with the FCC matrix, Figure 6.5, and the large amount of interphase boundaries result in a significant hardening effect by successfully impeding dislocation motion. As shown by the calculation of lattice misfit in Section 6.5 above, in Samples B and G, the carbides form a semicoherent interface with the FCC matrix. Thus, some precipitation hardening effects would be expected as they impede dislocation motion through the microstructure. However, this is significantly outweighed by the size and spacing of the precipitates. Figures 6.2 and 6.3 highlight the large particle radius and small number density of the carbide phases. Due to the large precipitate size, Orowan looping is believed to be the active dislocation mechanism, allowing the dislocations to bypass around the precipitates and reducing the overall strength of the alloy. Additionally, the significant interparticle spacings between the carbide precipitates are too large to provide extensive hardening. The necessary shear stress τ for continued dislocation motion is given by,

$$\tau = \frac{Gb}{L'} \cos \frac{\phi_c}{2}, \tag{6.3}$$

where G represents the shear modulus of the material, b the associated burgers vector for the lattice distortion, $L^{'}$ the effective mean spacing between the obstacles that impede

dislocation motion, and ϕ_c the angle of the slip system [313]. Thus, the maximum strength for an array of obstacles within a matrix is given by,

$$\tau_{\max} = \frac{Gb}{L}, \tag{6.4}$$

where L is the mean obstacle spacing.

6.7 Additive Manufacturing Preliminary Trials

A key aim of this study is to evaluate the amenability of the designed HEA compositions to AM techniques, ensuring their suitability for advanced engineering applications. AM, particularly laser powder bed fusion (LPBF) and direct energy deposition, has attracted significant interest within the HEA research community and the manufacturing industry. A relatively new manufacturing process, AM builds or "prints" components layer by layer from a metal powder feedstock [318]. These processes have the advantage of being able to construct complex geometries and internal structures that could not be achieved using more conventional manufacturing methods [318, 319]. Additionally, the powder feedstock utilised in AM enables a reduction in the usage and waste of raw materials as the complex parts can be constructed directly and excess powder recycled. AM also enables material repair and is already being implemented for the repair of tool materials by application of HEA coatings [320]. Thus, the development of new alloys, and in particular HEAs that are suitable for AM, is important for industry adoption of these materials. Hence, assessment of the propensity of the carbon reinforced HEAs developed in this work for AM is a key step towards their fabrication via AM and their alloy development. Substantial research has been conducted on the synergy and relationship of HEAs and AM, detailed in extensive review articles on the topic [321–324]. More specifically, LPBF has been used to fabricate a range of HEA compositions and is frequently used for laser cladding to create HEA coatings. For example, Chen *et al.* [325] utilised LPBF to fabricate the conventional CoCrFeMnNi alloy by *in situ* alloying a pre-alloyed powder and elemental Mn powder. This resulted in vaporisation of Mn as anticipated by the results within this work and thus a reduction of Mn in areas. However, Chen *et al.* [325] successfully showed *in situ* alloying of Mn via LPBF with homogeneous microstructure and single-phase FCC crystal structure. In addition to the archetypal CoCrFeMnNi HEA alloy, the application of AM

in other branches of the HEA space, such as Al-based and refractory HEAs have been investigated [318, 322]. Another key attraction for the application of AM processes to HEAs is the capability for high-throughput investigations, as discussed in Section 1.6.12. However, in this case the primary goal is to establish the suitability for these already cast alloy samples to be fabricated via AM. Hence, herein a preliminary investigation into the amenability of the carbon reinforced HEA compositions produced in this work, Samples B, G and H, to AM and in particular LPBF was conducted, with focus on the cracking susceptibility of the alloys. Sample I was excluded from the AM trials as it had already displayed significant cracking during conventional casting, thus would be unsuitable for AM processes. Before undertaking a complete AM investigation and printing a complete structure from HEA powder, a simplified test in the form of bead-on-plate experiments were conducted to assess the process and material propensity to cracking [326].

There are multiple different types of cracking that can occur in LPBF processes, such as solidification cracking, liquation cracking and solid-state cracking. Both solidification cracking and liquation cracking occur during solidification in the heat affected zone. In contrast, solid-state cracking occurs after the solidification process [327]. Each of these cracking categories can be further subdivided, however, due to their similarity these crack types will be considered collectively as solidification and solid-state cracking respectively.

6.7.1 Methodology

This initial laser scan investigation was conducted similar to other bead-on-plate tests performed on Ni-based superalloys [319, 328]. The surface laser scans were performed as described in Section 2.7.1, on arc-melted button ingots, fabricated as described in Section 6.2. The samples were ground to produce a plane surface using P1200 SiC grit for the laser to be rastered across and subsequently imaged, while minimising the optical reflectivity of the surface to mitigate back reflection of the laser. Laser melt tracks were completed using an Aconity Lab PBF-LB/M system. In the first investigation, five sets of laser scans were performed on each alloy sample. The laser power was held constant at 130 W and the laser velocity varied between 450 $\mathrm{mm\,s^{-1}}$ and 850 $\mathrm{mm\,s^{-1}}$ in increments of 100 $\mathrm{mm\,s^{-1}}$. These parameters were chosen as they are standard non-extreme parameters typically used for the fabrication of Inconel superalloys [329]. The oxygen content in the chamber was maintained below 250 ppm and the laser diameter was 80 μm. Additionally, a spacing

of 0.3 mm was implemented between the laser scan parameter sets to avoid interference due to secondary heating from previous laser scans. The input energy densities, calculated using Equation 2.5, are 3.61, 2.95, 2.50, 2.17, and 1.91 J mm^{-2}, corresponding to laser scan speeds 450–850 mm s^{-1} respectively. In the subsequent investigation, the laser velocity was additionally maintained constant at 450 mm s^{-1}, an energy density of 3.61 J mm^{-2}. However, the number of laser scans was increased incrementally from one to five over the same track. A pause between each scan over the same track was implemented to simulate how the material cools before being reheated as the laser rasters across the sample in layers during the LPBF process. This provides more information as to the propensity for material cracking during the repeated application of laser energy and subsequent localised heating in the LPBF procedure.

Following the laser scanning procedure, the surface of the samples was first imaged using an optical microscope. The samples were then sectioned perpendicular to the laser scan direction to expose the cross-section, which was subsequently mounted and prepared for SEM analysis according to the methodology described in Section 2.1.3. This approach allowed for investigation of both the laser tracks on the surface and the laser-affected zone in the subsurface region.

6.7.2 Variable Scan Speed Investigation Results

Results of the laser scans with variable scan speed are discussed and presented below. The optical micrographs of the sample surfaces are presented in Figure 6.14. No evidence of cracking is observed within Sample B following the laser scanning strategy at any of the energy densities. However, Sample G displays evidence of both solidification cracking within the melt pool and additional solid-state cracking at the highest energy density (leftmost track). Furthermore, substantial solid-state cracking is observed at an energy density of 2.17 J mm^{-2} (750 mm s^{-1} scan speed). This crack extends all the way across the bulk of the sample reaching the adjacent laser scans. The optical micrograph of Sample G also highlights its reduced carbide phase precipitation in comparison to the other samples investigated in Figure 6.14. The 2.50 J mm^{-2} energy density (650 mm s^{-1} scan speed) for Sample H is missing as this track was cut short, due to back reflectivity. For the remaining tracks within this sample, significant solidification and solid-state cracking was observed at all energy densities. The solidification cracking observed within the

melt pool region displays almost uniform distribution, with reduced spacing between the solidification cracks at higher energy density laser scans.

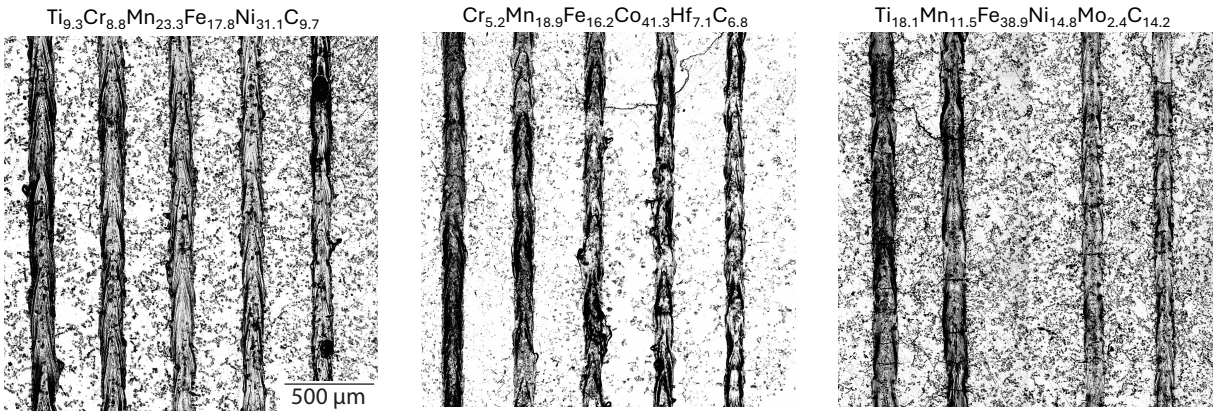


Figure 6.14: Optical micrographs of the surface of the carbon-reinforced Samples B, G, and H, from left to right respectively, following single laser scans at varying energy densities from 3.61–1.91 J mm^{-2}. The energy density decreases from left to right, corresponding to increasing laser scan speeds from 450–850 mm s^{-1}.

The cross-sections of the samples following laser scans with varied energy density are shown in Figure 6.15. Within all the samples it is clear that increasing the energy density results in an increase in meltpool and heat affected zone depth. It is possible for the larger carbides in the laser affected zone to be moved out of the region by the supplied energy, but this does not appear to be the case as large carbides are still present within the meltpool region of all samples at all energy densities. Furthermore, all samples show an elevated bump where the laser has passed, being significantly more pronounced at the higher energy densities. This raised bump is a common artifact within laser based AM and is the result of the application of energy to a highly localised region by the laser. The heating effect causes thermal expansion and redistribution of the material as it swells over. Additionally, under cooling residual stresses can cause distortions creating the raised region. The application of energy can also cause a change in microstructure, observed in some of the samples and discussed later in this section, leading to an increase in volume. The presence of a raised artifact above the heat affected zone can indicate overheating or the application of too much energy, but as discussed, it can also be the result of volume expansion due to unavoidable microstructural changes. However, if cracking of the sample is not observed at these higher energies then it follows that cracking propensity for lower energy densities will be minimised. Additionally, bulk samples differ considerably from powder samples as there is less absorption and more reflection of the laser from the bulk

sample surface. Hence, the higher energy densities investigated in this work could be too high for powder feedstock. Adjustments to process parameters, including laser power and speed, can mitigate the formation of surface artifacts, highlighting the importance of preliminary trials to ascertain the correct printing parameters for new alloy compositions.

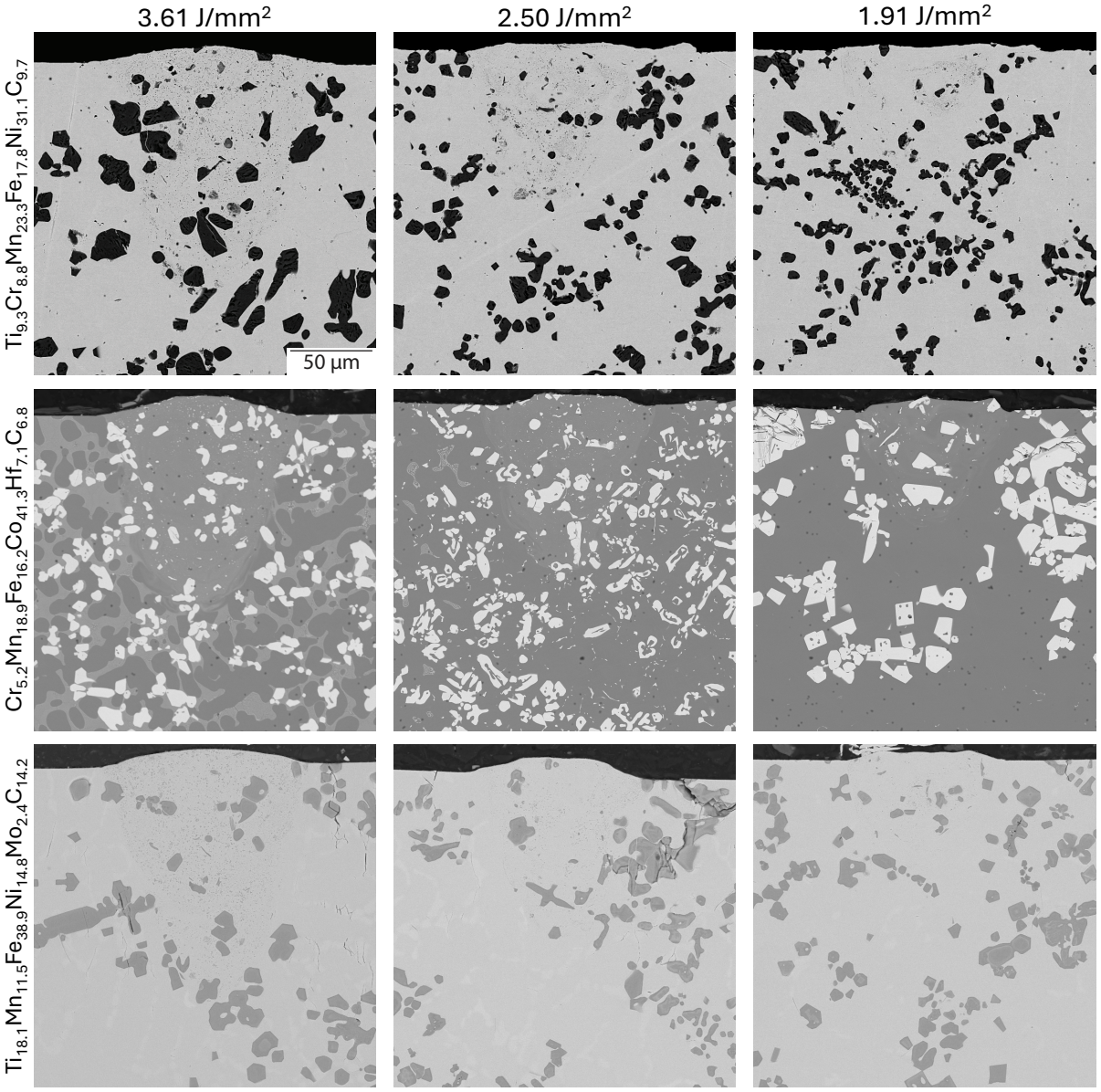


Figure 6.15: BSE micrographs of the cross-sections of the carbide samples following the laser scan strategy where scan speed was varied to produce a range of energy densities. Each column represents a different energy density, decreasing from left to right, and each row a different carbide Sample: B, G and H from top to bottom respectively.

Within Sample B, the single FCC matrix microstructure prevalent within the bulk is preserved. However, the carbides are clearly observed to break up into smaller precipitates within the heat affected zone, demonstrated in Figure 6.16. This breakup of the carbide precipitates is a promising result that indicates that the alloy compositions will be printable by LPBF and can potentially generate smaller carbide precipitates that will be beneficial for alloy performance.

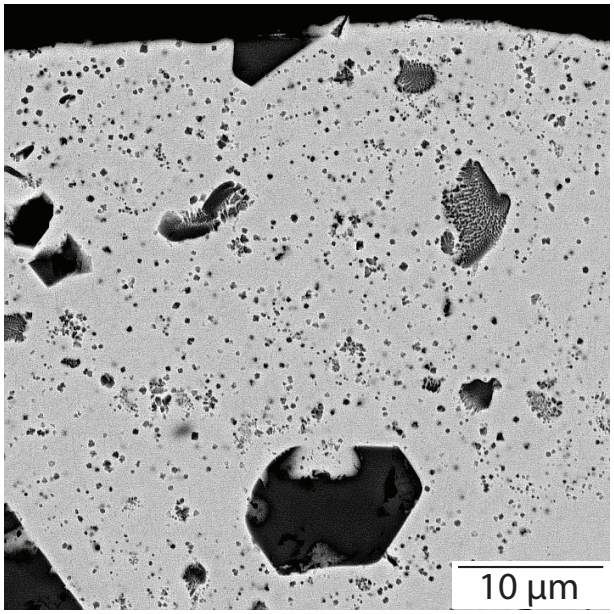


Figure 6.16: BSE micrograph of the heat affected zone following a laser scan at energy density 3.61 $\mathrm{J\,mm^{-2}}$ (450 $\mathrm{mm\,s^{-1}}$) of Sample B ($Ti_{9.3}Cr_{8.8}Mn_{23.3}Fe_{17.8}Ni_{31.1}C_{9.7}$). Demonstrates the break up of the carbide phase into smaller precipitates and the preservation of the bulk matrix.

In contrast, within Sample G, while breakup of the carbide precipitates is observed, a two phase cellular microstructure forms within the heat affected zone, Figure 6.17. This cellular microstructure is a common feature of AM processes and clearly shows the reformation of a secondary phase, which could be the same C14 Laves phase that is suppressed upon addition of carbon and still observed to be present within the bulk of the Sample in some regions (Figure 6.15). At these energy densities there is clear contrast between the microstructure inside and outside the meltpool. However, the formation of this two phase microstructure is also observed for the lowest energy density, 1.91 $\mathrm{J\,mm^{-2}}$, where the bulk microstructure is a single phase FCC crystal structure matrix. Therefore, the secondary phase must be reforming out of the matrix due to the energy input from the laser, and/or segregating as a result of the rapid solidification. These secondary phases may, however, be mitigated or eliminated through subsequent heat treatment. The ob-

served carbide breakup suggests again that the alloy composition is suitable for LPBF despite the concern of the extremely high melting point HfC carbide within the FCC matrix. However, the formation of the two phase cellular microstructure suggests that a different compositional and crystallographic structure to the as-cast alloys could form via the LPBF process.

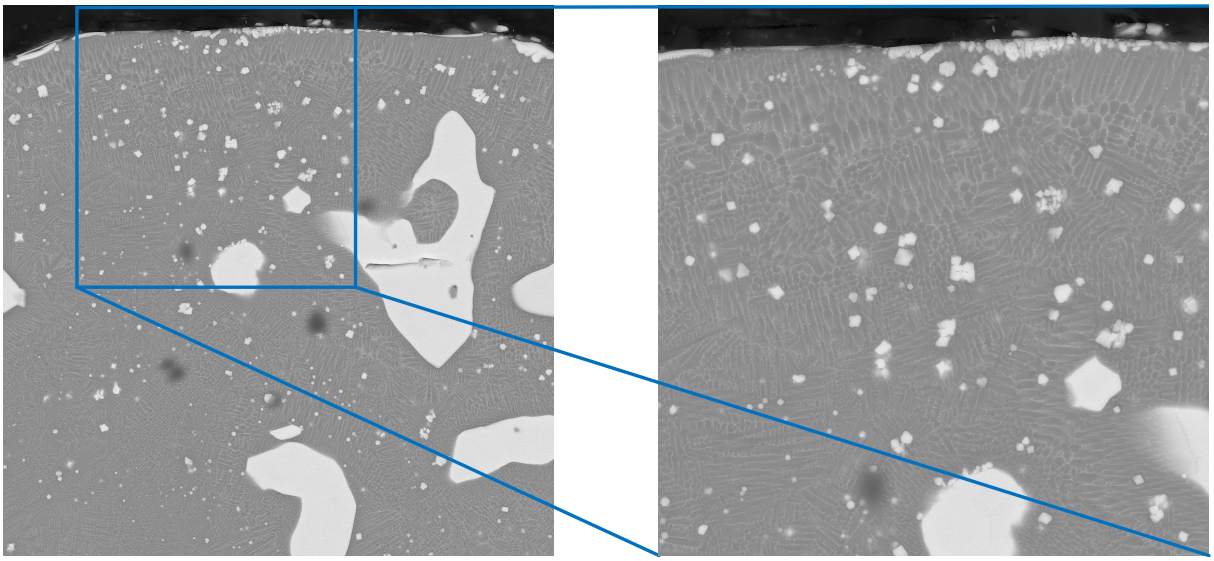


Figure 6.17: BSE micrograph of the heat affected zone following a laser scan at energy density 3.61 J mm^{-2} (450 mm s^{-1}) of Sample G ($Cr_{5.2}Mn_{18.9}Fe_{16.2}Co_{41.3}Hf_{7.1}C_{6.8}$). Demonstrates the break up of the carbide phase into smaller precipitates and formation of a two phase cellular microstructure that is characteristic of AM processes.

Critically, both Samples B and G, shown in the top two rows of Figure 6.15, exhibit no evidence of solidification or solid-state cracking, either within the bulk microstructure or specifically within the melt pool. However, while no solidification cracking is observed directly inside the meltpool of Sample H, there are clear signs of solid-state cracking within the microstructure. These cracks typically originate within the secondary intermetallic phase and propagate through this phase, stopping at the phase boundary with the FCC matrix phase. These cracks also tend to avoid the carbide precipitates, but in some cases permeate through these carbides when no alternative is available. This suggests that further addition of carbon to suppress the intermetallic C14 Laves phase and increase the carbide fraction could prevent this cracking under AM conditions. Furthermore, it is important to note that the amount of cracking decreases as the energy density decreases, with very little solid-state cracking observed for the lowest energy density of 1.91 J mm^{-2} (850 mm s^{-1}). No solidification cracks are observed within the meltpool of Sample H and this correlates with the microstructure of the meltpool for the maximum applied energy

density of 3.61 $\mathrm{J\,mm^{-2}}$ (450 $\mathrm{mm\,s^{-1}}$), detailed in Figure 6.18. This figure highlights the break up of the carbides into smaller precipitates by application of the laser energy and evidence of a cellular microstructure typical of AM, including a secondary phase forming which could be identical to the secondary phase observed within the bulk microstructure.

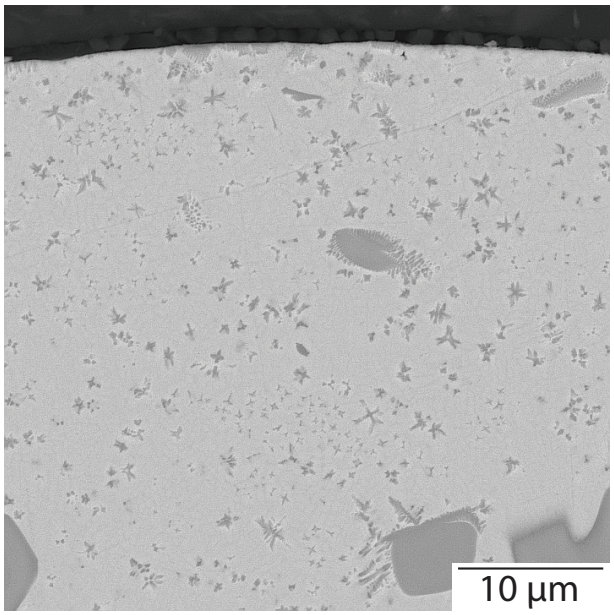


Figure 6.18: BSE micrograph of Sample H, ($Ti_{18.1}Mn_{11.5}Fe_{38.9}Ni_{14.8}Mo_{2.4}C_{14.2}$) following a laser scan at the maximum energy density of 3.61 J/mm^2 (450 mm/s). Demonstrates the break up of the carbide precipitates and the formation of a two phase cellular microstructure.

6.7.3 Repeated Scan Investigation Results

Results of the laser scan strategy where the energy density was fixed at 3.61 $\mathrm{J\,mm^{-2}}$ and repeated scans performed across the same region of sample surface are presented and discussed below. This repeated scan strategy at the highest energy density was conducted to try to exaggerate the break up of the carbides within the microstructure and replicate repeated heating effects. The optical micrographs of the sample surfaces are presented in Figure 6.19. In contrast to the single laser scan investigations, significant cracking is observed in all compositions. No solidification cracking is observed within the meltpool of Samples B and G for any of the laser scans. However, in both samples a significant crack forms on the surface. In the case of Sample B, this crack originates from the track with two laser scans and almost propagates across the surface to the adjacent laser tracks. For Sample G, it is not clear from which laser track this crack originates, however, it propagates across the surface and through the majority of the laser tracks. In

contrast, Sample H, the far right image in Figure 6.19 displays evidence of solidification cracking. Solidification cracks occur almost uniformly along the length of the laser tracks, perpendicular to the direction of laser travel. In some cases these cracks leave the heat affected zone and propagate into and through the bulk microstructure.

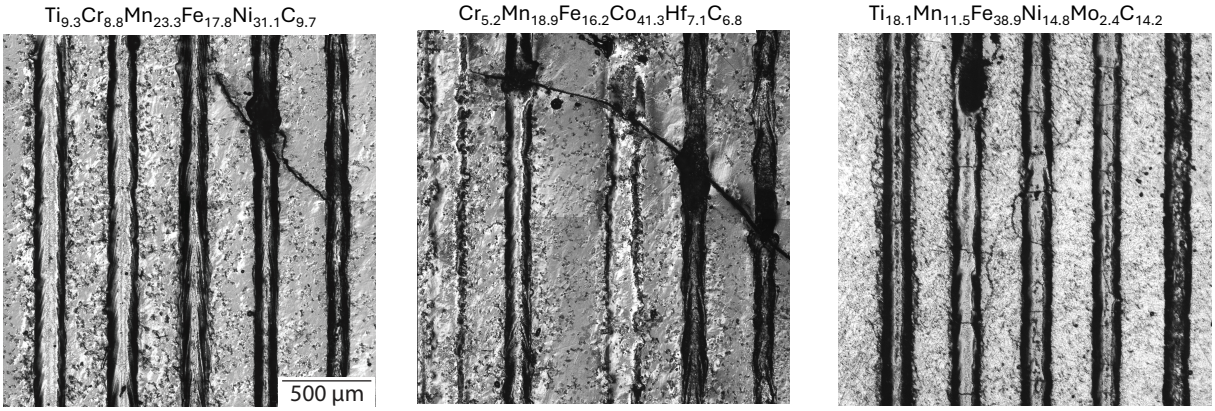


Figure 6.19: Optical micrographs of the surface of the carbon reinforced Samples; B, G, and H from left to right respectively, following repeated laser scans at a set energy density of 3.61 $J\,mm^{-2}$. The number of laser scans decreases incrementally from five on the far left to one on the far right. Thus, the total energy deposition on the sample surface from the laser decreases from left to right.

The cross-sections of the samples following the laser scans with fixed energy density but repeated scans across the same sample region are shown in Figure 6.20. As with the previous results, clear breakup and redistribution of the carbides is seen for all samples. Additionally, the raised artifact above the laser scan region is again observed in all samples except for the single laser scan of Sample G. This raised artifact is significantly more pronounced as the number of laser scans increases, due to the increased deposition of energy into the localised region. As with the results for the single scans in the prior section, the FCC matrix is preserved within the heat affected zone in Sample B and a secondary phase is observed to form in Sample G. This secondary phase is observed for all laser scan tracks despite the matrix in these regions consisting of a single phase FCC microstructure. Following the subsequent laser scans, some cracking is observed within the carbides in Samples B and G in the bulk microstructure around the heat affected zone. Furthermore, Sample H, the bottom row of Figure 6.20, demonstrates extensive cracking within the heat affected zone. Additional smaller cracking outside the meltpool is also observed. For 3 and 5 laser scans the crack passes directly through the bulk and meltpool until it reaches the surface of the raised artifact. In contrast, for the single laser scan, the crack has created a deep scar and an almost subduction like effect of the sample

surface. This evidence of cracking indicates that too much energy has been supplied to this sample and that the energy density utilised is too high for printing of this sample with its current composition of two phase matrix microstructure and carbide precipitates.

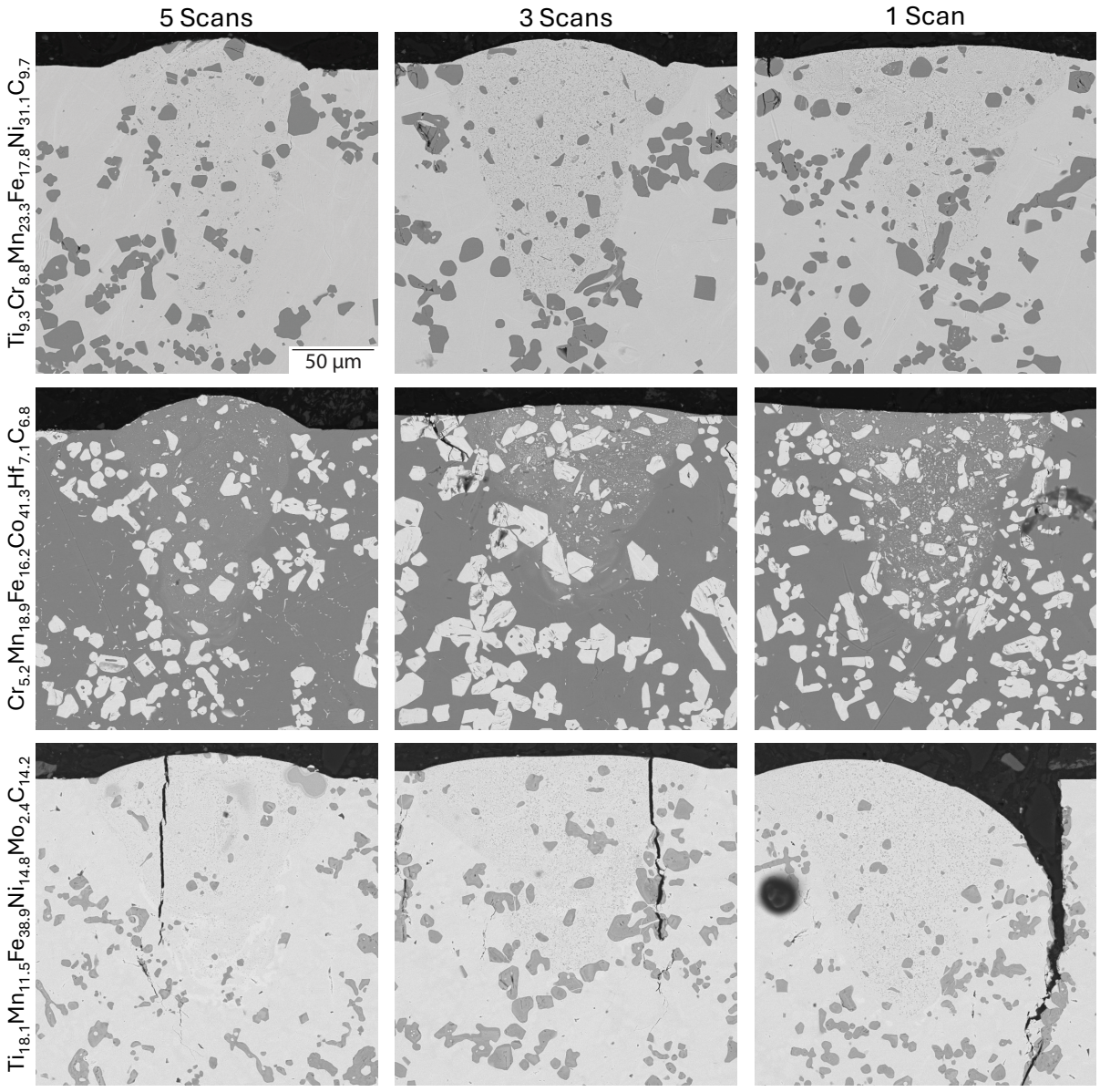


Figure 6.20: BSE micrographs of the cross-sections of the carbide samples following the laser scan strategy where energy density was fixed at 3.61 $J\,mm^{-2}$ and multiple scans across the same local region of sample surface performed. Each column represents a different number of laser scans, decreasing from left to right, and each row a different carbide Sample: B, G and H from top to bottom respectively.

6.8 Summary

Following the prediction and fabrication of the nine alloys discussed in Chapters 3 and 4 respectively, thermodynamic analysis via CALPHAD was utilised to determine suitable candidates for carbon reinforcement. This addition of carbon was hypothesised to suppress undesirable and brittle secondary intermetallic phases while simultaneously enhancing the mechanical properties of the alloys. Four alloy compositions, B, G, H, and I, as listed in Table 4.1, were downselected for carbon reinforcement due to their favourable microstructures, comprising an FCC matrix and additional intermetallic phases such as η or C14 Laves. Following thermodynamic analysis to determine a suitable carbon concentration, these new carbon reinforced HEAs were fabricated via vacuum arc melting. Results of the alloy characterisation showed that in the case of Sample B, $Ti_{9.3}Cr_{8.8}Mn_{23.3}Fe_{17.8}Ni_{31.1}C_{9.7}$ and Sample G, $Cr_{5.2}Mn_{18.9}Fe_{16.2}Co_{41.3}Hf_{7.1}C_{6.8}$ respectively, the secondary intermetallic phases were successfully suppressed. Resulting in the formation of a single phase FCC matrix with FCC monocarbides precipitating within the matrix, highlighting the accuracy of the thermodynamic calculations. The other two compositions, Sample H, $Ti_{18.1}Mn_{11.5}Fe_{38.9}Ni_{14.8}Mo_{2.4}$-$C_{14.2}$ and Sample I, $Mn_{21.76}Fe_{19.1}Co_{37.4}Nb_{12.1}Hf_{5.4}C_{4.2}$, also demonstrated the formation of an FCC matrix and carbide precipitation. However, secondary intermetallic phases were still present, most likely due to a lower carbon concentration than targetted, resulting from difficulties in the sample manufacturing process.

The carbon additions in the cases where the intermetallic phases were fully suppressed exhibited a reduction in hardness values measured. This reduction in hardness is likely due to the microhardness measurements primarily indenting the softer matrix phase rather than the carbide precipitates themselves, with the large size and wide spacing of the carbides also reducing their direct contribution to resisting dislocation motion during indentation. In contrast, in the samples where an intermetallic phase is still present a significant boost in hardness was observed. This effect arises from the presence of three distinct phases within the alloy, including carbide precipitates, each with phase boundaries and crystal structures that impede dislocation motion.

After successfully demonstrating the ability to suppress or significantly reduce, intermetallic phase formation within the HEAs by additions of carbon, the suitability of these alloy compositions to AM processes was assessed. To that end, preliminary bead-

on-plate trials were conducted on three out of the four carbon reinforced samples to both assess the alloy propensity to cracking and determine suitable printing parameters for these novel alloy compositions. Sample I ($Mn_{21.76}Fe_{19.1}Co_{37.4}Nb_{12.1}Hf_{5.4}C_{4.2}$), was excluded from this testing procedure due to its propensity to cracking in the conventional vacuum arc melting casting procedure. These preliminary trials concluded that the cracking susceptibility of alloy compositions B, $Ti_{9.3}Cr_{8.8}Mn_{23.3}Fe_{17.8}Ni_{31.1}C_{9.7}$ and G, $Cr_{5.2}Mn_{18.9}Fe_{16.2}Co_{41.3}Hf_{7.1}C_{6.8}$, was sufficiently low to be suitable for AM. On the other hand, Sample H, $Ti_{18.1}Mn_{11.5}Fe_{38.9}Ni_{14.8}Mo_{2.4}C_{14.2}$ displayed significant solid-state cracking during the bead-on-plate trials. However, it is possible that further carbon additions could fully suppress the C14 Laves intermetallic phase, thereby reducing the alloy's cracking susceptibility. In this case, the observed cracking is more likely attributable to suboptimal processing parameters rather than the solid-state cracking typically associated with phase formation.

Chapter 7

Machine Learning for Alloy Design II

The initial implementation of the coupled ML and CALPHAD-based thermodynamic analysis effectively accelerated the identification and development of promising alloy compositions tailored for metal-forming tooling applications. From the coupled methodology nine alloys were fabricated, with four of these being found suitable for further carbon reinforcement and three being selected for preliminary bead-on-plate investigations to assess their amenability to AM.

Despite the promising regions of compositional space identified in the earlier stages of this work, several limitations and areas for improvement in the ML methodology were identified. Consequently, a second iteration of the ML approach was conducted, incorporating an expanded dataset that includes the experimental findings from this study, an enhanced feature space, evaluations of alternative ML models, and high-throughput thermodynamic analysis using an updated thermodynamic database. This second iteration serves as the foundation for the work presented in this chapter.

7.1 Dataset Construction

The two datasets used in the first iteration of the ML design methodology, by Gorsse *et al.* [210] (corrigendum published in 2020 [279]) and Machaka *et al.* [209], provided information on the phase and hardness of 370 and 1362 HEAs respectively. However, the quality and quantity of this data was identified as one of the key limitations of the

first ML iteration. Significant amounts of data were missing, and the accuracy of the provided data from the original studies referenced was at times unreliable. Both before and after the publication of these datasets in 2018 and 2021 respectively, other collations of experimentally acquired HEA data have been published. These published datasets contain additional data that could expand the amount of data available for training the ML models, resulting in greater predictive power and performance. A number of individual published datasets were used to construct the expanded dataset for ML training and are detailed in Table 7.1. The datasets published by Gorsse *et al.* [210] and Machaka *et al.* [209] are also included within the construction of the expanded experimental HEA dataset. Critically, the experimental HEA data collected within this work is included within this dataset.

Table 7.1: Publicly available published datasets used to construct the dataset for the second iteration of the machine learning assessment.

Authors	**Year**	**Material Properties**	**Manufacturing Method and Processing History**	**Number of Datapoints**
Miracle *et al.* [49]	2017	Phase and hardness	Yes	648
Gorsse *et al.**[210]	2018	Phase and hardness	No	370
Couzinié *et al.* [157]	2018	Phase	Manufacturing, but limited post-processing	340
Wen *et al.* [238]	2019	Hardness	Yes, as-cast vacuum arc melting only	155
Roy *et al.* [330]	2020	Phase	No	340
Borg *et al.* [211]	2020	Phase and hardness	Manufacturing, but no post-processing	1545 and 530
Machaka *et al.* [209]	2021	Phase	Yes	1360
Fan Xiaojuan *et al.* [97]	2021	Phase and hardness	No	155
Detor *et al.* [212]	2022	Hardness	Yes, as cast only	82
Han *et al.* [196]	2022	Phase	Yes, as-cast only	1138
Fan Xuesong *et al.* [331]	2023	Phase and hardness	Yes	245

* Corrigendum published in 2020 [279].

In 2017, Miracle and Senkov[49] published a critical review of HEAs. With this review a dataset of 408 different HEA compositions was assembled, which after including different processing conditions resulted in 648 total data entries. Importantly, also included in the dataset are the type of mechanical property analyses performed on 354 HEA compositions from a variety of processing conditions. However, while the type of mechanical property analysis conducted is reported, the recorded value is not. Thus, to obtain the hardness

value associated with these HEA compositions, the original references have been manually scraped. However, in some cases the values are not reported outside of a figure, are not openly accessible or are not there entirely. This highlights a critical issue in how HEA data is recorded and presented in publications, and subsequently within collated datasets.

Couzinié *et al.* [157] and Gorsse *et al.* [210] both published datasets in 2018. The dataset by Gorsse *et al.* [210], was part of the first iteration of the ML work, and thus is discussed extensively in Section 3.1. The data compilation by Couzinié *et al.* [157], contains the phase and mechanical properties of 122 refractory metal HEAs. However, as the available mechanical property data does not include hardness values, and no empirical conversion to hardness was to be applied in this iteration, these compositions were excluded from further consideration. Furthermore, the published article associated with this dataset does not include supplementary material or provide easy access the dataset in a usable format. Instead, the dataset requires manual extraction and conversion into a machine-readable format, as it is presented exclusively as an image-based table. While this was likely not the authors' intent, it underscores systemic limitations in how datasets are published in traditional journals and highlights the importance of adopting open and FAIR (Findable, Accessible, Interoperable, Reusable) principles for effective data curation [332].

Wen *et al.* [238] employed a support vector regression model with a radial basis function to predict HEA hardness using a dataset compiled from both literature sources and their own experimental results. This dataset was made publicly available and contains 155 datapoints of hardness from only as-cast HEAs in a machine readable format. However, one potential drawback of this dataset is that all the compositions lie entirely within the Al-Co-Cr-Cu-Fe-Ni system.

In 2020, Roy *et al.* [265, 330] assembled a dataset from existing literature of experimental HEA phase formation of 340 compositions. The data is in a machine readable format with the phase formation already in a partially simplified schema. One of the key sources for the data used in this study is the dataset produced by Couzinié *et al.* [157]. This is a key trend for several of the datasets appearing in Table 7.1, as they often build upon the previously compiled data. The Roy *et al.* [330] dataset was included, as prior to the datasets use for model construction, an additional step of data cleaning and duplicate entry removal was conducted. Furthermore, Borg *et al.* [211] published a dataset in 2020 containing 1545 entries with phase information and 530 values of hardness for the HEA

compositions. This dataset is the most expansive yet, with a significant increase in the amount of data included over previous iterations. The data is also provided in a machine readable format with simplified phase information. Any phase not labelled BCC, FCC, HCP, L12, or B2 are labelled as secondary phases.

The data compiled by Machaka *et al.* [209] used in the first iteration of the ML in this work is discussed in detail in Section 3.1. Also in 2021, Fan *et al.* [97] published an investigation to determine or corroborate a relationship between strength and hardness of HEAs, such as Equation 1.24 utilised by Huang *et al.* [98] and in the first ML iteration within this work. In addition to the hardness data, the Fan *et al.* [97] dataset also contains phase information for the 155 different compositions, thus is ideal for this collated dataset. However, this dataset is not provided in a easily machine readable format and is only provided in the form of a table within the pdf.

The smallest dataset included in this work was published by Detor *et al.* [212] in 2022. This dataset contains only original data not derived from literature on the hardness of 82 different refractory HEA compositions, produced via arc melting from elemental feedstock. In the same year, Han *et al.* [196] utilised a range of ML models to predict phase constitution by training on a dataset of 1138 HEA compositions in the as-cast condition collated from the literature.

It is apparent from Table 7.1, that while a constant stream of data collation and dissemination was occurring from 2017–2022, to the author's knowledge, a decline in this has occurred, with only one new dataset being published from 2023 and 2024. This is despite the constant growth of HEA publications over this time period. In 2023, Fan *et al.* [331] published an open dataset on fracture and impact toughness of 245 HEAs from the literature. However, this dataset also includes phase information for each composition and hardness for 90 of the HEAs included in the dataset. At the end of 2023, Peivaste *et al.* [333] compiled a comprehensive dataset comprising 5,692 experimental records drawn from across the entire HEA literature space. Using this dataset, a series of ML models were trained, with XGBoost and RF achieving a phase prediction accuracy of 86 %. To address the inherent class imbalance in the dataset SMOTE was employed.

Table 7.1 is not a exhaustive list of all experimental HEA datasets or publications containing phase and hardness information. Numerous additional HEA data sources were not

incorporated into the dataset used herein, as documented in several studies (e.g., [131, 143, 149, 156, 205, 208]). A multitude of reasons for not including these datasets include for example, phase formation information being far too simplified to be useful, such as only providing amorphous or solid solution and being unable to corroborate the original source of the data. In addition, it is common, especially for data published preceding the work of Islam *et al.* [203] in 2018, for the data to not be made available in a machine readable format. Finally, the main reason for the omission of the majority of HEA data from publications is that the data is simply not made publicly available and is instead "available upon reasonable request to the corresponding author", typically equates to the data not being made available [334]. This is not conducive to the facilitation of the growth of the materials informatics field and highlights the critical need for data and code from studies to be made publicly available.

7.1.1 Data Collation

The first step in creating the final dataset was to eliminate irrelevant entries and those with missing data. The retained information included alloy composition, phase, hardness, processing details, data source, and a unique identifier. Once isolated, the compositions were converted into a machine-readable format.

A critical complication in data collation stems from the lack of a standardised way to report HEA compositions, resulting in significant variability across datasets. For instance, compositions can be represented as $Al_{0.25}MoNbTiV$, $Hf_{0.75}NbTa_{0.5}Ti_{1.5}Zr_{1.25}$, CoCrMnFeNi, $Cr_{20}Fe_6Co_{34}Ni_{34}Mo_6$, $Al_8(CoCrFeMnNi)_{92}$, or $(Al_7Co_{24}Cr_{21}Fe_{24}Ni_{24})_{89}Cr_{11}$. Multiple frameworks may even coexist within a single dataset. This compounds the already present problem of knowing which samples are getting over-sampled into the dataset. Furthermore, individual elements can be separated by spaces, dashes, or no delimiter at all. To standardise these variations and split compositions into their constituent elements in atomic fractions, the Python module Regular Expressions (RegEx) was used. In addition to standardising alloy compositions, hardness values were converted to HV for consistency. Measurements in MPa or GPa were converted to HV by dividing by a factor of 9.807 for MPa or 9.807×10^{-3} for GPa. These steps ensured uniform formatting across all individual datasets, facilitating their integration into the final dataset.

The final combined dataset was then constructed by collating together all the data outlined in Table 7.1 via a simple concatenation process. Separate datasets for the phase and hardness data were constructed to enable training of two independent ML models, resulting in 5985 and 1585 data points respectively prior to the data cleaning process.

7.1.2 Data Cleaning

Once the dataset was assembled the data necessitated cleaning. The data cleaning process was primarily focussed on getting the data into a suitable format for ML: removing duplicates, fixing formatting errors, misspellings, etc. However, a compromise between data quantity and data quality was also a critical focus of the data cleaning process. Effective model training and improved generalisability require a large quantity of data, but this often includes inconsistencies or uncertainties inherent in the datasets, which may be detrimental to model performance. These include, for example, classes containing a single data point or inaccurate/unreliable data. The data cleaning workflows utilised for the phase and hardness datasets are detailed below and illustrated in both Figures 7.1 and 7.2 respectively.

The first step in the cleaning process of both datasets was the removal of exact duplicate entries. Next, the processing method was simplified to contain only as-cast entries. This decision was made because of the difficulty of integrating the large variety of processing conditions within the model training, highlighted by the lack of studies integrating manufacturing to ML investigations within the HEA field [205]. If only as-cast data is included, the model can be used to predict initial phase formation, with CALPHAD offering supplementary insights and the user responsible for determining appropriate heat treatment regimes and post-processing to optimise alloy properties. Subsequently, all duplicate HEA compositions were addressed to ensure that only unique entries remained in the dataset. For the hardness dataset, the duplicates were averaged, with the mean hardness value retained. Conversely, in the phase dataset, only the first occurrence of each duplicate composition was preserved. In the phase dataset, an additional cleaning step was required. After consolidating the constituent phase datasets, 220 unique phase designations remained. This presented a challenge for classification due to the large number of classes which included overlapping categories, formatting inconsistencies, varying levels of complexity, and, in some cases, insufficient information.

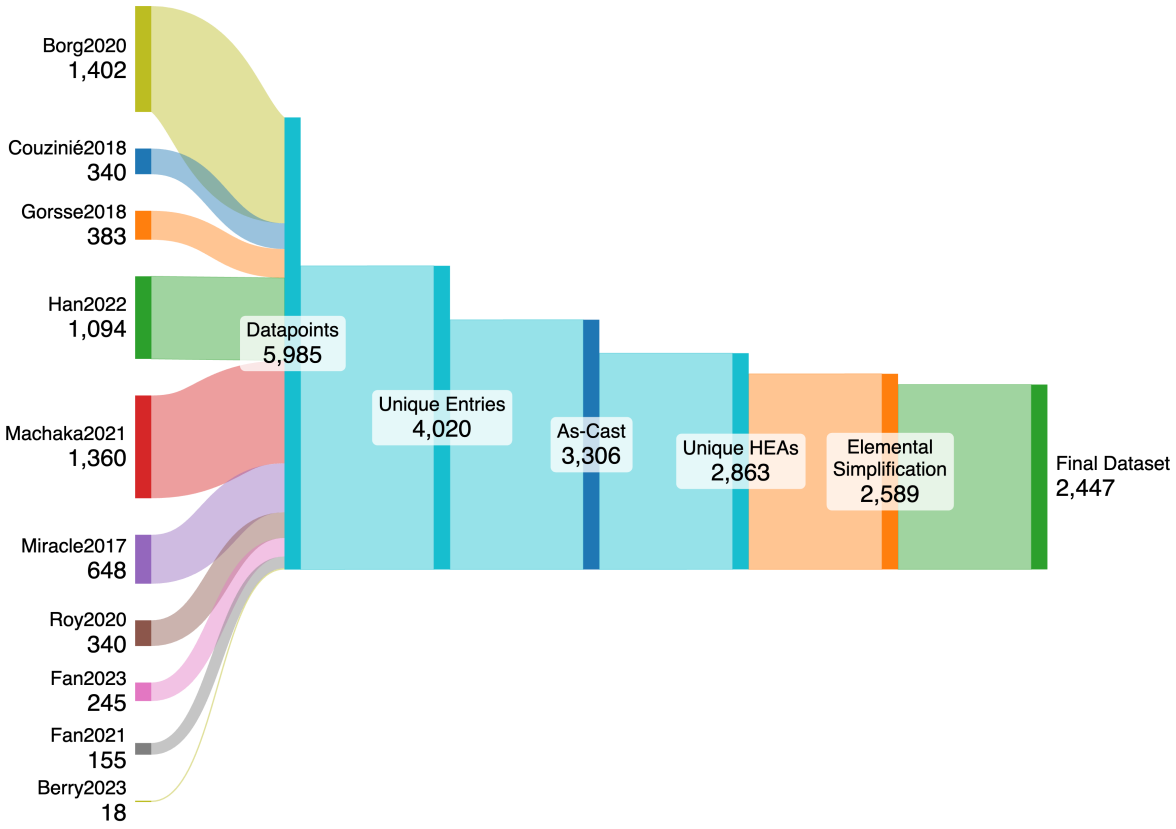


Figure 7.1: Sankey diagram illustrating the construction through collation, and data cleaning workflow for the phase dataset.

To improve the dataset's suitability for ML classification, the number of classes was systematically reduced. Phases containing multiple solid solutions with the same crystal structure were consolidated; for example, "BCC+BCC" was simplified to "BCC". Compositions lacking sufficient phase information, such as "unknown", "solid-solution", or "amorphous", were removed. Smaller classes were combined into broader categories; for instance, phases like "σ", "δ", "Laves" were grouped into a single class designated as "Im" (intermetallic). Additionally, compositions forming HCP phases were excluded due to their limited occurrence (24 instances), as HCP formation was not a focus of this study. These steps reduced the number of phase designations from 220 to 7. The simplified classes were determined following the classification framework of the dataset developed by Machaka et al. [209]. For both the hardness and phase datasets, specific elements were excluded based on several criteria: manufacturing challenges (e.g., Be, Bi, Cd, In, Ir, Os), high cost (e.g., Ag, Au, Pd, Pt, Re, Ru, Rh), classification as rare earth elements (e.g., Ce, Dy, Ho, Lu, Pr, Tb, Tm), consideration as minority additions best evaluated post-

downselection (e.g., B, C, N, O), limited data on intrinsic properties (e.g., Nd, Sb), and supply risk metrics, including HHI indices [287]. After applying this cleaning workflow, the final datasets contained 2447 and 672 unique as-cast HEA compositions for phase and hardness data, respectively.

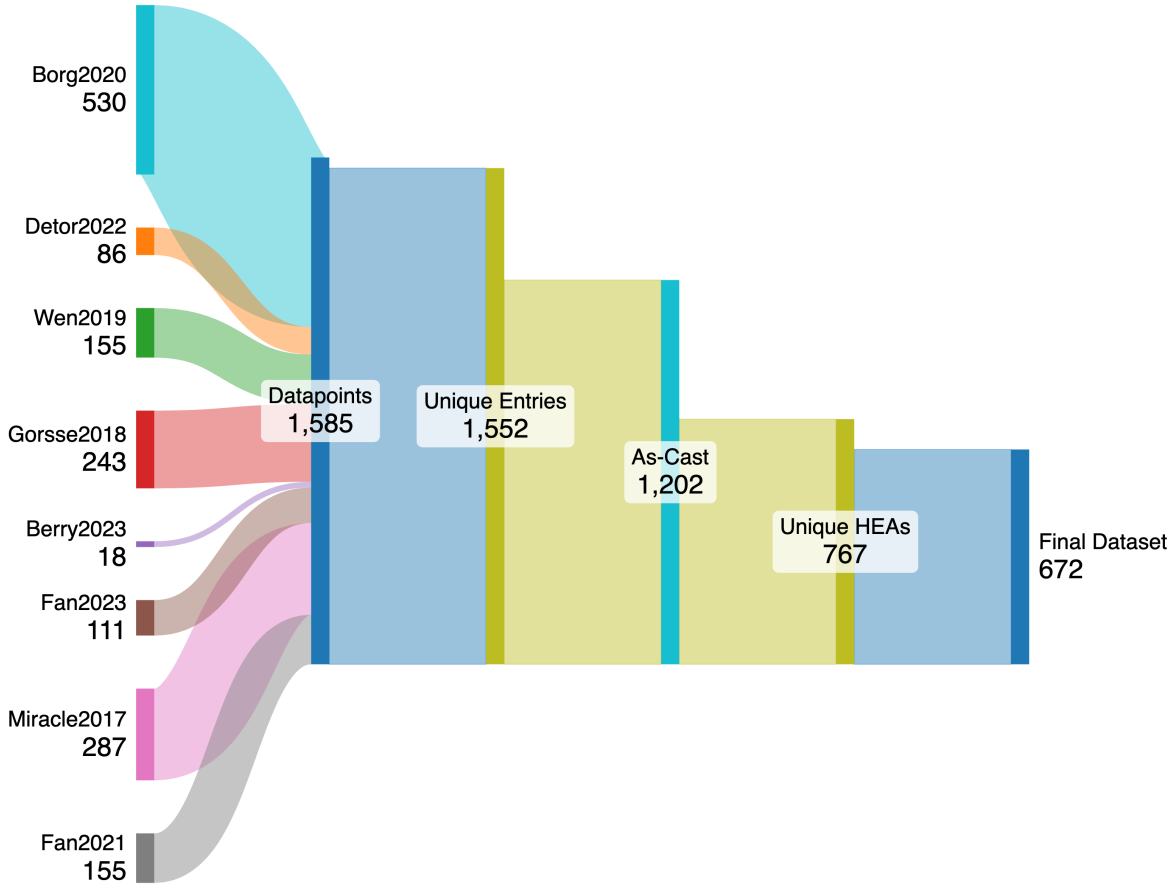


Figure 7.2: Sankey diagram illustrating the construction through collation, and data cleaning workflow for the hardness dataset.

7.1.3 Target Data Distribution Analysis

Before undertaking an ML task, it is critical to understand the structure of the data. Figure 7.3 presents a histogram of the phase distribution within the dataset, highlighting that the BCC phase is dominant, with a moderate class imbalance. This dominance of BCC is likely due to the inclusion of a significant amount of refractory HEA data, which commonly form BCC crystal structures. Class imbalance can negatively impact

model performance by biasing predictions toward the majority class, resulting in poor performance on minority classes and skewed evaluation metrics. To address this, strategies such as random oversampling or SMOTE were employed to balance the dataset and the impact on model performance assessed. The distribution of the hardness data is illustrated using a box and scatter plot in Figure 7.4.

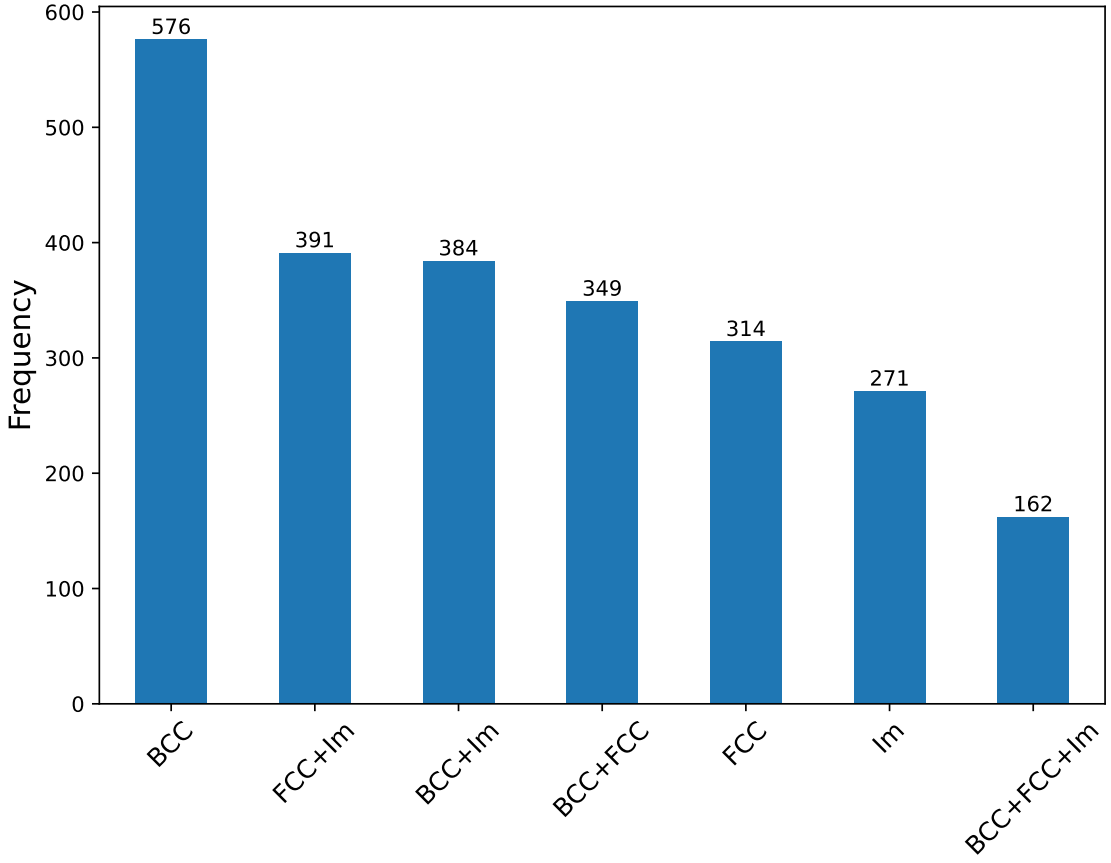


Figure 7.3: Histogram showing the distribution of the target variables within the constructed phase dataset. A moderate class imbalance is seen with BCC being the most represented class and BCC+FCC+Im being the least represented class.

The scatter plot in Figure 7.4 reveals that the hardness data is fairly uniformly distributed between 100 and 900 HV, with a single outlier detected exceeding 1000 HV. Upon closer inspection, this outlier corresponds to a composition with a significant amount of W, which likely accounts for its relatively high hardness. Since the point lies just outside the box plot whiskers and is not an extreme outlier, it was retained in the dataset. The box plot further shows that the median hardness is 486 HV, with a lower quartile of 318 HV and an upper quartile of 603 HV, resulting in an interquartile range of 285 HV. The maximum value is 1084 HV (the outlier), while the minimum value is 109 HV, marked by

the lower whisker. This range of hardness values aligns with expectations for the retained compositions and phases in the dataset. Compositions exhibiting hardness in the range of 1500—2500 HV were removed during the cleaning process. These compositions were primarily associated with significant C or B content, and/or involved extensive post-processing to achieve such high mechanical properties.

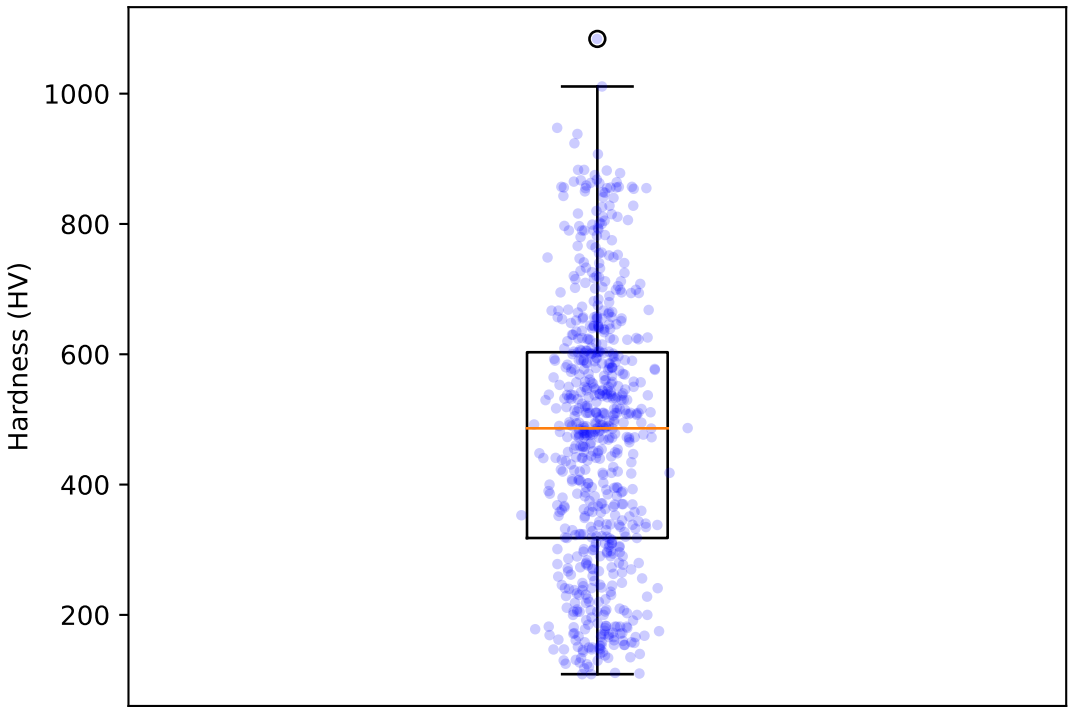


Figure 7.4: Box and overlaid scatter plot showing the distribution of hardness data and highlighting outliers.

7.2 Feature Engineering

The feature space used in the initial machine learning iteration, detailed in Chapter 3, was expanded to improve predictions of phase formation and hardness in HEAs. Additional features include the difference in melting temperature between constituent elements, denoted as ΔT_m; a geometrical parameter λ; shear modulus asymmetry $\Delta\mathcal{G}$; bulk modulus asymmetry $\Delta\mathcal{B}$; and average density ρ. The feature calculation process was also refined by adopting more reliable and traceable elemental constants [287]. The full feature set is presented in Table 7.2.

Table 7.2: The updated feature set used to mathematically describe the alloy compositions, enabling the ML models to make predictions on their phase formation and hardness [287]

Parameter Symbol	Parameter Name	Equation	Reference	
			Equation	Data
δ	Atomic Size Difference	$\delta = 100\sqrt{\sum_{i=1}^{n} c_i \left(1 - \frac{r_i}{\bar{r}}\right)^2}$	[85]	r_i [335–338]
γ	Atomic Packing Parameter	$\gamma = {\omega_S}/{\omega_L}$ $\omega_x = 1 - \sqrt{\frac{(r_x+\bar{r})^2 - \bar{r}^2}{(r_x+\bar{r})^2}}$	[85]	r_i [335–338]
$\Delta\chi$	Pauling Electronegativity Difference	$\Delta\chi = \sqrt{\sum_{i=1}^{n} c_i \left(\chi_i - \bar{\chi}\right)^2}$	[139, 146]	χ_i [338, 339]
VEC	Valence Electron Concentration	$\mathrm{VEC} = \sum_{i=1}^{n} c_i (\mathrm{VEC})_i$	[146, 147]	$(\mathrm{VEC})_i$ [340]
e/a	Number of Itinerant Electrons per Atom	$e/a = \sum_{i=1}^{n} c_i (e/a)_i$	[146, 153]	$(e/a)_i$ [147, 150]
ΔH_{mix}	Enthalpy of Mixing	$\Delta H_{\mathrm{mix}} = 4\sum_{i=1,i<j}^{n} c_i c_j \Omega_{ij}$	[85, 155]	Ω_{ij} [155]
ΔS_{mix}	Entropy of Mixing	$\Delta S_{\mathrm{mix}} = -R\sum_{i=1}^{n} c_i \ln c_i$	[85, 143]	
T_m	Weighted Melting Temperature	$T_m = \sum_{i=1}^{n} c_i (T_m)_i$	[156]	$(T_m)_i$ [338]
ΔT_m	Melting Temperature Difference	$\Delta T_m = \sqrt{\sum_{i=1}^{n} c_i \left(T_i - \bar{T}\right)^2}$	[341]	$(T_m)_i$ [338]
Ω	Yang Parameter	$\Omega = \frac{T_m S_{\mathrm{mix}}}{\lvert H_{\mathrm{mix}} \rvert}$	[156]	
λ	A Geometrical Parameter	$\lambda = \frac{\Delta S_{\mathrm{mix}}}{\delta^2}$	[159, 265]	
$\Delta\mathcal{E}$	Young's Modulus Asymmetry	$\mathcal{E} = \sqrt{\sum_{i=1}^{n} c_i \left(1 - \frac{E_i}{\bar{E}}\right)^2}$	[160]	E_i [338]
$\Delta\mathcal{B}$	Bulk Modulus Asymmetry	$\mathcal{B} = \sqrt{\sum_{i=1}^{n} c_i \left(1 - \frac{B_i}{\bar{B}}\right)^2}$		B_i [338, 342, 343]
$\Delta\mathcal{G}$	Shear Modulus Asymmetry	$\mathcal{G} = \sqrt{\sum_{i=1}^{n} c_i \left(1 - \frac{G_i}{\bar{G}}\right)^2}$	[265]	G_i [338, 343]
ρ	Average Density	$\rho = \sum_{i=1}^{n} c_i \rho_i$	[158]	ρ_i [338]

Within the table, quantities denoted with a bar indicate the average value, while quantities with an i indicate the *i'th* element. c represents the atomic fraction of the element, r denotes the atomic radii and E represents the Young's modulus. R is the molar gas constant. For γ, ω_x are dimensionless quantities related to the local packing efficiency around atoms with the largest and smallest radii in the alloy, represented by subscript L and S respectively. In ΔH_{mix}, Ω_{ij} is the enthalpy coefficient for elements i and j respectively. Following calculation of the feature space for the phase and hardness training data sets, three compositions had to be removed from the phase dataset and one composition from the hardness dataset due to a zero value of the enthalpy of mixing ΔH_{mix}, resulting in an infinite value for the Yang parameter Ω.

7.2.1 Feature Correlation Analysis

After constructing the feature space, PCC (Equation 1.25) was employed to evaluate multicollinearity among the parameters. Highly correlated features introduce redundancy, and one of the features can be removed based on model performance to mitigate overfitting. To visualise these relationships, two correlation heat maps were generated: one for the phase dataset (Figure 7.5) and another for the hardness dataset (Figure 7.6).

As evidenced by the two heat maps, the target variables were not included in the collinearity analysis. This decision allowed the focus to remain on the relationships among the features themselves, facilitating the identification of multicollinearity and redundant features. Alternative techniques to interrogate the relationship between the input features and target variables were performed after ML model construction. Additionally, in the case of the phase formation dataset where the target variable is categorical, Pearson correlation analysis was not appropriate as it assumes continuous numeric data. In this case, other tests such as analysis of variance would be required.

Determining an appropriate PCC cut-off value for identifying highly correlated features depends on the context and the degree of correlation within the dataset. For instance, in the first iteration of the ML analysis, the hardness dataset revealed a high positive correlation of 0.74 between the atomic size difference δ, and the atomic packing parameter γ. However, this correlation is anticipated, as both features are derived from the atomic radius of the constituent elements, but provide distinct perspectives on the atomic structure. Therefore, both features were retained. The strongest correlations occur be-

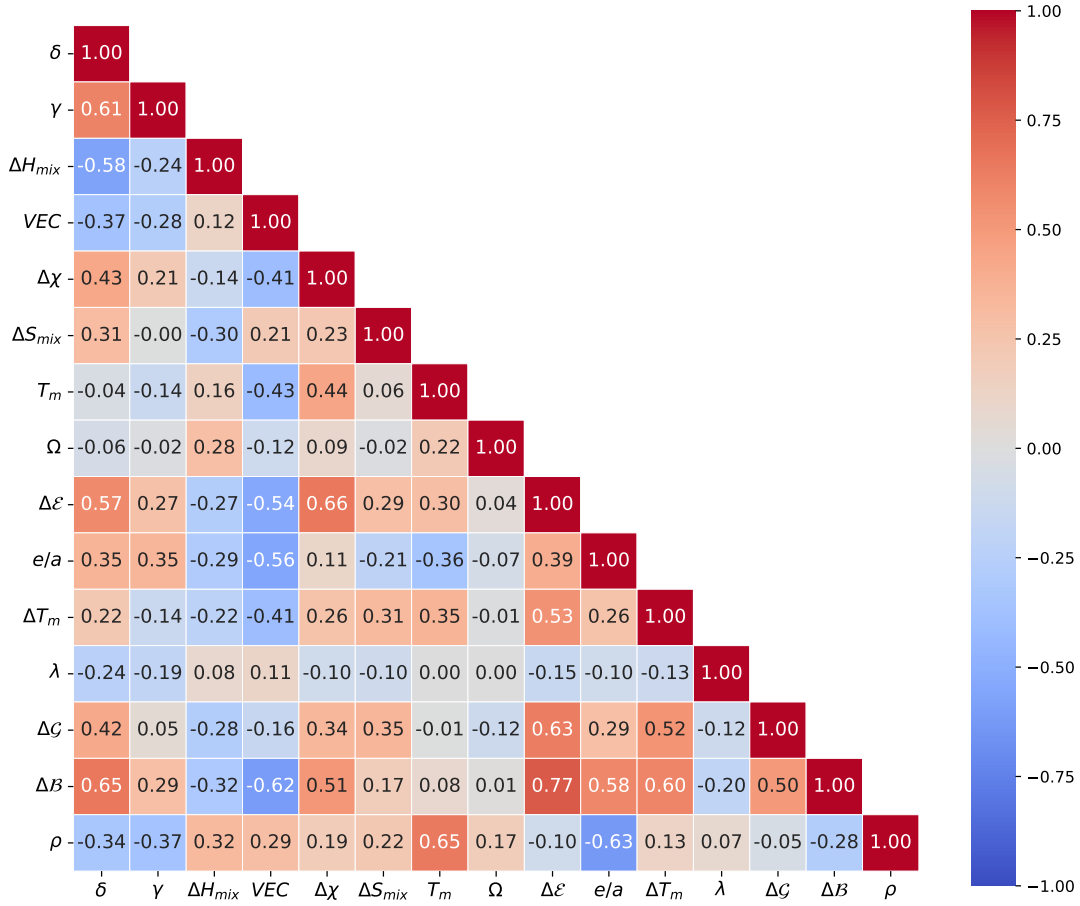


Figure 7.5: Correlation heat map between the features used as mathematical descriptors for the phase training dataset. The value in the grid shows the PCC between the different features and the colour intensity is proportional to the magnitude of the PCCs, with red denoting a positive correlation and blue denoting a negative correlation.

tween the bulk modulus asymmetry $\Delta\mathcal{B}$, and the number of itinerant electrons per atom e/a, and $\Delta\mathcal{B}$ and the Young's modulus asymmetry $\Delta\mathcal{E}$, with PCC values of 0.89 and 0.82 respectively. This is expected as the bulk modulus of a material is related to it's electronic structure and is an extension in three dimensions of the Young's modulus. To assess whether these features are strongly correlated, the distribution of the PCC data was investigated. A histogram of the correlation distribution for the features within the phase and hardness dataset is plotted in Figure 7.7.

The kernel density estimate of the hardness dataset correlations reveals two distinct peaks, indicating a cluster of strongly positively correlated features. Compared to the phase dataset, fewer features exhibit low correlation. $\Delta\mathcal{B}$, identified as strongly correlated with the two aforementioned features, was removed from the hardness feature set to reduce multicollinearity but retained for phase prediction.

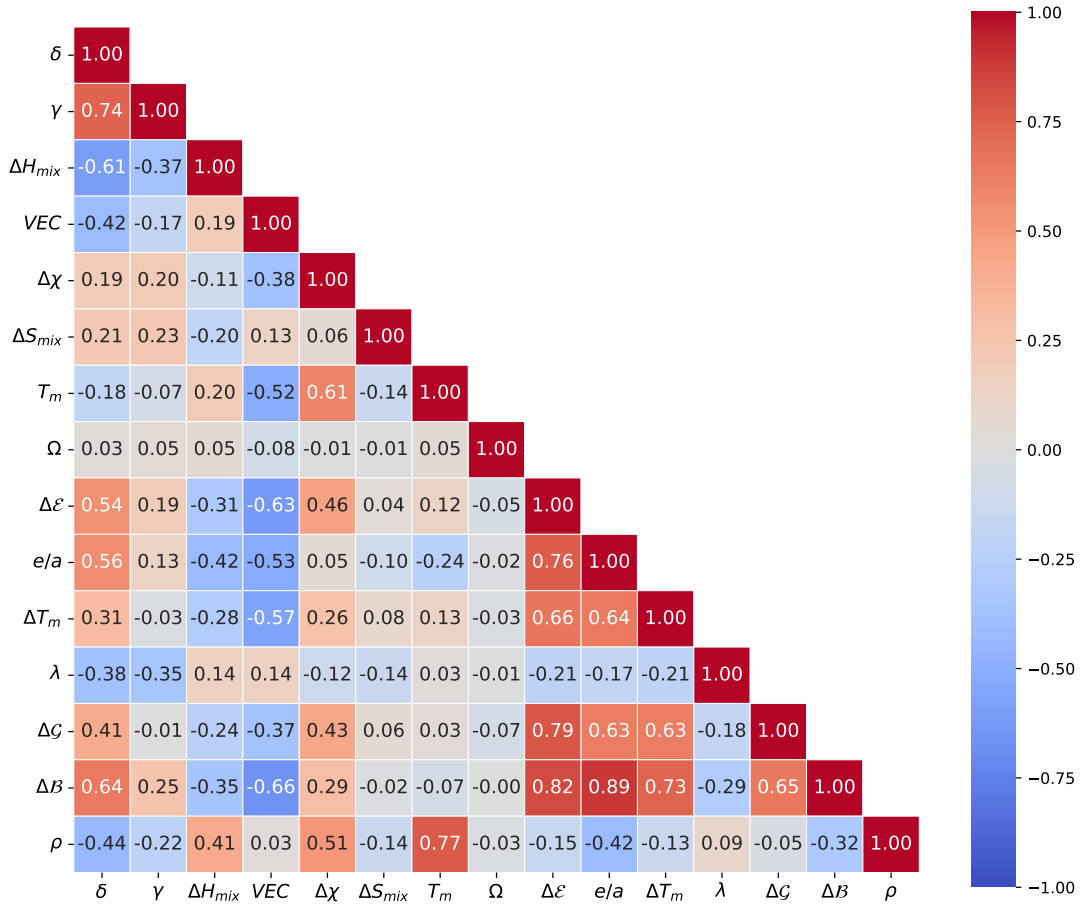


Figure 7.6: Correlation heat map between the features used as mathematical descriptors for the hardness training dataset. The value in the grid shows the PCC between the different features and the colour intensity is proportional to the magnitude of the PCCs, with red denoting a positive correlation and blue denoting a negative correlation.

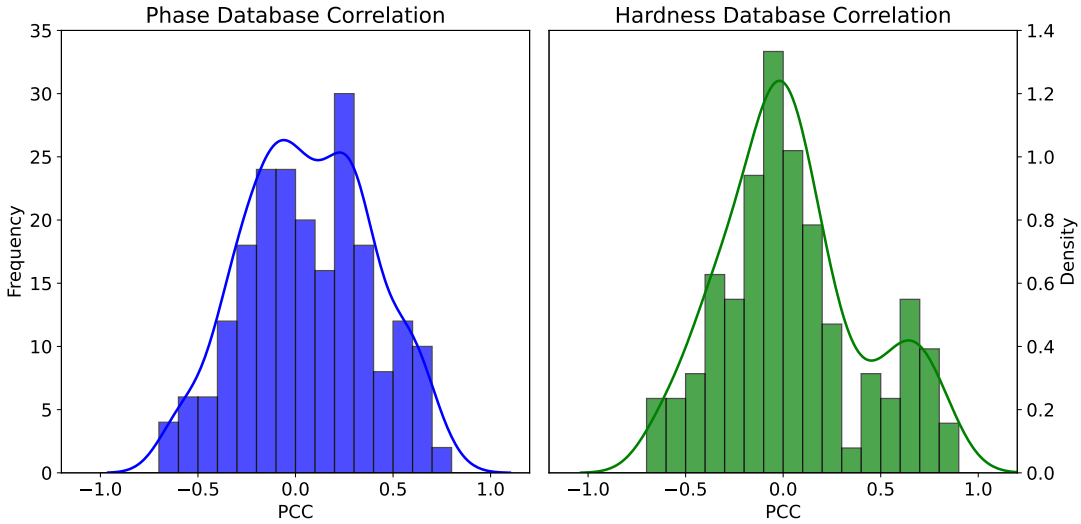


Figure 7.7: Histogram showing the distribution of correlation coefficients for the feature space of the phase and hardness datasets respectively. The line denotes the kernel density estimate, a smooth and continuos representation of the underlying distribution of the data, compared to the discrete bins of the histograms.

7.3 Machine Learning Model Selection

In the first iteration of the ML investigation detailed in Chapter 3, an RF model was chosen due to its performance on smaller training datasets, high level of interpretability, ability to handle both classification and regression tasks, and inherent resistance to over-fitting. However, as detailed in Section 1.6.7, the majority of ML studies within the HEA field trial a series of ML algorithms to find the one with the best performance for the provided data. Therefore, in this second iteration of the ML a range of different ML models were trialled including random forest (RF), support vector machines (SVM), extreme gradient boosting (XGBoost), k-nearest neighbours (k-NN), Gaussian process (GP) and artificial neural networks (ANN).

7.3.1 Model Training

All algorithms listed above were trained separately on the phase and hardness datasets to produce two independent models for each algorithm. The training process involved an 80 % training, 20 % testing split of the available data. All models were constructed using the Scikit-Learn [275] python package, except the neural network, which utilised Keras from the TensorFlow platform [276]. The models were subjected to feature normalisation and a cross-validated hyperparameter grid search to enhance performance during the training process. After the training procedure, each model was then tested on unseen data and its performance measured using the metrics described in Section 1.6.8. Finally a quick inspection of the feature importance, using the built in feature importance metrics for the decision tree based models and permutation feature importance for the other models, excluding the ANN, was performed. Both hardness and phase models were trained using the same methodology. However, the phase model was tested both with and without the application of the SMOTE technique, which synthetically increases under-represented cases in the dataset to improve class balance and potentially enhance model performance.

7.3.2 Hardness Model

The performance outputs of the hardness models are presented in Figure 7.8. An increase in R^2 and a decrease in both MAE and RMSE indicate improved model performance.

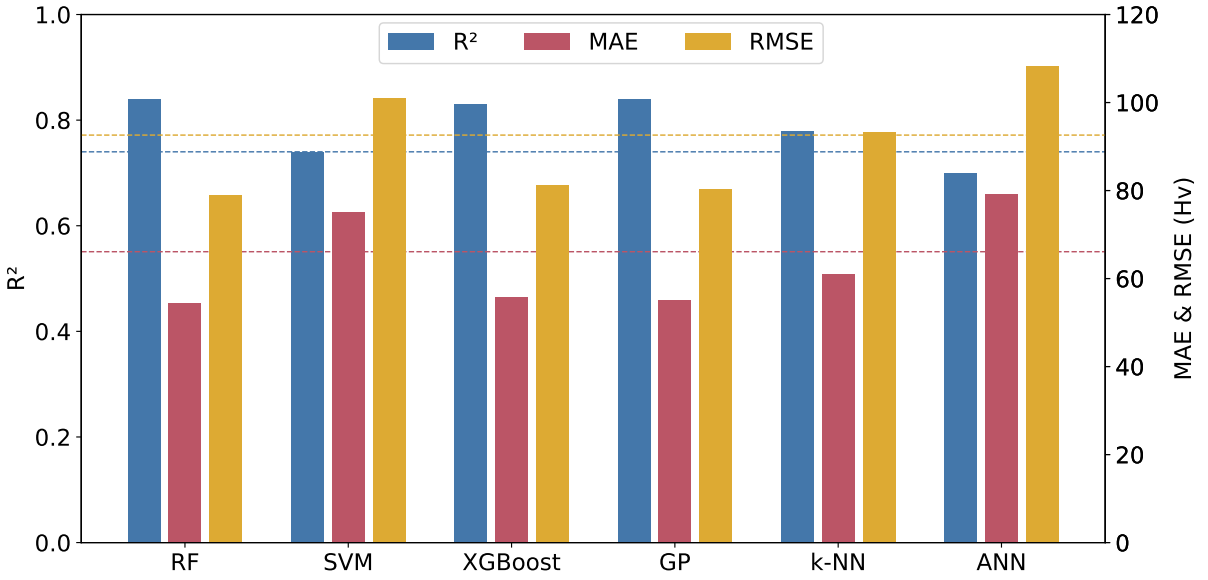


Figure 7.8: Bar chart demonstrating the prediction performance on the unseen test data of the ML models trained on the new expanded HEA hardness dataset. The dashed horizontal lines indicate the performance of the first iteration RF model trained on the Gorsse *et al.* [210] dataset.

As indicated by Figure 7.8, the RF, XGBoost, and GP models all demonstrated comparable performance and showed a marked improvement over the earlier RF model trained exclusively on the hardness dataset compiled by Gorsse *et al.* [210]. The overall best performing model was found to be RF, with an R^2 and MAE value of 0.84 and 54.5 HV respectively, compared to 0.74 and 66.1 HV for the first RF iteration. However, the improvement in model performance was relatively modest, despite the significant enhancements in data quality, quantity, and completeness, as well as the more rigorous data cleaning process and expanded feature set. In the first iteration there was a significant amount of imputed or empirically calculated data. Of the 370 total datapoints in the Gorsse *et al.* [210], only 235 contained actual reported hardness values, with some of these originating from duplicate compositions. Therefore, with the omission of missing data and removal of duplicate compositions by averaging the reported hardness values, the overall data quality of the dataset has improved. These results demonstrate the overall success of the collation of hardness data from across publications in the HEA space to improve the available training data and enhance prediction power of ML models. However, the results of the SVM and k-NN models indicate that these models are not as suitable for this hardness regression task, performing similarly to or in some cases worse than the first iteration RF model. These models are more suited to classification tasks

due to their hyperplane and clustering methodologies. The ANN performs the worst out of all the selected models and significantly worse than the original RF model. As stated previously, this result was anticipated due to the low quantity of data and relatively low complexity of the ML task. ANNs perform best on large amounts of data, typically in excess of multiple thousands of datapoints, compared to the 672 available in this dataset. Additionally, ANNs perform well on highly complex tasks such as image recognition or natural language processing.

Results of the permutation feature importance indicate that all models tested place high importance on both atomic size difference δ, and valence electron concentration, VEC, as in the first iteration of the RF model in Figure 3.3c. However, in the first ML iteration the single most important feature of the hardness model was $\Delta\mathcal{E}$, the Young's modulus asymmetry. In the updated models, this feature has been replaced by $\Delta\mathcal{G}$, the shear modulus asymmetry. Figure 7.9 illustrates the corresponding feature importances, as extracted from the XGBoost model trained on the hardness dataset. Additionally, the melting temperature difference, ΔT_m, another of the new features, is found to rank highly in the feature importance assessment of the hardness predictions. This indicates the success of the updated feature space as the new features have been found to be influential in the models predictions, in some cases replacing the original features as the most important in defining model outputs. In all models, the Yang parameter Ω had negligible influence on predictions and was therefore removed, resulting in a slight performance improvement in tree-based models and no significant change in others.

7.3.3 Phase Model

The accuracy scores following the training process for the phase models, with and without SMOTE data augmentation are shown in Figure 7.10. Additional performance outputs such as precision, recall and F_1 scores were also measured, but for simplicity in discussion, only the accuracy scores are shown as all metrics displayed equivalent behaviour. Despite the increased quantity of data, more rigorous data cleaning process and improved feature set, the performance metrics for all models trained on the phase data demonstrated a significant reduction when compared to the RF models trained in the first iteration. The best performance was obtained from the XGBoost model with a prediction accuracy of 62.5 % on the unseen test set. Due to the imbalanced nature of the phase data set,

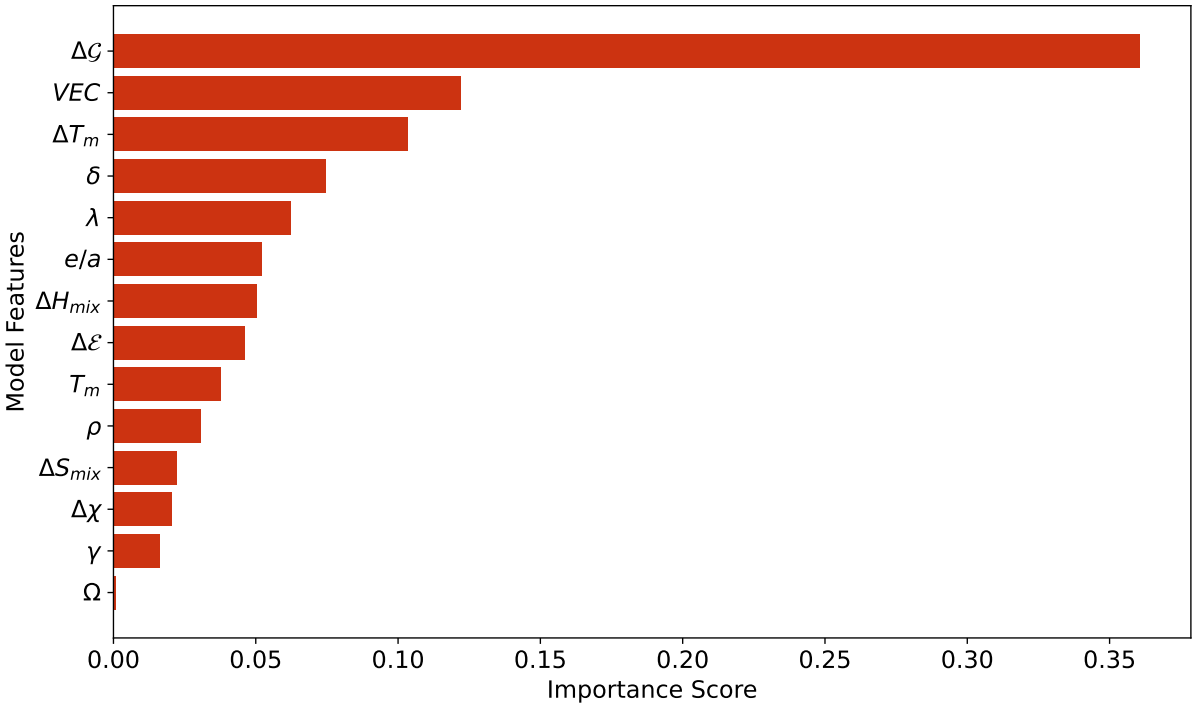


Figure 7.9: Feature importance from the XGBoost ML model predicting hardness of HEA compositions. Highlights the importance of the shear modulus asymmetry $\Delta\mathcal{G}$, and relative lack of impact on predictions of the Yang parameter Ω. Following this assessment, Ω was removed as a feature from all the models and a slight increase in performance was observed in the tree based models.

shown in Figure 7.3, and low performance across all ML algorithms trialled, SMOTE was utilised to balance the data across the seven classes and improve model performance. A variety of other techniques, such as principal component analysis, and the construction of ensemble models, were also trialled, but without success. Applying the SMOTE method to the data resulted in an increase in model performance across the board, as demonstrated in Figure 7.10. The best-performing model with the use of SMOTE was still XGBoost, with performance increasing marginally to an overall accuracy of 70.0 % from 62.5 %. However, this is still significantly lower than the overall average accuracy of 80.0 % obtained from the two RF models trained on the original Gorsse *et al.* [210] and Machaka *et al.* [209] datasets. As seen in Figure 7.10, all ML algorithms trialled on the new expanded phase dataset demonstrate similar levels of predictive performance on the unseen test data. Furthermore, results of the permutation feature importance, shown in Figure 7.11, indicate that all models tested place high importance on VEC, in good agreement with the literature and first iteration of the RF models in Figures 3.3a and 3.3b.

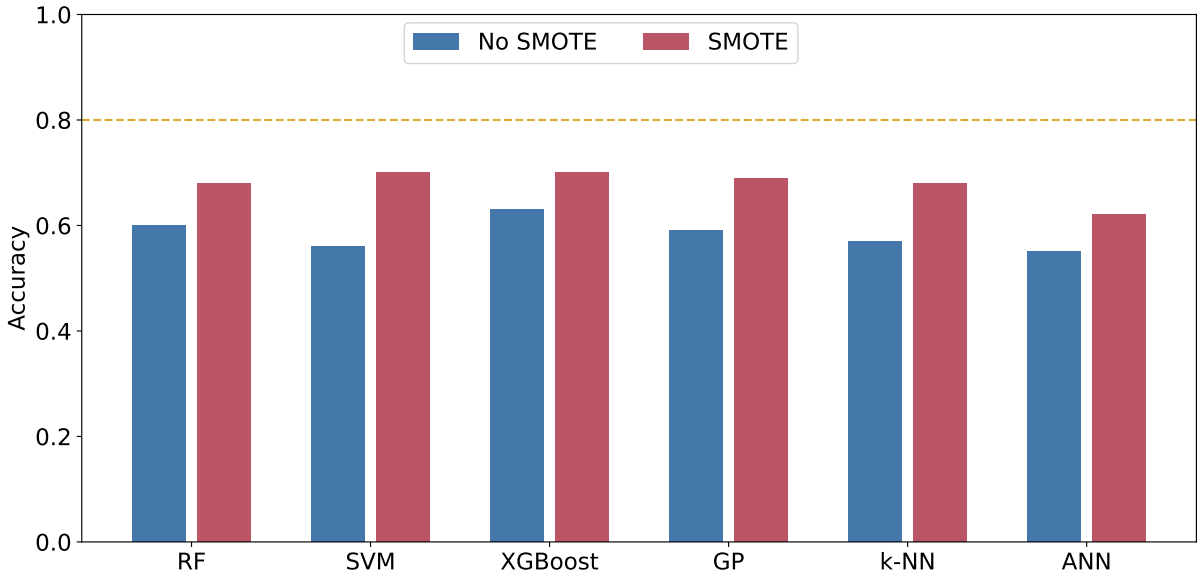


Figure 7.10: Prediction performance on unseen test data of the ML models trained on the new expanded HEA phase dataset. The dashed horizontal line indicates the average accuracy of the first iteration of RF models trained on the Gorsse *et al.* [210] and Machaka *et al.* [209] datasets.

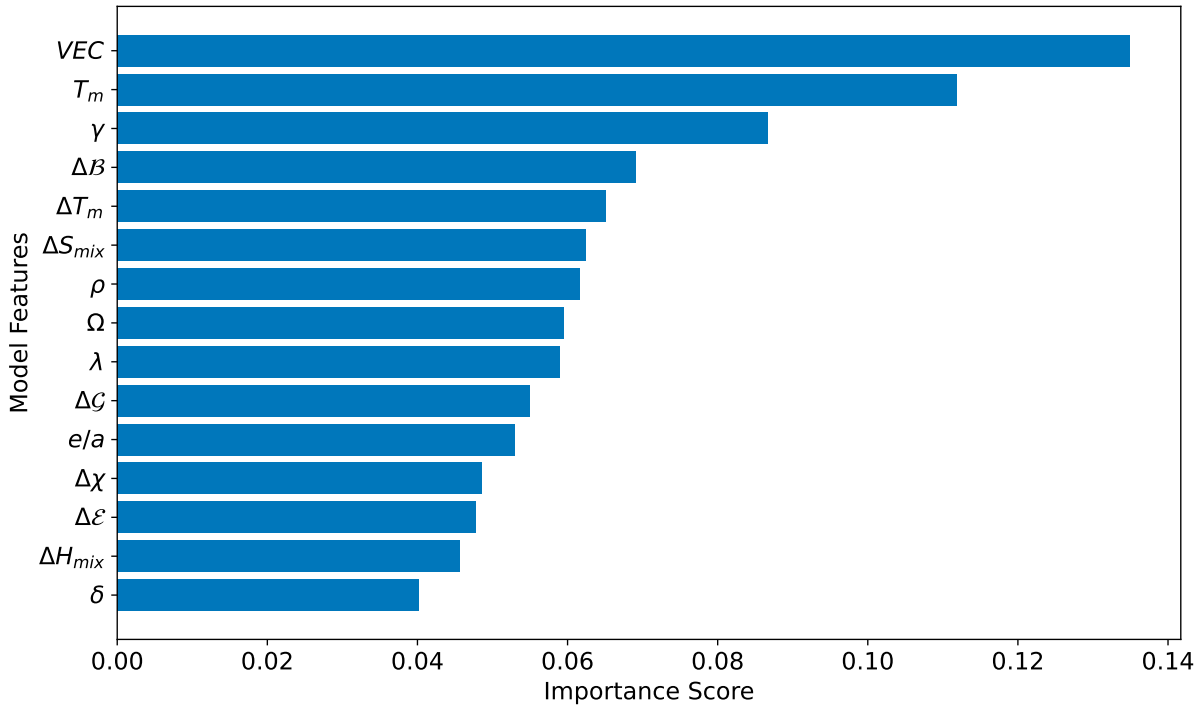


Figure 7.11: Feature importance from the XGBoost model predicting phase formation. Highlights the importance of VEC and overall effectiveness of all features included within the model training.

7.3.4 Analysis of Phase Prediction Model Performance

The performance results of the ML models trained on the expanded phase dataset indicate that increasing the amount of HEA data to train the models, does not directly equate to an improvement in performance, even in the case when all the data is collated from publications in scientific journals. This result strongly aligns with findings by Ottomano *et al.* [220], who reported that collating materials data from diverse sources reduced the performance of classical ML models, similar to those used in this work. In a similar manner to this work, they explored property prediction from literature-curated datasets spanning a wide range of compounds; however, their study also included simulated data such as DFT [344], whereas this thesis focuses solely on experimentally derived data.

In contrast to phase prediction results, as discussed earlier in Section 7.3.2, an expanded hardness dataset did result in an overall increase in model performance. However, the improvements observed for the hardness models are limited when considering that the amount of hardness data available has increased by almost 2.8 times over the first iteration. Additionally, hardness is a continuous numerical quantity and thus its reporting is much more consistent. In contrast, as evidenced in the data cleaning phase during construction of the expanded phase dataset, there are a significant number of viable ways of reporting observed phase formation with varying degrees of complexity. Furthermore, the prevalence and bias towards certain phases, resulting in significant class imbalance, compounds to make the phase classification task significantly more complex than the hardness task.

Therefore, the hardness models have shown that when expanding the quantity of training data, considering the quality of data is important. HEA phase data reported in the literature is inherently low quality. This low quality of data is evidenced by the low performance scores when evaluating the models on the very data it has been trained on. A very high performance accuracy score close to 100 % would be anticipated as the model has seen this data during the training phase and should have learned the trends and patterns within the training data. However, across the models, the average training accuracy is only 91.1 % and 79.3 % with and without SMOTE respectively. This result indicates an inherent problem with the data present within the dataset as the model cannot effectively predict the data that it has been trained on. Therefore, it would be highly unlikely that the models would be able to produce high prediction accuracy on

new unseen data. There is also significant overlap between experimental HEA datasets, with more recently published datasets referencing prior datasets as the source of data. Furthermore, there are often conflicting reports of what phases are present for the same HEA composition. This can be due to the impact of the manufacturing process, which is only sporadically reported, or simply due to conflicting results. Unlike the hardness data, where duplicate entries for a specific HEA composition can be averaged to account for multiple hardness measurements, this approach is not feasible for phase formation data. Instead, only the first reported phase for each composition was retained in the dataset. While not ideal, this method was the most time-efficient solution given the lack of alternative metrics for assessing data quality and accuracy. Following removal of duplicate compositions, compositional overlap still remains within the dataset, particularly in the case of very small deviations in composition being reported with different phase formation. This is evidenced by Figure 7.12, which demonstrates the prevalence of a small number of elements across the compositions within the dataset. Furthermore, by adding together data from different sources, such as refractory and non-refractory HEA datasets, HEA compositions at the extremes of the compositional space are being collated together with ML models attempting to make accurate predictions across the whole compositional space. For instance, compositions containing refractory elements such as Hf, Ta, and W represent only a small fraction of the dataset compared to those with more common transition metals like Fe, Ni, and Cr. As a result, predictions for refractory-containing alloys are expected to be less reliable due to the limited representation in the training data.

A crucial step in preparing input data for ML is data cleaning, which, for the phase dataset, includes the phase simplification process. Unlike the initial iteration of the ML, where the default phase representations from each dataset were used, this approach was not feasible for the expanded dataset. As noted earlier, the collation process resulted in 220 “different” phase classes. Far too many for an ML model to make accurate predictions given a training dataset of approximately 2000 data points. Moreover, many of these classes do not represent distinct phases, but are instead inconsistent ways of conveying the same information. Thus, the number of phase classes was simplified by omitting some compositions with certain phase formation and compressing other phases together, as described in Section 7.1.2. From the large number of original phase categories, the final ML-ready dataset was reduced to just seven classes, shown in Figure 7.3. A key step in

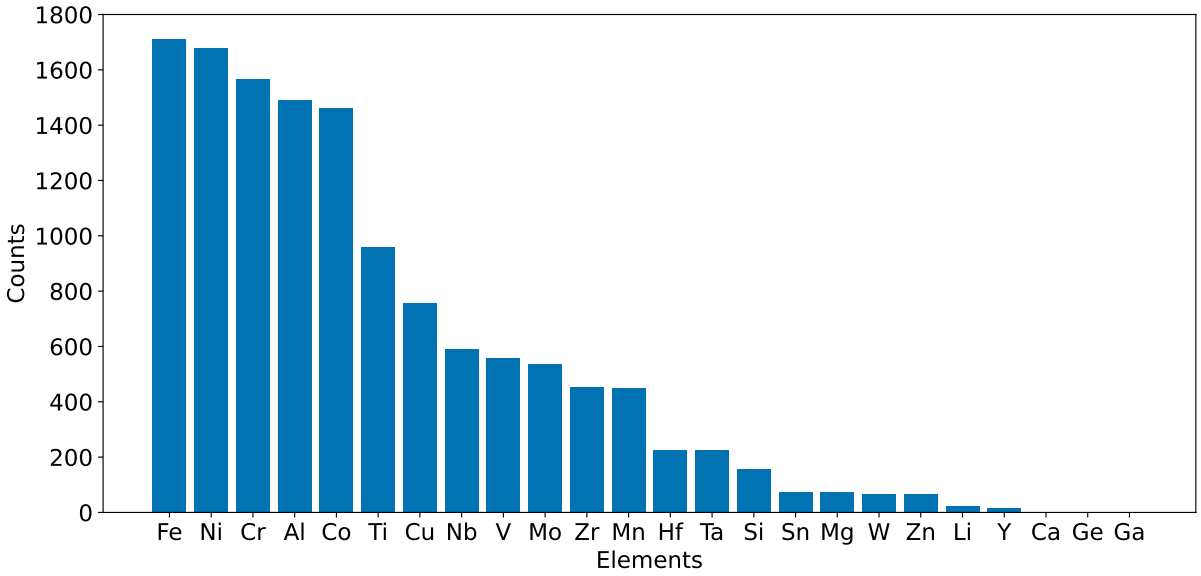


Figure 7.12: Bar chart illustrating the appearance of different elements within the constructed phase dataset. Highlights the dominance of a small number of elements within the dataset, namely Fe, Ni, Cr, Al, and Co.

this simplification process, which significantly impacts model performance, is the grouping of phases such as B2, Laves, and $L1_2$ into a single category labelled "Im", intermetallic. However, analysis of the feature distribution pair plots in Figure 7.13 suggests that this approach may not be optimal for reducing the number of classes in a way that benefits the ML models. The diagonal panels, which display histograms, reveal that the phases of the HEAs cannot be distinctly separated by clear boundaries within any single feature. However, the off-diagonal panels, portraying scatter plots of phase distributions as a function of feature pairs, do demonstrate some clustering of BCC and FCC phases at opposing sides of the feature space. In contrast, Im, which encompasses a diverse range of phases, is dispersed across the feature space, complicating the classification process.

Figure 7.14 shows a scatter plot based on the VEC–T_m coordinate system displaying the distribution of the seven phase classes across the feature space, taken from 7.13 and viewed in greater detail. This illustrates the distribution across the feature space and demonstrates the overlap of compositions close in the feature space but with different phase formation. The Im class and classes containing Im are widely distributed across all corners of the feature space due to the collation of a variety of different phases such as B2 and the various forms of Laves phases. Whereas for phases such as BCC and FCC, some clustering can be observed. In contrast to the distribution of phase classes across the feature space, Figure 7.15 illustrates a snapshot of the distribution of the hardness

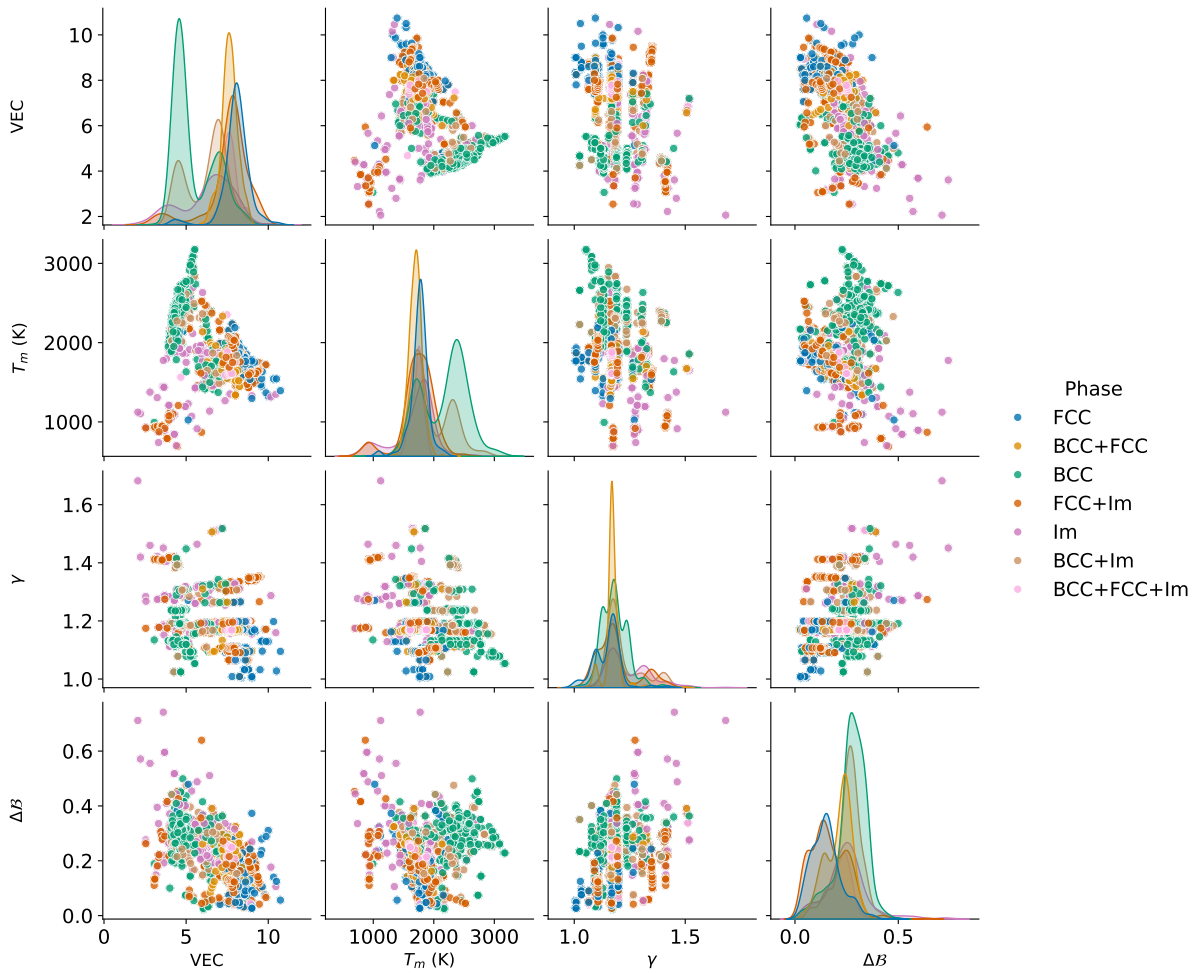


Figure 7.13: Scatter plots showing the distributions of the seven phases as a function of a pair of the four most important features in the XGBoost phase model. The histograms on the diagonal show the distribution of the phases at different feature values.

across the feature space. It is clear from Figure 7.15, that the distribution of the hardness data is more systematically clustered than the phase data. Resulting in the improved performance over the first iteration of ML models demonstrated in Figure 7.8, despite the collection of data from a variety of sources.

Without implementation of this phase labelling schema, the number of classes becomes too large, with many containing few entries, substantially hindering model performance. Consequently, many studies condense the problem by reducing it to a binary or ternary classification task [98, 196, 203, 231, 248]. These models typically predict whether a solid solution forms, or distinguish among solid solution, intermetallic, or amorphous phases. While this simplification can enhance predictive accuracy, it often comes at the cost of losing detailed insights into phase constitution.

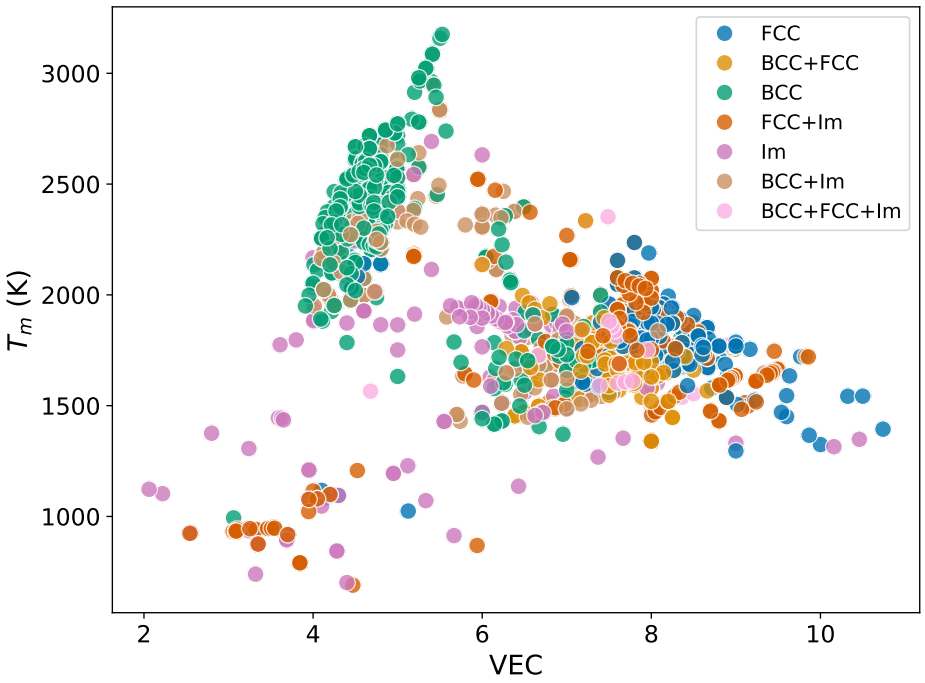


Figure 7.14: Scatter plot showing the distributions of the seven phases as a function of VEC and T_m, the two most important features in the XGBoost phase model.

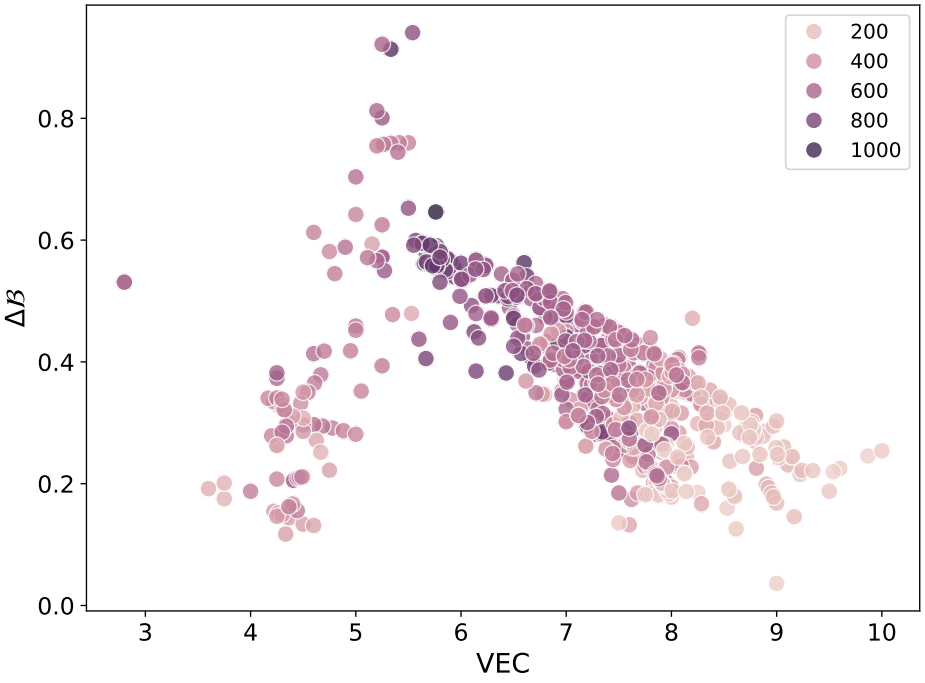


Figure 7.15: Scatter plot showing the distribution of the measured hardness as a function of VEC and $\Delta\mathcal{B}$ the two most important features in the XGBoost hardness model.

7.3.5 Limitations and Opportunities for Model Enhancement

Despite the extensive collation of HEA data from the literature, the underlying issue of a lack of data cannot be avoided. Starting with 5985 data points, the cleaning process removed 2408 entries, either as exact duplicates or duplicate compositions. This reduction does not account for additional exclusions stemming from the wide variety of manufacturing methods and processing conditions, which further narrow the available dataset. Compounding this issue is the significant imbalance in the distribution of the collated data, a key challenge for effective ML application.

Moreover, as demonstrated in this study and by Ottomano *et al.* [220], simply increasing the amount of data does not guarantee improved model performance or predictions. Adding data from unrelated systems with vastly different compositions, microstructures, and mechanical properties, reflective of the broad HEA space, often detracts from model accuracy. Instead, a more targeted approach, for example narrowing the dataset to well-defined smaller systems may offer a better path forward. This would allow ML to focus on exploring the uncertainties within a specific compositional space. Thus, improving data quality and ensuring its distribution across strategically important areas of the HEA field are essential for unlocking greater insights through ML.

Furthermore, there is a discussion as to the purpose of the application of ML to the HEA field and this intention needs to play a key role in decision making when constructing an ML based HEA task. Is it to optimise a chosen systems composition or narrow the total HEA space? These two tasks are not mutually exclusive, but differ significantly in the way the models need to be set up and the input data handled. In the case of this study, the objective was to cast a wide net and narrow the total unexplored HEA space. Therefore, the collation of data from a wide range of sources was a logical step. However, within this task of narrowing the unexplored regions of HEA space lies an important distinction: Is the aim of the model to highly accurately predict phase formation and mechanical properties, or to provide an informed direction for exploration within the compositional space? In this case, the goal of the application of the ML was to provide direction to search for new HEA compositions, even if the predictions themselves are not necessarily of the highest accuracy. The subsequent coupling with CALPHAD assessments enabled further insights to be collected on HEAs after the wide area screening of the ML models. However,

these were also found not to be perfectly accurate. In any ML task there are a significant amount of decisions to be made. In the first instance of the application of ML within Chapter 3 a number of decisions are made from an ML optimisation perspective and not a materials design perspective, such as the maximisation of data at any cost by ignoring manufacturing. In this second iteration, a more rigorous materials informed approach was taken towards the data cleaning process; eliminating data based on manufacturing methods used, elemental content, phase formation, etc. An improved feature space was also utilised. However, the end result is a model with significantly lower performance. Exploring the uncertainty within the HEA compositional space through applications of Bayesian optimisation, combined with an appropriate loss function, could be a more appropriate approach to help identify compositions in unexplored regions and minimise the existing gaps. Although the accuracy of the ML model has declined, the true performance of its predictions, particularly for novel compositions within a virtual candidate search space, remains uncertain. Validation through experimental investigations would be required to determine how well these predictions reflect real-world phase formation.

7.4 Summary

In the first iteration of the ML framework, presented in Chapter 3, the primary challenge identified was the low quantity and quality of available data, which significantly impacted model performance and predictive reliability. To address this limitation, a second iteration of the ML approach was developed with the aim of improving predictive accuracy and broadening the scope of the virtual candidate search space. This updated framework was designed to work in tandem with an enhanced CALPHAD procedure, incorporating high-throughput thermodynamic assessments via TC-Python and the integration of updated databases such as SSOL12 and TCHEA7. The refined approach aimed to facilitate the identification and selection of additional HEA compositions for experimental testing, aligned with the established design criteria for wear-resistant and damage-tolerant alloys, using hardness and phase composition as key proxies for these properties.

Building on the findings from the first ML iteration, several key improvements were implemented in the second iteration to address the identified limitations. Foremost among these was the creation of an expanded dataset, compiled from a broad range of literature

on the experimental assessment of HEAs, to increase both the quantity and diversity of available data. The feature set was also significantly enhanced by including new features, alongside more accurate calculations and improved traceability, to provide a more comprehensive representation of the alloy properties. A more rigorous data cleaning process was applied, removing inconsistent data to ensure a higher-quality dataset for ML analysis. Furthermore, rather than preselecting an RF model as in the first iteration, a wider range of ML models were evaluated to identify the one with the best predictive performance. These enhancements collectively contributed to a more robust and effective approach to tackling the design challenges of HEAs.

Despite the more robust approach, only a marginal increase in performance was observed for the hardness prediction model. The best-performing model, again an RF algorithm, achieved an R^2 value of 0.84 and a MAE of 54.5 HV. This represents an improvement over the first iteration, which achieved an R^2 of 0.74 and an MAE of 66.1 HV. However, this relatively modest enhancement in performance was surprising, given the over 2.8-fold increase in dataset size and the notable improvement in data quality, achieved by eliminating empirical calculations and imputed data.

More critically, the phase prediction model in the second ML iteration demonstrated a decrease in performance compared to the first iteration. The model achieved accuracies of 62.5 % and 70.0 % on the unseen test set for an XGBoost model with and without the application of SMOTE, respectively. These results were substantially lower than the average accuracy of 80.0 % observed in the first iteration. This decline occurred despite the collation of a larger dataset, a more thorough data cleaning process, and an improved feature space. This outcome aligns closely with the findings of Ottomano *et al.* [220], which suggest that increasing the amount of data for training, especially by collation from various sources, does not necessarily lead to improved model performance. The phase model's performance on the training data itself produced accuracies of 91.1% with SMOTE and 79.3 % without SMOTE, further indicating an underlying issue with the training data.

These outcomes, for both the hardness and phase models, highlight the persistent challenges associated with developing predictive models in the complex and diverse HEA design space, even with substantial advancements in data preparation and feature engineering. The reduced performance of the phase prediction model can be attributed to

several issues associated with the collation of experimental HEA phase data. Due to the wide variability in how phase formation is reported in the literature, both in terminology and classification, the number of phase categories was consolidated to ensure the dataset was appropriate for ML. However, this condensation often grouped phases with distinct feature space characteristics into the same categories, complicating classification. Additionally, combining datasets from different HEA types, such as transition metal and refractory HEAs, further increased the complexity of the classification task. Compounding these issues is the large quantity of duplicate compositions, reflecting a lack of exploration across the HEA design space. Managing these duplicates is particularly challenging when different studies report conflicting phase information for the same composition, introducing additional uncertainty. Thus, insufficient data coverage remains a fundamental issue across the vast HEA compositional space, severely limiting the model's ability to learn and generalise effectively.

Consequently, improving data quality and ensuring its distribution across strategically important areas of the HEA field are essential for unlocking greater insights through ML. Addressing issues such as the lack of standardisation and the insufficient exploration of the compositional space will be critical in enabling ML to realise its full potential in guiding the design of HEAs with targeted properties.

Chapter 8

Concluding Remarks

This project aimed to design novel metallic alloys for metal tooling applications, a field currently dominated by WC-Co cemented carbides. To identify viable alternatives, the potential for HEAs to meet key requirements such as wear resistance, damage tolerance and suitability for AM was investigated by leveraging ML methodologies to rapidly screen the vast HEA compositional space. Thus, the work performed in this study was divided into two distinct sections. Firstly, the construction and development of a coupled ML and CALPHAD methodology to enable screening of the vast HEA compositional space, and secondly the experimental analysis of the downselected HEA compositions from the computational investigation.

In Chapter 3, a series of RF models were constructed and trained from publicly available experimental HEA databases to predict phase formation and hardness across the vast HEA compositional space. These properties were chosen as proxies for the ductility, damage tolerance and wear resistance required by materials for tooling application. Three RF models were trained across the two publicly available databases, achieving an average phase prediction accuracy of 80.5 % and an R^2 score of 73.7 % for hardness. The models were then used to make predictions on unseen data across an expansive virtual candidate search space of over 2 million HEA compositions. This was reduced to approximately 24,000 HEA compositions predicted to form FCC structures by the ML, with CALPHAD then being employed as a tool to provide supplementary insights to phase formation and guide the alloy downselection process for experimental characterisation. FCC phase

compositions were targetted to enable enhanced ductility within the alloys and to aid in their suitability for AM. The result of this work was the downselection of nine novel HEA compositions for experimental investigation to both validate the ML and CALPHAD methodology and more importantly assess their suitability for the design case.

Building on this work, Chapter 4 presents the results of the experimental characterisation of the nine downselected HEA compositions microstructural and mechanical properties. Although most alloys exhibited an FCC solid solution as predicted by the ML, all alloys also displayed significant intermetallic phase formation, which persisted through homogenisation treatments. Furthermore, the results of the hardness measurements align with the microstructural observations, with the alloys containing higher fractions of intermetallics exhibiting increased hardness.

Chapter 5 contains a more in depth discussion on the results of the ML and CALPHAD investigation and their relationship with the findings of the experimental characterisation. As demonstrated in Chapter 4, none of the fabricated alloys exhibited the single-phase FCC microstructure predicted by the ML model. Three alloys primarily formed BCC and B2 phases, while another three showed a primary FCC solid solution phase accompanied by undesirable secondary intermetallics. In contrast, the alloys predicted to form an FCC phase by the ML and an additional C14 Laves phase as indicated by CALPHAD, did demonstrate this microstructure upon fabrication in the as-cast state. However, subsequent homogenisation revealed additional microstructural evolution, with the emergence of additional C36 Laves and μ phases. Accuracy of the alloy hardness predictions was limited with some agreement observed within the margins of error. The average percentage difference between the predicted and experimentally measured hardness values was (21 $\pm$ 13) % for as-cast measurements and (16 $\pm$ 13) % for heat-treated measurements, indicating a consistent deviation in the ML model predictions. The inconsistency between phase predictions and experimental observations was attributed to the insufficient amount of experimental HEA data available and the limited availability and integration of manufacturing and processing condition data into the models. These discrepancies were not entirely unexpected due to the targetting of FCC regions in unexplored space to maximise alloy hardness. Resulting in ML phase predictions with inherently low confidence. In contrast, while the hardness prediction accuracies could also be attributed to the limited data, the performance was further impacted by the reliance on empirical calculations

and imputed values to bolster the database, particularly for FCC compositions. Despite the limitations of the ML predictions, Chapter 5 highlights the overall success of combining ML with CALPHAD. This integrated methodology has effectively accelerated the alloy design process, enabling the identification of novel HEA compositions with promising potential for the intended application, which may not otherwise have been isolated through conventional methods.

Chapter 6 investigated the carbon reinforcement of four of the nine downselected HEA compositions, that were deemed suitable through additional thermodynamic assessment via CALPHAD. This addition of carbon was hypothesised to simultaneously suppress the undesirable and brittle secondary intermetallic phases such as η and C14 Laves, while enhancing mechanical properties. Two of the four HEA compositions successfully demonstrated complete suppression of the intermetallic phase formation upon the addition of carbon. In contrast, secondary intermetallic phases were still present within the other two HEA compositions microstructure. However, this is likely due to a lower carbon concentration within the alloys than targetted due to difficulties in the manufacturing process. Thus, additional carbon and/or heat treatment process could result in the full suppression of intermetallic phase formation within these alloys. In contrast, hardness investigations showed less clear results. Despite anecdotally displaying significantly higher hardness and wear resistance, the indentation measurements showed a reduction in alloy hardness where the intermetallic phases were fully suppressed. This observation was attributed to the softer FCC matrix being indented and deforming, with the carbide precipitates not playing a significant active role. Following the carbon reinforcement of the HEA compositions, Chapter 6 also demonstrated the amenability of three of these compositions to AM, with preliminary bead-on-plate trials. Two of the samples, those that displayed clear suppression of the intermetallic phases, displayed a sufficiently low susceptibility to cracking for AM. However, the third sample, which still showed evidence of intermetallic phase formation displayed significant cracking during the bead-on-plate trials. As discussed previously, this cracking is likely to decrease with further carbon additions and full suppression of intermetallic phases.

Finally, in Chapter 7, the ML work presented in Chapter 3 was further developed and refined. From the challenges identified and lessons learned in the first iteration, an improved ML for HEAs pipeline was proposed, and new ML models constructed. This second it-

eration aimed to facilitate downselection of new HEA compositions to investigate from an expanded virtual candidate search space, using the established ML and CALPHAD methodology. However, despite the implementation of an expanded dataset, enhanced feature set, wider range of ML models, and more rigorous data cleaning workflow, only an increase in hardness prediction performance was attained. More critically, a significant decrease in model performance was observed compared to the first iteration. With model accuracies falling from an average of 80.0 % in the first iteration, to a maximum performance of 62.5 % for an XGBoost model, which increased to 70.0 % following the application of SMOTE. Investigation of the model training process revealed a underlying issue with the data as the models predictive accuracy on the training data could not exceed 91.1 % even with the application of SMOTE. This result prevented the downselection of new HEA compositions due to the reduced performance accuracy. This outcome of reduced performance on an expanded dataset, collated from across the HEA literature, agrees strongly with the literature, suggesting that increased data collated from various sources does not necessarily lead to an improved model performance. Furthermore, this result highlights the persistent challenges associated with developing predictive models in the complex and diverse HEA space. Improving data quality and ensuring its distribution across strategically important areas of the HEA field are just as critical to the success of ML for HEA studies as the generation of more data.

Whilst an array of conclusions can be drawn from the individual chapters in this work, overall this thesis has illustrated that ML is an exceptionally powerful tool for accelerating the alloy design process, particularly within the HEA compositional space. The goal of this research was not to develop new ML methodologies but to leverage ML as a tool to facilitate the acceleration of alloy design for tooling applications. Although the ML predictions did not directly agree with experimental observations, ML successfully identified novel alloy compositions with interesting and potentially useful properties, warranting further experimental investigation. These compositions could not have been identified and studied within the accelerated time frame without the synergistic application of ML and CALPHAD. The additional integration of CALPHAD to aid the ML also proved successful, further enabling the alloy downselection process and leading to the experimental confirmation of three compositions that form an FCC plus C14 Laves microstructure. Additionally, the carbon reinforcement programme demonstrated that the

secondary phases formed within the HEAs can be effectively suppressed by the addition of carbon, simultaneously improving wear resistance while retaining damage tolerance. These carbon reinforced compositions were also found to be amenable for AM, meeting one of the project's key design criteria. The HEA compositions presented in this work can be taken forward to further assess the mechanical properties beyond hardness and conducting full-scale AM printing trials to assess their suitability for industrial applications. Although the second iteration of the ML model did not deliver the anticipated performance improvements, despite the expanded HEA database and refined methodology, it provided valuable insights into the challenges and future directions for ML to ensure successful application of ML to the HEA field. As HEAs are still a relatively new area of research, the current amount of data is insufficient for ML to achieve its full potential. Therefore, significantly larger datasets and, critically, the establishment of standardised data reporting practices are essential. As HEA databases improve in both quality and quantity, ML will play a pivotal role in accelerating the discovery of new HEAs, enabling the exploration of uncharted compositional regions to address demanding industrial applications. This includes the potential replacement of long-standing materials like WC-Co, which have dominated tooling applications for almost a century. Additionally, advancements in ML, particularly the integration of large language models (LLMs), will further enhance alloy design processes as these technologies become more widely accepted and mainstream. Additional discussion of potential areas for further work are detailed in Chapter 9.

Chapter 9

Future Work

Throughout this thesis, several areas have been identified that merit further exploration. These can be broadly categorised into two main directions: the continued experimental evaluation of the alloy compositions investigated in this work and the further development of ML methodologies to enhance predictive capabilities and broader applicability.

The experimental work on the fabrication and preliminary AM investigation of carbide reinforced samples could be expanded to full-scale AM printing trials. To enable successful printing, mixtures of pre-alloyed matrix and carbide precipitate powder compositions could be trialled in small quantities, leveraging the optimised parameters established in Chapter 6. Using pre-alloyed matrix and carbide precipitate powders increases the likelihood of achieving the desired phase constitution during the AM process. In contrast, printing with mixtures of elemental powders or fully pre-alloyed systems may lead to undesired phase compositions due to the significantly different melting and evaporation points of the constituent elements. For this purpose, small quantities of pre-alloyed powder could be fabricated using ultrasonic atomisation, providing a tailored approach to ensure success.

Additionally, AM can be adopted for the high-throughput evaluation of both future and prior model predictions, facilitating the rapid characterisation of a wide range of HEA compositions. Such an approach could support the creation of an in-house database, serving as a valuable resource for training future ML models. This can be realised using equipment such as the Formalloy alloy development feeder, which enables the rapid de-

position of up to 16 different alloys or alloy blends in a single setup. By accelerating the experimental aspect of this work, it will be possible to enhance performance and maintain alignment with the rapid advancements in ML methodologies.

To advance ML predictions and generate deeper insights, more sophisticated models specifically designed for materials property prediction, such as CrabNet, could be employed to generate more accurate and meaningful results from the available data. Additionally, LLMs, such as OpenAI's GPT or Meta's LLaMA, present a promising avenue for improving predictions of microstructural and mechanical properties of HEAs from experimental data. This can be achieved through two complementary approaches: prompt engineering and fine-tuning. Prompt engineering involves crafting precise and targeted inputs to effectively leverage the general capabilities of pre-trained LLMs without the need for additional training. This approach is computationally efficient and allows for rapid adaptation of LLMs to specific tasks, such as analysing and synthesising trends in experimental HEA datasets. Fine-tuning on the other hand, entails adapting a pre-trained LLM to a specific domain by training it further on a smaller, more focused dataset. This process customises the model's general knowledge for applications in HEA research, potentially enhancing its predictive accuracy. However, fine-tuning LLMs requires substantial computational resources, making it a resource-intensive strategy. Both approaches face challenges associated with the poor-quality data often encountered in HEA studies, which can result in suboptimal performance or biased outputs. However, despite these challenges, the integration of LLMs through prompt engineering and fine-tuning offers an approach to improve the prediction of microstructural and mechanical properties of HEAs.

The application of ML to the HEA field, as discussed in this thesis, has primarily focused on single-task problems, such as predicting phase formation and hardness using separate, distinct models. However, hardness is directly linked to the phase formation of an alloy composition. Exploring a multitask learning approach, where predictions for phase formation and hardness are integrated into a single model, could improve performance across both tasks by benefitting from shared representations and knowledge transfer. Additionally, ML predictions and the corresponding experimental validations could be extended to include other critical properties such as corrosion resistance, oxidation resistance, and ductility. These could also be incorporated within a unified multitask learning framework

to enable more comprehensive materials design. A significant challenge in predicting alloy properties for HEAs lies in the critical role of manufacturing and processing conditions on these properties. Expanding the scope to include alternative manufacturing methods, such as powder metallurgy, or integrating manufacturing parameters into the model architecture without overly fragmenting the dataset, would be highly beneficial. Such efforts would enable better utilisation of the currently available data in the HEA field and improve the robustness and applicability of ML models.

Despite the significant volume of data consistently published in the HEA field, much of it remains underutilised. LLMs, as discussed earlier, could be harnessed for automated data scraping and database generation. By extracting key information from published papers and integrating it into a centralised database, LLMs can achieve levels of accuracy and efficiency far beyond manual methods. Leveraging LLMs for data collection ensures that published information is more effectively utilised, enhancing both the comprehensiveness and reliability of HEA datasets. This approach has the potential to reduce compositional gaps and minimise overlap in existing databases, thereby supporting further advancements in ML-driven materials discovery.

More generally, much of the focus on ML application to the HEA field is likely to centre on developing newer and more sophisticated models. However, a critical area requiring attention is the generation of high-quality data from unexplored regions of the HEA compositional space. Ensuring that databases are populated with accurate and diverse information will significantly enhance the predictive power of both ML models and CALPHAD approaches. This, in turn, will improve the efficiency and effectiveness of accelerated alloy design processes. Moreover, the continued application of high-throughput experimental methodologies will assist in improving the accuracy of predictions for HEA systems as more data becomes available.

Bibliography

1. Berry, J. & Christofidou, K. A. Supervised machine learning for multi-principal element alloy structural design. *Materials Science and Technology* **41,** 773–790 (2025).
2. Berry, J. *et al.* Design and selection of high entropy alloys for hardmetal matrix applications using a coupled machine learning and calculation of phase diagrams methodology. *Advanced Engineering Materials* **26,** 2302064 (2024).
3. Gilman, J. J. *Chemistry and [hysics of mechanical hardness* 1st Edition. (Wiley, Hoboken, NJ, 2009).
4. Ettmayer, P. Hardmetals and Cermets. *Annual review of materials science* **19,** 145–164 (1989).
5. García, J., Collado Ciprés, V., Blomqvist, A. & Kaplan, B. Cemented carbide microstructures: A review. *International Journal of Refractory Metals and Hard Materials* **80,** 40–68 (2019).
6. Konyashin, I. Approaching the 100th anniversary of the hardmetal invention: From first WC-Co samples towards modern advanced hardmetal grades. *International Journal of Refractory Metals and Hard Materials* **111** (2023).
7. Koc, R. & Kodambaka, S. K. Tungsten carbide (WC) synthesis from novel precursors. *Journal of the European Ceramic Society* **20,** 1859–1869 (2000).
8. Wang, K.-F., Tang, X.-L., Jiao, S., Chou, K.-C. & Zhang, G.-H. A short and facile process to synthesize WC-Co cemented carbides. *International Journal of Refractory Metals and Hard Materials* **92** (2020).
9. U.S. Geological Survey. *Mineral commodity summaries 2021* (U.S. Geological Survey, 2021). `https://pubs.usgs.gov/publication/mcs2021`.
10. Shemi, A., Magumise, A., Ndlovu, S. & Sacks, N. Recycling of tungsten carbide scrap metal: A review of recycling methods and future prospects. *Minerals Engineering* **122,** 195–205 (2018).

11. Polini, R. *et al.* Toward greener synthesis of WC powders for cemented tungsten carbides manufacturing. *ACS Sustainable Chemistry & Engineering* **9,** 8458–8466 (2021).
12. Yang, Q. *et al.* A novel route for the synthesis of ultrafine WC-15 wt% Co cemented carbides. *Journal of Alloys and Compounds* **748,** 577–582 (2018).
13. Hewitt, S. A., Laoui, T. & Kibble, K. K. Effect of milling temperature on the synthesis and consolidation of nanocomposite WC–10Co powders. *International Journal of Refractory Metals and Hard Materials* **27,** 66–73 (2009).
14. De Luca, F. *et al.* Nanomechanical behaviour of individual phases in WC-Co cemented carbides, from ambient to high temperature. *Materialia* **12,** 100713 (2020).
15. Katiyar, P. K., Maurya, R. & Singh, P. K. Failure behavior of cemented tungsten carbide materials: A case study of mining drill bits. *Journal of Materials Engineering and Performance* **30,** 6090–6106 (2021).
16. Sun, J., Zhao, J., Gong, F., Ni, X. & Li, Z. Development and application of WC-based alloys bonded with alternative binder phase. *Critical Reviews in Solid State and Materials Sciences* **44,** 211–238 (2019).
17. Teppernegg, T. *et al.* High temperature mechanical properties of WC–Co hard metals. *International Journal of Refractory Metals and Hard Materials* **56,** 139–144 (2016).
18. Novikov, N. V., Bondarenko, V. P. & Golovchan, V. T. High-temperature mechanical properties of WC-Co hard metals (Review). *Journal of Superhard Materials* **29,** 261–280 (2007).
19. Emani, S. V., Ramos dos Santos, A. F. C., Shaw, L. L. & Chen, Z. Investigation of microstructure and mechanical properties at low and high temperatures of WC–6 wt% Co. *International Journal of Refractory Metals and Hard Materials* **58,** 172–181 (2016).
20. Rosa, J. M. B. *et al.* Study of characteristics and properties of spark plasma sintered WC with the use of alternative Fe-Ni-Nb binder as Co replacement. *International Journal of Refractory Metals and Hard Materials* **92** (2020).
21. Prakash, L. J. Application of fine grained tungsten carbide based cemented carbides. *International Journal of Refractory Metals and Hard Materials* **13,** 257–264 (1995).

22. Liu, W., Song, X., Zhang, J., Yin, F. & Zhang, G. A novel route to prepare ultrafine-grained WC–Co cemented carbides. *Journal of Alloys and Compounds* **458,** 366–371 (2008).
23. Sun, J. *et al.* A review on binderless tungsten carbide: Development and application. *Nano-Micro Letters* **12,** 1–37 (2019).
24. Mukhopadhyay, A. & Basu, B. Recent developments on WC-based bulk composites. *Journal of Materials Science* **46,** 571–589 (2010).
25. Heydari, L., Lietor, P. F., Corpas-Iglesias, F. A. & Laguna, O. H. Ti(C,N) and WC-based cermets: A review of synthesis, properties and applications in additive manufacturing. *Materials* **14,** 6786 (2021).
26. Nie, H. & Zhang, T. Development of manufacturing technology on WC–Co hardmetals. *Tungsten* **1,** 198–212 (2019).
27. Venter, R., Critchley, S. & de Malherbe, M. C. The evaluation of tungsten carbide properties as applied to high pressure equipment. *Materials Science and Engineering* **19,** 201–210 (1975).
28. Pittari, J. J. *et al.* Sintering of tungsten carbide cermets with an iron-based ternary alloy binder: Processing and thermodynamic considerations. *International Journal of Refractory Metals and Hard Materials* **76,** 1–11 (2018).
29. Pötschke, J., Vornberger, A., Gestrich, T., Berger, L.-M. & Michaelis, A. Influence of different binder metals in high entropy carbide based hardmetals. *Powder Metallurgy* **65,** 373–381 (2022).
30. De Oro Calderon, R., Edtmaier, C. & Schubert, W.-D. Novel binders for WC-based cemented carbides with high Cr contents. *International Journal of Refractory Metals and Hard Materials* **85** (2019).
31. De Oro Calderon, R., Agna, A., Gomes, U. U. & Schubert, W.-D. Phase formation in cemented carbides prepared from WC and stainless steel powder – An experimental study combined with thermodynamic calculations. *International Journal of Refractory Metals and Hard Materials* **80,** 225–237 (2019).
32. Fazili, A., Nikzad, L., RahimiPour, M. R., Razavi, M. & Salahi, E. Effect of Al_2O_3 ceramic binder on mechanical and microstructure properties of spark plasma sintered WC-Co cermets. *International Journal of Refractory Metals and Hard Materials* **69,** 189–195 (2017).

33. Sandoval, D. A. *et al.* WC-base cemented carbides with partial and total substitution of Co as binder: Evaluation of mechanical response by means of uniaxial compression of micropillars. *International Journal of Refractory Metals and Hard Materials* **84** (2019).
34. Silvestroni, L. *et al.* Binderless WC with high strength and toughness up to 1500 °C. *Journal of the European Ceramic Society* **40,** 2287–2294 (2020).
35. Straumal, B. & Konyashin, I. WC-based cemented carbides with high entropy alloyed binders: A review. *Metals* **13** (2023).
36. Prieto, E., Vaz-Romero, A., Gonzalez-Julian, J., Guo, S. & Alvaredo, P. Novel high entropy alloys as binder in cermets: From design to sintering. *International Journal of Refractory Metals and Hard Materials* **99,** 105592 (2021).
37. Zhang, Y., Yang, X. & Liaw, P. K. Alloy design and properties optimization of high-entropy alloys. *JOM* **64,** 830–838 (2012).
38. Murty, B. S., Yeh, J. W. & Ranganathan, S. *High-entropy alloys* (Elsevier : Butterworth-Heinemann, London, England, 2014).
39. Bloomfield, M. E. *et al.* The influence of Fe variations on the phase stability of $CrMnFe_xCoNi$ alloys following long-duration exposures at intermediate temperatures. *Intermetallics* **131,** 107108 (2021).
40. Cantor, B. Multicomponent high-entropy Cantor alloys. *Progress in materials science* **120.** Actually a pretty terrible paper, just Cantor blowing his own trumpet essentially., 100754 (2021).
41. Gao, M. C., Yeh, J.-W., Liaw, P. K. & Zhang, Y. *High-entropy alloys: Fundamentals and applications* (Springer, 2016).
42. Yeh, J. W. *et al.* Nanostructured high-entropy alloys with multiple principal elements: Novel alloy design concepts and outcomes. *Advanced Engineering Materials* **6,** 299–303 (2004).
43. Cantor, B., Chang, I. T. H., Knight, P. & Vincent, A. J. B. Microstructural development in equiatomic multicomponent alloys. *Materials Science and Engineering. A* **375-377,** 213–218 (2004).
44. Lu, Z. P. *et al.* An assessment on the future development of high-entropy alloys: Summary from a recent workshop. *Intermetallics* **66,** 67–76 (2015).
45. Miracle, D. *et al.* Exploration and development of high entropy alloys for structural applications. *Entropy* **16,** 494–525 (2014).

46. Yeh, J.-W. Alloy design strategies and future trends in high-entropy alloys. *JOM* **65,** 1759–1771 (2013).
47. Yeh, J.-W. Physical metallurgy of high-entropy alloys. *JOM* **67,** 2254–2261 (2015).
48. Miracle, D. B. Critical Assessment 14: High entropy alloys and their development as structural materials. *Materials Science and Technology* **31,** 1142–1147 (2015).
49. Miracle, D. B. & Senkov, O. N. A critical review of high entropy alloys and related concepts. *Acta Materialia* **122,** 448–511 (2017).
50. El Atwani, O. *et al.* A quinary WTaCrVHf nanocrystalline refractory high-entropy alloy withholding extreme irradiation environments. *Nature Communications* **14,** 2516 (2023).
51. Tunes, M. A. *et al.* Perspectives on novel refractory amorphous high-entropy alloys in extreme environments. *Applied Materials Today* **32,** 101796 (2023).
52. Srikanth, M., Annamalai, A. R., Muthuchamy, A. & Jen, C.-P. A review of the latest developments in the field of refractory high-entropy alloys. *Crystals* **11** (2021).
53. Huang, X. *et al.* Noble-metal-based high-entropy-alloy nanoparticles for electrocatalysis. *Journal of Energy Chemistry* **68,** 721–751 (2022).
54. Moghaddam, A. O. & Trofimov, E. A. Toward expanding the realm of high entropy materials to platinum group metals: A review. *Journal of Alloys and Compounds* **851,** 156838 (2021).
55. Rost, C. M. *et al.* Entropy-stabilized oxides. *Nature Communications* **6,** 8485 (2015).
56. Ko, J. Y. & Hong, S. I. Microstructural evolution and mechanical performance of carbon-containing CoCrFeMnNi-C high entropy alloys. *Journal of Alloys and Compounds* **743,** 115–125 (2018).
57. Castle, E., Csanádi, T., Grasso, S., Dusza, J. & Reece, M. Processing and properties of high-entropy ultra-high temperature carbides. *Scientific Reports* **8,** 8609 (2018).
58. Yuan, Y. *et al.* Rare-earth high-entropy alloys with giant magnetocaloric effect. *Acta Materialia* **125,** 481–489 (2017).
59. Zhang, L. J. *et al.* Effects of rare-earth element, Y, additions on the microstructure and mechanical properties of CoCrFeNi high entropy alloy. *Materials Science and Engineering: A* **725,** 437–446 (2018).
60. Jawańska, M. *et al.* Role of the rare-earth elements effect in transforming the oxidation behavior of Al_xCoCrFeNi high entropy alloys. *Corrosion Science* **222,** 111412 (2023).

61. Troparevsky, M. C., Morris, J. R., Kent, P. R. C., Lupini, A. R. & Stocks, G. M. Criteria for predicting the formation of single-phase high-entropy alloys. *Physical Review. X* **5,** 011041 (2015).
62. Pickering, E. & Jones, N. High-entropy alloys: A critical assessment of their founding principles and future prospects. *International Materials Reviews* **61** (2016).
63. Ren, W., Zhang, Y.-F., Wang, W.-L., Ding, S.-J. & Li, N. Prediction and design of high hardness high entropy alloy through machine learning. *Materials & Design* **235** (2023).
64. Manzoni, A. M. & Glatzel, U. New multiphase compositionally complex alloys driven by the high entropy alloy approach. *Materials Characterization* **147,** 512–532 (2019).
65. Joseph, J. *et al.* Computational design of thermally stable and precipitation-hardened Al-Co-Cr-Fe-Ni-Ti high entropy alloys. *Journal of Alloys and Compounds* **888,** 161496 (2021).
66. Chen, Y.-T., Chang, Y.-J., Murakami, H., Gorsse, S. & Yeh, A.-C. Designing high entropy superalloys for elevated temperature application. *Scripta Materialia* **187,** 177–182 (2020).
67. Shafiei, A. Design of eutectic high entropy alloys. *Metallurgical and Materials Transactions A* **53,** 4349–4361 (2022).
68. Lu, Y. *et al.* Promising properties and future trend of eutectic high entropy alloys. *Scripta Materialia* **187,** 202–209 (2020).
69. Otto, F. *et al.* Decomposition of the single-phase high-entropy alloy CrMnFeCoNi after prolonged anneals at intermediate temperatures. *Acta Materialia* **112,** 40–52 (2016).
70. Biswas, K., Yeh, J.-W., Bhattacharjee, P. P. & DeHosson, J. T. M. High entropy alloys: Key issues under passionate debate. *Scripta Materialia* **188,** 54–58 (2020).
71. Elsevier. 2024. `https://www.scopus.com/search/form.uri`.
72. Miracle, D. B. High-entropy alloys: A current evaluation of founding ideas and core effects and exploring "nonlinear alloys". *JOM* **69,** 2130–2136 (2017).
73. George, E. P., Raabe, D. & Ritchie, R. O. High-entropy alloys. *Nature Reviews Materials* **4,** 515–534 (2019).

74. George, E. P., Curtin, W. A. & Tasan, C. C. High entropy alloys: A focused review of mechanical properties and deformation mechanisms. *Acta Materialia* **188,** 435–474 (2020).

75. Miracle, D. B. *et al.* Defining pathways for realizing the revolutionary potential of high entropy alloys. *JOM* (2021).

76. Gwalani, B. *et al.* Interplay between single phase solid solution strengthening and multi-phase strengthening in the same high entropy alloy. *Materials Science and Engineering. A* **771,** 138620 (2020).

77. Wu, W.-H., Yang, C.-C. & Yeh, J.-W. Industrial development of high-entropy alloys. *European Journal of Control* **31,** 737–747 (2006).

78. Vela, B. *et al.* High-throughput exploration of the WMoVTaNbAl refractory multi-principal-element alloys under multiple-property constraints. *Acta Materialia* **248,** 118784 (2023).

79. Yeh, J.-W. *et al.* Formation of simple crystal structures in Cu-Co-Ni-Cr-Al-Fe-Ti-V alloys with multiprincipal metallic elements. *Metallurgical and Materials Transactions A* **35,** 2533–2536 (2004).

80. Yeh, J.-W. Recent progress in high-entropy alloys. *Annales de Chimie Science des Matériaux* **31,** 633–648 (2006).

81. Laurent-Brocq, M., Perrière, L., Pirès, R. & Champion, Y. From high entropy alloys to diluted multi-component alloys: Range of existence of a solid-solution. *Materials & Design* **103,** 84–89 (2016).

82. Otto, F., Yang, Y., Bei, H. & George, E. P. Relative effects of enthalpy and entropy on the phase stability of equiatomic high-entropy alloys. *Acta Materialia* **61,** 2628–2638 (2013).

83. He, F. *et al.* Solid solution island of the Co-Cr-Fe-Ni high entropy alloy system. *Scripta Materialia* **131,** 42–46 (2017).

84. Owen, L. R. *et al.* An assessment of the lattice strain in the CrMnFeCoNi high-entropy alloy. *Acta Materialia* **122,** 11–18 (2017).

85. Zhang, Y., Zhou, Y. J., Lin, J. P., Chen, G. L. & Liaw, P. K. Solid-solution phase formation rules for multi-component alloys. *Advanced Engineering Materials* **10,** 534–538 (2008).

86. Hume-Rothery, W. *Elements of structural metallurgy* (Institute of Metals, London, 1961).

87. Tsai, K. Y., Tsai, M. H. & Yeh, J. W. Sluggish diffusion in Co–Cr–Fe–Mn–Ni high-entropy alloys. *Acta Materialia* **61,** 4887–4897 (2013).
88. Paul, A. Comments on "Sluggish diffusion in Co–Cr–Fe–Mn–Ni high-entropy alloys" by K.Y. Tsai, M.H. Tsai and J.W. Yeh, Acta Materialia 61 (2013) 4887–4897. *Scripta Materialia* **135,** 153–157 (2017).
89. Tsai, K.-Y., Tsai, M.-H. & Yeh, J.-W. Reply to comments on "Sluggish diffusion in Co-Cr-Fe-Mn-Ni high-entropy alloys" by K.Y. Tsai, M.H. Tsai and J.W. Yeh, Acta Materialia 61 (2013) 4887-4897. *Scripta Materialia* **135,** 158–159 (2017).
90. Zhang, C. *et al.* Understanding of the elemental diffusion behavior in concentrated solid solution alloys. *Journal of Phase Equilibria and Diffusion* **38,** 434–444 (2017).
91. Dąbrowa, J. *et al.* Demystifying the sluggish diffusion effect in high entropy alloys. *Journal of Alloys and Compounds* **783,** 193–207 (2019).
92. Verma, V., Belcher, C. H., Apelian, D. & Lavernia, E. J. Diffusion in high entropy alloy systems – A review. *Progress in Materials Science* **142** (2024).
93. Ranganathan, S. Alloyed pleasures: Multimetallic cocktails. *Current Science* **85,** 1404–1406 (2003).
94. Li, Z., Zhao, S., Ritchie, R. O. & Meyers, M. A. Mechanical properties of high-entropy alloys with emphasis on face-centered cubic alloys. *Progress in Materials Science* **102,** 296–345 (2019).
95. Li, W. *et al.* Mechanical behavior of high-entropy alloys. *Progress in Materials Science* **118** (2021).
96. Gwalani, B. *et al.* Optimizing the coupled effects of Hall-Petch and precipitation strengthening in a $Al_{0.3}$CoCrFeNi high entropy alloy. *Materials & Design* **121,** 254–260 (2017).
97. Fan, X., Qu, R. & Zhang, Z. Relation between strength and hardness of high-entropy alloys. *Acta Metallurgica Sinica (English Letters)* **34,** 1461–1482 (2021).
98. Huang, W., Martin, P. & Zhuang, H. L. Machine-learning phase prediction of high-entropy alloys. *Acta Materialia* **169,** 225–236 (2019).
99. Kumar, J. *et al.* Novel alloy design concepts enabling enhanced mechanical properties of high entropy alloys. *Frontiers in Materials* **9** (2022).
100. Bracq, G. *et al.* The fcc solid solution stability in the Co-Cr-Fe-Mn-Ni multi-component system. *Acta Materialia* **128,** 327–336 (2017).

101. Wu, Z., Bei, H., Otto, F., Pharr, G. M. & George, E. P. Recovery, recrystallization, grain growth and phase stability of a family of FCC-structured multi-component equiatomic solid solution alloys. *Intermetallics* **46,** 131–140 (2014).

102. Wu, Z., Bei, H., Pharr, G. M. & George, E. P. Temperature dependence of the mechanical properties of equiatomic solid solution alloys with face-centered cubic crystal structures. *Acta Materialia* **81,** 428–441 (2014).

103. Bloomfield, M. E. *et al.* Phase stability of the Al_xCrFeCoNi alloy system. *Journal of Alloys and Compounds* **926** (2022).

104. Jones, N. G., Christofidou, K. A. & Stone, H. J. Rapid precipitation in an $Al_{0.5}$CrFeCoNiCu high entropy alloy. *Materials Science and Technology* **31,** 1171–1177 (2015).

105. Jones, N. G., Izzo, R., Mignanelli, P. M., Christofidou, K. A. & Stone, H. J. Phase evolution in an $Al_{0.5}$CrFeCoNiCu High Entropy Alloy. *Intermetallics* **71,** 43 (2016).

106. He, J. Y. *et al.* A precipitation-hardened high-entropy alloy with outstanding tensile properties. *Acta Materialia* **102,** 187–196 (2016).

107. Zhang, L., Zhou, Y., Jin, X., Du, X. & Li, B. Precipitation-hardened high entropy alloys with excellent tensile properties. *Materials Science and Engineering: A* **732,** 186–191 (2018).

108. Yang, H. *et al.* Nanophase precipitation and strengthening in a dual-phase $Al_{0.5}$CoCrFeNi high-entropy alloy. *Journal of Materials Science & Technology* **72,** 1–7 (2021).

109. Liu, L. *et al.* Nanoprecipitate-strengthened high-entropy alloys. *Advanced Science* **8,** 2100870 (2021).

110. Callister, W. D. & Rethwisch, D. G. *Materials science and engineering* 9th Edition, SI version. (Wiley, Hoboken, New Jersey, 2015).

111. Liu, W. H. *et al.* Ductile CoCrFeNiMo_x high entropy alloys strengthened by hard intermetallic phases. *Acta Materialia* **116,** 332–342 (2016).

112. Tong, Y. *et al.* Outstanding tensile properties of a precipitation-strengthened FeCoNiCr$Ti_{0.2}$ high-entropy alloy at room and cryogenic temperatures. *Acta Materialia* **165,** 228–240 (2019).

113. Peng, J. *et al.* Carbide precipitation strengthening in fine-grained carbon-doped FeCoCrNiMn high entropy alloy. *Journal of Alloys and Compounds* **803,** 491–498 (2019).

114. Gao, N. *et al.* Strengthening of a CrMnFeCoNi high-entropy alloy by carbide precipitation. *Journal of Alloys and Compounds* **792,** 1028–1035 (2019).

115. Su, J., Raabe, D. & Li, Z. Hierarchical microstructure design to tune the mechanical behavior of an interstitial TRIP-TWIP high-entropy alloy. *Acta Materialia* **163,** 40–54 (2019).

116. Wu, J., Liu, X., Sang, P., Xu, Y. & Zhu, H. In situ TiC particles-reinforced body-centered-cubic $Ni_{0.6}CoFe_{1.4}$ medium-entropy alloys for high hardness and good wear resistance. *Metallurgical and Materials Transactions A* **55,** 992–997 (2024).

117. Fahrenholtz, W. G. & Hilmas, G. E. Ultra-high temperature ceramics: Materials for extreme environments. *Scripta Materialia* **129,** 94–99 (2017).

118. Wyatt, B. C., Nemani, S. K., Hilmas, G. E., Opila, E. J. & Anasori, B. Ultra-high temperature ceramics for extreme environments. *Nature Reviews Materials* (2023).

119. Wang, Z., Li, Z.-T., Zhao, S.-J. & Wu, Z.-G. High-entropy carbide ceramics: A perspective review. *Tungsten* **3,** 131–142 (2021).

120. Kaufmann, K. *et al.* Discovery of high-entropy ceramics via machine learning. *npj Computational Materials* **6,** 42 (2020).

121. Harrington, T. J. *et al.* Phase stability and mechanical properties of novel high entropy transition metal carbides. *Acta Materialia* **166,** 271–280 (2019).

122. Gild, J. *et al.* High-entropy metal diborides: A new class of high-entropy materials and a new type of ultrahigh temperature ceramics. *Scientific Reports* **6,** 37946 (2016).

123. Zhou, J. *et al.* High-entropy carbide: A novel class of multicomponent ceramics. *Ceramics International* **44,** 22014–22018 (2018).

124. Wang, Y. Processing and properties of high entropy carbides. *Advances in Applied Ceramics* **121,** 57–78 (2021).

125. Pötschke, J., Dahal, M., Vornberger, A., Herrmann, M. & Michaelis, A. Production and properties of high entropy carbide based hardmetals. *Metals* **11** (2021).

126. Low, I. M. *Advances in ceramic matrix composites* 1st Edition. (Woodhead Publishing, Oxford, 2014).

127. Ye, W. *et al.* Microstructure and tribological properties of in-situ carbide CoCrFeNiMn high entropy alloy composites synthesized by flake powder metallurgy. *Tribology International* **181** (2023).

128. Xin, B., Zhang, A., Han, J., Su, B. & Meng, J. Tuning composition and microstructure by doping Ti and C for enhancing mechanical property and wear resistance of $Al_{0.2}Co_{1.5}CrFeNi_{1.5}Ti_{0.5}$ high entropy alloy matrix composites. *Journal of Alloys and Compounds* **836** (2020).

129. Zhou, P. F., Xiao, D. H. & Yuan, T. C. Comparison between ultrafine-grained WC–Co and WC–HEA-cemented carbides. *Powder Metallurgy* **60,** 1–6 (2016).

130. Zhou, P. L., Xiao, D. H., Zhou, P. F. & Yuan, T. C. Microstructure and properties of ultrafine grained AlCrFeCoNi/WC cemented carbides. *Ceramics International* **44,** 17160–17166 (2018).

131. Chen, R. *et al.* Development of cemented carbides with Co_xFeNiCrCu high-entropy alloyed binder prepared by spark plasma sintering. *International Journal of Refractory Metals and Hard Materials* **103** (2022).

132. Velo, I. L., Gotor, F. J., Alcalá, M. D., Real, C. & Córdoba, J. M. Fabrication and characterization of WC-HEA cemented carbide based on the CoCrFeNiMn high entropy alloy. *Journal of Alloys and Compounds* **746,** 1–8 (2018).

133. Vornberger, A., Pötschke, J., Gestrich, T., Herrmann, M. & Michaelis, A. Influence of microstructure on hardness and thermal conductivity of hardmetals. *International Journal of Refractory Metals and Hard Materials* **88** (2020).

134. Yan, Y., Lu, D. & Wang, K. Accelerated discovery of single-phase refractory high entropy alloys assisted by machine learning. *Computational Materials Science* **199,** 110723 (2021).

135. Joseph, J., Annasamy, M., Hodgson, P. D., Barnett, M. R. & Fabijanic, D. M. Exploring the limits of Fe content in Al-Co-Cr-Fe-Ni-based eutectic high entropy alloys using CALPHAD-based alloy design. *Journal of Alloys and Compounds* **1002** (2024).

136. Wang, Y. P., Li, B. S., Ren, M. X., Yang, C. & Fu, H. Z. Microstructure and compressive properties of AlCrFeCoNi high entropy alloy. *Materials Science and Engineering: A* **491,** 154–158 (2008).

137. Li, B. S., Wang, Y. P., Ren, M. X., Yang, C. & Fu, H. Z. Effects of Mn, Ti and V on the microstructure and properties of AlCrFeCoNiCu high entropy alloy. *Materials Science and Engineering: A* **498,** 482–486 (2008).

138. Tong, C.-J. *et al.* Microstructure characterization of Al_xCoCrCuFeNi high-entropy alloy system with multiprincipal elements. *Metallurgical and Materials Transactions A* **36,** 881–893 (2005).

139. Fang, S., Xiao, X., Xia, L., Li, W. & Dong, Y. Relationship between the widths of supercooled liquid regions and bond parameters of Mg-based bulk metallic glasses. *Journal of Non-Crystalline Solids* **321** (2003).

140. Wang, Z., Huang, Y., Yang, Y., Wang, J. & Liu, C. T. Atomic-size effect and solid solubility of multicomponent alloys. *Scripta Materialia* **94,** 28–31 (2015).

141. Kube, S. A. *et al.* Phase selection motifs in high entropy alloys revealed through combinatorial methods: Large atomic size difference favors BCC over FCC. *Acta Materialia* **166,** 677–686 (2019).

142. Tian, F., Varga, L. K., Chen, N., Shen, J. & Vitos, L. Empirical design of single phase high-entropy alloys with high hardness. *Intermetallics* **58,** 1–6 (2015).

143. Guo, S. & Liu, C. T. Phase stability in high entropy alloys: Formation of solid-solution phase or amorphous phase. *Progress in Natural Science: Materials International* **21,** 433–446 (2011).

144. Guo, S., Hu, Q., Ng, C. & Liu, C. T. More than entropy in high-entropy alloys: Forming solid solutions or amorphous phase. *Intermetallics* **41,** 96–103 (2013).

145. Ji, X. Relative effect of electronegativity on formation of high entropy alloys. *International Journal of Cast Metals Research* **28,** 229–233 (2015).

146. Guo, S., Ng, C., Lu, J. & Liu, C. Effect of valence electron concentration on stability of fcc or bcc phase in high entropy alloys. *Journal of Applied Physics* **109** (2011).

147. Mizutani, U. & Sato, H. The physics of the Hume-Rothery electron concentration rule. *Crystals* **7,** 9 (2017).

148. Guo, S., Ng, C., Wang, Z. & Liu, C. T. Solid solutioning in equiatomic alloys: Limit set by topological instability. *Journal of Alloys and Compounds* **583,** 410–413 (2014).

149. Poletti, M. G. & Battezzati, L. Electronic and thermodynamic criteria for the occurrence of high entropy alloys in metallic systems. *Acta Materialia* **75,** 297–306 (2014).

150. Mizutani, U. & Sato, H. Determination of electrons per atom ratio for transition metal compounds studied by FLAPW-Fourier calculations. *Philosophical Magazine* **96,** 3075–3096 (2016).

151. Calvo-Dahlborg, M. & Brown, S. G. R. Hume-Rothery for HEA classification and self-organizing map for phases and properties prediction. *Journal of Alloys and Compounds* **724,** 353–364 (2017).

152. Calvo-Dahlborg, M., Dahlborg, U., Brown, S. G. R. & Juraszek, J. Influence of the electronic polymorphism of Ni on the classification and design of high entropy alloys. *Journal of Alloys and Compounds* **824** (2020).

153. Calvo-Dahlborg, M. *et al.* Prediction of phase, hardness and density of high entropy alloys based on their electronic structure and average radius. *Journal of Alloys and Compounds* **865,** 158799 (2021).

154. Takeuchi, A. & Inoue, A. Calculations of mixing enthalpy and mismatch entropy for ternary amorphous alloys. *Materials transactions, JIM* **41,** 1372–1378 (2000).

155. Takeuchi, A. & Inoue, A. Classification of bulk metallic glasses by atomic size difference, heat of mixing and period of constituent elements and its application to characterization of the main alloying element. *Materials Transactions* **46,** 2817–2829 (2005).

156. Yang, X. & Zhang, Y. Prediction of high-entropy stabilized solid-solution in multi-component alloys. *Materials Chemistry and Physics* **132,** 233–238 (2012).

157. Couzinié, J. P., Senkov, O. N., Miracle, D. B. & Dirras, G. Comprehensive data compilation on the mechanical properties of refractory high-entropy alloys. *Data in Brief* **21,** 1622–1641 (2018).

158. Shen, L. *et al.* Predicting phases and hardness of high entropy alloys based on machine learning. *Intermetallics* **162,** 108030 (2023).

159. Singh, A. K., Kumar, N., Dwivedi, A. & Subramaniam, A. A geometrical parameter for the formation of disordered solid solutions in multi-component alloys. *Intermetallics* **53,** 112–119 (2014).

160. Rickman, J. M., Balasubramanian, G., Marvel, C. J., Chan, H. M. & Burton, M. T. Machine learning strategies for high-entropy alloys. *Journal of Applied Physics* **128** (2020).

161. Roy, A. & Balasubramanian, G. Predictive descriptors in machine learning and data-enabled explorations of high-entropy alloys. *Computational Materials Science* **193,** 110381 (2021).

162. Leong, Z., Huang, Y., Goodall, R. & Todd, I. Electronegativity and enthalpy of mixing biplots for High Entropy Alloy solid solution prediction. *Materials Chemistry and Physics* **210,** 259–268 (2018).

163. Leong, Z., Morley, N. & Goodall, R. Dilatational strain biplots against enthalpy of mixing for predicting high-entropy alloys and complex concentrated alloys phase stability. *Materials Chemistry and Physics* **262,** 124241 (2021).

164. Domínguez, L. A., Goodall, R. & Todd, I. Prediction and validation of quaternary high entropy alloys using statistical approaches. *Materials Science and Technology* **31,** 1201–1206 (2015).

165. Spencer, P. J. A brief history of CALPHAD. *Calphad* **32,** 1–8 (2008).

166. Yang, S., Lu, J., Xing, F., Zhang, L. & Zhong, Y. Revisit the VEC rule in high entropy alloys (HEAs) with high-throughput CALPHAD approach and its applications for material design - A case study with Al–Co–Cr–Fe–Ni system. *Acta Materialia* **192,** 11–19 (2020).

167. Chen, H.-L., Mao, H. & Chen, Q. Database development and Calphad calculations for high entropy alloys: Challenges, strategies, and tips. *Materials Chemistry and Physics* **210,** 279–290 (2018).

168. Saal, J. E., Berglund, I. S., Sebastian, J. T., Liaw, P. K. & Olson, G. B. Equilibrium high entropy alloy phase stability from experiments and thermodynamic modeling. *Scripta Materialia* **146,** 5–8 (2018).

169. Redlich, O. & Kister, A. T. Algebraic representation of thermodynamic properties and the classification of solutions. *Industrial & Engineering Chemistry* **40,** 345–348 (1948).

170. Saunders, N. & Miodownik, A. P. *CALPHAD (calculation of phase diagrams): A comprehensive guide* (Elsevier, 1998).

171. Zhang, C. & Yang, Y. The CALPHAD approach for HEAs: Challenges and opportunities. *MRS Bulletin* **47,** 158–167 (2022).

172. Andersson, J.-O., Helander, T., Höglund, L., Shi, P. & Sundman, B. Thermo-Calc & DICTRA, computational tools for materials science. *Calphad* **26,** 273–312 (2002).

173. Gorsse, S. & Tancret, F. Current and emerging practices of CALPHAD toward the development of high entropy alloys and complex concentrated alloys. *Journal of Materials Research* **33,** 2899–2923 (2018).

174. Guo, L., Gu, J., Gong, X., Ni, S. & Song, M. CALPHAD aided design of high entropy alloy to achieve high strength via precipitate strengthening. *Science China Materials* **63,** 288–299 (2020).

175. Choi, W.-M., Jung, S., Jo, Y. H., Lee, S. & Lee, B.-J. Design of new face-centered cubic high entropy alloys by thermodynamic calculation. *Metals and Materials International* **23,** 839–847 (2017).

176. Li, T. *et al.* CALPHAD-aided design for superior thermal stability and mechanical behavior in a TiZrHfNb refractory high-entropy alloy. *Acta Materialia* **246,** 118728 (2023).

177. Wu, M., Wang, S., Huang, H., Shu, D. & Sun, B. CALPHAD aided eutectic high-entropy alloy design. *Materials Letters* **262** (2020).

178. Rahul, M. R. & Phanikumar, G. Design of a seven-component eutectic high-entropy alloy. *Metallurgical and Materials Transactions A* **50,** 2594–2598 (2019).

179. Senkov, O. N., Miller, J. D., Miracle, D. B. & Woodward, C. Accelerated exploration of multi-principal element alloys with solid solution phases. *Nature Communications* **6,** 6529 (2015).

180. Senkov, O. N., Miller, J. D., Miracle, D. B. & Woodward, C. Accelerated exploration of multi-principal element alloys for structural applications. *Calphad* **50,** 32–48 (2015).

181. Sholl, D. S. & Steckel, J. A. *Density functional theory: A practical introduction* (Wiley, Hoboken, N.J., 2009).

182. King, D. J. M., Middleburgh, S. C., McGregor, A. G. & Cortie, M. B. Predicting the formation and stability of single phase high-entropy alloys. *Acta Materialia* **104,** 172–179 (2016).

183. Huhn, W. P. & Widom, M. Prediction of A2 to B2 phase transition in the high-entropy alloy Mo-Nb-Ta-W. *JOM* **65,** 1772–1779 (2013).

184. Rogal, Ł., Czerwinski, F., Jochym, P. T. & Litynska-Dobrzynska, L. Microstructure and mechanical properties of the novel $Hf_{25}Sc_{25}Ti_{25}Zr_{25}$ equiatomic alloy with hexagonal solid solutions. *Materials & Design* **92,** 8–17 (2016).

185. Harvey, J. N. On the accuracy of density functional theory in transition metal chemistry. *Annual Reports Section "C" (Physical Chemistry)* **102,** 203–226 (2006).

186. Molnar, C. *Interpretable machine learning: A guide for making black box models explainable* 2nd Edition. (2022).

187. Pilania, G. Machine learning in materials science: From explainable predictions to autonomous design. *Computational Materials Science* **193,** 110360 (2021).

188. De Luna, P. *Accelerated materials discovery: How to use artificial intelligence to speed up development* (Walter de Gruyter GmbH & Co KG, 2022).

189. Bhat, N., Birbilis, N. & Barnard, A. S. Unsupervised learning and pattern recognition in alloy design. *Digital Discovery* (2024).

190. Morgan, D. & Jacobs, R. Opportunities and challenges for machine learning in materials science. *Annual Review of Materials Research* **50,** 71–103 (2020).

191. Hart, G. L. W., Mueller, T., Toher, C. & Curtarolo, S. Machine learning for alloys. *Nature Reviews. Materials* **6,** 730–755 (2021).

192. Kaufmann, K. & Vecchio, K. S. Searching for high entropy alloys: A machine learning approach. *Acta Materialia* **198,** 178–222 (2020).

193. Maglogiannis, I. G. *Emerging artificial intelligence applications in computer engineering: Real word AI systems with applications in ehealth, HCI, information retrieval and pervasive technologies* (IOS Press, Washington, DC, 2007).

194. Wang, A. Y.-T. *et al.* Machine learning for materials scientists: An introductory guide toward best practices. *Chemistry of Materials* **32,** 4954–4965 (2020).

195. Zhu, W. *et al.* Machine learning-based hardness prediction of high-entropy alloys for laser additive manufacturing. *JOM* **75,** 5537–5548 (2023).

196. Han, Q., Lu, Z., Zhao, S., Su, Y. & Cui, H. Data-driven based phase constitution prediction in high entropy alloys. *Computational Materials Science* **215,** 111774 (2022).

197. Vazquez, G., Chakravarty, S., Gurrola, R. & Arróyave, R. A deep neural network regressor for phase constitution estimation in the high entropy alloy system Al-Co-Cr-Fe-Mn-Nb-Ni. *npj Computational Materials* **9,** 68 (2023).

198. Liu, Y., Wang, J., Xiao, B. & Shu, J. Accelerated development of hard high-entropy alloys with data-driven high-throughput experiments. *Journal of Materials Informatics* **2,** 3 (2022).

199. Zhang, J., Cai, C., Kim, G., Wang, Y. & Chen, W. Composition design of high-entropy alloys with deep sets learning. *npj Computational Materials* **8** (2022).

200. Akhil, B., Bajpai, A., Gurao, N. P. & Biswas, K. Designing hexagonal close packed high entropy alloys using machine learning. *Modelling and Simulation in Materials Science and Engineering* **29,** 85005 (2021).

201. Huang, X., Jin, C., Zhang, C., Zhang, H. & Fu, H. Machine learning assisted modelling and design of solid solution hardened high entropy alloys. *Materials & Design* **211,** 110177 (2021).

202. Chen, C., Ma, L., Zhang, Y., Liaw, P. K. & Ren, J. Accelerating the design of high-entropy alloys with high hardness by machine learning based on particle swarm optimization. *Intermetallics* **154,** 107819 (2023).

203. Islam, N., Huang, W. & Zhuang, H. L. Machine learning for phase selection in multi-principal element alloys. *Computational Materials Science* **150,** 230–235 (2018).

204. Bhandari, U., Rafi, M. R., Zhang, C. & Yang, S. Yield strength prediction of high-entropy alloys using machine learning. *Materials Today Communications* **26** (2021).

205. Bakr, M., Syarif, J. & Hashem, I. A. T. Prediction of phase and hardness of HEAs based on constituent elements using machine learning models. *Materials Today Communications* **31** (2022).

206. Liu, X., Zhang, J. & Pei, Z. Machine learning for high-entropy alloys: Progress, challenges and opportunities. *Progress in Materials Science* **131,** 101018 (2023).

207. Jain, R., Lee, U., Samal, S. & Park, N. Machine-learning-guided phase identification and hardness prediction of Al-Co-Cr-Fe-Mn-Nb-Ni-V containing high entropy alloys. *Journal of Alloys and Compounds* **956,** 170193 (2023).

208. Ye, Y. F., Wang, Q., Lu, J., Liu, C. T. & Yang, Y. High-entropy alloy: Challenges and prospects. *Materials Today* **19,** 349–362 (2016).

209. Machaka, R., Motsi, G. T., Raganya, L. M., Radingoana, P. M. & Chikosha, S. Machine learning-based prediction of phases in high-entropy alloys: A data article. *Data in Brief* **38,** 107346 (2021).

210. Gorsse, S., Nguyen, M. H., Senkov, O. N. & Miracle, D. B. Database on the mechanical properties of high entropy alloys and complex concentrated alloys. *Data in Brief* **21,** 2664–2678 (2018).

211. Borg, C. K. H. *et al.* Expanded dataset of mechanical properties and observed phases of multi-principal element alloys. *Scientific Data* **7,** 430 (2020).

212. Detor, A., Oppenheimer, S., Casey, R. & Crawford, C. Refractory high entropy alloy dataset with room temperature ductility screening. *Data in Brief* **45,** 108582 (2022).

213. Chen, S. *et al.* Fatigue dataset of high-entropy alloys. *Scientific Data* **9,** 381 (2022).

214. Zhang, L. *et al.* Machine learning reveals the importance of the formation enthalpy and atom-size difference in forming phases of high entropy alloys. *Materials & Design* **193** (2020).

215. Debnath, A. *et al.* Generative deep learning as a tool for inverse design of high entropy refractory alloys. *Journal of Materials Informatics* **1,** 3 (2021).

216. Jain, A. *et al.* Commentary: The Materials Project: A materials genome approach to accelerating materials innovation. *APL Materials* **1** (2013).

217. Pei, Z., Yin, J., Hawk, J. A., Alman, D. E. & Gao, M. C. Machine-learning informed prediction of high-entropy solid solution formation: Beyond the Hume-Rothery rules. *npj Computational Materials* **6** (2020).

218. Beniwal, D. *et al.* Distilling physical origins of hardness in multi-principal element alloys directly from ensemble neural network models. *npj Computational Materials* **8** (2022).

219. Bundela, A. S. & Rahul, M. R. Machine learning-enabled framework for the prediction of mechanical properties in new high entropy alloys. *Journal of Alloys and Compounds* **908** (2022).

220. Ottomano, F., De Felice, G., Gusev, V. V. & Sparks, T. D. Not as simple as we thought: A rigorous examination of data aggregation in materials informatics. *Digital Discovery* **3,** 337–346 (2024).

221. Lee, S. Y., Byeon, S., Kim, H. S., Jin, H. & Lee, S. Deep learning-based phase prediction of high-entropy alloys: Optimization, generation, and explanation. *Materials & Design* **197** (2021).

222. Gilligan, L. P. J., Cobelli, M., Taufour, V. & Sanvito, S. A rule-free workflow for the automated generation of databases from scientific literature. *npj Computational Materials* **9** (2023).

223. Dagdelen, J. *et al.* Structured information extraction from scientific text with large language models. *Nature Communications* **15,** 1418 (2024).

224. Sayeed, H. M., Mohanty, T. & Sparks, T. D. Annotating materials science text: A semi-automated approach for crafting outputs with Gemini Pro. *Integrating materials and manufacturing innovation* **13,** 445–452 (2024).

225. Risal, S., Zhu, W., Guillen, P. & Sun, L. Improving phase prediction accuracy for high entropy alloys with machine learning. *Computational Materials Science* **192** (2021).

226. Elreedy, D. & Atiya, A. F. A comprehensive analysis of synthetic minority oversampling technique (SMOTE) for handling class imbalance. *Information Sciences* **505,** 32–64 (2019).

227. Bansal, A. *et al.* Accelerated design of high entropy alloys by integrating high throughput calculation and machine learning. *Journal of Alloys and Compounds* **960** (2023).

228. Singh, S., Katiyar, N. K., Goel, S. & Joshi, S. N. Phase prediction and experimental realisation of a new high entropy alloy using machine learning. *Scientific Reports* **13,** 4811 (2023).

229. Hareharen, K., Panneerselvam, T. & Raj Mohan, R. Improving the performance of machine learning model predicting phase and crystal structure of high entropy alloys by the synthetic minority oversampling technique. *Journal of Alloys and Compounds* **991** (2024).

230. Hastie, T., Friedman, J. H. & Tibshirani, R. *The elements of statistical learning : Data mining, inference, and prediction* 2nd Edition. (Springer, New York, 2009).

231. Krishna, Y. V., Jaiswal, U. K. & Rahul, R. M. Machine learning approach to predict new multiphase high entropy alloys. *Scripta Materialia* **197,** 113804 (2021).

232. Yang, C. *et al.* A machine learning-based alloy design system to facilitate the rational design of high entropy alloys with enhanced hardness. *Acta Materialia* **222,** 117431 (2022).

233. Zeng, Y., Man, M., Bai, K. & Zhang, Y.-W. Revealing high-fidelity phase selection rules for high entropy alloys: A combined CALPHAD and machine learning study. *Materials & Design* **202,** 109532 (2021).

234. Debnath, A. & Reinhart, W. F. Investigating representation schemes for surrogate modeling of high entropy alloys. *Computational Materials Science* **230,** 112460 (2023).

235. Syarif, J., Elbeltagy, M. B. & Nassif, A. B. A machine learning framework for discovering high entropy alloys phase formation drivers. *Heliyon* **9,** e12859 (2023).

236. Li, M. *et al.* Composition driven machine learning for unearthing high-strength lightweight multi-principal element alloys. *Journal of Alloys and Compounds* **1008,** 176517 (2024).

237. He, J. *et al.* Machine learning-assisted design of high-entropy alloys with superior mechanical properties. *Journal of Materials Research and Technology* **33,** 260–286 (2024).

238. Wen, C. *et al.* Machine learning assisted design of high entropy alloys with desired property. *Acta Materialia* **170,** 109–117 (2019).

239. Zhang, Y. *et al.* Phase prediction in high entropy alloys with a rational selection of materials descriptors and machine learning models. *Acta Materialia* **185,** 528–539 (2020).

240. Li, S., Li, S., Liu, D., Zou, R. & Yang, Z. Hardness prediction of high entropy alloys with machine learning and material descriptors selection by improved genetic algorithm. *Computational Materials Science* **205,** 111185 (2022).

241. Machaka, R. Machine learning-based prediction of phases in high-entropy alloys. *Computational Materials Science* **188,** 110244 (2021).

242. James, G., Witten, D., Hastie, T. & Tibshirani, R. *An introduction to statistical learning : With applications in R* (Springer, New York, 2013).

243. Campbell, M. J. *Statistics at square one* 12th Edition. (Wiley Blackwell, Hoboken, N.J., 2021).

244. Akoglu, H. User's guide to correlation coefficients. *Turkish Journal of Emergency Medicine* **18,** 91–93 (2018).

245. Papageorgiou, S. N. On correlation coefficients and their interpretation. *Journal of Orthodontics* **49,** 359–361 (2022).

246. Lundberg, S. M. & Lee, S.-I. *A unified approach to interpreting model predictions* in *Proceedings of the 31st International Conference on Neural Information Processing Systems* (Curran Associates Inc., Long Beach, California, USA, 2017), 4768–4777.

247. Shapley, L. S. A value for n-Person games. *Contributions to the Theory of Games* **2,** 307–317 (1953).

248. Choudhury, A., Konnur, T., Chattopadhyay, P. P. & Pal, S. Structure prediction of multi-principal element alloys using ensemble learning. *Engineering Computations* **37,** 1003–1022 (2020).

249. Dalianis, H. *Evaluation Metrics and Evaluation* in *Clinical text mining: Secondary use of electronic patient records* 45–53 (Springer International Publishing, 2018).

250. Chang, Y.-J., Jui, C.-Y., Lee, W.-J. & Yeh, A.-C. Prediction of the composition and hardness of high-entropy alloys by machine learning. *JOM* **71,** 3433–3442 (2019).

251. Lee, C.-Y., Jui, C.-Y., Yeh, A.-C., Chang, Y.-J. & Lee, W.-J. Inverse design of high entropy alloys using a deep interpretable scheme for materials attribution analysis. *Journal of Alloys and Compounds* **976** (2024).

252. Wang, J., Kwon, H., Kim, H. S. & Lee, B.-J. A neural network model for high entropy alloy design. *npj Computational Materials* **9,** 60 (2023).

253. Zeng, Y. *et al.* Machine learning-based inverse design for single-phase high entropy alloys. *APL Materials* **10** (2022).

254. Debnath, A. *et al.* Comparing forward and inverse design paradigms: A case study on refractory high-entropy alloys. *Journal of Materials Research* **38,** 4107–4117 (2023).

255. Lee, J. *et al.* Machine learning-based inverse design methods considering data characteristics and design space size in materials design and manufacturing: A review. *Materials Horizons* **10,** 5436–5456 (2023).

256. Kaushik, N., Meena, A. & Mali, H. S. High entropy alloy synthesis, characterisation, manufacturing & potential applications: A review. *Materials and Manufacturing Processes* **37,** 1085–1109 (2021).

257. Liu, F., Xiao, X., Huang, L., Tan, L. & Liu, Y. Design of NiCoCrAl eutectic high entropy alloys by combining machine learning with CALPHAD method. *Materials Today Communications* **30,** 103172 (2022).

258. Zhang, Y. & Xing, Q. *High entropy alloys: Manufacturing routes* in *Encyclopedia of Materials: Metals and Alloys* (ed Caballero, F. G.) 327–338 (Elsevier, Oxford, 2022).

259. Huang, E. W. *et al.* Machine-learning and high-throughput studies for high-entropy materials. *Materials Science and Engineering: R: Reports* **147** (2022).

260. Moorehead, M. *et al.* High-throughput synthesis of Mo-Nb-Ta-W high-entropy alloys via additive manufacturing. *Materials & Design* **187** (2020).

261. Vecchio, K. S., Dippo, O. F., Kaufmann, K. R. & Liu, X. High-throughput rapid experimental alloy development (HT-READ). *Acta Materialia* **221** (2021).

262. Baird, S. G. & Sparks, T. D. What is a minimal working example for a self-driving laboratory? *Matter* **5,** 4170–4178 (2022).

263. MacLeod, B. P. *et al.* A self-driving laboratory advances the Pareto front for material properties. *Nature Communications* **13,** 995 (2022).

264. Szymanski, N. J. *et al.* An autonomous laboratory for the accelerated synthesis of novel materials. *Nature* **624,** 86–91 (2023).

265. Roy, A., Babuska, T., Krick, B. & Balasubramanian, G. Machine learned feature identification for predicting phase and Young's modulus of low-, medium- and high-entropy alloys. *Scripta Materialia* **185,** 152–158 (2020).

266. Sai, N. J., Rathore, P. & Chauhan, A. Machine learning-based predictions of fatigue life for multi-principal element alloys. *Scripta Materialia* **226** (2023).

267. Boettinger, W. J., Kattner, U. R., Moon, K.-W. & Perepezko, J. H. *Chapter Five - DTA and heat-flux DSC measurements of alloy melting And freezing* in *Methods for phase diagram determination* (ed Zhao, J. C.) 151–221 (Elsevier Science Ltd, Oxford, 2007).

268. Pawley, G. Unit-cell refinement from powder diffraction scans. *Journal of Applied Crystallography* **14,** 357–361 (1981).

269. Schneider, C. A., Rasband, W. S. & Eliceiri, K. W. NIH Image to ImageJ: 25 years of image analysis. *Nature Methods* **9,** 671–675 (2012).

270. Broitman, E. Indentation hardness measurements at macro-, micro-, and nanoscale: A critical overview. *Tribology Letters* **65** (2016).

271. ASTM-International. *Standard test method for microindentation hardness of materials* ASTM E384-22 (American Society for Testing and Materials, West Conshohocken, PA, Nov. 2022).

272. ASTM-International. *Metallic materials: Instrumented indentation test for hardness and materials parameters Part 1: Test method* ASTM 14577 (International Organization for Standardization, Geneva, Switzerland, 2021).

273. ASTM-International. *Standard terminology relating to nanotechnology* ASTM E2456-06 (American Society for Testing and Materials, West Conshohocken, PA, 2020).

274. Guo, Q. *et al.* In-situ characterization and quantification of melt pool variation under constant input energy density in laser powder bed fusion additive manufacturing process. *Additive Manufacturing* **28,** 600–609 (2019).

275. Pedregosa, F. *et al.* Scikit-learn: Machine learning in Python. *Journal of Machine Learning Research* **12,** 2825–2830 (2011).

276. Chollet, F. *Keras* 2015. `https://keras.io`.

277. Thermo-Calc. *The TC-Python API Programmer Guide 2024b* [Accessed: 2024-08-09]. `https://thermocalc.com/support/documentation/`.

278. Archard, J. Contact and rubbing of flat surfaces. *Journal of Applied Physics* **24,** 981–988 (1953).

279. Gorsse, S., Nguyen, M. H., Senkov, O. N. & Miracle, D. B. Corrigendum to database on the mechanical properties of high entropy alloys and complex concentrated alloys, data in brief 21 (2018) 2664–2678. *Data in Brief* **32,** 106216 (2020).

280. Wen, C. *et al.* Modeling solid solution strengthening in high entropy alloys using machine learning. *Acta Materialia* **212,** 116917 (2021).

281. Toda-Caraballo, I. & Rivera-Díaz-del-Castillo, P. E. J. Modelling solid solution hardening in high entropy alloys. *Acta Materialia* **85,** 14–23 (2015).

282. Caruana, R. & Niculescu-Mizil, A. An empirical comparison of supervised learning algorithms. *Proceedings of the 23rd International Conference on Machine learning* **2006,** 161–168 (2006).

283. Breiman, L. Random forests. *Machine Learning* **45,** 5–32 (2001).

284. Gilman, J. J. *Electronic basis of the strength of materials* (Cambridge University Press, 2003).

285. Zhao, D. Q., Pan, S. P., Zhang, Y., Liaw, P. K. & Qiao, J. W. Structure prediction in high-entropy alloys with machine learning. *Applied Physics Letters* **118,** 231904 (2021).

286. Lundberg, S. M. & Lee, S.-I. *A unified approach to interpreting model predictions* Conference Paper. 2017.

287. Lee, S., Chen, C., Garcia, G. & Oliynyk, A. Machine learning descriptors in materials chemistry used in multiple experimentally validated studies: Oliynyk elemental property dataset. *Data in Brief* **53,** 110178 (2024).

288. McInnes, L., Healy, J. & Melville, J. UMAP: Uniform manifold approximation and projection for dimension reduction. *arXiv preprint* (2018).

289. Kresse, T., Meinhard, D., Bernthaler, T. & Schneider, G. Hardness of WC-Co hard metals: Preparation, quantitative microstructure analysis, structure-property relationship and modelling. *International Journal of Refractory Metals and Hard Materials* **75,** 287–293 (2018).

290. Samsonov, G. V. *Mechanical properties of the elements* in *Handbook of the Physicochemical Properties of the Elements* 387–446 (Springer US, Boston, MA, 1968).

291. Stein, F., Palm, M. & Sauthoff, G. Structure and stability of Laves phases. Part I. Critical assessment of factors controlling Laves phase stability. *Intermetallics* **12,** 713–720 (2004).

292. Stein, F. & Leineweber, A. Laves phases: A review of their functional and structural applications and an improved fundamental understanding of stability and properties. *Journal of Materials Science* **56,** 5321–5427 (2021).

293. Wang, L. *et al.* Identification of Laves phases in a Zr or Hf containing γ-γ' Co-base superalloy. *Journal of Alloys and Compounds* **805,** 880–886 (2019).

294. Stein, F., Palm, M. & Sauthoff, G. Structure and stability of Laves phases. Part II. Structure type variations in binary and ternary systems. *Intermetallics* **13,** 1056–1074 (2005).

295. Lu, X. *et al.* Experimental investigation of phase equilibria in the Co–Hf system. *Journal of Alloys and Compounds* **627,** 251–260 (2015).

296. Chen, K., Peterson, E. & Thoma, D. $HfCo_2$ Laves phase intermetallics. Part I. Solubility limits and defect mechanisms. *Intermetallics* **9,** 771–783 (2001).

297. Levy, O., Hart, G. & Curtarolo, S. Hafnium binary alloys from experiments and first principles. *Acta Materialia* **58,** 2887–2897 (2010).

298. Fedorayev, I. I., Gusalova, M. I., Kerimov, E. Y., Chernyshev, V. V. & Slyusarenko, E. M. Crystal structure of ternary Laves phases in Co-Mn-Nb, Co-Mn-Ta, Co-Re-Nb, and Co-Re-Ta systems. *Russian Chemical Bulletin* **66,** 2009–2014 (2017).

299. Stein, F. *et al.* Experimental reinvestigation of the Co–Nb phase diagram. *Intermetallics* **16,** 785–792 (2008).

300. Šlapáková, M. *et al.* Atomic scale configuration of planar defects in the Nb-rich C14 Laves phase $NbFe_2$. *Acta Materialia* **183,** 362–376 (2020).

301. Kim, Y.-K., Yu, J.-H., Kim, H. S. & Lee, K.-A. In-situ carbide-reinforced CoCrFeMnNi high-entropy alloy matrix nanocomposites manufactured by selective laser melting: Carbon content effects on microstructure, mechanical properties, and deformation mechanism. *Composites Part B: Engineering* **210,** 108638 (2021).

302. Xu, F., Gao, X., Cui, H., Song, Q. & Chen, R. Lightweight and high hardness $(AlNbTiVCr)_{100-x}Ni_x$ high entropy alloys reinforced by Laves phase. *Vacuum* **213,** 112115 (2023).

303. Livingston, J. In situ composites - A review. *Composites* **4,** 70–78 (1973).

304. Liu, X. *et al.* Improving high-temperature mechanical properties of cast CrFeCoNi high-entropy alloy by highly thermostable in-situ precipitated carbides. *Journal of Materials Science & Technology* **72,** 29–38 (2021).

305. Xu, H. *et al.* Effects of boron or carbon on solidification behavior of Co-Ni-Al-W-based superalloys. *Journal of Alloys and Compounds* **891,** 161965 (2022).

306. Diao, G., He, A., Wu, M., Xu, Z. & Li, D. Y. Using C to enhance the wear resistance of $AlCrFe_2Ni_4Ti_2$ high-entropy alloy via replacing brittle phases by in-situ formed TiC in a matrix with improved ductility. *Wear* **523,** 204822 (2023).

307. Tsai, M.-H., Tsai, R.-C., Chang, T. & Huang, W.-F. Intermetallic phases in high-entropy alloys: Statistical analysis of their prevalence and structural inheritance. *Metals* **9,** 247 (2019).

308. Stein, F. & Leineweber, A. Laves phases: A review of their functional and structural applications and an improved fundamental understanding of stability and properties. eng. *Journal of Materials Science* **56,** 5321–5427 (2020).

309. Liu, S. S., Zhang, M., Zhao, G. L., Wang, X. H. & Wang, J. F. Microstructure and properties of ceramic particle reinforced FeCoNiCrMnTi high entropy alloy laser cladding coating. *Intermetallics* **140,** 107402 (2022).

310. Qin, G. *et al.* CoCrFeMnNi high-entropy alloys reinforced with Laves phase by adding Nb and Ti elements. *Journal of Materials Research* **34,** 1011–1020 (2019).

311. Shatynski, S. R. The thermochemistry of transition metal carbides. *Oxidation of Metals* **13,** 105–118 (1979).

312. Porter, D. A., Easterling, K. E. & Sherif, M. Y. *Phase transformations in metals and alloys* 3rd Edition. (Taylor and Francis Group, Boca Raton, Florida, 2009).

313. Courtney, T. H. *Mechanical behavior of materials* 2nd Edition. (McGraw-Hill, Boston, 2000).

314. Bhattacharyya, A. & Maurice, D. On the evolution of stresses due to lattice misfit at a Ni-superalloy and YSZ interface. *Surfaces and Interfaces* **12,** 86–94 (2018).

315. Nakamura, K. & Yashima, M. Crystal structure of NaCl-type transition metal monocarbides MC (M=V, Ti, Nb, Ta, Hf, Zr), a neutron powder diffraction study. *Materials Science and Engineering: B* **148,** 69–72 (2008).

316. Zagorac, D., Muller, H., Ruehl, S., Zagorac, J. & Rehme, S. Recent developments in the Inorganic Crystal Structure Database: Theoretical crystal structure data and related features. *Journal of Applied Crystallography* **52,** 918–925 (2019).

317. Taylor, J. R. *An introduction to error analysis: The study of uncertainties in physical measurements* 3rd Edition. (University Science Books, New York, 2022).

318. Farquhar, L. *et al.* In-situb alloying of CoCrFeNiX high entropy alloys by selective laser melting. *Metals* **12** (2022).

319. Christofidou, K. A. *et al. Eutectic superalloys for laser powder bed fusion* in *Superalloys 2024* 860–870 (The Minerals, Metals & Materials Society, 2024).

320. Cao, J. *et al.* Manufacturing of advanced smart tooling for metal forming. *CIRP Annals* **68,** 605–628 (2019).

321. Zhang, W., Chabok, A., Kooi, B. J. & Pei, Y. Additive manufactured high entropy alloys: A review of the microstructure and properties. *Materials & Design* **220** (2022).

322. Ostovari Moghaddam, A., Shaburova, N. A., Samodurova, M. N., Abdollahzadeh, A. & Trofimov, E. A. Additive manufacturing of high entropy alloys: A practical review. *Journal of Materials Science & Technology* **77,** 131–162 (2021).

323. Torralba, J. M. & Campos, M. High entropy alloys manufactured by additive manufacturing. *Metals* **10** (2020).

324. Chen, S., Tong, Y. & Liaw, P. K. Additive manufacturing of high-entropy alloys: A review. *Entropy* **20** (2018).

325. Chen, P., Li, S., Zhou, Y., Yan, M. & Attallah, M. M. Fabricating CoCrFeMnNi high entropy alloy via selective laser melting in-situ alloying. *Journal of Materials Science & Technology* **43,** 40–43 (2020).

326. Strobl, D. *et al.* Efficient bead-on-plate weld model for parameter estimation towards effective wire arc additive manufacturing simulation. *Welding in the World* **68,** 969–986 (2024).

327. Fardan, A. *et al.* Fine-tuning melt pools and microstructures: Taming cracks in powder bed fusion—laser beam of a non-weldable Ni-base superalloy. *Materialia* **34,** 102059 (2024).

328. Zhou, N. *et al. Development of a new alumina-forming crack-resistant high-γ' fraction Ni-base superalloy for additive manufacturing* in *Superalloys 2020* (Springer International Publishing, 2020), 1046–1054.

329. Livera, E. *et al.* Microstructural control of LPBF Inconel 718 through post processing of intentionally placed AM discontinuity distributions. *Materialia* **36** (2024).

330. Roy, A. & Balasubramanian, G. *Phases and Young's modulus dataset for high entropy alloys* [Accessed: 2024-11-18]. Aug. 2020. `https://edx.netl.doe.gov/dataset/phases-and-young-s-modulus-dataset-for-high-entropy-alloys`.

331. Fan, X. *et al.* Dataset for fracture and impact toughness of high-entropy alloys. *Scientific Data* **10,** 37 (2023).

332. Wilkinson, M. D. *et al.* The FAIR Guiding Principles for scientific data management and stewardship. *Scientific data* **3,** 1–9 (2016).

333. Peivaste, I., Jossou, E. & Tiamiyu, A. A. Data-driven analysis and prediction of stable phases for high-entropy alloy design. *Scientific Reports* **13,** 22556 (2023).

334. Page, M. J. *et al.* Data and code availability statements in systematic reviews of interventions were often missing or inaccurate: a content analysis. *Journal of Clinical Epidemiology* **147,** 1–10 (2022).

335. Senkov, O. N. & Miracle, D. B. Effect of the atomic size distribution on glass forming ability of amorphous metallic alloys. *Materials Research Bulletin* **36,** 2183–2198 (2001).

336. Daams, J. L. C., Villars, P. & van Vucht, J. H. N. *Atlas of crystal structure types for intermetallic phases* (ASM International, Materials Park, OH, 1991).

337. *International tables for X-ray crystallography* (eds MacGillavry, C. H. & Rieck, G. D.) (Kynoch Press, Birmingham, England, 1968).

338. Winter, M. *WebElements™ Periodic Table, Professional Edition* University of Sheffield, UK. [Accessed: 2024-03-03]. `https://www.webelements.com`.

339. Allred, A. Electronegativity values from thermochemical data. *Journal of Inorganic and Nuclear Chemistry* **17,** 215–221 (1961).

340. Keeler, J. & Wothers, P. *Chemical structure and reactivity: An integrated approach* 2nd Edition. (Oxford University Press, New York, 2014).

341. Qiao, L., Liu, Y. & Zhu, J. A focused review on machine learning aided high-throughput methods in high entropy alloy. *Journal of Alloys and Compounds* **877,** 160295 (2021).

342. Hao, Y.-J., Zhang, L., Chen, X.-R., Li, Y.-H. & He, H.-L. Phase transition and elastic constants of zirconium from first-principles calculations. *Journal of Physics: Condensed Matter* **20,** 235230 (2008).

343. Lyapin, A. G., Gromnitskaya, E. L., Yagafarov, O. F., Stal'gorova, O. V. & Brazhkin, V. V. Elastic properties of crystalline and liquid gallium at high pressures. *Journal of Experimental and Theoretical Physics* **107,** 818–827 (2008).

344. Gaultois, M. W. *et al.* Data-driven review of Thermoelectric materials: Performance and resource considerations. *Chemistry of Materials* **25,** 2911–2920 (2013).